

**REACTIONS IN SMALL CLUSTERS
STUDIED BY
TIME-RESOLVED LASER SPECTROSCOPY**

Thesis by
Lawrence Weimin Peng

*In Partial Fulfillment of the Requirements
for the Degree of
Doctor of Philosophy*

California Institute of Technology
Pasadena, California

1991
(submitted 1 October 1990)

ABSTRACT

Molecular solute/solvent clusters are an ideal medium for studying solvent effects from the van der Waals complex to the solution bulk limit. Such clusters are conveniently produced using molecular beams. Thus, a new apparatus for making time-resolved measurements of large neutral clusters was constructed and is described in detail herein. The apparatus consists of a molecular beam interrogated by two picosecond lasers. Detection is by laser-induced fluorescence and resonance-enhanced multiphoton ionization. The laser and molecular beam combination permits the study of the role of solvation on the solute's excited electronic-state dynamics for a specific cluster size.

Picosecond time-resolved laser spectroscopy is applied to neutral solute/solvent clusters to study the effect of solvation on charge-transfer reactions in real-time. *p*-(Dimethylamino)benzonitrile (4-DMABN) and α -naphthol (α -NpOH) are used as model systems since the charge-transfer is solvent dependent. The S_1 excited state dynamics of gas-phase 4-DMABN has been studied both in a supersonic jet expansion and in a thermalized vapor. The jet studies show that 1:1 complexes with water, ammonia, methanol, and acetonitrile do not undergo charge-transfer. At higher jet temperatures, emission is observed from 4-DMABN self-complexes. Charge-transfer fluorescence from 4-DMABN self-complexes is observed in a thermalized vapor. Studies have been done on the S_1 excited state dynamics of gas phase α -NpOH clustered with ammonia, piperidine and water. The measurements reveal cluster-size dependent dynamics for α -NpOH clustered with ammonia and piperidine, but not with water. The fast-time dynamics in the ammonia and piperidine clusters indicates the occurrence of proton-transfer reactions in these solute/solvent clusters. The cluster size, solvent dependence and the timescale for the reactions serve to emphasize the importance of the local solvent environment.

ACKNOWLEDGEMENTS

The past six years have witnessed many new and exciting scientific discoveries by the Zewail group, and being a member of the Zewail team has afforded me the opportunity to learn many new techniques and technologies. To accomplish this has required the support of many individuals, of whom several deserve mention.

First, I would like to thank my research advisor, Professor Ahmed Zewail, for allowing me to be a participant in his group, and for his support and guidance during my graduate studies. I must express admiration for the long hours that he is spending to keep the operation running smoothly and generously funded. The research presented in this thesis was supported by grants from the National Science Foundation and the Air Force Office of Scientific Research.

All members of the Zewail group have, at one time or another, given advice concerning experiments and other problems for which I am grateful. Several individuals stand out in particular. Dr. Brian Keelan, formerly of the Zewail group, was my student-mentor for my first two years. From him I learned patience and organization. His willingness to pass on to a novice all his knowledge concerning the science and engineering of the laboratory he had constructed (and which I inherited) proved to be invaluable, especially for the work presented in Chapter four. The new laboratory for doing time-resolved experiments on clusters, which I helped to construct, could not have been built without the extensive contributions of past and present group members: Peijun Cong (electronics), Dean Willberg (laser system), and Dr. Jack Breen (molecular beam). I also thank Dr. Martin Gruebele, currently of the Zewail group, and Peijun Cong for assistance in proofreading this manuscript.

The support of the staff members also deserves special acknowledgement. Fran Bennett never failed to handle numerous urgent purchase requests. Tom Dunn of the electronics shop always had the knack of solving our electronics problems the first time. The members of the chemistry department machine and instrument shops (Tony Stark, Ray Garcia, Guy Duremberg, Jess Miller, Paul Svitek, and the retired Jim Gangwer and Delmer Dill) provided many hours of assistance with the design and construction of our laboratory and other equipment for which it is impossible to thank them adequately. Without the staff's good cheer and tolerance of my neverending demands, my graduate studies would have taken much longer.

TABLE OF CONTENTS

VOLUME ONE

1. Introduction	1
References	13
2. Formation of Neutral Clusters Using Supersonic Beams	18
2.1. Introduction	19
2.2. Supersonic Beams	21
2.3. Supersonic Cluster Beams	25
1. Modeling of Supersonic Cluster Beams	25
2. Characterization of Supersonic Cluster Beams	33
2.4. Empirical Observations of Cluster Formation in Supersonic Jets	35
1. Pressure and Temperature Effects	35
2. Influence of the Nozzle Geometry	36
3. Pulsed versus Continuous Sources	41
4. Mixed Expansions	42
2.5. Effusive and Flow Aggregation Techniques	43
2.6. References	45
Figure Captions	49
Figures	50
3. Apparatus for Cluster Experiments by Time-Resolved Pump-Probe Laser Spectroscopy	53
3.1. Introduction	54
3.2. The Molecular Beam Apparatus	55
1. Vacuum Chambers	56
2. Nozzle Assembly	58
3. The Ionizer Cube	59
4. Electronics	61
3.3. Detection Methods	62
1. Laser-induced Fluorescence	62
2. Time-of-Flight Mass Spectrometry	62
3. The Electron Impact/Time-of-Flight Source	64
1. TTL Pulse Delay Generator Box	65
2. Wavetek 50MHz Pulse Generator	66
3. The Electron Impact (EI) Box	66
A. AC Power	66
B. Filament Power	66
C. Bias Voltage	67
D. Gate Pulse Voltage and Trigger	67
E. Repeller Pulse Voltage and Trigger	67
F. Outputs	67
4. Miscellaneous	68

3.4.	The Two-Color Picosecond Laser System	68
1.	The Mode-Locked Q-Switched Nd:YAG Laser	69
2.	The Cavity-Dumped Dye Lasers	69
3.	Time Resolution by Michelson Interferometry	71
4.	Pulse Characterization	72
5.	Optimizing and Aligning the Laser System	73
1.	The Mode-Locked Q-Switched Nd:YAG Laser	73
2.	The Cavity-Dumped Dye Lasers	74
3.5.	Data Acquisition and Analysis	76
3.6.	References	79
	Figure Captions	80
	Figures	81
4.	Stepwise Solvation of the Intramolecular-charge-transfer molecule p-(Dimethylamino)benzonitrile	92
	Abstract	93
4.1.	Introduction	94
4.2.	Experimental	97
4.3.	Results	99
	A. Isolated DMABN	99
	B. Complexes of Solvent/DMABN	100
	C. Self-Complexes of DMABN	102
4.4.	Conclusions	105
4.5.	References	107
	Figure Captions	110
	Figures	112
5.	Real-time Probing of Reactions in Clusters I: α-Naphthol with Ammonia	121
	References	125
	Figure Captions	128
	Figures	129
6.	Real-time Probing of Reactions in Clusters II: α-Naphthol with Ammonia, Piperidine, and Water	131
	Abstract	132
6.1.	Introduction	133
6.2.	Experimental	136
	A. The Pump-Probe Apparatus	136
	1. Expansion and Buffer Chambers	137
	2. The TOF Chamber	139
	3. Time-of-Flight Mass Spectrometer	139
	4. Electronics	140
	5. The Mode-Locked Q-Switched Nd:YAG Laser	141
	6. The Cavity-Dumped Dye Lasers	142
	7. Data Acquisition and Analysis	143
	B. Picosecond Fluorescence Apparatus	144

6.3. Results & Discussion	145
A. Preliminaries and Spectroscopy	145
B. Picosecond Pump-Probe Studies: α -NpOH•(NH ₃) _n	146
C. Picosecond Pump-Probe Studies: α -NpOH•(C ₅ H ₁₁ N) _n and α -NpOH•(H ₂ O) _n	148
D. Discussion	149
6.4. Conclusions	159
6.5. References	160
Tables	165
Figure Captions	168
Figures	169
 7. Summary and Conclusions	 178
 Appendix	
Dynamics of Intramolecular Vibrational Energy Redistribution in Deuteriated Anthracenes: Rotational Band Contour Analysis and Time-Resolved Measurements	184
Abstract	185
I. Introduction	186
II. Experimental Section	187
III. Vibrational-State Densities	189
A. Anthracene-h ₁₀	189
B. State Densities of the Isotopes	190
IV. Results and Discussion	191
A. Fluorescence Excitation Spectra	191
B. Dispersed Fluorescence Spectra	193
C. Temporal Behavior	194
D. Rotational Band Contour Analysis: Medium Resolution	194
E. Computer Simulation of Contours	196
F. The Restricted IVR Region: An Example	198
1. Frequency-Resolved Spectra	198
2. Temporal Behavior	200
V. Conclusions	202
VI. References	203
Tables	205
Figure Captions	216
Figures	218

TABLE OF CONTENTS

VOLUME TWO

1. Introduction to the Data Acquisition and Data Analysis Programs .	1
References	5
 2. System and Hardware Requirements	 6
2.1. Introduction	7
2.2. System and Hardware	7
2.3. NI-488 Software Installation	8
2.4. References	12
 3. Overview of the Data Acquisition and Data Analysis Programs. . .	 13
3.1. Introduction	14
3.2. General Overview	14
3.3. Menu Summary	16
1. APPLE	16
2. FILE and EDIT	16
3. COMMUNICATIONS (<i>Data Acquire</i>)	16
4. COLLECTION	17
5. FITTING.	18
6. DISPLAY	18
7. TRANSFORM	18
8. FUNCTIONS (<i>Data Analysis</i>)	19
9. WINDOWS	19
3.4. Use of special features	19
1. Communication Menu Dialog Boxes (<i>Data Acquire</i>)	19
1. The Unidex Dialog Box	20
2. The CAMAC Crate Dialog Box	21
3. The Boxcar Dialog Box	23
4. The Spex CD2A Dialog Box	23
2. Selective Plotting	25
3. Data Acquisition Control	26
4. Fitting and Convolution	28
1. Nonlinear Least Squares Fitting	28
2. Convolution	30
3. Nonlinear Least Squares Convolution	32
5. Data Manipulation	33
6. Using the Second Plot Window	34
7. Reconstructing Transients from Mass Spectra	35
8. Saving Data to Files	36
3.5. References	37
Tables	38
Figure Captions	40
Figures	43

4. Global Structure of the Data Acquisition and Data Analysis Programs	65
4.1. Introduction	66
4.2. Overview of Program Operation	67
4.3. Program Segmentation	69
4.4. Program Resources	70
1. Menu Resources	72
2. Dialog Resources	72
3. Window Resources	73
4. Icon Resources	73
5. Version Resources	74
4.5. Data Arrays and Memory Allocation	75
4.6. Notes about Numerical Recipes Routines	76
4.7. Filenames and Data File Creation	77
4.8. Variable Type Conversions	78
4.9. Plotting on the Plot Window	79
4.10. References	81
Figure Captions	82
Figures	83
 5. Source Files and Libraries Description	 87
5.1. Introduction	88
5.2. Macintosh Interface	92
5.3. Memory Allocation	98
5.4. Plotting	99
5.5. File Management	100
5.6. Data Analysis	102
5.7. Data Acquisition	106
5.8. Project Name and Resources	109
5.9. C Programming Environment Libraries	109
5.10. References	111
 6. Program Modification: A Tutorial	 112
6.1. Introduction	113
6.2. Creating the Resources	114
6.3. Modifying the Code to Use the New Resources	115
6.4. Code for Calculation and Plotting	119
6.5. Testing and Final Comments	120
Figure Captions	122
Figures	123

7. Troubleshooting	131
7.1. Introduction	132
7.2. Loss of Communication between the Computer and Data Acquisition Boards	132
7.3. Crashes due to a Bad Trigger	133
7.4. Crashes that are due to the Delay Line Unidex Controller	133
7.5. Crashes that are due to the Data Acquisition Boards or Bad Data Acquisition System Files	134
7.6. Crashes that are due to a Bad Data File	135
7.7. Crashes due to the Development Environment	136
7.8. References	137

8. Development Environment Parameters	138
Reference	141
Table	142

Appendix

Update Notes for National Instruments NI-488 and LabDriver Software	144
---	-----

CHAPTER 1

INTRODUCTION

A fundamental problem in chemical dynamics is to understand the properties of chemical reactions. The traditional Arrhenius description is a phenomenological one that describes the temperature dependence of reaction rates in the bulk, while the transition-state theory provides a useful interpretation of the Arrhenius rate law in terms of molecular properties. Contemporary kineticists are concerned with the interpretation of chemical reactions at the molecular level by developing a microscopic picture of the reaction dynamics. The goal is the detailed understanding of how the initial conditions affect the outcome of a chemical reaction. Such initial conditions include the reactant structure and partitioning of energy in the activation process between the various degrees of freedom. The reaction outcome is specified by how the initial conditions affect the products. Of interest is the quantum state of the products, and the rate at which the products are formed. This microscopic picture is crucial to understanding the multidimensional potential energy surface, and the detailed quantum description of chemistry on a state-to-state level.

The challenge to experimentalists is to design experiments capable of defining the aforementioned initial conditions, and then to be able detect products with quantum state resolution. Over the past two decades, major advances have come from application of molecular beam and laser techniques [1]. Using molecular beams permits the study of atomic and molecular processes in the absence of external perturbations. Molecular beams formed from supersonic expansions have the added advantage of being able to cool molecules rapidly to temperatures on the order of 4-50 K, which greatly simplifies the spectroscopy by minimizing vibrational and rotational congestion. The result of this fast temperature reduction is that the molecular beam expansion quenches the internal motions of the molecules, and the final ensemble on which the experiments are performed is approximately microcanonical. The application of lasers to molecular spectroscopy provides a sensitive probe of molecular quantum states. Selective detection of most organic molecules is possible because of the wide tunability of dye lasers.

The application of ultrashort laser pulses with picosecond or femtosecond resolution to molecular beams has enabled the reaction process to be viewed directly [1b-d]. The experiment begins with the excitation of a molecular beam by an ultrashort laser pulse. One then directly time-resolves the fluorescence, or uses a second ultrashort laser pulse (delayed in time) to probe a transient species directly. Since the timescale for any sequence of elementary steps constituting a chemical reaction is dictated by the rapidity of the nuclear rearrangement, typically in the range of femtoseconds to picoseconds, ultrafast time-resolved laser spectroscopy reveals the transitional reaction dynamics by directly time-resolving the nuclear motion. Thus, using ultrashort laser pulses allows one to observe the actual passage through the transition states and to view them in real-time. This real-time approach provides complementary information to studies, such as crossed-beam experiments [*e.g.*, 2], and photofragment product-state distributions [*e.g.*, 3], which address the asymptotic properties of the reaction. Asymptotic studies have established that chemical reactions may be described in terms of collisions between reactant species. They also give information concerning the strength and range of intermolecular forces and the effect of precollision states on the products. However, the results of these asymptotic studies are effectively time-integrated over the course of the collision, whereas real-time measurements focus on providing a direct view of the reaction process.

The molecular systems of interest in this thesis are clusters, and in addition to producing cold beams of isolated molecules, molecular beams (both subsonic and supersonic) are often used for the formation and study of clusters [4-6]. A cluster is broadly defined as a chemical species held together by forces weaker than the average chemical bond. The nucleation-condensation forces usually involved are van der Waals or hydrogen bonding in molecular clusters, electrostatic forces in ionic clusters, and metal-metal bonding in metal clusters [4]. Using molecular beams, one can produce and study clusters ranging in size from dimers to thousands and millions of molecules [*e.g.*, 7-13].

Of particular importance is that the clusters are produced under the controlled conditions of the molecular beam. By suitable adjustment of the expansion conditions, it is possible to produce clusters of almost any size and composition. Thus it is possible to conduct cluster studies as a function of specific cluster size.

Much of the early work on clusters focussed on characterizing the intermolecular potential in clusters, and determining their structure [14], and this work continues today. It has largely dealt with small clusters, dimers and trimers, because of their relatively simple spectra. For example, small van der Waals molecules generated by a molecular beam have been used as model systems for studying photochemical processes such as vibrational predissociation [15-16], unimolecular decomposition and intramolecular vibrational energy redistribution (IVR) [14-16]. Time-resolved experiments on the predissociation of clusters have been carried out [17,18]. Of interest was the role of IVR in the predissociation, and the question of whether the rates of dissociation could be predicted by RRKM theory. Another time-resolved study demonstrated mode-dependent predissociation of clusters of t-stilbene-rare gases [18,19].

Clusters are thought to provide a bridge for understanding the dynamics of a system in the gas phase versus its behavior in the condensed phase. Being larger than ordinary molecules but smaller than bulk objects, clusters represent a state of matter that is intermediate between molecules and the condensed phase. Thus, a common theme has been to use clusters to understand the transition from atomic and molecular properties to the bulk with increasing cluster size. Of interest is how the process is influenced by solvation and how large a solvent shell must be to make a bulk solution phase reaction thermodynamically favorable. Clusters are attractive for study since they present small theoretically tractable systems that can be used to test our understanding of solids, surfaces, catalysis, liquids, solvation, and other finite-system properties [20]. Clusters are also important in fields ranging from atmospheric chemistry to industrial catalysis. Their

reactivity and large surface-to-volume ratio make them useful for studying the solid state, crystal growth, and selective chemical catalysis [20]. Furthermore, nanometer-sized clusters can be used to construct new materials with enhanced mechanical and electro-optical properties [21].

In the case of solvation, clusters may be useful for understanding how the solvent molecules affect the properties of chemical reactions. The extent of solvation is often of crucial importance since reaction intermediates and products can be stabilized by the solvent. The solvent may play a passive role, as in the cage effect where the solvent traps the reacting solute particles within a volume, or the solvent may be a direct participant in the reaction. In the liquid phase, the very short times between collisions with the surrounding molecules (femtosecond to picosecond) bring an intrinsically short timescale to elementary relaxation processes involving energy or phase-coherence loss through interaction with the environment. Molecules move, exchange vibrational energy with their surroundings, transfer charge, undergo excitation; dissociate and undergo geminate recombination and respond to sudden changes in their environment on a picosecond or shorter timescale [22,23]. Some of the phenomena are unique to the condensed phase, requiring a surrounding heat bath or dielectric medium. Liquid-phase dynamics is very complex because of the fluctuating nature of the solvent environment. The study of the solvent effect at the molecular level poses difficulties because the reaction coordinate is complicated, typically involving both intramolecular motions of the solute, and extensive coupling to motion of the adjacent solvent molecules during the creation of the reaction products. Attempts to understand the influence of the solvent have led to investigations that compare picosecond kinetics of gas phase reactions to that in solvents with different viscosities [24]. Such comparisons of gas-phase and solution phase studies have revealed extraordinary differences in the kinetics, which attest to the profound influence of the solvent.

Spectroscopy provides a variety of experimental routes for the exploration of the structures, energetics, and dynamics of clusters. While the spectroscopy of isolated molecules and crystalline solids is highly advanced, there is a *terra incognita* between the isolated molecule and the bulk limit that remains to be explored by investigating finite systems such as atomic or molecular clusters. The experimental methods typically couple various laser and mass spectroscopic techniques [*e.g.*, 25-35], such as laser-induced fluorescence (LIF) and resonance-enhanced multiphoton ionization (REMPI), with molecular beams. REMPI and LIF are complementary, but differ in two significant respects. REMPI is more species-specific for different masses, and it can distinguish between species that have similar LIF spectra. The properties of the cluster are reflected by the spectroscopic properties of a probe atom or molecule in the cluster via the cluster-probe interaction [25]. This allows one to measure electronic absorption and emission spectra of size-selected clusters and hence to follow the environmental, internal, and size dependence of the thermodynamic, kinetic, and other photophysical and photochemical and spectral properties. A detailed understanding of the physics and chemistry of clusters would also allow a more precise description of liquids, amorphous solids, and disordered materials, for which our present knowledge is still fairly rudimentary.

Investigators have used microsolvent clusters, consisting of a probe atom or molecule attached to a number of solvent molecules, to study solvation as a function of specific solvent-cluster size [*e.g.*, 25, 36-39,40(a)-(c)]. This enables one to study the role of solvation on the physical, chemical, and dynamical behavior from the solvent-solute van der Waals complex to the solution bulk limit. Many questions arise when describing solvent clusters or the solvation process on an atomic scale [25]: What are the solvent cluster structures? To what extent is the structure of the solvent-cluster representative of the undoped cluster? Does the solute control the solvent cluster structure? Do solvation isomers exist, and are they energetically competitive with the minimum-energy structure?

How strong are the interactions that are responsible for solvation, and how do these interactions affect the behavior of the solute? To what extent do the cluster structures depend on temperature? Are the clusters solidlike or liquidlike and can solid-liquid transitions be observed? Is it possible to identify the first and successive solvent layers? Is it possible to see the appearance of bulklike behavior already in finite clusters? Studies in cold microsolvent clusters are complementary to investigations of gas-phase ion chemistry in which a wide range of protonated solvent clusters have been studied. The gas-phase ion studies have yielded a wealth of thermochemical data on ionic solvent clusters at room temperature or above [41-44].

In this thesis, excited-state electron- and proton-transfer reactions are of interest. Such reactions form the basis for many important natural processes such as enzyme catalysis [45] and photosynthesis [46,47], as well as for many artificial processes such as organic conductors and superconductors and the generation of electricity. Many of these processes occur in the condensed phase. Compared to the gas phase, the condensed phase environment can markedly influence the energetics of chemical reactions. This is especially true for charge-transfer reactions since the interaction energy of the charge with the solvent can approach chemical binding energies. Studies in solution have shown experimentally that changes in nuclear or molecular configuration control the dynamics of electron- [48] and proton-transfer processes [49] in molecules, the latter differing in that localized configuration changes are important. Fast charge rearrangements in excited states may involve charge redistribution within a molecule altered by excitation, or the reorganization of medium dipoles around the altered molecular dipole. The medium can be the solvent, the molecule itself or an external matrix. The effect of solvation on charge-transfer processes might be systematically investigated at the molecular level if the charge-separated system is studied in an intermediate state between the gas phase and the condensed phase. Condensed phase studies give results that are averaged over all solvent molecules.

Microsolvent cluster studies have been applied to a wide range to solute and solvent combinations. These include diatomic molecules in rare gas clusters [14,50], large nonpolar aromatic molecules in rare gas clusters [51], polar aromatic molecules in hydrogen-bonding solvents [40] and solvated electrons in polar solvents [52]. These studies investigated the effect of solvent on the solute intramolecular dynamics. The major effects of solvent clusters on the solute electronic absorption spectra are to shift the peak locations, to broaden the width of the bands, and to change the band shapes. Key experimental findings are that the changes may be very specific and highly dependent on cluster size, and the trends in the band shifts, bandwidths, and band shapes can be very nonmonotonic. The above systems are all nonreacting in nature.

Recently, microsolvent clusters have been used to study chemical reactions as a function of specific solvent cluster size [*e.g.*,25,33,36-39,40,53-57]. In this vein, charge-transfer reactions are of interest since they can be both intra- and intermolecular in nature. Pertinent to this thesis is intermolecular excited-state proton transfer from a seed molecule to the solvent shell. The acidities and basicities of optically excited molecules are different from the ground states [56]. Aromatic amines and alcohols are more acidic in the S_1 state, while aromatic acids, ketones, and certain nitrogen heterocyclics are more basic. With ultrafast techniques, the initial excited state can be formed by photoexcitation, and the equilibrium constant for proton dissociation or association can be changed on a very short timescale. From spectral emission data, distinct solvent-size threshold effects have been inferred for the excited states such as α -naphthol [57], β -naphthol [55], phenol [33,36], and for the ground electronic state of aniline cation [37]. However, the emission data were sensitive only to the equilibria between reactant and product. Direct time-resolved measurements of reactions in clusters are currently few [33,53-55]. Studies done in matrices [55] and by pump-probe molecular beam studies [33,54] have clearly

demonstrated a solvent-size dependence for the proton-transfer dynamics, and for the recombination dynamics of the anion of molecular iodine solvated by carbon dioxide [53].

Previous work on solution-phase excited-state proton transfer (ESPT) indicated that the change in the fluorescence maximum is pH-dependent [58] because of changes in the excited-state acid dissociation constant (pK_a^*). Emission studies demonstrate that the deprotonated acid emits at one wavelength, whereas the neutral alcohol emits at a different wavelength. The most straightforward method for determination of the pK_a^* is the Förster cycle [58]. Weller studied the solution kinetics of ESPT reactions in many organic acids and bases [59], and extended the initial, largely thermodynamic theories of Förster as embodied in the Förster cycle [58]. Weller's analysis was based on both steady-state and time-resolved measurements. The validity of this approach was demonstrated by obtaining values for pK_a^* that were in agreement with the results of Förster cycle calculations. pK_a^* changes of up to six units have been observed [60]. Furthermore, Weller's analysis, which determines the excited-state acid-base equilibrium constant based on the ratio of the forward and reverse ESPT reaction rates, avoids the implicit assumptions of the Förster cycle [61]. Since this pioneering work, numerous investigations of ESPT reactions using a variety of experimental techniques have been reported and reviewed [56]. The vast majority of previous studies of ESPT relied extensively on steady-state spectroscopy and a Förster cycle analysis. Because of this approach, the results of such studies focused exclusively on the role of the solute structure and reactivity in ESPT reactions. A smaller number of kinetic studies of ESPT using either time-resolved or steady-state spectroscopic methods have attempted to evaluate the influence of solvent on the ESPT process [62-64].

In addition to studies using microsolvent clusters, the microscopic understanding of acid-base reactions has been advanced from other fields. A wide range of gas-phase ion chemistry studies have dealt with solvation of protons in gas-phase clusters [41-43], and have provided insights into the energetics and structures of ionic microsolvent clusters.

Photoemission studies on frozen and liquid aqueous solutions have probed directly the solvation stabilization of individual ions (conjugate bases) [65]. Picosecond-emission studies employing fluorescent excited-state acids in solution have recently enabled highly detailed kinetic investigations of the primary steps in proton transfer in fluid media [66].

This thesis is composed of two volumes. This volume, Volume One, constitutes the main body of the thesis and is concerned with addressing the given scientific problem. Volume Two is a complete and exhaustive discussion of the data acquisition and data analysis programs used in this thesis. The programs are custom applications written by the author for the Apple Macintosh II platform. They are complete and integrated packages controlling all facets of the user interface, laboratory equipment interface, plotting, file creation, printing, etc. Volume Two serves several important purposes. First, it is the user's manual for both programs illustrating the use of their various features. Second, it is designed to be a trouble-shooting manual for solving commonly encountered problems. Finally, the discussion is intended to provide instruction, hints, and warnings about how the programs work internally. Included is a tutorial on how to modify the interface for the inclusion of new features. The discussion is sufficiently complete so that future users can feel secure about making any additions. A complete listing of the source code for both programs is available (see Professor Ahmed H. Zewail, California Institute of Technology).

The remainder of Volume One is organized into six chapters and an appendix, and is outlined in the following paragraphs. The objective is to study charge-transfer reactions and to examine the effect of the solvent on the threshold of charge transfer and changes in the dynamics of the process. In order to further understanding of charge-transfer dynamics in neutral molecular clusters, a new laboratory was built. It is a combination molecular beam and picosecond laser system specifically designed for the study of large neutral clusters. Since inhomogeneous broadening of the linewidths occurs in clusters, temporal resolution is essential for measuring and understanding the dynamics that occurs in these

clusters. The lifetimes were measured as a function of the cluster size. Such experiments will offer insight into solvent effects on the excited electronic-state dynamics of the molecule. The study of clusters may help to provide a microscopic picture of the condensed phases, since direct observation of intermolecular dynamics in bulk samples is often masked by averaging over a number of sites. By careful measurement of cluster properties as a function of cluster size, it is hoped that a clear picture of the connection between bulk and microscopic properties can be achieved.

In Chapters 2 and 3, the background considerations and design of the newly constructed molecular beam and picosecond laser system are given. In Chapter 2, an attempt is made to understand how cluster formation in molecular beams is related to the properties of the gas expansion through the nozzle. Since the nature of the gas expansion is often determined by the characteristics of the nozzle, the focus is on relating cluster formation to the flow properties and geometry of the nozzle. Several empirical rules exist for optimizing cluster formation. These rules involve the variation of the nozzle temperature, nozzle-stagnation pressure, and sample density (T_0 , P_0 , ρ). The discussion, by necessity on a very simple level, is intended to give the reader an appreciation for the basis of these various empirical rules. The molecular beam apparatus and the picosecond pump-probe laser system design are described in exhaustive detail in Chapter 3.

Chapter 4 presents results for both frequency and time-resolved studies on the intramolecular electron transfer in p-(Dimethylamino)benzonitrile (DMABN) within a cluster of solvent molecules. DMABN is characterized by radical changes in its dipole moment upon excitation to the first excited singlet electronic state. In solution, twisting of the dimethylamino moiety about the aromatic ring after excitation results in the formation of a twisted-intramolecular-charge-transfer (TICT) state. The formation of the TICT state is experimentally manifested by a dual fluorescence in polar solvents, versus a single fluorescence in nonpolar solvents indicating no TICT state formation. Polar solvents are

believed to assist the electron-transfer process by stabilizing the charge-separated TICT state and lowering the TICT barrier. Time-resolved fluorescence measurements in solution have suggested that formation of the charge-transfer state is facilitated by ground state DMABN-solvent complex formation [67]. Therefore, it might be possible that fluorescence could be produced in clusters under supersonic jet conditions. It is shown that one solvent molecule is insufficient to induce the formation of the TICT state, whereas clusters produced in a vapor cell may exhibit charge-transfer under certain conditions.

Chapters 5 and 6 present results of time-resolved studies on the intracuster proton transfer between the molecule α -naphthol and surrounding solvent molecules. α -naphthol is characterized by radical changes in its acidity upon excitation to the first excited singlet electronic state. This optically switchable acidity change can be used to investigate the dynamics of proton transfer and of chemical reactions induced by a rapid pH jump. In solution, the formation of the proton-transfer state is experimentally manifested by a dual fluorescence in sufficiently basic solvents; otherwise a single fluorescence is observed, indicating no proton-transfer. In this case, the proton transfer is believed to depend on the proton affinity of the solvent [57]. Recent spectroscopic work indicates that a threshold exists for the number of solvent molecules required for proton-transfer to occur [57]. Similar findings were reported in time-resolved studies in matrices of β -naphthol [55]. Chapter 5 presents initial results of time-resolved studies on the intracuster proton transfer between the solute α -naphthol and the solvent ammonia. In Chapter 6, these studies are extended to additional solvents and the results related to both other cluster studies and to the solution studies of similar systems.

The principal conclusions of the thesis are given in Chapter 7, followed by the appendix. The appendix reports on frequency and time-resolved work on intramolecular vibrational energy redistribution (IVR) in the deuteriated anthracenes. This study extends the previously successful efforts studying IVR in anthracene [68, 69].

REFERENCES

1. (a). R. D. Levine and R. B. Bernstein, *Molecular Reaction Dynamics and Chemical Reactivity* (Oxford University Press, New York 1987).
 (b). M. Gruebele and A. H. Zewail, *Physics Today*, May 1990, 24-33 (1990) and references therein.
 (c). J. L. Knee and A. H. Zewail, *Spectroscopy*, **3**, 44-53 (1988) and references therein.
 (d). A. H. Zewail and R. B. Bernstein, *Chem. and Eng. News* **66**, 24-43 (1988) and references therein.
2. (a) D. R. Herschbach, *Angew. Chem. Int. Ed. (Eng.)*, **26**, 1221 (1987).
 (b) Y. T. Lee, *Angew. Chem. Int. Ed. (Eng.)*, **26**, 936 (1987).
 (a) J. C. Polanyi, *Angew. Chem. Int. Ed. (Eng.)*, **26**, 952 (1987).
3. (a) S. J. Riley and K. R. Wilson, *Farad. Disc. Chem. Soc.* **53**, 132 (1972).
 (b) G. E. Busch and K. R. Wilson, *J. Chem. Phys.* **56**, 3626 (1972).
 (c) M. J. Dzvonik, S. Yang, and R. Bersohn, *J. Chem. Phys.* **61**, 4408 (1974).
 (d) H. W. Cruse, P. J. Dagdigian and R. N. Zare, *Farad. Disc. Chem. Soc.* **55**, 277 (1973).
 (e) R. N. Zare and P. J. Dagdigian, *Farad. Science* **185**, 739 (1974).
 (f) C. H. Green and R. N. Zare, *Ann. Rev. Phys. Chem.* **33**, 119 (1982).
 (g) C. H. Green and R. N. Zare, *J. Chem. Phys.* **78**, 6741 (1983).
 (h) J. L. Kinsey, *J. Chem. Phys.* **66**, 2560 (1977).
4. A. W. Castleman Jr., R. G. Keese, *Ann. Rev. Phys. Chem.* **37**, 525-50 (1986).
5. R. S. Bowles, J. J. Kolstad, J. M. Calo, and R. P. Andres, *Surf. Sci.* **106**, 117-124 (1981).
6. C. G. Granqvist and R. A. Buhrman, *J. Appl. Phys.* **47**(5), 2200-19 (1976) and references therein.
7. S. B. Ryali and J. B. Fenn, *Ber. Bunsenges. Phys. Chem.* **88**, 245-253 (1984).
8. T. A. Milne, A. E. Vandegrift, and F. T. Greene, *J. Chem. Phys.* **52**, 1552 (1970).
9. R. J. Gordon, Y. T. Lee, and D. R. Herschbach, *J. Chem. Phys.* **54**, 2393 (1971).
10. O. F. Hagen and W. Obert, *J. Chem. Phys.* **56**, 1793 (1972).
11. D. Golomb, R. E. Good, A. B. Bailey, M. R. Busby, and R. Dawbarn, *J. Chem. Phys.* **57**, 3844 (1972).
12. W. G. Dorfled and J. B. Hudson, *J. Chem. Phys.* **59**, 1253 (1973).
13. J. M. Calo, *J. Chem. Phys.* **62**, 4904 (1974).
14. R. E. Miller, *Science*, **240**, 4851, (1988).

15. D. V. Brumbaugh, J. E. Kenny, and D. H. Levy, *J. Chem. Phys.*, **78**, 3415 (1983).
16. J. J. F. Ramaekers, H. K. van Dijk, J. Langelaar, and R. Rettschnick, *J. Chem. Soc. Faraday Disc.* **75**, 183 (1983).
17. J. L. Knee, L. R. Khundkar, A. H. Zewail, *J. Chem. Phys.*, **87**, 115 (1987).
18. D. H. Semmes, J. S. Baskin, A. H. Zewail, *J. Am. Chem. Soc.* **109**, 4104, (1987).
19. P. Cong, L. W. Peng, A. H. Zewail, unpublished results.
20. M. R. Duncan and D. H. Rouvray, *Sci. Amer.*, 110-115, December 1989.
21. (a) R. Birringer, *Mater. Sci. Eng.*, **A117**, 33-43 (1989).
(b) J. Eastman and R. Siegel, *Res. and Dev.*, **31**(1), 56-60 (1989).
(c) D.R. Ulrich, *Chem. and Eng. News* 28-40, January 1, 1990.
(d) L.L. Hench and J.K. West, *Chem. Rev.*, **90**(1), 33-72 (1990).
(e) D. Segal, *Chem. Br.*, **25**(2), 151-56 (1989).
22. G. R. Fleming and P. G. Wolynes, *Physics Today*, May 1990, 36-43 (1990).
23. G. R. Fleming, *Chemical Applications of Ultrafast Spectroscopy* (Oxford, New York, 1986).
24. See, for example:
(a) M. Maroncelli, J. MacInnis, and G. R. Fleming, *Science* **243**, 1674 (1989).
(b) G. Rothenberg, D. K. Negus, and R. M. Hochstrasser, *J. Chem. Phys.* **79**, 5360 (1983).
(c) J. A. Syage, P. M. Felker, and A. H. Zewail, *J. Chem. Phys.* **81**, 4706 (1984).
25. S. Leutwyler and Jürg Bösigler, *Chem. Rev.* **90**(3), 489-507 (1990) and references therein.
26. R. E. Smalley, *Laser Chem.* **2**, 167-184 (1983).
27. D. A. Gobeli, Y. Y. Yang, and M. A. El-Sayed, *Chem. Rev.* **85**, 529 (1985).
28. R. N. Compton and J. C. Miller, in *Laser Applications in Physical Chemistry*, edited by K. Evans (Dekker, New York, 1989).
29. D. B. Smith and J. C. Miller, *J. Chem. Phys.* **90**(9), 5203-5205 (1989).
30. M. P. Casassa, *Chem. Rev.* **88**(6), 815-826 (1988).
31. D. J. Nesbitt, *Chem. Rev.* **88**(6), 843-870 (1988).
32. F. G. Celii and K. C. Janda, *Chem. Rev.* **86**(3), 507-520 (1986).
33. J. Steadman and J. A. Syage, *J. Chem. Phys.* **92** (7), 4630 (1990).

34. *Lasers and Mass Spectrometry*, edited by D. M. Lubman (Oxford, New York, 1990).
35. J. Grotemeyer and E. W. Schlag, *Angew. Chem. Int. Ed. Engl.* **27**, 447-459 (1988) and references therein.
36. D. Solgadi, C. Jouvét, and A. Tramer, *J. Phys. Chem.* **92**, 3313 (1988).
37. J. A. Syage, *J. Phys. Chem.* **93**, 170 (1989).
38. J. A. Syage, *J. Chem. Phys.* **92**(3), 1804-1810 (1990).
39. J. A. Syage and J. Steadman, *Chem. Phys. Lett.* **27**, 6076 (1990).
40. (a) P. M. Felker, W.R. Lambert and A.H. Zewail, *J. Chem. Phys.*, **77**, 1603 (1982).
(b) P. M. Felker, W.R. Lambert and A.H. Zewail, *J. Chem. Phys.*, **78**, 5266 (1983).
(c) P.M. Felker and A.H. Zewail, *Chem. Phys. Lett.*, **94**, 448 and 454, (1983).
(d) K. Fuke and K. Kaya, *Chem. Phys. Lett.*, **94**, 97, (1983).
(e) R. Bombach, E. Honegger, and S. Leutwyler, *Chem. Phys. Lett.*, **118**, 449 (1985).
(f) E. Honegger, R. Bombach, and S. Leutwyler, *J. Chem. Phys.*, **85**, 1234 (1986).
(g) K.Fuke, H Yoshiuchi and K.Kaya, *J. Phys. Chem.*, **88**, 5840 (1984).
(h) N.P. Ernsting, *J. Phys. Chem.*, **89**, 4932 (1985).
41. J. D. Payzant, A. J. Cunningham, and P. Kebarle, *Can. J. Chem.* **51**, 3242 (1973).
42. P. Kebarle, *Ann. Rev. Phys. Chem.* **28**, 445 (1977).
43. D. H. Aue and M. T. Bowers, in *Gas Phase Ion Chemistry*, Vol 2, edited by M. T. Bowers (Academic, New York, 1979), Chapter 9.
44. Thematic issue: Mass Spectrometry and Negative Gas-Phase Ions, *Chem. Rev.* **87**(3),483-669 (1987).
45. (a) D. G. Nicholls, *Bioenergetics, An Introduction to the Chemiosmotic Theory* (Academic, London, 1982);
(b) W. P. Jencks, *Catalysis in Chemistry and Enzymology* (McGraw-Hill, New York, 1969).
46. K. Sauer, *Acc. Chem. Res.* **11**, 257 (1978).
47. K. R. Miller, *Sci. Am.* **241**, 102 (1979).
48. M. D. Newton and N. Sutin, *Ann Rev. Phys. Chem.* **35**, 437-480 (1984).
49. E.M. Kosower and D.Huppert, *Ann Rev. Phys. Chem.* **37**,127-156 (1986).
50. D.H. Levy, *Adv. Chem. Phys.*, **47** (Part 1), 323 (1981).

51. (a) A. Amirav, U. Even, and J. Jortner, *J. Chem. Phys.*, **74**, 3725 (1981).
(b) A. Amirav, U. Even, and J. Jortner, *J. Chem. Phys.*, **75**, 2489 (1981).
(c) A. Amirav, U. Even, and J. Jortner, *J. Chem. Phys.*, **86**, 3345 (1986).
52. (a) H. Haberland, H. Langush, H.G. Schindler and D.R. Worsnop, *Surf. Sci.* **156**, 157 (1985).
(b) H. Haberland, H.G. Schindler and D.R. Worsnop, *J. Chem. Phys.*, **81**, 3342, (1984).
(c) J.V. Coe, J.T. Snodgrass, C.B. Freidhoff, K.M. McHugh and K.H. Bowen, *J. Chem. Phys.*, **83**, 3169, (1985).
(d) M. Knapp, O. Echt, D. Kreisle and E. Recknagle, *J. Chem. Phys.*, **85**, 636, (1986).
(e) M. Knapp, O. Echt, D. Kreisle and E. Recknagle, *J. Phys. Chem.*, **88**, 270, (1984).
53. D. Ray, N. E. Levinger, J. M. Papanikolas, and W. C. Lineberger, *J. Chem. Phys.* **91**(10), 6533-34 (1989).
54. J. J. Breen, L. W. Peng, D. M. Willberg, A. Heikal, P. Cong, and A. H. Zewail, *J. Chem. Phys.* **92**(1), 805-807 (1990).
55. G.A. Brucker and D.F. Kelley, *J. Chem. Phys.*, **90**, 5243, (1989).
56. J. F. Ireland and P. A. H. Wyatt, *Adv. Phys. Org. Chem.* **12**, 131 (1976).
57. (a) O. Cheshnovsky and S. Leutwyler, *J. Chem. Phys.*, **88**, 4127, (1988).
(b) R. Knochenmuss, O. Cheshnovsky and S. Leutwyler, *Chem. Phys. Lett.*, **144**, 317, (1985).
58. (a) T. Forster, *Naturwissenschaften* **36**, 186 (1949).
(b) T. Forster, *Z. Electrochem.* **54**, 531 (1950).
59. (a) A. Weller, *Z. Electrochem.* **56**, 662 (1952).
(b) A. Weller, *Prog. React. Kinet.* **1**, 187 (1961).
(c) A. Weller, *Z. Phys. Chem.* **17**, 224 (1958).
60. W. Klopffer, *Adv. Photochem.* **10**, 311 (1977).
61. G. C. Pimentel, *J. Amer. Chem. Soc.* **79**, 3323 (1957).
62. J. Lee, R. D. Griffin, and G. W. Robinson, *J. Chem. Phys.* **82**, 4920 (1985).
63. D. H. Huppert, A. Jayaraman, R. G. Mains, D. W. Steyert and P. M. Rentzepis, *J. Chem. Phys.* **81**, 5596 (1984).
64. S.P. Webb, L.A. Philips, S.W. Yeh, L.M. Tolbert and J.H. Clark, *J. Phys. Chem.*, **90**, 5154 (1986).
65. P. Delahay, *Acc. Chem. Res.* **15**, 40 (1982).
66. K. K. Smith, D. Huppert, M. Gutman, and K. J. Kaufman, *Chem. Phys. Lett.* **64**, 522 (1979).

- 67. Y. Wang and K. B. Eisenthal, *J. Chem. Phys.* **77**, 6076 (1982).
- 68. B. W. Keelan, *Ph.D. Thesis*, California Institute of Technology (1987).
- 69. P. M. Felker, *Ph.D. Thesis*, California Institute of Technology (1985).

CHAPTER 2

FORMATION OF NEUTRAL CLUSTERS USING SUPERSONIC BEAMS

2.1 INTRODUCTION

This chapter is principally concerned with the mechanisms and methods of the clustering process as it expands supersonically through a nozzle. It is well known that an adiabatic expansion of a gas or vapor can bring about supersaturation with respect to a solid or liquid phase of one or more of its constituent species. If the expanding gas contains foreign particles, ions, or sufficiently large clusters of its own molecules, extremely rapid condensation will occur on these seed species to form a dispersion of droplets or crystallites. A challenge has been to understand the homogeneous nucleation process, *i.e.*, the formation of nuclei comprising aggregates or clusters of the gas constituents. Homogeneous nucleation leads to condensation in pure gases that are sufficiently supersaturated.

A generation ago the timescale of most gaseous adiabatic expansions was very long relative to the timescale of the nucleation-condensation process kinetics at the molecular level. Consequently, the earliest observable stages of the process were relatively late in that even the smallest aggregations of the newly formed condensed phase had already grown to a relatively large size and had properties approaching those of bulk materials. Information about the microscopic details was obtainable by inference from observation on such quantities as temperature, pressure, composition and degree of supersaturation of the reactant gas along with the number density, size distribution, and sometimes the appearance rate for the product droplets or crystallites. Then in 1956, Becker and Henkes noted that condensation was a phenomenon to be reckoned with in supersonic jets expanding into vacuum from very small nozzles [1]. Since being proposed by Kantrowitz and Grey in 1951 [2] as sources for molecular beams, having actually been used for the purpose nearly 25 years earlier by Johnson [3], such free jets have become a widely used means and ends for research. Because these jets are so small in dimension, issuing from nozzles with diameters usually less than several hundred microns, the timescale of the expansion is of

the same order as the timescale of the nucleation-condensation process. The net result is that the earliest stages of the processes can be resolved and studied. More importantly, the processes can be arrested at any stage along the way. Thus, by appropriate combinations of the nozzle-stagnation pressure (P_0) and temperature (T_0), and the composition of the source gas, it has become possible to produce in free-jet expansions aggregates or clusters of molecules of any intermediate size and to study their chemical and physical properties.

Cluster-beam sources may involve cluster growth from a monomeric vapor, or cluster growth from species within a carrier gas. The appropriate method for producing clusters depends on the average bond energy per monomer in the cluster. Molecular beams of clusters with weak van der Waals bonds require production methods that subject the monomeric vapor to intense cooling before reaching a collisionless regime. The cooling is typically provided by supersonic expansions. While multistage pumping configurations may be necessary to make van der Waals clusters, generation of the monomer units is often trivial since most have low cohesive energies (even in the bulk) and are typically gases under ambient conditions. In contrast, generation of clusters with large average bond energies requires less stringent expansion conditions, but the price one must pay to produce the monomer units is substantially higher. Examples of this are the metal clusters, which employ pulsed lasers as the heating source [4-6]. Supersonic expansions yielding beams of charged clusters, positive and negative, can also be made [7,8].

There are three general classes of cluster-formation methods: effusive flow [9], flow aggregation (sometimes referred to as the gas evaporation technique) [10,11], and supersonic expansions. Although the main focus of this chapter is the major technical problems associated with the production of neutral molecular clusters in a supersonic expansion, the effusive flow and flow-aggregation methodologies are also discussed.

The remainder of this chapter is organized as follows. Section 2.2 briefly outlines the supersonic expansion. Modeling and characterization of cluster beams is discussed in

Section 2.3. Section 2.4 is concerned with empirical observations about cluster formation with respect to various experimental parameters. Finally a brief summary of the various effusive and flow aggregation techniques is given in Section 2.5.

2.2 SUPERSONIC BEAMS

The general principles of supersonic expansions for a monatomic gas have been discussed at length [12]; thus only a brief discussion is given here. Supersonic flow is formed when a gas is expanded through an aperture from high pressure (P_0) to low pressure (P), and the ratio of high to low pressure exceeds a critical value given by

$$\frac{P_0}{P} = \left[\frac{\gamma+1}{2} \right]^{\frac{\gamma}{\gamma-1}} \quad \text{where} \quad \gamma = \frac{C_P}{C_V} \quad (2.1)$$

In the above equation, C_P and C_V are the usual specific heats for the gas at constant pressure and volume. For most gases, the threshold pressure ratio is about 2.1 [13]. When this ratio is exceeded, the flow velocity at the throat (u^*) is at the local speed of sound in the gas (a^*). The superscript * refers to conditions when the sound and flow velocities are equal. Under these conditions, the nozzle is often said to be "choked" or in "critical flow." The flow velocity under "critical flow" conditions is given by

$$a^* = \left[\frac{\gamma k T}{m} \right]^{\frac{1}{2}} \quad (2.2)$$

where T is the local static temperature that would be registered by a thermometer moving at the same velocity as the gas. In Equation 2.2, k is Boltzmann's constant, and m is the mass of a molecule of the gas. At pressure ratios greater than the critical value, the gas

issuing from the nozzle exit comprises an underexpanded jet whose pressure as it leaves is greater than P_2 . The jet expands radially and longitudinally downstream from the nozzle exit in such a way as to achieve supersonic velocity. Beyond the nozzle aperture, the translational temperature and collision frequency each decrease rapidly in a predictable way. The microscopic result of the gas expansion is that the random thermal distribution of atomic velocities is converted into a narrow distribution directed along the line of flow, and that the molecules are effectively isolated from outside influences (*e.g.*, wall collisions). The temperature of the gas, determined by the width of its velocity distribution, can be lowered well below its freezing point to only a few Kelvins [14].

The jet gas expands to the point where its pressure equals the pressure of the ambient gas (P_2) in the region downstream of the nozzle. Thus the boundary of the jet is the locus of points where these two pressures are equal. As the gas expands around the corner of the nozzle exit, it gives rise to a fan of expansion waves traveling with the speed of sound in the jet gas. At the jet boundary, where the expansion in the radial direction stops, these waves are reflected as compression waves, also with the velocity of sound and with a component of velocity toward the jet axis. Because such a compression wave warms the gas slightly, each succeeding wave travels faster than its predecessor and overtakes it. Consequently, the succession of waves merges into a single steep pressure front or shock wave that forms what is often called the shock barrel somewhat inside the jet boundary. At a singularity sometimes referred to as the triple point, this barrel shock bifurcates. The inside branch is a plane shock wave normal to the jet axis, and is commonly called the Mach disc.

The mathematical description of the flow behavior that leads to this free-jet structure is beyond the scope of this chapter [15, 16], but the results for an ideal monatomic gas and isentropic flow can be summarized by the following equations:

$$T = T_0 \left[1 + \frac{1}{2}(\gamma-1) M_{\text{eff}}^2 \right]^{-1} \quad (2.3)$$

$$n = n_0 \left[1 + \frac{1}{2}(\gamma-1) M_{\text{eff}}^2 \right]^{\frac{-1}{(\gamma-1)}} \quad (2.4)$$

$$z = (2)^{1/2} n \sigma \tilde{v}_0 \left[1 + \frac{1}{2}(\gamma-1) M_{\text{eff}}^2 \right]^{-1/2} \quad (2.5)$$

$$M_{\text{eff}} = 3.26 \left(\frac{x}{D} - 0.075 \right)^{2/3} - 0.61 \left(\frac{x}{D} - 0.075 \right)^{-2/3} \quad (2.6)$$

where T is the temperature of the expanding gas, γ is 5/3 for a rare gas, M_{eff} is the effective Mach number, n is the number density, z is the collision frequency, σ is the hard-sphere collision cross section, \tilde{v}_0 is the mean molecular velocity, x is the distance the gas has expanded, D is the nozzle diameter, and the subscript zero refers to the condition in the high-pressure reservoir.

Equations 2.3 through 2.6 are valid over the region in which the expansion is isentropic. Unfortunately, the theory for determining exactly where the boundaries of the isentropic region are is currently lacking [17,18]. However, it has been found that a simple, general and accurate empirical relation can be used.

$$\frac{L_m}{D} = 0.667 \left(\frac{P_0}{P_2} \right)^{1/2} \quad (2.7)$$

Equation 2.7, which is independent of γ , accurately reflects experimental results for monatomic, diatomic and triatomic molecules [19,20,21]. L_m is the distance of the Mach

disc from the exit of a nozzle whose throat flow diameter is D . Unfortunately, the estimation of the diameter D_m of the jet at the Mach disc is not on a firm basis. Values of D_m/L_m have been found to range from 0.3 for argon ($\gamma = 5/3$) to 0.5 for CO_2 ($\gamma = 9/7$).

Implicit in Equation 2.7 is the fact that the characteristic scale dimension of the jet is the nozzle diameter. Not just the Mach disc distance, but all other properties are scaled with respect to downstream distance in terms of nozzle diameters. At a given number of nozzle diameters downstream, a particular gas from a given set of source conditions has undergone the same state change, no matter what the absolute distance. Because the gas velocity does not depend upon nozzle size, the rate of state change becomes very large when the nozzle diameters are small. Adiabatic cooling rates of 10^{10} K/s can be achieved.

The above analysis for free-jet expansions are based on continuum concepts of fluid flow. This picture begins to blur literally if the expansion is into a vacuum, and results in densities so low that the mean free path of both jet and ambient gas becomes large relative to the dimension of the jet. Shock waves become several mean-free paths in diameter. Thus the jet boundaries, barrel shock, and Mach disc become diffuse regions of scattering collisions between jet and background molecules. Under these circumstances, which apply to the experiments of concern in this thesis, the important problem becomes the size of the region in which there is no appreciable penetration of background molecules. As shown by Fenn and Anderson [22], and others [23], the appearance of background molecules on the jet centerline occurs at distances only slightly upstream of the nominal Mach disc location predicted by Equation 2.7. Nevertheless, Equation 2.7 remains a convenient first-order estimate, even at very low background pressure, of the extent of undisturbed flow.

Supersonic expansions are used to remove internal energy from atoms and molecules, and to isolate them from external perturbations. This greatly simplifies the spectra by minimizing vibrational and rotational congestion. When a polyatomic molecule is seeded into an expansion of a carrier gas, collisions between the polyatomic molecule

and the carrier gas (as the gas mixture flows through the aperture) tends to equilibrate the temperature of the polyatomic with that of the carrier gas. The polyatomic is accelerated to approximately the same speed as the carrier gas, and its velocity distribution is similarly sharpened. The internal degrees of freedom of the polyatomic are cooled to varying degrees depending on the cross section for collisional relaxation for each type of motion [24]. Typical temperatures for translation, rotation, and vibration may be 1K, 10K, and 50K, respectively.

2.3 SUPERSONIC CLUSTER BEAMS

2.3.1 Modeling of supersonic cluster beams

The supersonic expansion provides a suitable flow field to investigate clustering and condensation kinetics, but quantitation of cluster formation in supersonic beams is a challenging problem from both the theoretical and experimental viewpoint. Theoretical modeling of supersonic cluster beams is nontrivial since the pressure, temperature, and particle density during the expansion vary by large amounts. Most of the kinetic parameters are strongly temperature-dependent, and cluster densities are very nonlinear with respect to monomer densities. The flow field of the expansion is not separable as an external bath since the cluster growth process continuously releases its heat of condensation. Significant clustering heats up the gas expansion, increasing the temperature (T) and decreases the average beam velocity (u). The cluster distribution within supersonic beams has been extensively measured by electron-impact-ionization mass spectrometry, but electron impact tends to result in extensive fragmentation following ionization [7,25]. When the cluster size distribution is measured by mass spectrometers, the measurement may be biased by the response of the instrument. The influence of the solid angle sampled is also important because different sized clusters possess different perpendicular speed ratios (S). The speed ratio is mean velocity divided by the thermal velocity spread.

Differences in speed ratios between clusters tends to concentrate the heavier clusters on the centerline of the beam. The use of skimmers and collimators enhance this concentration effect. Finally, metastable clusters may fragment from the time of formation to the time of analysis.

The theoretical and experimental difficulties mean that the description of cluster growth in molecular beams has not been as well characterized quantitatively as has the expansion of a monatomic gas. As a result, determination of the conditions for optimal cluster formation is still largely an empirical endeavor. Although modeling efforts continue [e.g., 26], empirical techniques have been relied on for the work in this thesis. To illustrate the complexity in modeling cluster formation, two cases are discussed. First is one approach to the "simple" case of dimer formation in a gas. The second case is for larger and more heavily condensed systems. Finally, some experimental results are provided, which attempt to correlate the production and cluster distribution with empirical parameters.

The models for dimerization are discussed first. Note that for the purposes of linking chemistry and fluid mechanics, it is more convenient to describe the species in a flow by their mass fraction, rather than by the number or mole fraction. The conservation of total mass for the incompressible flow of a fluid moving at velocity (u) is given by

$$\rho \left[\frac{\partial u}{\partial x} + \frac{\partial u}{\partial y} + \frac{\partial u}{\partial z} \right] = 0 \quad (2.8)$$

where ρ is the fluid density. The conservation equation for any species (i) in a flow field, assuming steady-state and negligible diffusion, viscosity and heat conduction of the walls, is given by the Navier-Stokes equation as

$$\rho \left[\frac{\partial N_i}{\partial x} + \frac{\partial N_i}{\partial y} + \frac{\partial N_i}{\partial z} \right] = r_i \quad (2.9)$$

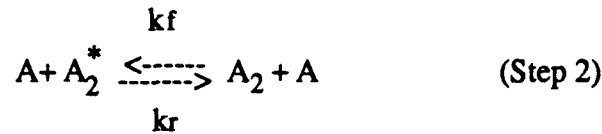
where $N_i = \rho_i V_i$ is a mass flux vector and r_i is the mass production rate(g/s/cm³). Using the conservation of total mass Equation 2.8, the steady-state species conservation equation becomes

$$\rho \frac{D\omega_i}{Dt} = r_i \quad \text{where } \omega = \frac{\rho_i}{\rho} \quad (2.10)$$

where ρ is total density and ω is the local mass fraction for the species of interest. Along a streamline and at steady state, we get

$$\frac{d\omega_i}{dS} = \frac{r_i}{\rho u} \quad (2.11)$$

where the derivative is with respect to the speed ratio. For argon dimer formation, a two-step mechanism is used [27,28] involving a virtual orbiting intermediate state, stabilized by collision with a third body:



The first reaction is assumed to be in equilibrium, and the rate of change of n_{A_2} , the number density of A_2 , becomes

$$\frac{dn_{A_2}}{dt} = k_f \left[K_1 n_A^3 - \frac{n_{A_2} n_A}{K_2} \right] \quad (2.12)$$

Using Knuth's [29] analysis for the equilibrium constants K_1 , K_2 and the forward rate constant k_f , noting that $r_i = m_i (dn_i / dt)$, and substituting into Equation 2.11 (with subscript i denoting the A_2 dimer) gives

$$\frac{d\omega_{A2}}{d\left(\frac{S}{d}\right)} = \frac{\rho d}{m_{Au}} C_1 \exp\left(-\frac{0.6\epsilon}{kT}\right) \cdot$$

$$\left\{ 11.28\sigma^3\left(\frac{\epsilon}{kT}\right)^{1/2} \frac{2\rho}{m_A} (1-\omega_{A2})^3 - 2.237\left(\frac{\epsilon}{kT}\right) \left[\exp\left(\frac{\epsilon}{kT}\right) - \left(1 + \frac{\epsilon}{kT}\right) \right]^{-1} \omega_{A2}(1-\omega_{A2}) \right\}$$

(2.13)

where C_1 is given by the expression

$$C_1 = 0.56\pi\sigma^2\Omega^{(2,2)} \left[\frac{12kT}{\pi m_A} \right]^{1/2} \quad (2.14)$$

The interaction between atoms and/or molecules is assumed to be adequately represented by a Lennard-Jones potential; thus ϵ and σ are the usual Lennard-Jones parameters. $\Omega^{(2,2)}$ is the Lennard-Jones collision integral [30] for collisions between A and the virtual orbiting state of the A_2 dimer (see Step 2). This equation for dimer-formation kinetics can now be integrated along any streamline in the flow field. The energy equation for the flow can now be corrected using the dimer heat of formation. However, since this model is valid only for small dimer concentrations, it is a good approximation to neglect the coupling of the kinetics to the external flow.

Equation 2.13 is complicated and represents just one of several kinetic models for dimerization [27,31,32]. Several combinations of dimensionless groups can be extracted but the complexity of the equations suggests that a straightforward general scaling equation

to predict terminal dimer concentration may not be easy to find. An important item to note in Equation 2.13 is that the formation rate is proportional to p^2d ($\approx P_o^2d$), whereas the destruction rate is proportional to pd ($\approx P_o d$).

For more heavily condensed systems, three calculation methods have been applied to describe cluster formation. The first is the steady-state [33-35] and time-dependent [36] macroscopic classical nucleation theory. The overall range and limitations of the method have been discussed by Stein [37]. The second is the direct microscopic approach of molecular dynamics or Monte Carlo simulations [38-40], and the third is a phenomenological microscopic approach [41].

The classical nucleation theory has been developed for isothermal infinite supersaturated gases, and gives the classical steady-state nucleation rate as

$$J_{ss} = \left(\frac{p_s}{kT} \right)^2 \left(\frac{2\sigma}{\pi m} \right)^{1/2} V_c \exp \left(\frac{-\Delta G^*}{kT} \right) \quad (2.15)$$

where σ is the macroscopic surface tension, p_s is the saturation vapor pressure, V_c is the condensed-phase atomic volume, and ΔG^* is the Gibbs free energy of formation of the critical-size condensation nucleus, given by

$$\Delta G^* = \frac{16\pi\sigma^3}{[3(\rho_L \cdot kT \cdot \ln S)^2]} \quad \text{where } S = \frac{p}{p_s} \quad (2.16)$$

where ρ_L is the bulk-liquid density, and S is the supersaturation, and the other symbols have their usual meanings.

The direct application of the classical nucleation theory to cluster formation has been questioned for several reasons. First, it may be inconsistent to apply a macroscopic theory for surfaces, along with its bulk variables, to systems that may not yet exhibit bulk properties. The problem may be partially accounted for by using effective macroscopic

variables. Molecular dynamics calculations suggest that the interfacial density profile in microclusters is very similar to that of an infinite sheet [38]. Second, the approximation for the Gibbs free energy of the critical-size nucleus ignores the translational and rotational degrees of freedom of the microcluster. However, it turns out that correct calculations differ only quantitatively [42]. Third, the rapid changes in density and temperature may violate the assumption inherent in nucleation rate theory: isothermality and local thermodynamic equilibrium. This is partially offset by time-dependent calculations that relate to steady-state rates by the introduction of a nucleation time lag [37,43,44]. The time lag (τ_n) is a function of temperature and pressure, and is related to the nucleation rate as

$$J_t = J_{ss} \left[1 - \exp\left(-\frac{t}{\tau_n}\right) \right] \quad (2.17)$$

where J_t is the time-dependent nucleation rate. The condition of local thermodynamic equilibrium is usefully approximated by a sudden-freeze surface model, in which the location of the surface is a function of the local nucleation rate coefficient. Fourth, the physical cross section of the expanding gas flow remains finite, compared to the assumption of an infinite system in nucleation rate theory. In finite systems a minimum in the free energy occurs, which corresponds to a stable cluster size [38]. Despite these limitations, extensive application of the time-dependent nucleation rate theory coupled to the equation for supersonic compressible gas flow has been made to relatively slow expansions such as Laval nozzles by Stein and coworkers [45]. Viscous effects of the nozzle need to be included explicitly, and the method is not applicable to fast free-jet expansions with a rate of 10^9 to 10^{11} K/s.

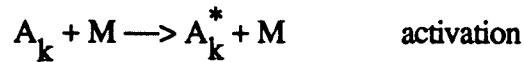
Monte Carlo simulation techniques have been applied to supersonic expansions and to clustering [39-41,46-49], but not to both simultaneously. The cluster studies indicate that the monomer hypothesis of the nucleation theory needed to be modified, and that

cluster-cluster coagulation processes are important to cluster formation. The cluster formation rate is given by

$$\dot{\rho} = \frac{1}{2} \sum_{i=1}^{k-1} K(i, k-i) \rho_i \rho_{k-i} + \rho_k \sum_{j=1}^{\infty} K(k, j) \rho_j \quad (2.18)$$

At the beginning of the expansion, the monomer concentration is largest, and therefore the monomer addition channel is the most important single channel leading to cluster formation of size n . However, the number of channels increases as $n/2$ so that cluster-cluster reactions may quickly become important or dominant. This is especially true for the formation of larger clusters. The importance of cluster-cluster reactions is evident for heavily condensed beams, in which the monomer concentration ceases to be an important mass fraction early in the expansion.

The phenomenological approach includes four types of reactions:



collisions that result in a union, dissociation by loss of a fragment, deactivation and activation by collision with another atom or molecule. Cluster growth is viewed as a competing process between the four types of reactions, and modeling is done by various numerical simulations [41,46].

Perhaps the most useful results at this point are some empirical rules for the onset of clustering, following the scaling laws of Hagena [50]. To avoid formation of trimers and larger cluster in monatomic gases, a safe upper limit is not to exceed a critical value of the dimensionless parameter, C^* where

$$C^* = \frac{P_0 \sigma^3}{\epsilon} \left(\frac{d}{\sigma} \right)^{0.88} \left(\frac{\epsilon}{kT_0} \right)^{2.3} < 15 \quad (2.19)$$

For room-temperature sources of small diameter (about 25 microns) this criterion suggests the onset of significant clustering in the range of $5 < P_0 d (\text{torr-cm}) < 10$. Helium is the special exception because the dimer is unstable, and the critical $P_0 d$ for clustering appears to be greater than 200 torr-cm.

Knuth's analysis [29], when coupled with a sudden freeze model (which assumes that the dimer concentration increases from its stagnation value in accordance with the local thermodynamic equilibrium until the freeze line of the expansion is reached), correlates the avoidance of dimer formation exceeding about 1% in monatomic gases if the parameter D^* does not exceed 0.1:

$$D^* = \frac{P_0 \sigma^3}{\epsilon} \left(\frac{d}{\sigma} \right)^{0.4} \left(\frac{\epsilon}{kT_0} \right)^{2.4} < 0.1 \quad (2.20)$$

A 10% dimer fraction criterion increases D^* to about 0.4. The different scaling of source diameter from that in the previous equation should be noted.

From the above results, and from other calculations that attempt to describe the state of the gas as a function of its location in the expansion [24,51], several noteworthy features emerge. The point at which supersaturation begins depends much more strongly on T_0 than upon P_0 , but it does move upstream with increases in the latter. Moreover, the degree of supersaturation at any point depends very strongly upon P_0 . Thus, raising P_0

increases not only the interval of distance and time over which supersaturation occurs, but also the magnitude of supersaturation at a points in that interval. In addition, the frequency of three-body collisions that are necessary for dimer formation, presumably the first step in nucleation-condensation, also depends strongly upon pressure. Consequently, it would be surprising if the extent of clustering and condensation in a free-jet expansion could be characterized by a simple dependence upon P_0 raised to some power, as is assumed by many investigators.

2.3.2 Characterization of supersonic cluster beams

Two major experimental approaches have been adapted to analyze cluster growth and concentrations and growth kinetics. Compared to electron-impact ionization, they are nondestructive (or at least less destructive) techniques. The first is laser spectroscopy in the form of laser-induced fluorescence (LIF), resonant two-photon ionization (R2PI), and laser depletion [14,52-54]; and the second is the cluster-beam helium-beam scattering technique devised by Buck and Meyer [55-57] .

An example of the use of laser-spectroscopic techniques to study cluster concentrations is the study of the formation of the first seven van der Waals complexes of tetracene (T) with Argon by Amirav et al. [52]. In this work, the data were modeled assuming that the formation of all tetracene-argon complexes were due to three-body collisions:



Studying the excitation spectra of the molecular beam expansion, they identified seven transitions red of the origin band of bare tetracene which they attributed to the origin bands

of seven complexes of argon. The intensity of the excitation bands as a function of the argon backing pressure in the expansion was described by the equation,

$$\frac{I(\text{Ar}_n)}{I} = (Kp^2)^n \quad (2.21)$$

where K is a constant and p is the pressure in the molecular beam reservoir. Thus, higher argon pressures increase the number of three-body collisions, which increases the concentration of clusters in the expansion.

From a study of Argon cluster-helium beam scattering [56], and by measuring the ratio of cluster densities, specifically Ar_n/Ar and Ar_n/Ar_2 , the exponents for a scaling law were found

$$\frac{\rho(\text{Ar}_n)}{\rho(\text{Ar})} \approx p^{\alpha_n} \cdot d^{\beta_n} \quad (2.22)$$

For clusters up to $n = 6$, $\alpha_n = n-1$, and since $\rho(\text{Ar}) \approx p$, one finds that $\rho(\text{Ar}_n) \approx p^n$. When comparing previous work for the pressure dependence α exponents, the comparison fails after $n = 2$, presumably because of cluster fragmentation.

The use of scaling rules to estimate and predict relative and absolute terminal cluster mole fractions, and average cluster size, as a function of stagnation pressure, source temperature, and nozzle diameter have been extremely popular [50,58-61]. Many of these rules were obtained using electron-impact ionization as the experimental technique. However, the electron-impact results are susceptible to bias by fragmentation so that the absolute use of these rules is no longer clear.

2.4 EMPIRICAL OBSERVATIONS OF CLUSTER FORMATION IN SUPERSONIC JETS

In the production of supersonic cluster beams, there are three important parameters to be considered: the stagnation pressure behind the nozzle, the nozzle geometry, and the initial temperature of the gas before the expansion. In general, cluster content and size increase with stagnation pressure and aperture cross section, and decrease with increasing gas temperature [7].

2.4.1 Pressure and Temperature effects

We initially confine the discussion to continuous jet sources. Clustering is qualitatively described in the following macroscopic picture. The isentropic expansion leads to a decreasing gas density and gas temperature as the distance from the nozzle aperture increases. Density and temperature drop until the expansion reaches background pressure, where essentially all collisions have ceased. The cooling process is not an equilibrium one; thus local regions may exist where local pressures are higher than the corresponding vapor pressure [25]. This local supersaturation leads to clustering if the time remaining (before the expansion runs out of collisions) is long enough. It is important to note that clustering releases energy that heats up the molecular beam.

For a fixed cross section and gas temperature, the supersaturation point moves upstream with increasing stagnation pressure, and the degree of supersaturation increases. The net result is an increase in the number of collisions possible after conditions of supersaturation have been achieved. Since vapor pressure is often exponential with respect to temperature, decreasing the temperature can have an even more profound effect on the amount of clustering. The source temperature is extremely important, since the saturation vapor pressure and thus the supersaturation depend strongly on temperature. The onset of condensation in rare gases has been correlated to temperature as $T^{-2.2}$ to $T^{-2.4}$ [59,62,63].

It has been found [25] that the characteristic length in axially symmetric free jets is the nozzle diameter, or more exactly, the effective flow diameter (Section 2.4.2). This means that all else being the same, identical beam conditions occur downstream of the nozzle at the same number of nozzle diameters. Thus collisions cease earlier for smaller nozzle apertures, and smaller-aperture nozzles typically have larger cooling rates than larger-aperture nozzles. Another useful nozzle geometry, especially for absorption experiments, is the slit nozzle [64]. In such a two-dimensional geometry, gas density and temperature fall off much less rapidly than for an axially symmetric nozzle for the same stagnation pressure and temperature.

2.4.2 Influence of the nozzle geometry

The effective flow diameter through the nozzle is determined by the discharge coefficient (C_D) of the orifice. The discharge coefficient is the ratio of the actual mass flow to the ideal isentropic value. For a given nozzle, this amounts to being the square of the ratio of effective flow diameter to the geometric flow diameter. The discharge coefficient is determined by the Reynolds number at the flow cross section where the velocity is sonic. The Reynolds number (Re), a dimensionless parameter expressing the ratio of the inertial forces over the viscous forces, is of great importance when discussing turbulent flow.

An analysis for a choked axisymmetric nozzle was done by Tang and Fenn [65]. The analysis is based on several frequently used assumptions. First, the fluid is a perfect gas with a constant specific heat. Second, the nozzle walls are assumed to be adiabatic. Third, the Prandtl number (Pr) is unity. The Prandtl number is a dimensionless parameter, which is the ratio of the viscosity of the material to its thermometric conductivity and is important in the discussion of convective heat transfer. It is a constant of the material in question and independent of the flow properties, and on the order of 1 for gases [30]. Fourth, the viscosity has a linear dependence upon temperature. Fifth, external to the

boundary layer, the flow is inviscid and one-dimensional. With the above assumptions, an analytical expression obtained is given below.

$$C_D = 1 - \left(\frac{\gamma+1}{2}\right)^{3/4} \left[\frac{1}{3(\gamma+1)}\right] \left\{ 72 + (6)^{1/2} [4(\gamma+1)-32] \right\} \left(\overline{Re}_D^*\right)^{-1/2} \\ + \left[\frac{2(\gamma-1)(\gamma+2)}{3}\right] \left(\frac{2}{\gamma+1}\right)^{1/2} \left(\overline{Re}_D^*\right)^{-1} \quad (2.23)$$

where γ is the specific heat ratio for the gas. \overline{Re}_D^* is a modified Reynolds defined as

$$\overline{Re}_D^* = Re_e^* \left[\frac{r_t}{(r_c)(Pr)} \right]^{1/2} \quad (2.24)$$

where Re_e^* is the Reynolds number at the nozzle throat. Re_e^* is defined as

$$Re_e^* = \left(\frac{\rho_e u_e D_e}{\mu_e} \right)^* \quad (2.25)$$

where D is the diameter of the nozzle throat, u is the speed of the gas flow, and ρ and μ are, respectively, the density and viscosity of the gas. The radius of the nozzle throat is given by r_t , and r_c is the radius of curvature of the nozzle throat. The subscript e indicates free-stream values. The asterisk indicates that the values are taken where the speed is Mach 1. For an ideal converging nozzle, this is at the plane of the nozzle orifice.

Equation 12 is a relatively simple and straightforward means for computing the discharge coefficient of an axisymmetric nozzle in critical flow over a range of Reynolds numbers (>200), provided only that the radius of curvature at the throat is finite and known. No other empirically adjustable parameters are involved. It has been empirically

found that experimental data are better matched with theory if Pr is figured into the square root of equation 12, but the correction is often only a few percent [30]. Regardless of the wall contour used, the interaction of real gases with the nozzle walls will always result in a boundary layer at the wall, which decreases the effective flow diameter relative to the geometric diameter. It has been found that clustering generally requires a Reynolds number of greater than 400, and that the effective flow diameter for a simple converging supersonic nozzle is often at least 0.9 times the nozzle exit diameter for high Reynolds numbers [65,66]. For lower Reynolds numbers, between 200-10000, the effective flow diameter can easily be reduced by 20% [30].

There are two extreme cases for the wall contour in simple converging nozzles. In case one, the radius of curvature for the wall becomes extremely small. This results in a nozzle, known as a sharp-edged orifice (SEO), which is configured like a short tube of constant cross section with one end capped by a smaller diameter aperture. Theoretical predictions of discharge coefficients for a SEO are not well developed, but some experimental results are available [21]. For a SEO the locus of all points at which the flow velocity is sonic is not the exit plane of the orifice, but a convoluted surface that is convex in the direction of flow at the center, and concave at the edges [67]. In case two, the radius of curvature is infinite, *i.e.*, a tube of constant cross section. For a tube with a large enough aspect ratio (length/diameter), supersonic flow is attained upstream of the tube exit because of viscous pressure drop along the tube length caused by the presence of a viscous boundary layer. Supersonic flow upstream of the tube exit means that supersaturation is obtained over a longer period in the early stages of the expansion, and the expansion has more time to form clusters [68]. The behavior of the sonic surface with respect to the nozzle being a SEO or a tube is shown schematically in Figure 1. The shape of the sonic surface in the tube is parabolic, and convex in the direction of the gas flow. Calculations of the centerline Mach number versus axial distance from the nozzle exit for a simple

converging nozzle, a SEO, and a tube of constant cross section indicate little difference, however clustering was shown to be greater for the tube. Classical nucleation rate calculations indicate that clustering occurs over many more nozzle diameters for the tube (Figure 2), and experimental measurements of argon dimer concentrations indicate at least a factor of 2 improvement for the tube [68]. This observation prompted the question of whether increases in cluster formation associated with partial confinement of the expansion within the tube could be further enhanced by the addition of a diverging section to the nozzle downstream of the sonic throat.

It is well established that the geometry of the nozzle has profound effects on cluster formation. For axial nozzles, there are four basic geometries: sonic, laval, cylindrical, and conical. Figure 3 shows the relevant nozzle geometries. Hagena and Obert measured the centerline flux as a function of source-stagnation pressure for CO_2 for the three geometries [69]. For constant stagnation pressure and aperture, highest centerline intensities and average cluster size were obtained for conical nozzles. It has been found for alkali metal clusters that a conical nozzle allowed formation of larger clusters versus a similarly configured cylindrical nozzle, and that the optimum cone angle for a conical nozzle is 30 degrees [70]. The observations are rationalized in terms of constrained expansion zones for conical nozzles relative to sonic nozzles. The constrained expansion allows more collisions before the expansion terminates, resulting in larger clusters [50]. Of the four major geometries, sonic nozzles are the worst for cluster generation for comparable nozzle diameters and stagnation pressures. Of course, this makes the sonic nozzle the nozzle geometry of choice when cluster formation is undesirable. Further, for just producing high-intensity molecular beams, it has been found that the sonic nozzle and capillaries work best [71] and are easier to fabricate than their converging-diverging counterparts.

The reason that sonic nozzles without diverging sections work better as beam sources is that in throat Reynolds number ranges permitted by affordable pumping speeds

the boundary layer builds up so rapidly in diverging sections that they become filled with boundary layer, and the isentropic core disappears so that the effective exit Mach number is much lower than the nozzle area ratio would provide for truly inviscid flow. The boundary layer build-up is so extensive because the gas density drops so rapidly. Thus the Mach number, given by

$$M = \frac{\rho u \pi D^2}{4} \quad (2.26)$$

(where D is the diameter of the nozzle throat, u is the speed of the gas flow, and ρ is the density of the gas) results in the Reynolds number varying as $1/D$ and dropping rapidly as nozzle diameter increases along the diverging section. The rate of decrease is tempered somewhat by the fact that viscosity also decreases as the free-stream temperature decreases. Moreover, in the diverging section the boundary layer is shielded from the oncoming free stream by the nozzle wall and is not as effectively swept away as it is in the converging section upstream of the nozzle throat. The boundary layer is always at its minimum thickness at the nozzle throat where the Reynolds number has the highest value. In the production of molecular beams, the velocity distribution and intensity depend very strongly on what happens during the last stages of the expansion. Even if boundary layer effects do not intrude on the centerline gas until near the exit of the nozzle, they can still reduce the quality of the beam by broadening the velocity distribution and decreasing the intensity. Since the flow is contained, viscous effects are important in a thin region near the walls. The combination of small dimensions and low densities mean that you have low Reynolds numbers, which are characteristic of flow regimes in which viscous effects such as boundary layers become important [72]. This is a familiar problem in rarefied gas dynamics. Nozzles designed to give streams or jets at high Mach numbers and low density give rise to very thick boundary layers in the diverging section [12].

In cluster formation, on the other hand, it is the early stages of the expansion, where the density and local Reynolds number are high, that determine the cluster density and size distribution. These characteristics of the cluster population are not nearly as sensitive to collisions with wall-thermalized boundary layer gas as are the velocity components of individual molecules. Therefore, nozzles with diverging sections can favor cluster formation even though they are less useful as sources for generating highly collimated beams with narrow velocity distributions. It must be borne in mind, however, that in order to elucidate the kinetics and thermodynamics of cluster formation, one needs complete information on the time-temperature-density history of a gas sample from stagnation conditions to the terminal state of a cluster beam that is usually characterized by mass analysis and other kinds of spectrometry. When boundary-layer effects are present in the diverging section of a nozzle, it becomes difficult if not impossible to determine that history. Consequently, although by empirical juggling of nozzle design parameters and operating conditions an investigator might optimize with a converging-diverging nozzle the production of clusters for a particular purpose, it is unlikely that such juggling will provide much fundamental understanding of the cluster-formation process.

2.4.3 Pulsed versus continuous sources

Going to higher stagnation pressures quickly becomes a major challenge for continuous jet sources, as the capacity of the pumping system is quickly overwhelmed. Using pulsed sources offers several advantages. The sample consumption rate is very low because of the low duty cycle. This minimizes the consumption of precious samples. Since the valve is open for only a short time, typically several-hundred microseconds or less, the aperture size and stagnation pressure may be significantly higher than for a continuous system. The noise from scattered light can be dramatically reduced. Furthermore, the larger aperture and stagnation pressures allowed by pulsed systems

increase the Reynolds number and reduce the problems that are due to the boundary layer between the flow and the nozzle.

From the point of view of the cluster beam, there are two potential concerns with pulsed systems. First is the low duty cycle. This is usually a minor problem since the experiment will often use pulsed lasers and detectors with comparable or lower duty cycles. The second disadvantage can be more serious. Pulsed systems give beam velocity, temperature, and cluster distributions that are not uniform throughout the pulse [73]. This problem is rationalized as being due to a minimum opening time after which the terminal temperature becomes independent of pulse length. This time comprises the time required for the gas behind the nozzle to be accelerated to the exit velocity, the time necessary to form an expansion buffer beyond the nozzle, plus the time required for this buffer zone to equilibrate. For a typical pulsed expansion of 2000 torr of argon through a 500 micron cylindrical aperture, the time is 15.1 microseconds [73]. However, if uniformity of the cluster gas pulses is not a stringent requirement, the uneven cluster distribution within a pulse can be used to advantage. Since lighter clusters are intersected earlier in the pulse, one can discriminate somewhat against larger cluster sizes.

2.4.4 Mixed expansions

Enhanced cluster formation can also be achieved if an inert carrier gas is added. The explanation is that the carrier gas leads to more efficient removal of condensation energy by means of collisions with the clusters. Increasing the partial pressure of carrier gas decreases the number of collisions between cluster-containing species. Without removal of condensation energy, a cluster can fragment in order to release excess energy. This fragmentation reduces the size of clusters that are generated. Eventually the dilution effect dominates and no further gains in maximum cluster size or intensity is seen. At very low monomer partial pressures, one can generate clusters containing one central monomer

unit surrounded by a shell of carrier gas atoms or molecules. This is an ideal point to start rigorous studies of solvation.

The nature of the carrier gas can also be of critical importance in determining the extent of clustering with the carrier gas [74]. This is believed to be due to the relative magnitudes of the interactions involved. For large differences in condensation energy between carrier and seed, the survival of solvation complexes is unlikely, and clustering is determined primarily by the number of allowed collisions involving seed-gas species. This means that heavier carrier gases (giving slower beams) give more time for clustering. The effect of terminal translational temperature seems minimal. For small differences in interaction energy between carrier and seed, solvation complexes and terminal translational temperature play a vital role.

2.5 EFFUSIVE AND FLOW AGGREGATION TECHNIQUES

In effusive flow, a sample of material is vaporized in an oven by heating and effuses from the oven into a high-vacuum (10^{-6} torr) detector region. Since the vaporized sample is largely confined to the oven, the vapor has sufficient time to reach thermal equilibrium. The vapor is primarily composed of monomers, but some clusters in thermal equilibrium at the given temperature and pressure may be present. The subsonic effusive molecular beam is highly divergent and has a broad velocity distribution. Compared to nonequilibrium methods, cluster abundances are low.

Aggregation methods modify the effusive technique by allowing the monomer units to effuse into millitorr to several torr of cold quench gas. The resultant cluster size range depends on the dimensions of the source and time allowed for cluster growth. The monomer units are entrained in a carrier gas flow and mildly expanded into a growth chamber through an aperture a few millimeters in diameter. Quench gas is added to the growth chamber through a separate gas line. Cluster growth is terminated by interfacing

the growth zone with a detector chamber at sufficiently low pressure to terminate further collisions. The vaporization and aggregation regions may be in the same chamber, simplifying the arrangement. Molecular beams from aggregation sources are subsonic with low centerline intensities and broad velocity distributions. Cluster-size distributions (rather than being equilibrium ensembles) are predicated by kinetic, entropic, and thermodynamic effects that are not well understood. Because of the mild expansion conditions, clusters in these beams have higher internal temperatures than comparable species formed in a supersonic expansion. Furthermore, although the method does provide higher intensities and larger clusters than the effusive sources, the reproducibility (particularly with regard to relative cluster intensities) are quite variable [75] Because of the critical influence of the nature of the quench gas and its temperature.

The flow aggregation method can be taken a step further by carrying out multiple expansions [11]. The first expansion is supersonic into a counterpropagating flow of quench gas defining a quench region, followed by a second expansion into high vacuum. Turbulence in the quench region produces large supersaturation ratios. The quench region is small, so that clustering is thought to occur after the second expansion. The multiple expansion technique alleviates the problems associated with flow aggregation methods to some degree since the initial expansion into the quench region is supersonic.

2.6 REFERENCES

1. E. W. Becker and W. Henkes, *Z. Phys.* **146**, 333 (1956).
2. A. Kantrowitz and J. Grey, *Rev. Sci. Instrum.* **22**, 328 (1951).
3. T. H. Johnson, *Nature* **113**, 745 (1927); *J. Franklin Inst.* **206**, 301 (1928); *Phys. Rev.* **31**, 103 (1928).
4. T.G. Dietz, M.A. Duncan, D.E. Powers, and R.E. Smalley, *J. Chem. Phys.*, **74**(11), 6511-12 (1981).
5. V.E. Bondybey and J.H. English, *J. Chem. Phys.*, **76**(5), 2165-79 (1982).
6. R.E. Smalley, *Laser Chem.*, **2**, 167-184 (1983).
7. M. Kappes and S. Leutwyler, in *Atomic and Molecular Beam Methods*, edited by G. Scoles (Oxford, New York, 1988).
8. T. Mark and A. W. Castleman, Jr., *Advances in Atomic and Molecular Phys.*, vol. 20 (Academic Press, New York, 1985).
9. K. Hilpert, *Ber. Bunsenges. Phys. Chem.*, **88**, 260 (1984) and references therein.
10. A. Pfund, *Phys. Rev.* **35**, 1434 (1930); C.G. Granqvist and R.A. Buhrman, *J. Appl. Phys.*, **47**(5), 2200-19 (1976) and references therein.
11. R. S. Bowles, J. J. Kolstad, J. M. Calo, and R. P. Andres, *Surf. Sci.*, **106**, 117-124 (1981).
12. (a) J.B. Anderson, R.P. Andres, and J.B. Fenn, *Advances in Chemical Physics*, **10**, pp. 275-317 edited by J. Ross (John Wiley, New York, 1966).
13. D. R. Miller, in *Atomic and Molecular Beam Methods*, edited by G. Scoles (Oxford, New York, 1988).
14. R. E. Smalley, L. Wharton, and D. H. Levy, *Acc. Chem. Res.* **10**, 139 (1977).
15. P.L. Owen and C. K. Thornhill, *Aeronat. Res. Council*, UK R&M, 2616 (1948).
16. D. M. Lubman, C. T. Rettner, and R. N. Zare, *J. Phys. Chem.* **86**, 1129 (1982).
17. T. C. Adamson and J. A. Nicholls, *J. Aerospace Sci.* **26**, 16 (1959).
18. W. S. Young, *Phys. Fluids* **18**, 1421 (1975).
19. K. Bier and B. Schmidt, *Z. Angew. Phys.* **13**, 34 (1961).
20. S. Crist, P. M. Sherman, and D. R. Glass, *AIAA J.* **4**, 68 (1966).
21. H. Ashkenas and F. S. Sherman, in *Rarefied Gas Dynamics*, vol. 2, p. 84, edited by J. H. DeLeeuw (Academic Press, New York, 1966).

22. J. Fenn and J. B. Anderson, in: *Rarefied Gas Dynamics*, vol. 2, p311, edited by J. H. DeLeeuw (Academic Press, New York, 1966).
23. (a) R. F. Brown and J. H. Heald, in: *Rarefied Gas Dynamics*, vol. 2, p1407, edited by C. L. Brundin (Academic Press, New York, 1967).
 (b) E. P. Muntz, B. B. Hamel, and B. L. Maguire, *AIAA J.* **8**, 1651 (1970).
 (c) R. Campargue, *J. Chem. Phys.* **52**, 1795 (1970).
 (d) J. Brook and B. B. Hamel, *Phys. Fluids* **14**, 1898 (1972).
 (e) J. Brook, B. B. Hamel, and E. P. Muntz, *Phys. Fluids* **18**, 517 (1975).
 (f) A. K. Rebrov, in: *Rarefied Gas Dynamics*, edited by J. L. Potter (AIAA Publ., New York, 1977); *Progr. in Astro. and Aero.* **51**(2), 811 (1977).
 (g) E. P. Muntz, B. B. Hamel, and P. B. Scott *Entropie* **42**, 28 (1971).
24. (a) D. H. Levy, L. Wharton, and R. E. Smalley in *Chemical and Biological Applications of Lasers*, Volume VII, edited by C. B. Moore (Academic, New York, 1977).
 (b) D. H. Levy, *Ann. Rev. Phys. Chem.* **31**, 197 (1980).
25. S. B. Ryali and J. B. Fenn, *Ber. Bunsenges. Phys. Chem.* **88**, 245-253 (1984).
26. L.S. Bartell, *J. Phys. Chem.*, **94**(12), 5102-5109 (1990) and references therein.
27. R. J. Gordon, Y. T. Lee, and D. R. Herschbach, *J. Chem. Phys.* **54**, 2393 (1971).
28. D. L. Bunker, *J. Chem. Phys.* **32**, 1001 (1960).
29. E. L. Knuth, *J. Chem. Phys.* **66**, 3515 (1977).
30. R. B. Bird, W. E. Stewart, and E. N. Lightfoot, *Transport Phenomena*, pp. 19-26, 253-263 (John Wiley, New York, 1960).
31. D. Golomb, R. Good, and R. Brown, *J. Chem. Phys.* **52**, 1545 (1970).
32. W. Dorfeld and J. Hudson, *J. Chem. Phys.* **59**, 1253 (1973).
33. R. Becker and W. Doering, *Ann. Physik* **24**, 719 (1935).
34. F. F. Abraham, *Homogeneous Nucleation Theory* (Academic Press, New York, 1974).
35. A. C. Zettlemoyer, *Nucleation Phenomena* (John Wiley, New York, 1977).
36. A. Kantrowitz, *J. Chem. Phys.* **19**, 1097 (1951).
37. G. D. Stein, *Surf. Sci.* **156**, 44 (1985).
38. M. Rao, B. J. Berne, and M. H. Kalos, *J. Chem. Phys.* **68**, 1325 (1978).
39. W. H. Zurek and W. C. Schieve, *J. Chem. Phys.* **68**, 840 (1978).
40. W. H. Zurek and W. C. Schieve, *J. Phys. Chem.* **84**, 1479 (1980).

41. D. Lippmann, W. C. Schieve, and C. Canestaro, *J. Chem. Phys.* **81**, 4969 (1984).
42. D. J. McGinty, *J. Chem. Phys.* **55**, 580 (1971).
43. F. F. Abraham, *J. Chem. Phys.* **51**, 1632 (1969).
44. A. Beylich and F. Robben, *Z. Angew. Math. Phys.* **25**, 443 (1974).
45. O. Abraham, S. S. Kim, and G. D. Stein, *J. Chem. Phys.* **75**, 402 (1981).
46. J. W. Brady, J. D. Doll, and D. L. Thompson, *J. Chem. Phys.* **71**, 2467 (1979).
47. J. W. Brady, J. D. Doll, and D. L. Thompson, *J. Chem. Phys.* **73**, 2767 (1980).
48. J. W. Brady, J. D. Doll, and D. L. Thompson, *J. Chem. Phys.* **74**, 1026 (1981).
49. J. W. Brady, J. D. Doll, and D. L. Thompson, in *Potential Surfaces and Dynamics Calculations*, edited by D. G. Truhlar (Plenum Press, New York, 1981).
50. O. F. Hagen, *Surf. Sci.* **106**, 101-116 (1981).
51. M. Labowsky, S. Ryali, J. B. Fenn, and D. R. Miller, *Rarefied Gas Dynamics* Ed. S. S. Fisher, Progr. in Astro. and Aero. **74**, 695, AIAA, New York 1981.
52. A. Amirav, U. Even, and J. Jortner, *J. Chem. Phys.* **75**, 2489 (1981).
53. A. Amirav, U. Even, and J. Jortner, *Chem. Phys. Lett.* **83**, 1 (1981).
54. A. Amirav, U. Even, and J. Jortner, *J. Phys. Chem.* **86**, 3345 (1982).
55. U. Buck and H. Meyer, *Phys. Rev. Lett.* **52**, 109 (1984).
56. U. Buck and H. Meyer, *Surf.Sci.* **156**, 275 (1985).
57. U. Buck and H. Meyer, *J. Chem. Phys.* **84**, 4854 (1986).
58. T. A. Milne, A. E. Vandegrift, and F. T. Greene, *J. Chem. Phys.* **52**, 1552 (1970).
59. O. Hagen, in *Molecular Beams and Low Density Gas Dynamics*, p. 93, edited by P. P. Wegener (Dekker, New York, 1974)
60. A. van Deursen, A. van Lumig, and J. Reuss, *Int. J. Mass. Spect. Ion. Phys.* **18**, 129 (1975).
61. P. M. Dehmer and S. T. Pratt, *J. Chem. Phys.* **76**, 843 (1982).
62. D. Golomb, R. E. Good, A. B. Bailey, M. R. Busby, and R. Dawbarn, *J. Chem. Phys.* **57**, 3844 (1972).
63. O. Hagen and W. Obert, *J. Chem. Phys.* **56**, 1793 (1972).

- 64. A. Amirav, U. Even, and J. Jortner, *Chem. Phys. Lett.* **83**, 1 (1981).
- 65. S. P. Tang and J. B. Fenn, *AIAA J.* **16**, 41 (1978).
- 66. S. P. Tang, in *Rarefied Gas Dynamics*, vol. 2, p. 870, edited by R. Campargue, CEA Paris, 1979.
- 67. H. W. Liepmann, *J. Fluid Mech.* **10**, 65 (1961).
- 68. H. R. Murphy and D. R. Miller, *J. Phys. Chem.* **88**, 4474-78 (1984).
- 69. O. F. Hagena and W. Obert, *J. Chem. Phys.*, **56**(5), 1793-1802 (1972).
- 70. M. Kappes, M. Schar, P. Radi, and E. Schumacher, *J. Chem. Phys.* **84**, 1863 (1986).
- 71. E. W. Becker and K. Bier, *Z. Naturforsch.* **A9**, 975 (1954).
- 72. S. Whitaker, *Introduction to Fluid Mechanics*, pp. 421-454 (Prentice Hall, Englewood Cliffs, 1968).
- 73. K. Saenger, *J. Chem. Phys.* **75**, 2467 (1981).
- 74. O. Abraham, S. Kim, and G. D. Stein, *J. Chem. Phys.* **75**(1), 402-411 (1981).
- 75. H. Schaber and T. Martin, *Surf. Sci.* **156**, 64 (1985).

FIGURE CAPTIONS

- Figure 1:** A schematic of three nozzles ranging from a sharp edged orifice (SEO) to a tube of constant cross section. The dashed lines indicate the qualitative nature of the sonic surface. Taken from Reference 61.
- Figure 2:** Classical nucleation rate at various axial distances in free jets from the three types of nozzles in Figure 2. The source gas is argon at 130K and 2000 Torr. Taken from Reference 61.
- Figure 3:** The four common nozzle geometries used in supersonic-jet expansions. Conical nozzles have been experimentally found to be optimal for cluster formation, while the sonic nozzles produce optimal cooling.

Effects of Nozzle Geometry on Free-Jet Expansions

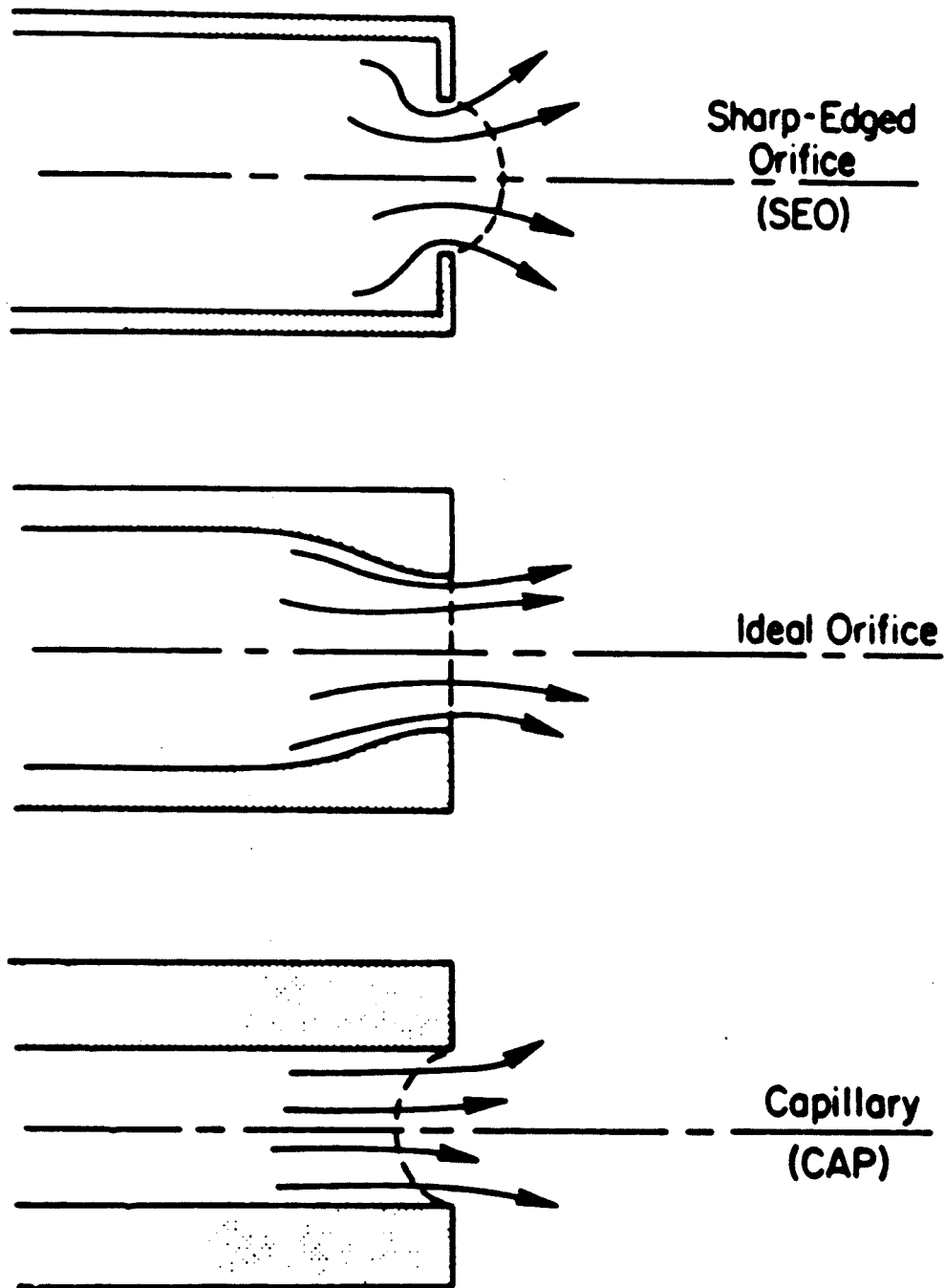


Figure 1

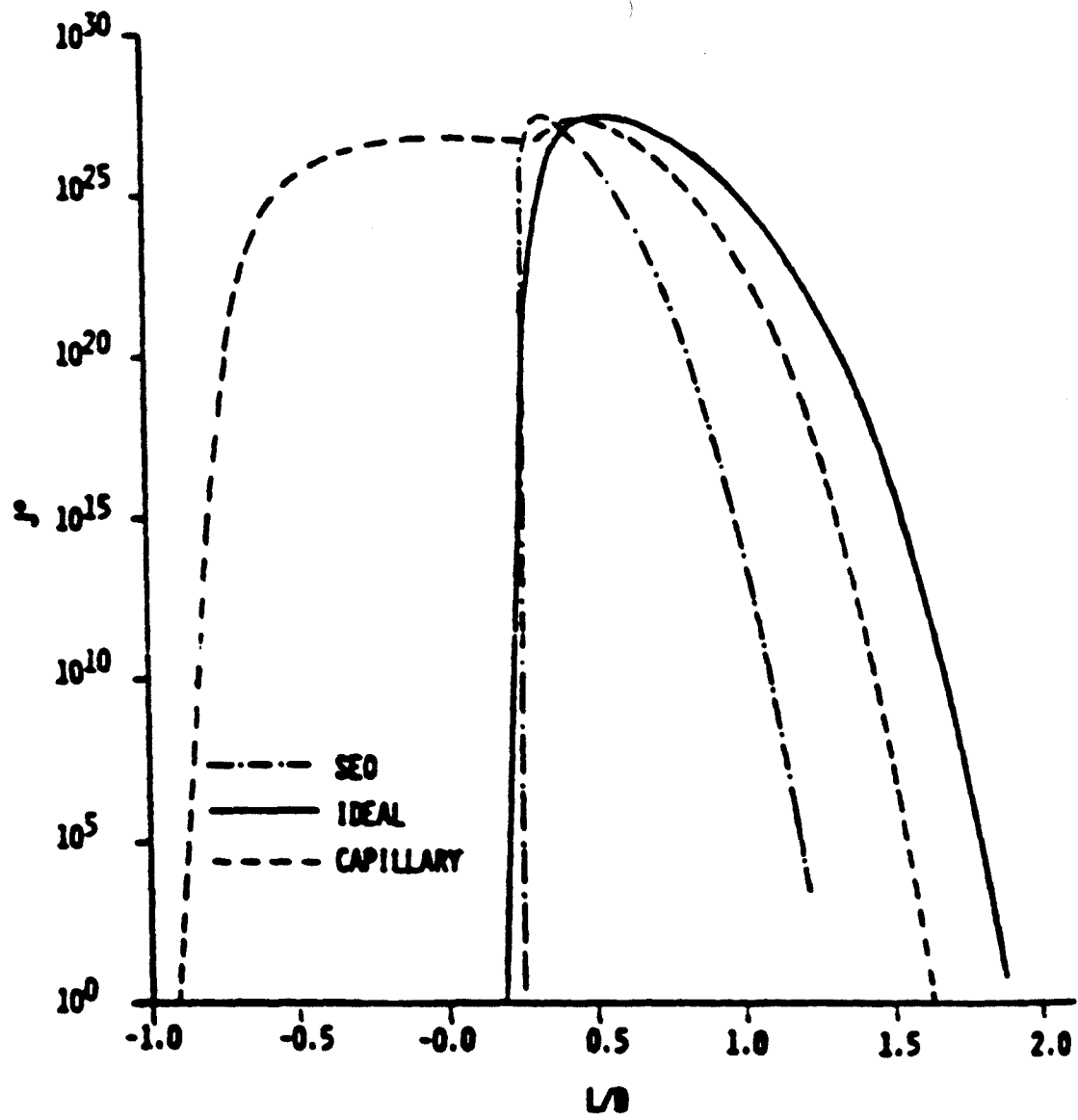
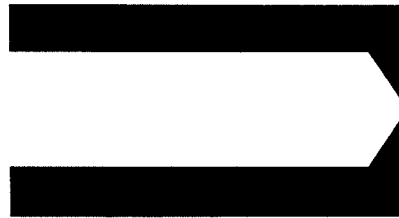
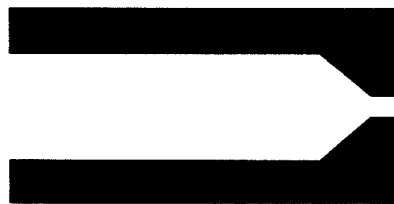


Figure 2

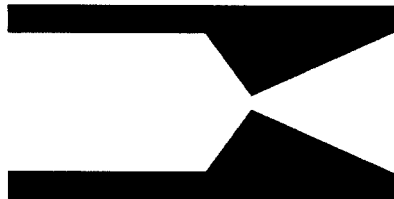
NOZZLE GEOMETRIES



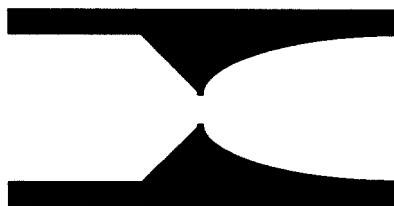
SONIC



CYLINDRICAL



CONICAL



LAVAL

Figure 3

CHAPTER 3

APPARATUS FOR CLUSTER EXPERIMENTS BY TIME-RESOLVED PUMP-PROBE LASER SPECTROSCOPY

3.1 INTRODUCTION

Several experimental apparatuses were used in this thesis. The first apparatus is a new two color picosecond pump-probe laser system coupled with a molecular beam machine, and was used to make real-time measurements by pump-probe laser spectroscopy. The real-time measurements use two-color resonance-enhanced multiphoton ionization (REMPI) to ionize clusters selectively, and time-of-flight (TOF) mass spectrometry to mass-resolve the resultant cluster ions. The second apparatus employs a scanning Nd:YAG pumped dye laser coupled with a pulsed supersonic expansion, and was used to obtain excitation and dispersed fluorescence spectra [1]. The third apparatus is a time-correlated single-photon counting apparatus coupled with a continuous-jet supersonic expansion, and was used to obtain dispersed fluorescence spectra and time-resolved fluorescence decays [2]. The latter two apparatuses have been described before in detail [1,2]. In this chapter, a detailed description is given for the new picosecond pump-probe laser system and molecular beam machine. This new apparatus was designed and constructed for the study of molecular clusters.

Conceptually, the time-resolved pump-probe experiment is simple. To identify spectroscopically the states attained in both the reagent and product, two independently tunable sources are required. The first photon source (pump) is chosen to match an optical transition in the reagent. The second photon source (probe) is chosen either to ionize the reagent to the ionization continuum, or to excite the reagent to a higher level and monitor the laser-induced fluorescence. Ionization is done as close to threshold as possible to minimize excess energy in the reagent. In the case of clusters, ionization near threshold minimizes two fragmentation channels: fragmentation during ionization, and fragmentation of the ion after its formation. The ultimate time resolution of the experimental apparatus is determined by the duration of the individual laser pulses, and by the relative jitter between the pump and probe pulses.

Supersonic expansions have proven useful for the generation and study of clusters. However, using a supersonic expansion results in two experimental constraints. First, the concentration of the clusters of interest in the molecular beam is often very low. Second, the interaction volume of the molecular beam with the laser is small. Hence, a powerful source with a high-photon flux is desirable. In addition, most organic molecules that are conveniently seeded in a molecular beam absorb in the ultraviolet. Ultraviolet wavelengths are typically generated from the visible output of a dye laser by frequency-doubling the dye laser output using a nonlinear material. Visible-to-ultraviolet conversion efficiencies are strongly dependent on the intensity of the light beam employed.

It should be noted that the molecular beam design in the pump-probe apparatus is very versatile. In addition to REMPI, the apparatus is also configured for electron-impact ionization (EI) and laser-induced fluorescence (LIF). LIF can be performed on either a free jet, or a collimated molecular beam [3]. Furthermore, if low signal is a problem in ionization experiments, the first skimmer may be removed resulting in a two-stage system. Finally, given the high throughput of the pumps, the apparatus can be run as a continuous-jet. For continuous-jet operation, the magnetic actuator in the nozzle is removed, and both the nozzle-aperture size and the stagnation pressure are reduced.

3.2 THE MOLECULAR BEAM APPARATUS

The molecular beam was designed for the formation and characterization of cluster beams. High throughput diffusion pumps and a pulsed valve in the nozzle are used to allow for the highest possible stagnation pressure and cross section. The molecular beam apparatus consists of three vacuum chambers: the expansion chamber, the buffer chamber, and the Time-Of-Flight (TOF) chamber (Figure 1). The three chamber design permits operation of the nozzle at high stagnation pressures, resulting in moderate vacuum in the expansion chamber, while maintaining high vacuum in the TOF chamber. Unless

otherwise noted, the apparatus is constructed out of stainless steel and aluminum. The material grades used were stainless steel 304 and aluminum 2024.

A booklet was created to fully document the molecular beam apparatus. The booklet consists of an overall view of the apparatus, a table listing the parts used to construct the apparatus, and a mechanical drawing for each part listed in the table. Included are vacuum hardware, mounts for the TOF assemblies and LIF, and the mechanical driver for the nozzle assembly. Additional parts such as vacuum gauges and feedthroughs are not included. For each part listed, the table shows the drawing's number, size, and title. Original drawing sizes are indicated in the table, since many of the drawings have been reduced to 8.5 x 11 inch size. The drawings and drawing number sequence were created by Mr. Richard Erich, formerly of the chemistry department's instrument shop. The booklet is available for examination (see Professor Ahmed H. Zewail, California Institute of Technology).

3.2.1 Vacuum Chambers

The molecular beam is about 7 feet above the floor. The height is determined by the size of the beam apparatus, and by the size of the pumps employed. The entire molecular beam assembly rests on three 1.75 inch thick aluminum plates. The plates rest on a 4 x 6 foot iron platform, and are approximately 6 feet above the floor. I-beams cross the platform's frame to provide support for the plates. The port sizes on the pumps and the molecular beam vacuum chambers dictate the size of the plates. The beam is bolted to the plates through the the pump ports, the pumps themselves are bolted on the opposite side, and the pump holes are staggered with respect to the chamber holes. The rest of the platform is left open for wires, access to the bottom of the molecular beam, or covered by black painted plywood for mounting other needed equipment.

The expansion chamber is pumped by a high-throughput 10 inch diffusion pump (Varian VHS-10), while the buffer and TOF chambers are each pumped by a 6 inch diffusion pump (Varian VHS-6). All three diffusion pumps are equipped with liquid nitrogen cold traps, and pneumatic gate valves. The diffusion pumps are pumped by mechanical pumps (a Leybold D90A for the VHS-10 pump, and a single Leybold D60A for the two VHS-6 pumps). Under normal operating conditions (50 psi stagnation pressure, 500 microsecond pulsewidth, and the pulsed nozzle operating at 100 Hz), the pressure in the expansion chamber is approximately 5×10^{-5} torr, and the pressure in the TOF chamber is only about 7×10^{-7} torr. Pressure inside each of the three vacuum chambers is monitored using standard thermocouple and ion gauges, and a pressure gauge controller (Granville-Phillips Series 307). The gauges are mounted on flanges that connect to spare ports on the top of each of the three chambers.

The cylindrical expansion and buffer chambers are 16 inches in diameter, and are made of stainless steel (0.250 inch wall) to insure mechanical stability for the alignment of the molecular beam. Each chamber has eight main ports, arranged in two crosses (Figure 1). The chambers are separated by a central flange assembly. The crosses closer to the central flange are used to conduct the experiment, whereas the other cross is used for the pumps and other utilities. For each chamber, 2.75 inch utility ports are attached to the main ports where convenient, and to the end opposite the central flange assembly. On the expansion chamber, the 2.75 inch ports opposite the central flange assembly are used for mounting feedthroughs for the nozzle assembly driver, gas input, heater inputs, and temperature outputs.

The central flange assembly consists of three stainless steel flanges. The main flange is a 20 inch diameter flange, with a 8.5 inch diameter hole bored through the center. Into the 8.5 inch hole goes a 9.5 inch diameter mounting flange. A 5 inch diameter hole is bored through the center of the 9.5 inch diameter flange. Into the 5.5 inch diameter hole

goes a 6 inch diameter plate on which is mounted a nickel skimmer (Beam Dynamics, Model 2, 1.5 mm aperture). Mounted to the 9.5 inch diameter flange are the mounts for the TOF chamber ionizer cube, and four 18 inch long guiding rods (Thomson Industries, Case 60L AISI C-1060 steel-hardened to Rockwell 58-63C, 0.5 inch nominal diameter) for the nozzle assembly. The four guiding rods are capped at the other end by an aluminum plate. The pieces mounted to the 9.5 inch diameter flange are discussed in more detail in Sections 3.2.2 and 3.2.3. For LIF experiments, optical baffles are used for the laser entrance and exit ports of the expansion chamber in order to reduce scattered light. Further scattered light reduction is achieved by painting the inside of the expansion chamber and the front of the nozzle assembly with Xylan 1010, a black fluoropolymer paint (Whitford Corporation).

The TOF chamber is composed of a 13 inch wide tee, a 6 inch diameter tube 26 inches in length, a 4 inch inner diameter transition tube 5.125 inches in length, and the ionizer cube (see Section 3.2.3). All the components are made of stainless steel, except for the cube which is made of aluminum. On the end of the chamber opposite the ionizer cube is attached a flange containing a microchannel plate (MCP) detector (Galileo model FTD 2003) for ionization experiments. The wall thickness of both the tube and the tee is 0.125 inches. The TOF chamber extends into the buffer chamber by way of the transition tube and includes the ionizer cube. The ionizer cube is discussed in more detail in Section 3.2.3.

3.2.2 Nozzle Assembly

The nozzle assembly contains the nozzle, pulsed valve, and a reservoir for nonvolatile samples. It is mounted on two aluminum plates held 6.5 inches apart. The nozzle and the valve are a single unit manufactured by General Valve Corporation (Series 9), and are mounted on the front plate. The sample reservoir is mounted on the rear plate. The mounts for the valve and sample holder fit into the slots in the aluminum plates (Figure 1) and are made out of a ceramic (Macor) to minimize heat-conduction losses. The valve is

solenoid-activated and is usually operated at 100 Hz, with a pulse length of approximately 500 microseconds. For enhanced formation of clusters a conical-shaped (30° cone) nozzle is used, with an aperture of 150 microns in diameter. The nozzle and the sample reservoir can be independently heated. For the sample holder, a cartridge heater (Chromolax CIR-2012) is used, whereas a 2 foot long and 0.5 inch wide Samox fiber heating tape (VWR) is used for the nozzle and valve. Temperature is regulated by two temperature controllers (Omega Engineering CN310KC). The nozzle is kept about 10°C hotter than the sample reservoir in order to reduce clogging of the nozzle aperture by condensation of the sample.

The nozzle assembly moves on the guiding rods using ball bushings (Thomson Industries A-81420-SS). A ball nut and ball screw combination (Warner Electric R-0308) is used to drive the nozzle assembly. The ball nut is screwed into the back plate of the nozzle assembly, and the ball screw is anchored to the aluminum capping plate by means of a retaining ring and retaining nut. The ball screw has been modified for connection to the retaining ring, and is connected to a micrometer (MDC model BRM-275) through a flexible coupling (Figure 1). The micrometer is attached to the external end flange on the expansion chamber (Figure 1), and has a steel extension rod attached to it which inserts into the flexible coupling. The nozzle assembly is positioned close to the first skimmer for TOF experiments, or farther back above the four-way cross in the expansion chamber for LIF spectroscopy on the free jet. Two nuts are loosely fit onto two of the four guiding rods. The nuts define the limit of forward motion of the nozzle assembly, and are thick enough to prevent the nozzle assembly from causing accidental damage to the first skimmer.

3.2.3 The Ionizer Cube

The center of the ionizer cube is coincident with the intersection of the molecular beam axis and the centerline of the port used for the TOF drift tube (Figure 1). This puts the position of the cube center 4.56 inches from the buffer chamber face of the 20 inch

diameter central flange. The cube is oriented so that the four faces not intersecting the molecular beam are parallel to the main ports of the buffer chamber. The cube's 6 faces are used for various purposes. The faces orthogonal to the molecular beam axis are the entrance and exit of the TOF chamber. The face closest to the central flange assembly (containing the pinholes) is the molecular beam entrance, and is covered by a flange which has a nickel skimmer attached to it (Beam Dynamics, Model 2, 2 mm aperture). The opposite face is covered by a flange, which has a 2 mm hole in the center for the molecular beam exit. The face farthest from the MCP is used for mounting a flange containing the ionizer assembly, the ion optics of the TOF mass spectrometer, and a pulsed electron gun for EI. The cube face closest to the MCP is attached to the transition tube, which is attached to the buffer chamber port associated with the TOF chamber by an O-ring seal. The two remaining faces are used for entrance and exit of the laser beams. The face farthest from the ceiling is the laser entrance port. A short focal length lens, mounted on a vertical translation mount, focuses the lasers onto the molecular beam. The vertical translation mount allows for fine adjustment of the lens focal-point position. A flat window is mounted on the flange covering the laser exit face.

The ionizer cube is mounted on the cube mounts attached to the 9.5 inch diameter plate of the central flange assembly. The cube mounts consist of an aluminum plate and a solid aluminum ring. The aluminum plate has a 4 inch diameter hole bored through the center, and attaches to the cube on the corners of the cube skimmer face. In turn, the plate is attached to the aluminum ring. The ring has as much material as possible bored out of its sides to facilitate pumping in the region enclosed by the ring. The orientation of the cube and mounting pieces with respect to the central flange and nozzle assemblies is fixed by mechanical alignment using pins. Mechanical alignment ensures that the location is accurate and reproducible to a few thousandths of an inch. The high vacuum is required by the MCP in the TOF chamber. Having all the critical components mounted on a single

flange means that the entire experimental assembly is removable from the main chambers as one unit. The assembly is removed from the main chambers through the end of the buffer chamber, and the main chambers need not be separated.

3.2.4 Electronics

The electronics controlling the actuation of the pulsed valve solenoid and the triggering of the laser was built in our laboratory. The control box is a dual pulse generator. A schematic of the circuitry is shown in Figures 2A and 2B. For each TTL component, the relevant pin number connections are indicated. Specifications for each component are given in Reference 4. The two pulsed outputs are independently adjustable for pulse duration and pulse delay. The repetition rate may be set from 1-200 Hz. These quantities, as well as the total number of pulses, may be displayed on a digital read-out with a variable sampling time. A fan and vent provide circulation of air over all the components.

The first pulsed output triggers a Wavetek pulse generator (Model 802), which in turn triggers the Q-switch driver box for the Nd:YAG and the voltage pulses on the TOF ionizer. The laser then triggers the Stanford delay generator, which triggers the Pockels cell electronics (see Section 3.4.2), the boxcar (EG&G model 162 mainframe/165 integrator) and an analog-to-digital interface (see Section 3.5), or the CAMAC crate based waveform analyzer (see Section 3.3.2 and 3.5).

The second pulsed output is sent to a valve-driver circuit (Figure 3) which amplifies the pulse to 105V. This amplified pulse drives the valve. It is delayed appropriately, relative to the first pulsed output, to synchronize the gas pulse with the arrival of the laser pulses.

3.3 DETECTION METHODS

3.3.1. Laser-induced fluorescence

The laser beams intersect the molecular beam about 10 mm downstream of the nozzle which corresponds to $x/d = 20$. Fluorescence is collected and collimated using a single plano-convex $f/1.5$ lens 2 inches in diameter (Figure 1). The lens is mounted in an aluminum cup, and secured by a retaining ring. The cup is mounted onto an extension tube, and the cup position is adjustable to allow optimization of the lens focal-point position. The extension tube is mounted to the expansion chamber port flange which is equivalent to the buffer chamber port used for TOF mass spectrometry. The extension tube has a series of holes bored into its sides to facilitate pumping of the extension tube and lens cup. A second 2 inch plano-convex lens focuses the fluorescence onto a photomultiplier (1P28) enclosed in a side-window housing (Pacific Instruments, model 3150RF). Another possibility is to pass the fluorescence through a monochromator before impinging on the photomultiplier. Appropriate filters (Schott, Corning) discriminate against resonance fluorescence and scattered laser light. If greater scattered light rejection is required, a second telescope is used with a pinhole separating the two telescopes. The pinhole is placed at the focus of the first telescope. The photomultiplier output can be amplified if necessary and is fed into a variable gain boxcar integrator. The boxcar's gate is triggered by a digital delay generator for synchronization with the laser system.

3.3.2 Time-of-Flight mass spectrometry

Ions are created by laser multiphoton ionization (MPI) or by electron-impact ionization (EI). MPI is used for time-resolved measurements, while EI is used for diagnostic purposes. The time-of-flight (TOF) mass spectrometer is used for mass analysis. The TOF spectrometer and ionization methods are briefly discussed below.

The principles of TOF mass spectrometry are well-established [5]. Positive ions are accelerated through a fixed potential so that they acquire a kinetic energy that is independent of their mass. The ions then travel through a field-free drift tube to a detector. Since the velocity of an ion is mass-dependent, the arrival time at the detector is proportional to the square root of the ion's mass. If the signal is resolvable in time, one can deduce the mass spectrum of the ions. The simplicity of the TOF mass spectrometer is counterbalanced by its achieving only a moderate resolution.

The molecular beam formed in the expansion chamber passes through the first skimmer on the central flange assembly when entering the buffer chamber, passes through the second skimmer as it enters the ionizer cube, and exits the cube through a 2 mm hole on the face opposite the second skimmer (Figure 1). The laser enters the ionizer cube perpendicular to the molecular beam and TOF mass spectrometer. The intersection of the laser and molecular beam is in the acceleration region of the ionizer assembly. The two-stage TOF mass spectrometer is based on the original Wiley-McLaren design [6]. Ions that are produced (either by EI or by REMPI) are accelerated through two stages of electric field, and are collimated by an Einzel lens. The drift tube is 1.2 m long and the ions are detected with the MCP. We have achieved a resolution of approximately $m/\Delta m = 1000$ with this system. The temporal and spatial characteristics of the pulsed molecular beam are easily evaluated by ionizing the carrier gas (typically helium or argon), using the pulsed electron gun. EI can also be used to ionize the cluster distribution in the molecular beam since it is not selective with regard to cluster mass. Necessary voltages for the ionizer assembly, the ion optics of the TOF mass spectrometer, and the pulsed electron gun for EI are provided by the feedthroughs (Ceramaseal, Inc.) on their mounting flange. These feedthroughs are connected to feedthroughs on a flange that is mounted on an external port of the buffer chamber (Figure 1).

The ions, whether generated by MPI or EI, are detected by the MCP. The ion signal is amplified immediately with a Stanford Research Systems 300 MHz preamplifier (Model SR440) to minimize both transmission losses, and possible interference from the RF noise generated by the modelocker. When taking a mass spectrum, a waveform analyzer is used to collect, digitize, and signal average the amplified MCP analog signal. The analyzer is based in a CAMAC crate (LeCroy 8013A). It consists of a 100 MHz transient digitizer (LeCroy 8818A), a LeCroy MM8103A memory module, and a LeCroy 6010 Magic controller unit. We have achieved a mass resolution of approximately $m/\Delta m=1000$ with this system. The transient digitizer is triggered by the digital delay generator in order to coordinate its collection time with the laser pulse. Figure 4 depicts a nonresonant photoionization mass spectrum of α -NpOH(NH₃)_n clusters showing a typical cluster distribution.

3.3.3 The Electron Impact/Time-of-Flight Source

The electron impact source is similar to that described in Reference 7, and is described in detail in this subsection. Included is a detailed description of how the pieces fit together, the circuitry, and the voltage timing. Particular emphasis is given to explaining the operation of equipment for obtaining an electron-impact (EI) ionization mass spectrum. A block diagram is given in Figure 5. The EI/TOF source is shown in Figure 6, and the timing and necessary voltages are indicated in Figure 7. The high-voltage pulser circuit is shown in Figure 8.

Briefly, a coiled tungsten filament, 0.005 inches in diameter, is mounted on an Alumina piece. Holes for necessary electrical connections are provided by feedthroughs on the mounting flange. The gate is a disc made of stainless steel, and has a 0.625 inch circular aperture. The aperture is covered with a 90% transmitting Nickel mesh (Buckabee-Mears) directly over the filament. The filament is biased to a constant positive DC voltage.

The gate is held at a voltage slightly lower (about 10-20V less) than the filament. It is pulsed high (amplitude of about 50 volts) for about a microsecond in tandem with the molecular beam valve. The repeller grid is simultaneously pulsed down to the same voltage as the accelerator grid for the duration of the electron pulse. The electron-impact energy is assumed to be equal to the voltage difference between the filament and the accelerator grid. The is typically set to 60 V or less.

The necessary equipment is given below. If a manufacturer's name is given, it is simply for making identification easier.

TTL Pulse Delay Generator box	Power supplies:
Wavetek 50 MHz pulse generator	Harrison Labs (200V, 3A)
Electron impact (EI) box	HP 6255A (50V, 1.5A)
Variac	EG&G Ortec (3kV)
Voltage divider	Keithley (3kV)

Microchannel Plate (MCP) Detector accessories:

Bertan (5kV) power supply

Stanford 300 MHz amplifier (SRS Model DG535)

3.3.3.1. TTL Pulse Delay Generator Box

This component provides the electronic signal to drive both the General Valve Series 9 pulsed valve (+10V square wave) and the Wavetek Pulse Generator (+TTL). Also provided is a variable delay, which allows for the temporal overlap of the gas pulse and the pulse of electrons. Nominally this delay is 1000 microseconds for a mostly helium beam and a nozzle to skimmer distance of 10 turns of the nozzle carriage micrometer.

3.3.3.2. Wavetek 50 MHz Pulse Generator

This component provides the electronic signals that control the gate and repeller-voltage pulses. In addition, the Wavetek also provides a synch out for either an oscilloscope input or the LeCroy Transient Digitizer System. The Wavetek receives its trigger input from channel 2 of the nozzle driver box. The output signal going to the gate (+ going SQW) comes out of the variable output BNC connector and goes to the P1/GATE BNC on the EI box. The output signal going to the repeller (- going SQW) comes out of the TTL bar BNC connector and goes to the P2/REPELLER BNC on the EI box. Both of these output signals are approximately 2 microseconds wide and are sent without any additional delay in the Wavetek. The variable output is also used to provide the synch-out to either the oscilloscope or the LeCroy Transient Digitizer System.

3.3.3.3. The Electron Impact (EI) box:

This is the central component of the electron impact/time-of-flight mass spectrometer. Its description is broken down into 6 parts.

A. AC Power

The box has no power switch. Power up by plugging the box into a wall socket using the three-prong receptacle marked BOX POWER.

B. Filament Power

The EI box contains a 14V/5 amp transformer for the filament. This transformer, which is biased at high voltage, receives its power from a Variac (set to approximately 80). The power from the Variac to the transformer is carried on a 115V extension cord and passes into the EI box through the 115V receptacle marked FIL POWER. The current through the filament (approximately 2.5 amps) is monitored with a Triplet ammeter mounted on the EI box.

C. Bias Voltage

There are three high voltages that are inputs into the EI box. The voltage going into the MHV connector marked GATE BIAS (740V) comes from one of the EG&G HV power supplies. The voltage going into the MHV connector marked FIL BIAS (750V) comes from the other EG&G HV power supply. The voltage going to the MHV connector marked REP BIAS (900V) comes from the voltage-divider box, which gets its power/voltage from the Keithley power supply.

D. Gate Pulse Voltage and Trigger

The voltage pulse going to the gate comes from the HP power supply (50V) and passes into the EI box through the BNC connector marked GATE/PV1. The electronic signal controlling the Gate pulse (+ going SQW - 2 microseconds) comes from the variable output on the Wavetek and passes into the EI box through the BNC marked GATE/P1.

E. Repeller Pulse Voltage and Trigger

The voltage pulse going to the repeller comes from the Harrison power supply (100V) and passes into the EI box through the BNC connector marked REP/PV2. The electronic signal controlling the Repeller pulse (- going SQW - 2 microseconds) comes from the TTL bar output on the Wavetek and passes into the EI box through the BNC marked REP/P2.

F. Outputs

The output voltages and filament current exiting the EI box pass through a group of 4 MHV connectors on the box near the Triplet ammeter. These connectors are clearly labelled as GAT-P1, REP-P2 and a pair marked FILAMENT. High-voltage cables are

used to carry the capacitively coupled bias voltages + voltage pulses and the high-voltage biased filament current to the MHV feedthroughs located on the molecular beam machine.

3.3.3.4. Miscellaneous

There are two other important items that have to be set. They regard the remaining voltages and the extent of MCP signal amplification. First, the remaining bias voltages to the TOF lens system, TOF2 (800V) and LENS (300V) comes from the voltage-divider box and are carried via long high-voltage cables to the MHV feedthroughs marked TOF2 and LENS on the molecular beam machine. Second, the MCP detector bias voltage, which comes from the Bertan power supply, is $\leq 2000\text{V}$, and the amplification via the Stanford amplifier should be 25X (5X per amplification stage).

3.4. THE TWO COLOR PICOSECOND LASER SYSTEM

The tunable, visible or ultraviolet, picosecond laser pulses are generated in distinct steps: (1) A CW Nd:YAG laser is mode-locked and Q-switched to give 1064 nm picosecond pulses; (2) the IR pulses are frequency-doubled to the visible, and the visible pulses are used to synchronously pump two dye lasers in tandem; (3) the dye lasers are cavity-dumped to give picosecond pulses in the visible; (4) the visible pulses, if necessary, are frequency-doubled to the ultraviolet; and (5) the visible or ultraviolet laser pulses are sent to the molecular beam. The laser system, based on a design from Stanford University [8] and schematically illustrated in Figure 9, is capable of producing 20 ps pulses with up to 10 microjoules visible light per pulse out of each of the two dye lasers. The laser repetition rate can easily be up to a kilohertz, although the experimental repetition rate may be less due to constraints from other equipment.

3.4.1 The Mode-Locked Q-Switched Nd:YAG Laser

The Nd:YAG laser is a homebuilt system built from components taken from a Quantronix 416 CW Nd:YAG laser (Figure 9). The acousto-optic modelocker (Model 352), acousto-optic Q-switch (Model 351), and their respective drivers are also from Quantronix. For optimal thermal stability the resonator cavity is supported by Invar rods, and all the critical mounts are made of stainless steel (Klinger). The resonator cavity is bound by a high-reflector mirror (200 cm radius), and an output coupler (-120 cm radius, 12% transmission).

The Nd:YAG is modelocked at 78 MHz. This produces a train of pulses, each with a FWHM of 100 ps and separated by 13 ns peak-to-peak. The Q-switch repetition rate is variable and the Q-switch can be triggered by an external source, which is typically the pulsed valve driver. The combined action of the Q-switch and modelocker results in a train of modelocked pulses inside a Q-switched envelope. This train of IR pulses (1064 nm) is then frequency-doubled with a 3 x 3 x 5 mm KTP crystal (Airtron) to 532 nm. The Nd:YAG laser energy output is about 640 microjoules per Q-switched envelope at 532 nm, and depends on the laser alignment and condition of the krypton arc lamp. The 532 nm green light is then split by a 50/50 beamsplitter in order to pump the two independent dye lasers.

3.4.2 The Cavity-Dumped Dye Lasers

The dye laser is synchronously pumped by the Nd:YAG. The dye laser cavity consists of a 1 mm pathlength dye cuvette, two flat broad band high reflecting mirrors, a 25 cm plano-convex lens as the focussing element, and an iris is also included for transverse mode selection (Figure 9). The laser beam waist in the cavity is located approximately on the rear mirror, which is next to the dye cuvette. The circulating dye is pumped through the cuvette by a micropump (Micropump Corporation; model 120 for the pump, model 415 for

the motor). The dye cuvette is set at the Brewster angle to maintain polarized light in the cavity, and is located as close as possible to the rear mirror. Best results were found when the focal point of the intracavity lens lies between the cuvette and rear mirror, and closer to the rear mirror. Dye laser performance is optimized by maximizing the overlap of the 532 nm pump, and the dye laser spot in the cuvette. This is achieved by focusing the pump light to match the dye laser spot size, and by bringing the pump light in as collinear as possible to the dye laser beam. The polarization of the pump beam and the dye laser should also be matched. The dye laser runs with optimum power when the dye solution in the cuvette absorbs approximately 90% to 95% of the incoming 532 nm pump. The dye solution concentration is optimized by starting with a 100 mg per liter solution, and then adding a concentrated solution of the same dye until maximum power is reached. After enough concentrate has been added, the laser power levels off. Further addition of dye may lead to reduced laser power. Once the dye solution is made, and assuming it is not contaminated, it should be necessary only to add methanol occasionally due to evaporation.

Synchronous pumping of the dye laser is achieved by carefully matching the optical pathlength of the dye laser to that of the Nd:YAG. Note that the optical path length differs from the actual cavity length because of the indices of refraction of the cavity components. By matching the optical path lengths, the oscillation period of a pulse in the dye laser is matched to the modelocking frequency of the Nd:YAG. As a pulse oscillates in the dye laser, it is amplified during each successive pass through the dye cuvette, by each successive modelocked pulse coming from the Nd:YAG. The pulse intensity in the dye laser increases until losses in the cavity are greater than the gain produced by incoming pump pulses (due to the profile of the Q-switched envelope). When the dye laser pulse is at its maximum intensity, it is cavity-dumped electro-optically.

The cavity dumper apparatus consists of a Pockels cell (Quantum Technology QK-10-1) coupled with a Glan laser escape window (Karl Lambrecht MGLA-SW-8). The

Pockels cell is essentially a KDP crystal that acts as a quarter-wave plate when a specified voltage, approximately 2.4 kV for 600 nm light, is applied axially. The Glan laser-escape window is a calcite polarizer that allows light of one linear polarization to pass through, but will reflect light of the opposite polarization out of the cavity. When the pulse in the cavity reaches its maximum intensity, a VFET switching circuit with a rise time of a few nanoseconds is triggered to place 2.4 kV across the Pockels cell [9]. After two passes through the Pockels cell, the pulse is of the opposite linear polarization, and is dumped out of the cavity by the Glan laser window. This near instantaneous high loss essentially stops lasing in the cavity until the next Q-switched pulse train arrives. The Pockels cell is triggered by a photodiode monitoring leakage from the high reflector of the Nd:YAG laser. A digital delay generator (Stanford Research Systems model DG535), is used to achieve the optimum dump time (Figure 9). Note that this digital delay generator is also used to trigger the transient digitizer and the boxcar during the data acquisition process.

Two intracavity etalons (a 5 micron airgap and a 100 micron solid etalon, Virgo Optics ET-3 and ET-100, respectively) are used for wavelength selection. Both etalons are required to obtain resolution on the order of 3 cm^{-1} . The 5 micron etalon acts as a broad band filter, and the 100 micron etalon acts as a narrow band filter. The superposition of these two bands on the dye gain curve gives the laser frequency band. After cavity dumping, the visible light pulses are sent to the molecular beam, or if necessary, frequency-doubled to the UV using a LiIO_4 , BBO, or KDP crystal.

3.4.3 Time Resolution by Michelson Interferometry

The time resolution of the pump-probe experiments is achieved by delaying the probe pulse relative to the pump pulse, using Michelson interferometry techniques. The pump laser beam is collimated and sent down a static delay line before being directed into the molecular beam. The probe laser is sent down a variable delay line. The variable delay

line consists of a corner cube (Precision Lapping, 1 sec. accuracy w/MgF₂ coating) mounted on a stepper-motor-driven translation stage (1 micron/step). The difference in path length between the pump and probe pulses gives the temporal resolution for our experiment. The translation stage used is an Aerotech ATS224 linear positioning stage with a programmable Unidex I driver. The variable delay line can provide up to 4 ns of delay time per pass. Longer transients could be measured by making successive passes through the variable delay line, but laser power losses through the corner cube make this impractical with the present arrangement.

The laser beams are then recombined on a mirror after which they are propagated collinearly and focused onto the sample. Focusing was achieved by use of a lens mounted on the TOF cube laser inlet. The TOF cube is described in Section 3.3. The lens is mounted on a vertical-motion translation mount so that the position of the focal length can be adjusted as necessary. The position of the lens is normally placed to where the greatest enhancement is seen between the pump and probe signals.

3.4.4. Pulse Characterization

Laser pulses from the dye lasers are characterized by taking their autocorrelations and cross correlations. The dye laser output is split into two arms, with 50% of the light in each arm. One arm is a static delay, while the other arm is sent down the optical delay line. The returned beams are recombined and focused into a nonlinear crystal with a converging lens. The second harmonic generated by this technique is essentially zero except when the pulses are temporally overlapped in the crystal. Thus the method is essentially a zero-background method [10,11]. By suitable adjustments of spatial overlap, relative pathlengths and phase-matching angle, the cross correlation between the two dye laser outputs is also obtained.

3.4.5 Optimizing and Aligning the Laser System

There are a number of routine procedures for laser alignment and performance optimization. They are reported below for the benefit of others using this system or other similar systems.

3.4.5.1 The Mode-Locked Q-Switched Nd:YAG Laser

Turning on the Nd:YAG laser consists of first turning on the cooling water, followed by the ignition of the flashlamp. The lamp current is set so that the lamp will draw 10 to 12 amps when ignited. Then the current is slowly increased to the operational level, approximately 32 amps. The above procedure is done with the resonator cavity blocked, and with a beamstop placed in front of the KTP doubling crystal. Note that as lamps age they will require slightly more current in order to provide enough power and stability. The modelocker and Q-Switch should be turned on now since they need a warm-up period as well. The YAG is very stable and should not require a long warm-up period, with 30 to 40 minutes being sufficient.

The performance of the Nd:YAG is monitored by using the IR leakage through the high-reflecting mirror (about 0.1%) displayed on an oscilloscope (Tektronix 4650B, 400 MHz). The maximum value of the pulse train should be between 4 and 5 volts (with the current photodiode circuit). The maximum of the prelasing signal should be approximately 15 mV. The prelasing should follow the pulse train by 400 microseconds, and should display a stable, exponential decay. The timing jitter in the prelasing signal is about 20 microseconds. Currently, this does not seem to be a significant problem. At 500 Hz, the measured green power should be between 300 and 350 mW, corresponding to 600 to 700 microjoules per pulse train.

If the Nd:YAG needs adjustment, then the following steps can be taken. Any tuning of the laser cavity is done while monitoring both the 532 nm power, and the

prelasing on the oscilloscope. If the prelasing decay is unstable, nonexponential, or has no decay, the problem usually is that the cavity length is slightly off. This is corrected by tweaking the micrometer at the high-reflector end of the cavity. To further optimize the power and the prelasing, one can slightly tweak the X and Y axes adjustments on the high reflector mirror mount of the cavity. In day-to-day operation, tweaking of the high reflector mirror mount is often all that needs to be done.

If the Nd:YAG is still not optimal, then there are a few other possibilities. First check the arc lamp current, especially if the lamp has run for more than 200 hours. The stability of the laser output is affected by the lamp current. However, the lamp current should never exceed 35 Amps. Second, the lamp may need replacement. Third, although this rarely needs to be done, check the Q-Switch angle and RF power level. The directions for the the Q-switch angle and RF power adjustments are in the Quantronix 416 manual.

3.4.5.2 The Cavity-Dumped Dye Lasers

The dye lasers were aligned in a series of steps. First, lasing is established without any internal components present other than the dye cuvette and focusing lens. The laser beam is centered within the cavity and optimized. Then additional internal components are added one at a time, and lasing is reestablished between each addition. First the Pockels cell assembly is added, then the polarizer, and then the etalons. In the following discussion, rear mirror refers to the dye laser mirror, which is on the same side of the optical table as the output coupler of the Nd:YAG. Likewise, front mirror refers to the dye laser mirror, which is on the same side of the optical table as the high-reflector mirror of the Nd:YAG.

The dye laser, using only the dye cuvette and focussing lens, was aligned as follows. First, the end mirrors are set up so that the cavity length is close to the cavity length of the Nd:YAG laser. The dye cuvette should be set as close as possible to the rear

mirror, and the lens is set so that its focus is between the cuvette and the mirror. When lasing is achieved, the 532 nm pump beam coming from the Nd:YAG should come in almost collinear to the line of lasing in the dye laser, and the spot size of both laser beams on the cuvette should be about equal. The spot size of the pump beam is controlled by an external lens before it intercepts the cuvette, and should be passed through the approximate center of the cuvette. The next step is to focus the images of the cuvette and of the spot off the rear mirror onto the front mirror. This is accomplished by tweaking the X and Y angular axes on the rear mirror, and the vertical and horizontal position of the intracavity lens. This task is made easier by placing a white card in front of the front mirror so that the image is visible. Once this is done, the reflection off the front mirror should be reflected onto the rear mirror and cuvette. At this point, with no obstructions in the cavity, one may see lasing. If lasing does not occur, first tweak the location of the pump pulse on the cuvette. This is a very sensitive adjustment, and should be done slowly through a horizontal and vertical scan. If this fails to initiate lasing, then try tweaking the end mirrors. It may take several iterations of first tweaking the location of the pump pulse on the cuvette, and then tweaking the end mirrors.

Once lasing is achieved, the dye laser can be optimized for power. A photodiode is used to monitor leakage through the front mirror. The cavity length is optimized by adjusting the location of the front mirror so that the dye laser leakage intensity is maximized. If lasing is not centered on the end mirrors, the laser beam can be walked around inside the cavity by adjusting the two mirror angles relative to one another. This is possible since the end mirrors are flat. Using the pump-beam steering mirrors, maximize the overlap of the pump beam and the dye laser beams in the cuvette. The quality of the overlap can be judged by how close the pump and laser spots are on the rear mirror. The pump-spot size is adjustable by varying the location of the lens on the pump beam. These adjustments should have a significant effect on the leakage intensity.

The main difficulty with the installation of the cavity dumper and etalons is that the optics is relatively thick, and therefore significantly lengthens the optical pathlength of the laser. The 5 micron air-gap etalon also deflects the beam path as well. Therefore it is important to adjust the cavity length after the installation of each component. The Pockels cell is the most difficult component. The 100 micron etalon is installed last, since it is so thin that it does not deflect the beam path significantly.

Install the Pockels cell close to the front mirror. Have the beam path through the center of the aperture, and have the faces of the Pockels cell windows set approximately perpendicular to the beam. Adjust the cavity length to optimize the leakage signal. At this point it is possible to follow the instructions in the Quantum Technology manual for the alignment of the Pockels cell. By lining up two pinholes with the dye laser beam and then passing the HeNe beam through these two pinholes, we can line up the Pockels cell in the correct position for our beam.

3.5 DATA ACQUISITION AND ANALYSIS

An Apple Macintosh II computer is used to control data acquisition and perform data analysis. Two NuBus boards are used for interfacing the Macintosh II to the laboratory equipment. One is an A/D board (National Instruments NB-MIO-16H-9), and the other is an IEEE board with DMA (direct-memory access) capability (National Instruments NB-DMA-8-G). A typical transient is obtained by averaging a data point, using either the boxcar or transient digitizer, over a couple of hundred laser shots for each position of the optical delay line (Figure 10). If data are collected using the boxcar, the boxcar averages the signal over a prescribed window and then dumps the data point to the Macintosh II through an analog-to-digital interface (National Instruments Lab Driver). If the signal is collected through the transient digitizer, the completed signal-averaged spectrum is DMA-transferred to the Macintosh II. Since the signal-to-noise scales as the

square root of the number of scans, it is preferable to make multiple data scans with each scan being done as fast as possible. This reduces biasing that is due to the laser or molecular beam system drifting over time. Typically, a scan of the delay line takes about 6 minutes, and 50-100 scans were required for an acceptable signal-to-noise ratio.

When cluster sizes are small, the single cluster sizes can be excited. Thus, only one mass peak is of interest, and the signal from the MCP is directed toward a boxcar integrator. For larger clusters, a distribution of cluster sizes is seen. In this case single cluster transients are obtained using either the boxcar, or alternatively from experiments in which the signal for all clusters is averaged by the transient digitizer at each delay line position. In the latter case, individual transients are reconstructed from the averaged mass spectra.

The system response function is approximately Gaussian with an autocorrelation FWHM of about 40 ps. The autocorrelation pulsewidth is used to obtain rate constants from the measured transients. A standard nonlinear least-squares analysis based on the Marquardt algorithm is used [12]. If the rising edge of the transients is not fit by the system response, then the transients are fit with a calculated Gaussian response function whose width best matches the rising edge of the transient. The quality of the fit is judged by the value of the chi-square between the real and fit data.

The data acquisition and analysis software used in this laboratory was developed by the author. The software consists of two independent applications conforming to the Macintosh User Interface guidelines. The first is entitled **Data Acquire**, and is for data acquisition and some data analysis. From **Data Acquire**, instructions can be sent to, and received from, various laboratory hardware components such as the boxcar, transient digitizer, and optical delay line. The second is called **Data Analysis**, and retains all the data analysis features of **Data Acquire** plus more advanced data analysis and function generation capabilities. **Data Analysis** has no communication features for external

equipment. Both programs have capacities for plotting data on the computer monitor, reconstructing transients from previously saved mass spectra, data manipulation, curve fittings, convolution, file generation, and printing. A detailed description of both programs from the point of view of both the user and the programmer is given in Volume two of this thesis.

3.6 REFERENCES

1. B. W. Keelan, *Ph.D. Thesis*, California Institute of Technology (1987).
2. W. R. Lambert, *Ph.D. Thesis*, California Institute of Technology (1983).
3. D. W. Willberg, J. J. Breen, work in progress.
4. Texas Instruments, *The TTL Data Book, volume 2* (1985).
5. (a) See, *e.g.*, R. S. Lehrle and J. E. Parker, *MTP Int. Rev. Sci., Phys. Chem. Ser. 1*, Vol. 5 (North-Holland, Amsterdam, 1972), p. 219.
 (b) T. D. Mark, *Int J. Mass Spec. Ion Phys.*, **45**, 125 (1982).
 (c) C. Brunee, *Int J. Mass Spec. Ion Phys.*, **45**, 51 (1982).
6. W. C. Wiley, I. H. McLaren, *Rev. Sci. Instr.*, **26**, 1150 (1955).
7. J. E. Pollard and R. Cohen, *Rev. Sci. Instr.*, **58**, 32 (1987).
8. F. G. Patterson, *Ph.D. Thesis*, Stanford University (1985).
9. VFET circuit design is found in:
 J. C. Postelwaite, J.B. Miers, C. C. Reiner, D. D. Dlott, *IEEE J. Quantum Electronics*, **24**, 411 (1988).
10. E. P. Ippen and C. V. Shank, *Top. Appl. Phys.*, Vol. **18** (Springer-Verlag, New York, 1984).
11. G. R. Fleming, *Chemical Applications of Ultrafast Spectroscopy* (Oxford, New York, 1986).
12. W. H. Press, B. P. Flannery, S. A. Teukolsky, and W. T. Vetterling, *Numerical Recipes in C* (Cambridge Univ. Press, Cambridge, 1988).

FIGURE CAPTIONS

- Figure 1:** Overall top view of the 3-chamber molecular beam apparatus.
- Figure 2A:** One-half of the circuitry for the TTL pulse delay generator. Numbers on the TTL components (*e.g.*, 74221 Dual Monostable Multivibrator) correspond to pin numbers. The function of each pin is listed in Reference 4. The six lines with arrows at the right of the figure are connected to the six lines at the left of Figure 2B. The output TTL pulse from the combined circuit of Figures 2A and 2B is sent to the amplifier circuit (Figure 3).
- Figure 2B:** One-half of the circuitry for the TTL pulse delay generator. Numbers on the TTL components (*e.g.*, 74221 Dual Monostable Multivibrator) correspond to pin numbers. The function of each pin is listed in Reference 4. The six open lines at the left of the figure are connected to the six arrowed lines at the right of Figure 2A. The output TTL pulse from the combined circuit of Figures 2A and 2B is sent to the amplifier circuit (Figure 3).
- Figure 3:** The amplifier circuitry for the pulsed valve driver. The input pulse is shaped by TTL components (Figures 2A and 2B). The output pulse drives the magnetic actuator of the pulsed valve.
- Figure 4:** A nonresonant photoionization time-of-flight mass spectrum of α -NpOH(NH₃)_n clusters showing a typical cluster distribution.
- Figure 5:** A block diagram of the equipment for obtaining EI/TOF spectra.
- Figure 6:** A schematic of the EI/TOF source. Shown are the ionizer assembly, ion optics, and pulsed electron gun. The assembly is mounted on the ionizer flange, and housed in the ionizer cube.
- Figure 7:** The EI/TOF timing diagram and the necessary voltages.
- Figure 8:** The EI/TOF high voltage pulser circuitry.
- Figure 9:** Schematic of the picosecond laser system.
- Figure 10:** Schematic of the experimental arrangement depicting the picosecond laser system and cluster beam apparatus. The configuration is for performing resonance-enhanced multiphoton ionization (REMPI) experiments.

Molecular Beam Apparatus Schematic. Top View.

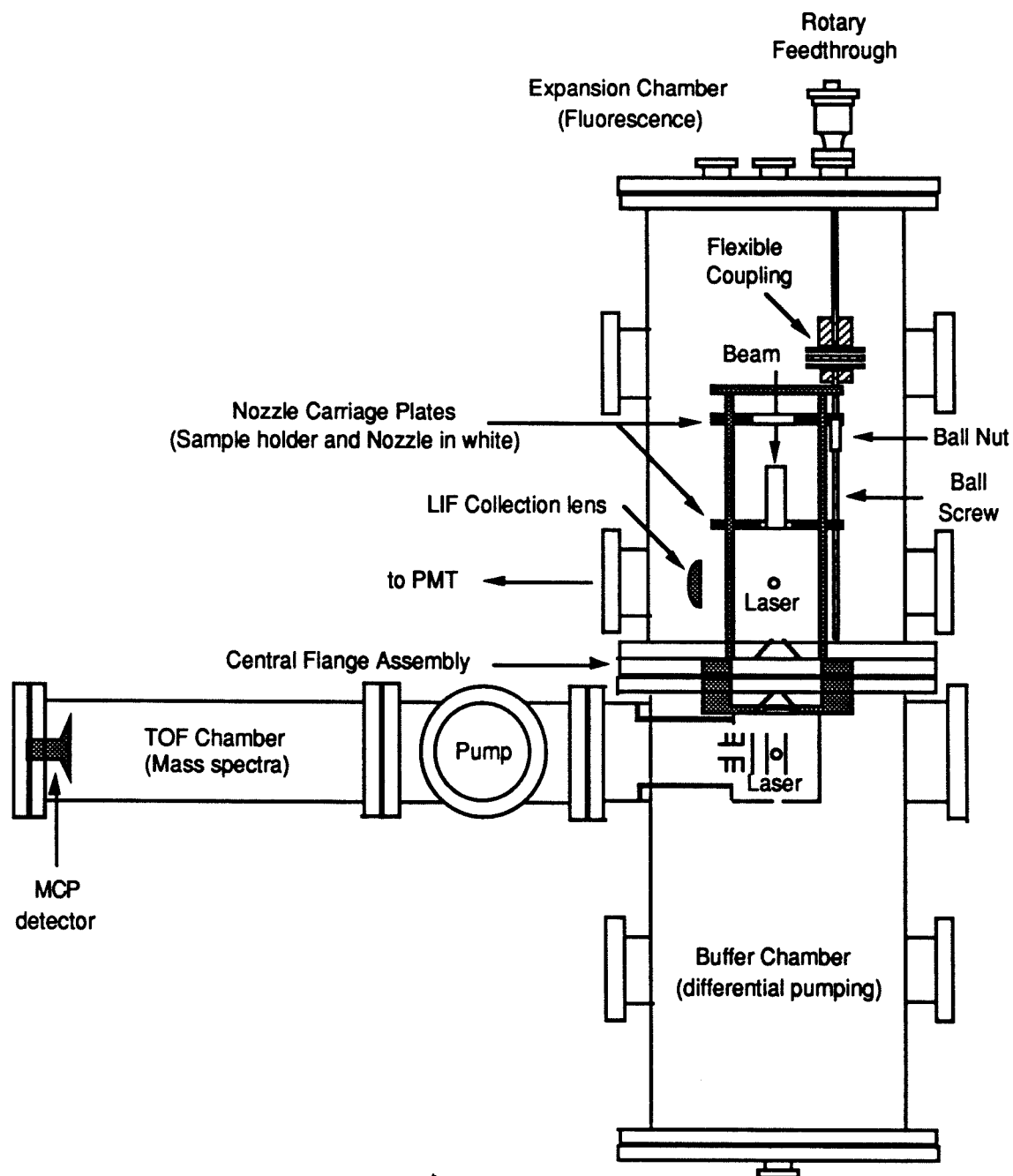


Figure 1

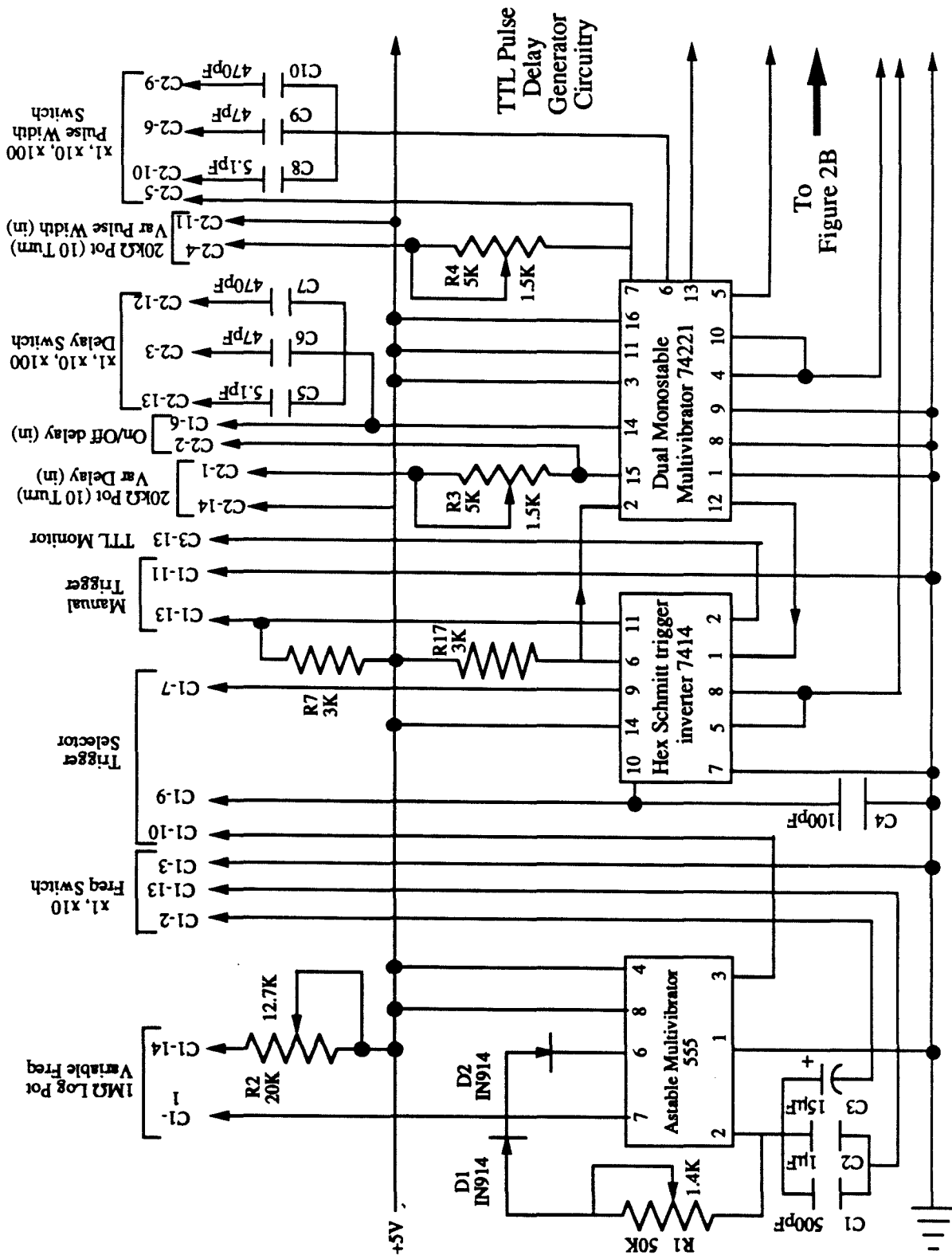


Figure 2A

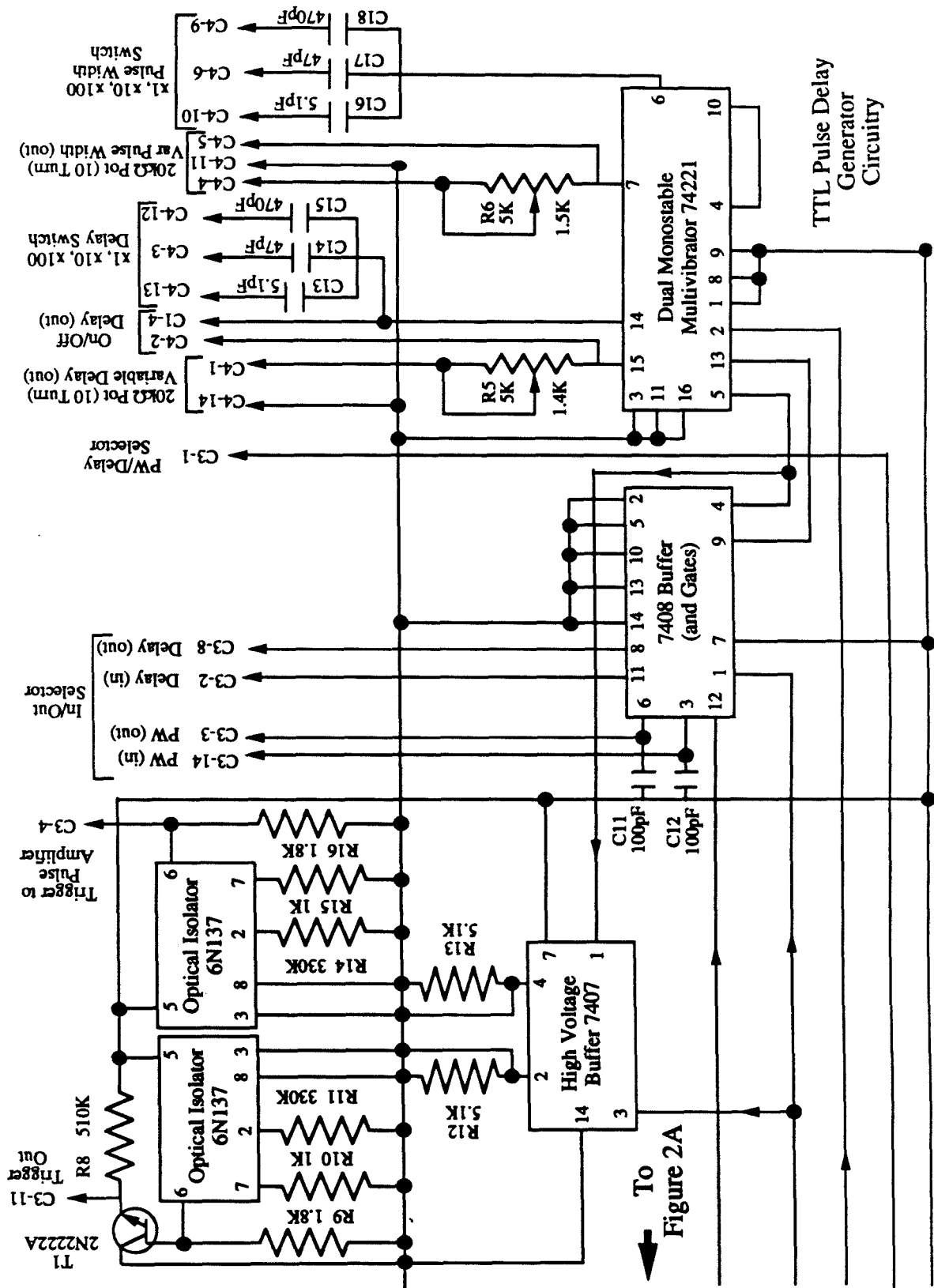


Figure 2B

To
Figure 2A

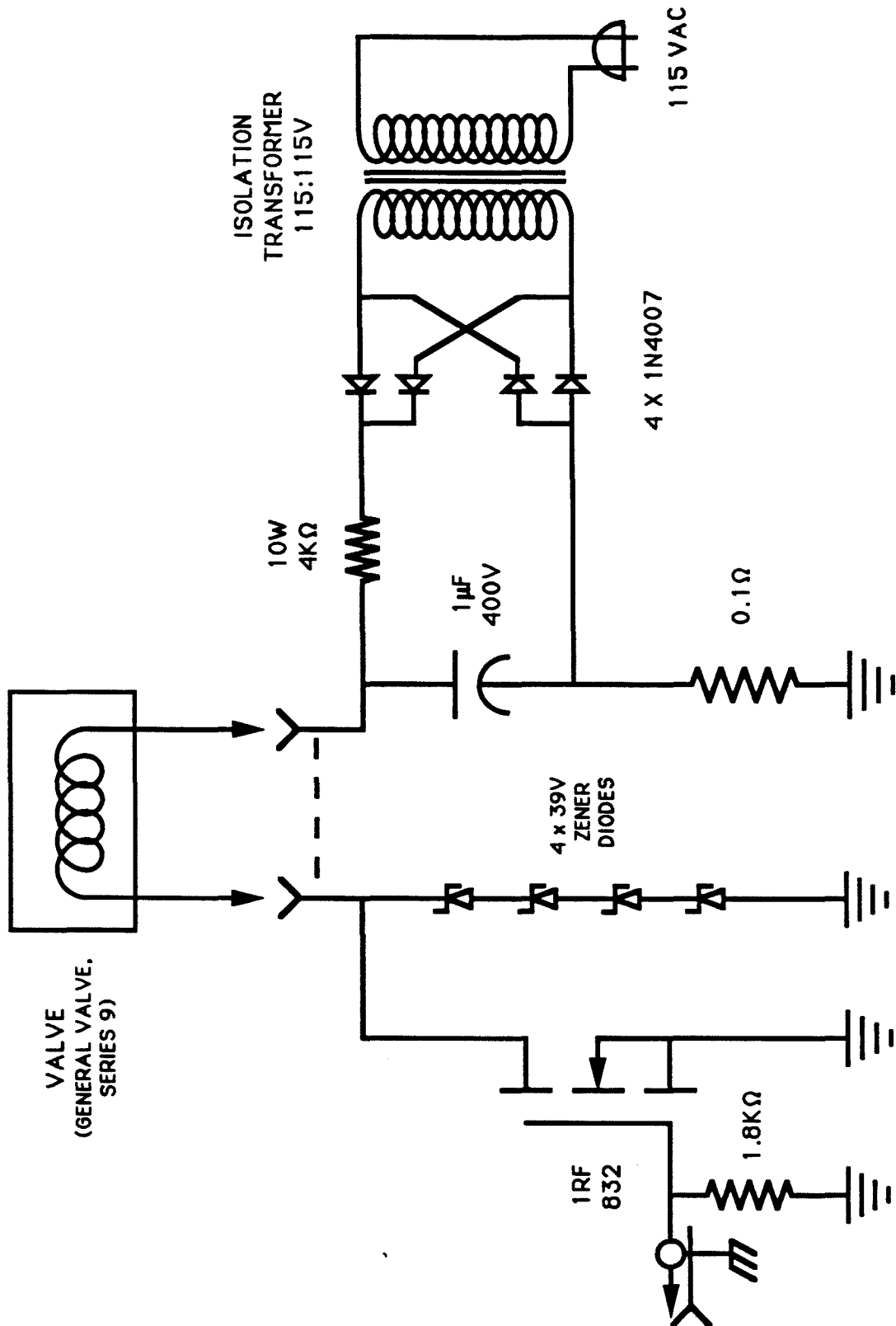


Figure 3

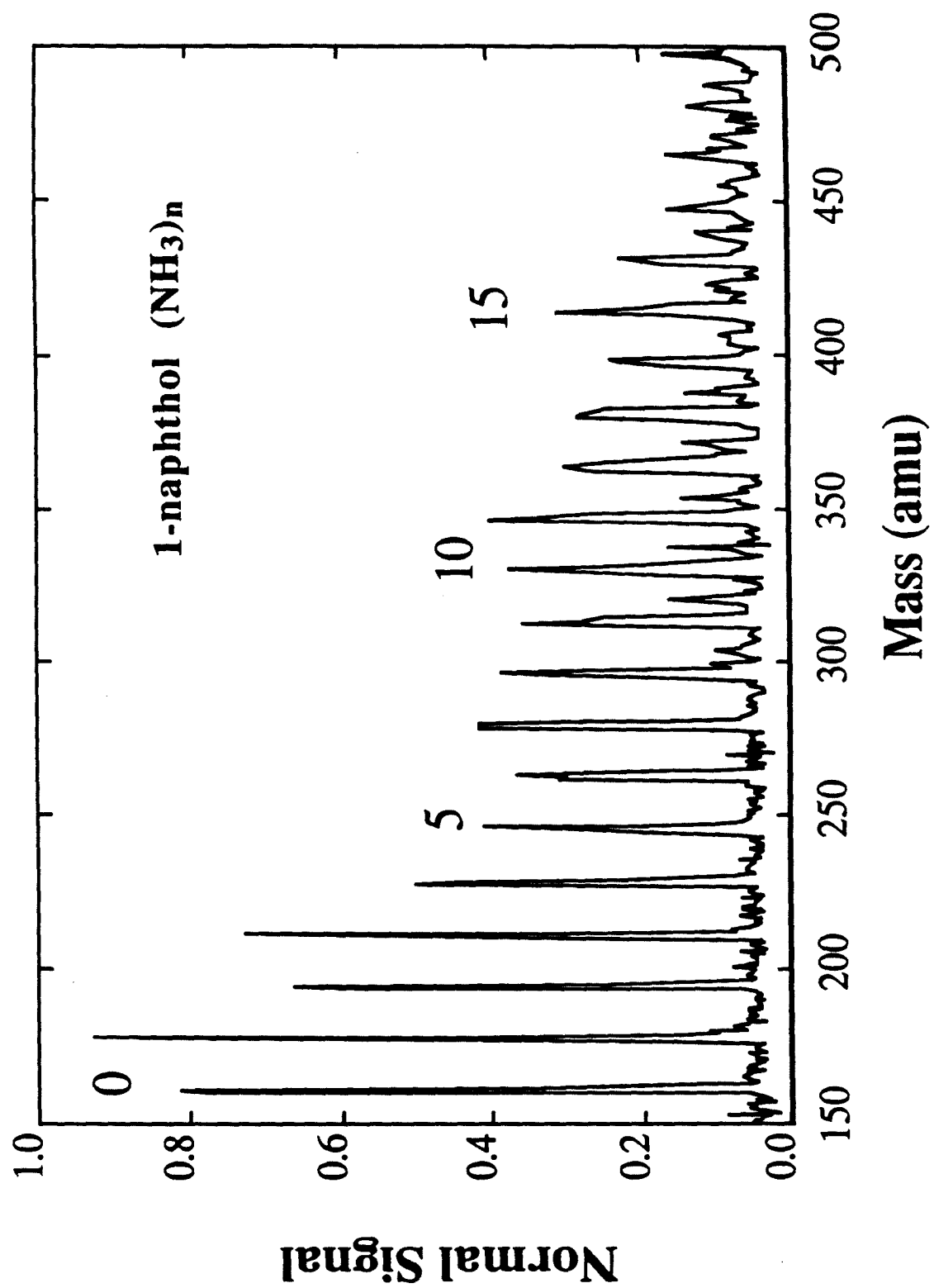


Figure 4

Block Diagram of EI/TOF Setup

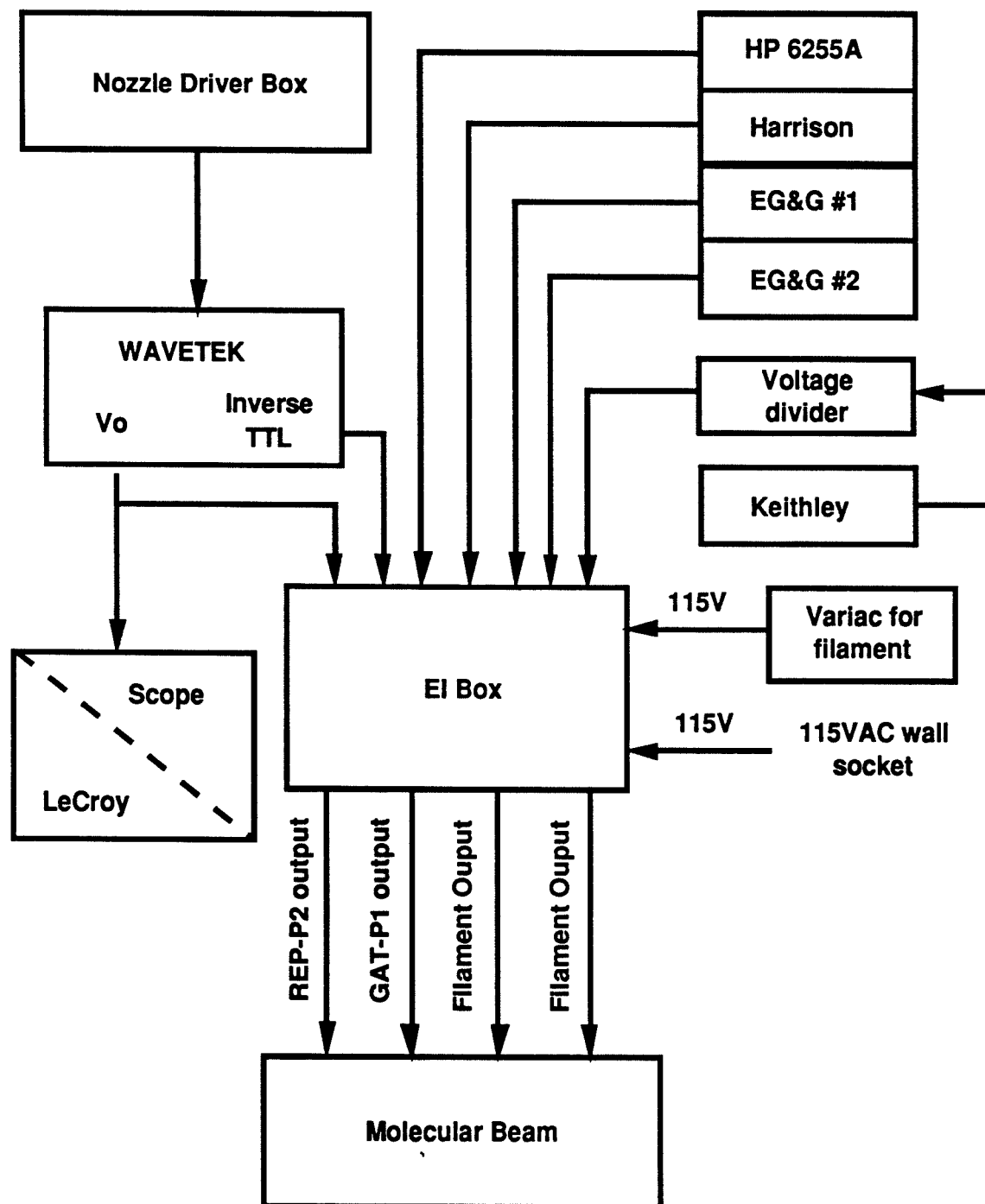


Figure 5

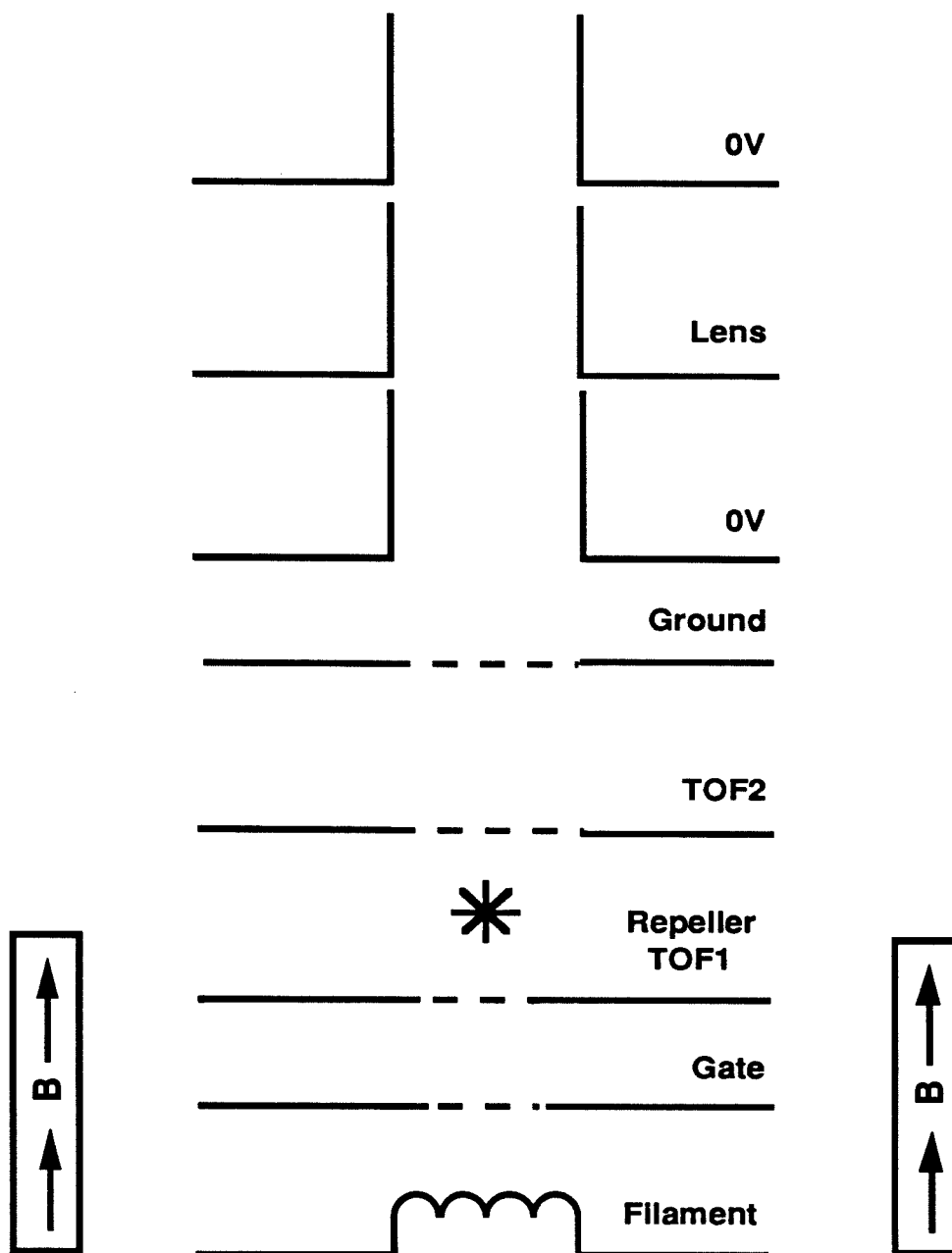
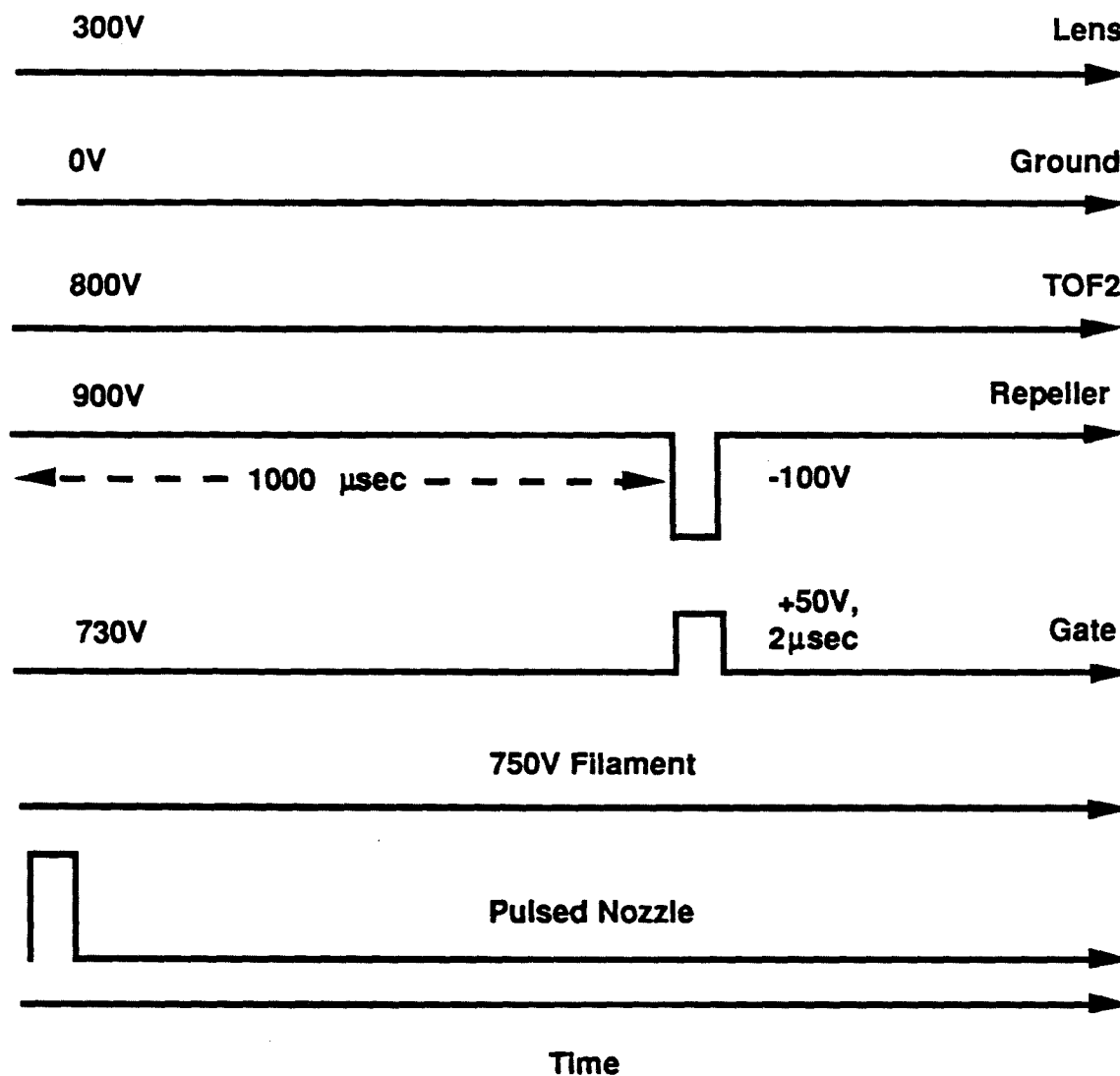
EI/TOF Ionizer Assembly

Figure 6

Timing Diagram for EI/TOF Voltages



Vertical Axis is Voltage

Pulse width for valve is approximately 550
microseconds

Figure 7

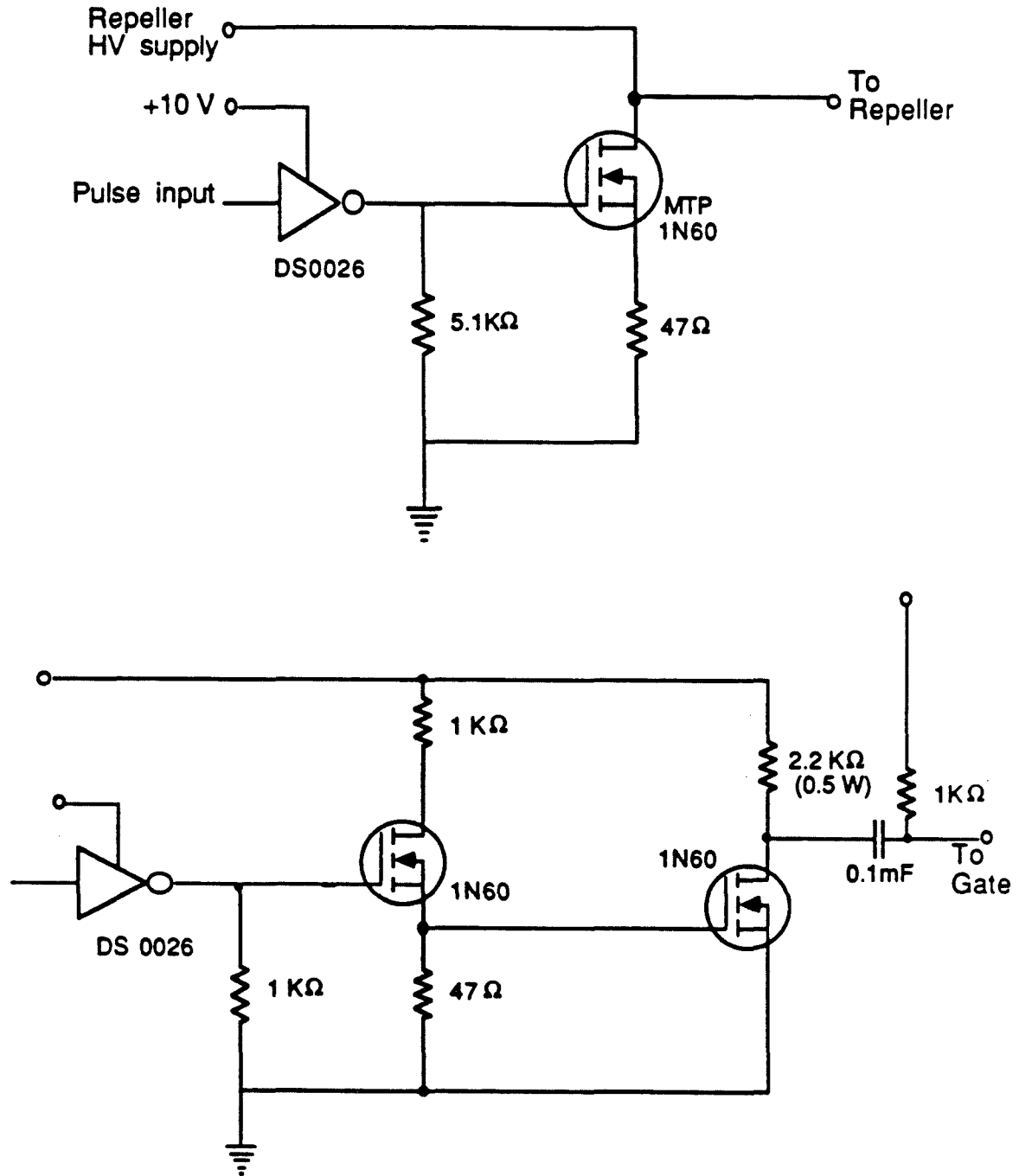


Figure 8

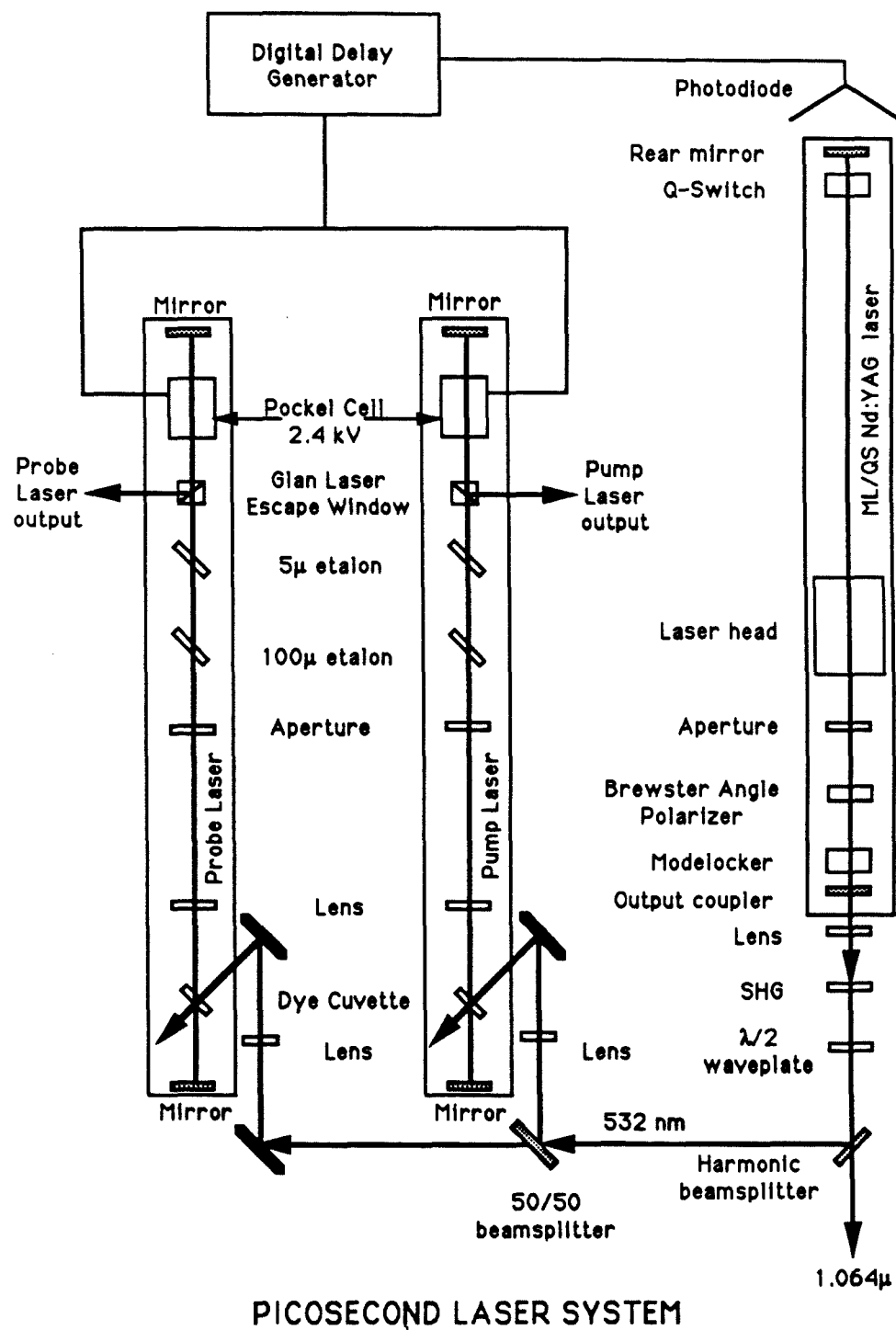


Figure 9

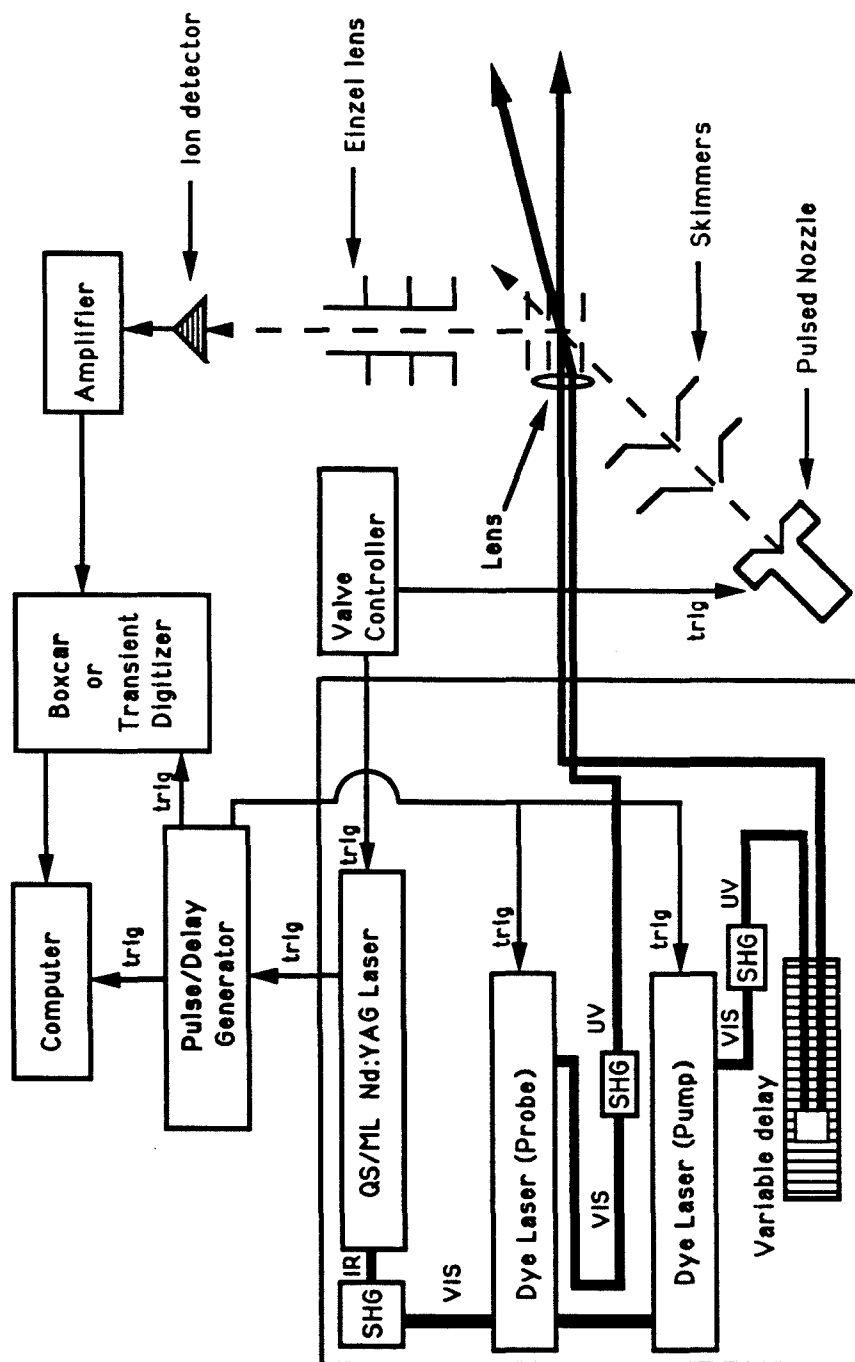


Figure 10

CHAPTER 4

STEPWISE SOLVATION OF THE INTRAMOLECULAR-CHARGE-TRANSFER MOLECULE **p-(Dimethylamino)benzonitrile**

This chapter was adapted from the publication:
L.W. Peng, M. Dantus, A.H. Zewail, K. Kemnitz, J.M. Hicks and K.B.
Eisenthal, "Stepwise Solvation of the Intramolecular-Charge-Transfer Molecule p-
(Dimethylamino)benzonitrile," *Journal of Physical Chemistry*, **91**, 6162-6167 (1987).

ABSTRACT

This chapter presents a systematic study, both in a supersonic jet expansion and in a thermalized vapor, of gas-phase p-(Dimethylamino)benzonitrile (4-DMABN). From the jet studies, the excited- and ground-state vibrational spectra of the isolated molecule are resolved, and the spectroscopy of the stoichiometric complex with water, methanol, ammonia, and acetonitrile in the beam is reported. It is concluded that 1:1 complexes are not sufficient for the local perturbation to cause charge separation. At higher temperature in the jet, we observe emission that we attribute to 4-DMABN self-complexes. Under high pressure and temperature conditions (>30 mTorr, 60°C), red-shifted fluorescence from 4-DMABN is observed. This is attributed to the charge-transfer state of 4-DMABN in self-complexes.

4.1 INTRODUCTION:

Many recent investigations have focused on the role of the solvent in the charge-transfer process for molecules in solution [1-20]. Both intramolecular [8-14] and intermolecular [15-17] charge separations have been studied. The solute-solvent interactions can be passive, as observed in the cage effect where the primary role of the solvent is to trap the solute particles within a volume, enabling them to collide and react with each other [18-20]. The solute can also be actively coupled to the medium, as in the case of charge-transfer reactions where the energies of initial, intermediate, and final states, the reaction pathways leading to different products, and the kinetics of the transitions can be dramatically affected by the solvent. Static [1,3,10] and dynamic [4,6,14] polarity effects, as well as local solute-solvent interactions [21] such as hydrogen bonding are important in these latter processes.

An example of a molecule that interacts strongly with polar solvents is *p*-(dimethylamino)benzonitrile (4-DMABN). In polar solvents, an excited 4-DMABN molecule undergoes a rotation of the dimethylamino group about the amino-phenyl bond to achieve a perpendicular geometry with respect to the plane of the benzene ring [22]. This motion results in charge separation, as evidenced by the measured increase in the excited-state dipole moment from 6 to 16D [23]. In polar solvents, the twisted, charge-separated form is stabilized, and a dual fluorescence appears. It consists of a UV component plus a new red-shifted emission that does not appear in nonpolar solvents. Rapid equilibration between the twisted and planar forms in polar media yields the dual fluorescence. This twisted internal-charge-transfer model (TICT), was first proposed by Grabowski and co-workers [22]. Picosecond spectroscopic studies [11,24] have confirmed that (i) the planar state is the precursor of the twisted state and (ii) equilibrium between the two states is established during the excited-state lifetime. Further, the dominant solvent effect on the dynamics of the charge separation in this case has recently been attributed to static polarity

effects [10]. The proposal of a barrier whose height changes with the polarity of the medium gives a simple explanation for the appearance of dual fluorescence in polar solvents and a single UV fluorescence in alkanes: A certain polarity is required before the TICT barrier is low enough to allow the forward TICT process to proceed within the lifetime of the initially excited state.

The recent work by Robinson et al. [25] and others [26] attempts to deduce the number of water molecules that must be present in order to induce effects such as the one described above for 4-DMABN. The idea is that a critical number of solvent molecules exist for a given charge-transfer or proton-transfer process. It is conceivable in the case of 4-DMABN that a 1:1 4-DMABN/solvent complex could provide sufficient stabilization by charge-transfer or dipolar interactions to permit the photoisomerization of 4-DMABN to its twisted charge-transfer state [27-30].

In order to investigate some of these ideas about the role of the solvent, we have undertaken studies of 4-DMABN in a supersonic beam and in a thermalized vapor as a complement to liquid-state studies. The beam studies are similar to earlier work on solvation in the isoquinoline/water [21] system and on charge transfer in the anthracene/dimethylaniline [31,32] system. In the gas phase, some derivatives of 4-DMABN have been studied [13,30]. Another compound thought to undergo TICT, 9,9'-bianthryl, has been studied in a supersonic jet [34], where it was found that charge transfer occurs on the addition of one acetone molecule to the solute [35]. However, in this case, no evidence was given for the 1:1 stoichiometry, and it is not ruled out that higher complexes were responsible for the observed charge-transfer fluorescence.

The idea of the beam work is to generate 1:n solute to solvent complexes (water, methanol, ammonia, and acetonitrile were the solvents in these studies), and to determine thereby the relation between the solute-solvent interactions and the TICT process. Among the issues concerning the twisted internal charge transfer of 4-DMABN are the critical

number of solvent molecules, the relative contribution of the local and the long-range stabilizing forces (the latter force can be important in liquids), and the details of the solute-solvent interaction, *e.g.*, steric effects, hydrogen bonding, and dipolar interactions. The high-pressure vapor work sought to determine if, in a gas-phase dimer or small cluster, 4-DMABN itself could act as a stabilizing solvent molecule to a photoexcited member of the cluster. Earlier work on very concentrated 4-DMABN/alkane solutions showed that a ground-state molecule could form a loose complex with an excited 4-DMABN [29] and thus provide the stabilization required for the photoisomerization to occur.

In this chapter, we present a systematic study of solvated 4-DMABN in a supersonic jet expansion. We resolve the excited- and ground-state spectra of the isolated molecule, and we report on the spectroscopy of the interaction complex with solvent in the beam. It is concluded that 1:1 complexes are not sufficient to allow charge separation. In the thermalized vapor experiments, we observe both the UV monomer emission and the visible emission that are due to the charge separation made possible by the stabilization of 4-DMABN self-complexes. Under appropriate conditions in the beam, and in the absence of solvent, we also observed visible emission that we attribute to 4-DMABN in self-complexes.

It should be noted that while this work was in various stages of publication, two additional supersonic jet studies appeared. One studied the complexes with H₂O and CF₃H [47]. The shift observed for water was the same as ours (18 cm⁻¹ to the blue). The second [48] studied complexes of 4-DMABN with H₂O and CH₃OH and has reported similar findings about the spectroscopic shifts. The fluorescence lifetimes of the base and methanol complex are in agreement with our results.

Finally, several other studies have appeared [49-51] since the publication of this work. Two-color time-of-flight mass spectrometry (TOFMS) has been employed to study 1:1 complexes of 3- and 4-DMABN with H₂O, CH₄, (CH₃)₂CO and CH₂Cl₂, and

CH₃CN [49]. This study also concluded that 1:1 solvation is not sufficient for charge-transfer to occur. LIF [50] and two-color TOFMS [51] have also been used to study various DMABN analogues in order to understand the spectroscopy of 4-DMABN. Of particular interest has been the conformation of the dimethylamino group. Lennard-Jones potential energy calculations have been performed on these systems [49,51] and the results suggest that the S₁ state is already displaced by 30° upon optical excitation from the ground state. However, the implications of these calculations with respect to the TICT state mechanism are still not clear.

4.2 EXPERIMENTAL:

The two sets of supersonic beam apparatus used for this study have been described previously in detail [36,37]. The expansion condition is noted in each figure. Most excitation spectra and dispersed fluorescence for 4-DMABN/H₂O complexes were recorded with a continuous-jet system [36]. The remaining spectra for the 4-DMABN/H₂O complexes, spectra for the other DMABN/solvent complexes, and spectra for the DMABN self-complexes were recorded with a pulsed-jet system [37]. In general, p-(dimethylamino)benzonitrile (4-DMABN) (Aldrich; 98%) and p-(diethylamino)benzonitrile (4-DEABN) (Pfaltz and Bauer; 97%) were seeded in different carrier gases: He, Ne, Ar, or N₂. The use of purified 4-DMABN (99.5%) gave the same results as shown here for the less pure preparation.

Different carrier gases were used at different stagnant pressures in order to determine the optimum cooling condition while minimizing the formation of van der Waals complexes. In the continuous jet, He at 40 psi backing pressure was used. For the pulsed jet, 50 psi He for 4-DMABN self-complexes was used, while 70 psi He was used for complexes with other solvents. The nozzle diameters for the continuous and pulsed jets were 100 and 500 microns, respectively. To form solvent/solute complexes, a careful

control of the solvent concentration was necessary. By controlling the temperature (from -70 to 25°C) of the wet-line reservoir and by using water solutions with different concentrations of calcium chloride (0-6M), we were able to change the partial pressure of solvent in the nozzle expansion.

For the continuous-jet apparatus, excitation spectra were obtained by using the frequency-doubled output of a nitrogen-pumped dye laser with an amplifier stage. Lifetime measurements and dispersed fluorescence studies in the beam were obtained by using the frequency-doubled output of a synchronously pumped, cavity-dumped dye laser [36]. Excitation spectra using the pulsed system were obtained by using the frequency-doubled output of a YAG-pumped dye laser (5-ns pulses) operated at 10 Hz. The signal was normalized with respect to laser intensity. Unlike the 0.4-3.2 Å resolution for the continuous apparatus that we used for recording the sharp features of the fluorescence, wider slits (resolution of 24 Å) were used for recording emission at high temperatures.

The study of 4-DMABN vapor at higher pressures and temperatures was carried out by heating doubly sublimed crystals in an open cell and irradiating the vapor above it. This procedure was found to be better than using a sealed evacuated cell containing crystals, since the presence of fluorescent adsorbed 4-DMABN species on the quartz walls contaminated the signal from the free vapor species. Using an MKS Baritron gauge, we measured the vapor pressure of 4-DMABN at 22°C to be 30 mtorr (uncorrected). The temperature of the vapor was measured by placing a Cu-constantan thermocouple at the top of the cell and reading from a calibrated Omega digital meter. Picosecond kinetics was measured by the method of single-photon counting, using a synchronously pumped, cavity dumped dye laser.

4.3 RESULTS

A. Isolated 4-DMABN

The excitation spectra of jet-cooled 4-DMABN and 4-DEABN are rich and show spectroscopic manifestations similar to other alkyylanilines [38]. The symmetry of the transition is effectively unchanged, and one expects the aniline-type modes to be active. In our excitation spectra, these modes (12 and 6a) can be assigned to observed bands with minor frequency shifts compared to aniline and p-alkylanilines.

Figure 1 displays a portion of the excitation spectra of the two molecules. The 0,0 region of 4-DMABN shows a structure of low-frequency bands similar to that found in alkylanthracene [32,39], bianthryl [34], and many alkyl aromatics [40]. This structure could be due to low-frequency torsional modes that display the properties of a double-well potential [34,40] and hence the unique Franck-Condon pattern. Also, it is possible that some of the bands, especially the weak ones, are due to different conformers that freeze-in during the expansion or due to aggregates. The actual assignment of the 4-DMABN origin cannot be made without a detailed analysis of the torsional structure similar to that done for bianthryl [34] and the systems described by Ito [40]. Thus we tentatively take the "origin" to be the strongest peak in the origin region.

For 4-DEABN, the 0,0 region of the excitation spectrum appears to be less rich than that of 4-DMABN. This observation may support the idea of the double-well potential, since here the "locking" of the amino group by the ethyl chains could result in a higher torsional barrier. Finally, the "origin" of 4-DEABN is red-shifted from that of 4-DMABN by 452 cm^{-1} . 4-DMABN is red-shifted by 1644 cm^{-1} from aniline and by 701 cm^{-1} from p-methylaniline.

The dispersed fluorescence spectra of 4-DMABN and 4-DEABN are shown in Figure 2 for different excitation wavelengths. The first point to be noted is that in all spectra, the dispersed fluorescence tails off after 6000 cm^{-1} . No further fluorescence was

observed (with our sensitivity) upon inspection of the region to the red of that shown in Figure 2, where charge-transfer fluorescence is expected to appear (red-shifted by 6300 cm^{-1}). This feature was found to be insensitive to the excitation wavelength in the region studied. For DMABN, this is true up to 280 nm. The 308.7 nm excitation of 4-DMABN and the 314.3 nm excitation of 4-DEABN are very similar and are consistent with characteristics of the excitation spectra. Excitation of the weak band of 4-DMABN at 309.9 nm (Figure 2, top) was recorded with lower resolution (because of weak intensity) and is shown here to emphasize that the major structures of its fluorescence spectrum are similar, although distorted somewhat because of the poorer resolution. From excitation and dispersed fluorescence, it is concluded that the isolated 4-DMABN molecule cannot by itself undergo charge transfer (up to given excitation energies).

B. Complexes of Solvent/4-DMABN

In order to establish the formation of complexes between solvent and 4-DMABN in the supersonic expansion, the fluorescence excitation spectra were recorded while the partial pressure of solvent was varied. In Figure 3, the spectral region about the strongest (308.7 nm) vibrational band is shown as a function of increasing water pressure ($\text{P}_{\text{H}_2\text{O}}$). A new band appears, which is blue-shifted by 18 cm^{-1} from the main peak, and increases at first approximately linearly with $\text{P}_{\text{H}_2\text{O}}$, independent of the carrier gas used. Similar new bands appeared on other vibrational transitions; *e.g.*, a new peak on the 309.1 nm band appeared blue-shifted by 15 cm^{-1} . We assign these new bands to the 1:1 4-DMABN/water complex. The same behavior was found with the solvents CH_3OH , CH_3CN , and NH_3 over the temperature range of 70 to -15°C . Attempts were made to form complexes with acetic acid and acetone. However, in spite of the fact that the DMABN signal drops significantly, we were unable to observe any new bands under similar beam conditions. Figure 4 shows the fluorescence excitation spectra (about the origin) of DMABN

complexed 1:1 with NH_3 , CH_3OH , and H_2O . (Note that the scale and wavelength scan direction are different from Figure 3). The spectral shift relative to the strongest band of DMABN (308.7 nm) is 21, 15, and 18 cm^{-1} , respectively, to the blue (when CH_3CN is used there is a very weak band blue-shifted by 254 cm^{-1}). We assign these blue-shifted peaks as the 1:1 4-DMABN/solvent complex. The shifts for the three solvents are similar, but it is difficult to know from the shift the exact site for complexation.

A search for the long-wavelength emission that is characteristic of the CT band was made by exciting the complexes. In Figure 5, we have aligned the fluorescence spectra obtained by exciting the isolated and water-complexed 4-DMABN at 308.7 and 308.5 nm, respectively. These spectra are seen to be almost identical except for a constant shift because of the binding of the water. More important perhaps is the noted absence of a new red-shifted emission for the complex, indicating that charge transfer does not occur.

Further support for the conclusion that charge transfer in the excited state does not occur for the complex comes from lifetime measurements. The isolated 4-DMABN molecule under beam conditions has a lifetime of 5.3 ns (measured at 308.7 nm). The band at 308.5 nm of the complex has a lifetime of 5.3 ns. Since the fluorescence lifetime does not change, we conclude that the planar excited 4-DMABN is the emitting state; *i.e.*, the twisted charge-transfer state has not been formed. This is consistent with other studies where it was found that excitation below the barrier for dissociation gives similar lifetimes for the complex as for the parent molecule [41].

It is possible that if enough internal energy is given to the 1:1 complex, charge separation will occur similar to the situation found in anthracene/DMA systems [31,32]. In view of this, dispersed fluorescence spectra were recorded, under conditions for complex formation, for excitation at the same wavelengths as that of the isolated molecule. Spectra were also taken for excitation wavelengths corresponding to peaks attributed to the 1:1 complex. The dispersed fluorescence gave no CT red-shifted emission. We have

attempted to measure the lifetime of the water complex and the parent molecules at higher excess vibrational energies, similar to the isoquinoline study [21]; however, because of spectral congestion, we could not measure the signal for the complex. For the isolated 4-DMABN molecule, lifetimes of 4.89 and 4.69 ns were measured for excess energies of 624 and 948 cm^{-1} , respectively. We plan to pursue this study by using picosecond mass spectrometry, as was done in the case of phenol/benzene complexes [41].

Our beam results indicate that one solvent molecule (CH_3CN , H_2O , CH_3OH , NH_3) is not sufficient to stabilize the charge-transfer form of 4-DMABN. Studies on the solvated electron by Kenney-Wallace [42], Kevan [43], and others indicate that several alcohol molecules are required to stabilize the bare electron. In recent work by Robinson and co-workers [25], it was pointed out that for electrons and protons, a water cluster of 4 ± 1 members is the effective charge acceptor. With this in mind we have attempted to increase the density of solvation around 4-DMABN in the beam to observe a threshold for the formation of the charge-transfer state.

In the attempt to make 1:n complexes of 4-DMABN/solvent, a decrease in the parent molecule signal was observed. In addition, at high solvent vapor pressures, the background signal increases. This problem is similar to the one found by Even and Jortner [44] in their studies of fluorene complexes with water. We are attempting a new design in the beam to enhance the formation of large clusters.

C. Self-Complexes of 4-DMABN

When the temperature of the nozzle of the jet containing 4-DMABN was raised, a broad emission centered at 385 nm was observed. This band, which spans 48 nm, was especially apparent at high backing pressure. Therefore, we assign this fluorescence to aggregates of 4-DMABN itself.

Figure 6 shows the pressure dependence of the emission band at 385 nm when exciting at 309.9 nm. Variation in temperature affects the intensity of the band. At high backing pressure (50 psi) the broad 385-nm emission is observed, while at low backing pressure (10 psi) emission typical of the planar "monomer" (under 24 Å resolution) was observed centered at 330 nm. Intermediate pressures gave spectra with peaks at 330 and 385 nm. This general behavior with pressure and temperature was observed over the range of the aggregate emission (280-320 nm). Under conditions that gave optimum aggregate formation, dispersed fluorescence spectra were taken for excitation of the aggregate at the same wavelengths used for the bare molecule and for the times when solvents were used. All spectra gave an emission composed of the monomer plus a contribution from the aggregate. The aggregate contribution was checked by taking spectra at low backing pressure and verifying that only monomer-type emission remained. We observed no red-shifted emission that could be attributed to charge transfer.

The excitation spectrum of 4-DMABN under optimum conditions for aggregate formation was taken over the range of 320-280 nm. Spectra were recorded under two detection conditions: total fluorescence and by scanning the laser with the monochromator set at 400 nm (2.4 nm resolution). The setting of the monochromator at 400 nm allowed maximum detection of the aggregate fluorescence, while trying minimize contributions from the monomer. The excitation spectrum using total fluorescence shows the monomer bands on top of a broad background. With the monochromator set at 400 nm, smaller monomer band intensity on a structureless background is observed. The background signal was observed to begin at 320 nm and to rise slowly as the excitation wavelength was scanned down to 280 nm.

These aggregates were also studied in the vapor above an open cell containing crystalline 4-DMABN. By varying the temperature of the vapor and the excitation wavelength, we observed various bands that we attribute to the planar monomer, the planar

dimer (or n-mer), and the twisted dimer (or n-mer). At 90°C and excitation wavelength ≤ 310 nm, an emission centered at 330 nm is observed (Figure 7), which we attribute to the planar monomer. The band rises instantaneously within our resolution, and decays with a lifetime of 400 ± 100 ps, independent of the wavelength observed [45]. No visible emission is seen under these conditions. At $\approx 66^\circ\text{C}$, and for excitation wavelengths of 290-320 nm, two red-shifted emitting species can be distinguished. (See Scheme I in Figure 8). A band at ≈ 380 nm appears instantaneously and decays with two lifetimes: 90% of the intensity decays in 60 ± 30 ps and the remaining 10% decays in 700 ± 200 ps. A broad visible emission, centered at 500 nm, is observed to have a rise time of 60 ± 30 ps and a decay time of 1000 ± 200 ps (Figure 9). The visible emission therefore originates from the 380-nm band. The two excited species appear to be equilibrated, as evidenced by the fact that they have approximately the same long lifetime. We attribute these two bands to the planar $[(M_n^*)_P]$ and the charge-separated $[(M_n^*)_T]$ forms of a 4-DMABN aggregate. From the different lifetimes of the 330- and 380-nm fluorescence bands, it is apparent that there is no equilibrium established between the monomer and aggregate forms in the excited state. This is not surprising, since the collision time between 4-DMABN species at the very low vapor pressures of these experiments is longer than the typical lifetimes of the excited states.

The 380-nm species observed in the vapor above an open cell corresponds to the 385-nm emission observed in the beam experiment (reported herein) and to that observed in the concentrated hexane solution at 228 K [29]. However, in these latter two cases, no charge-transfer fluorescence accompanied the UV band. At the lower temperatures of these two experiments, there is apparently not enough energy to cross the excited-state barrier. This is in spite of the fact that for the beam work, excitation of the aggregate was carried up to 3300-cm^{-1} corresponding monomer excess energy. In contrast, we do observe charge transfer from a 4-DMABN vapor at higher temperatures ($\approx 66^\circ\text{C}$), presumably where the

thermal population and/or aggregate size is such that barrier crossing can be achieved. At still higher temperature ($\approx 90^\circ\text{C}$) the aggregates dissociate, and hence we see on monomer emission.

The absorption spectrum of 4-DMABN in the gas phase contained in a cell at 30 mTorr and room temperature yields a broad band centered at 280 nm. For a change in temperature from 12 to 90°C , the band shifts from 290 to 272 nm. These two bands are thought to represent absorption by the 4-DMABN aggregate (dimer or n-mer) and monomer, respectively. This is a reasonable assignment based on the absorption bands for 4-DMABN in hexane, at 282 nm, and as a polycrystalline powder, at 307 nm. The fluorescence spectrum shows a transition from visible to UV emission upon raising the temperature, and is coincident with the temperature-dependent changes in the absorption spectrum that we attribute to an increasing monomer/dimer(n-mer) ratio at higher temperatures.

4.4 CONCLUSIONS

We conclude from these studies in a thermalized vapor that self-complexes of 4-DMABN (dimer or n-mer) can undergo a twisted internal-charge-transfer excited-state isomerization, on the basis of the observed visible emission characteristic of this polar state. Self-complexes were also formed in the beam, but charge transfer was not observed. Presumably, this reflects the differences in the internal temperature and/or size of the aggregates formed in the jet versus those formed in the vapor. In contrast, the beam studies reveal that the isolated molecule and the 1:1 complex with water, methanol, acetonitrile, or ammonia do not undergo a charge-transfer isomerization. These results can be understood in terms of the argument that a sufficiently polar solvent molecule or molecules are required before excited-state charge transfer and structural twist can occur. One solvent molecule is not enough to stabilize the charge-separated form. Although in the

beam the solvent is frozen out, the evidence from liquid-state studies [10a] indicates that solvent dielectric relaxation (*i.e.*, solvent motion) does not control the dynamics of TICT. Also of importance is the possible role of specific interactions between the solute and solvent. In protic solutions, hydrogen bonding is thought to oppose the charge transfer in 4-DMABN by withdrawing electron density from the amino nitrogen [10b]. Since the geometry of the 4-DMABN/solvent complex is not yet known, it is difficult to make any conclusions about the effects of hydrogen bonding on the dynamics of CT formation.

Acknowledgements

We acknowledge the support of this work from the following granting agencies: National Science Foundation Grant DMR-8521191, Air Force Office of Scientific Research Grant AFOSR-87-0071, and the Joint Services Electronics Program 29-85-K-0049. We also thank Professor Rudy Marcus for many informative discussions and Dr. K. Bhattacharya for his assistance.

Registry No. DMABN, 1197-19-9; DEABN, 2873-90-7; H₂O, 7732-18-5; CH₃OH, 67-56-1; NH₃, 7664-41-7; CH₃CN, 75-05-8.

4.5 REFERENCES

1. R. A. Marcus and N. Sutin, *Biochim. Biophys. Acta* **811**, 265 (1985).
2. W. J. Albery, *Annu. Rev. Phys. Chem.* **31**, 227 (1980).
3. V. Balzani and F. Scandola, *Energy Resources through Photochemistry and Catalysis*; edited by T. J. Gratzel (Academic, New York, 1983) p. 1.
4. D. F. Calef and P. G. Wolynes, *J. Phys. Chem.* **87**, 3387 (1983); *J. Chem. Phys.* **78**, 470 (1983).
5. J. T. Hupp and M. J. Weaver, *J. Phys. Chem.* **89**, 1601 (1985).
6. G. Van der Zwan and J. T. Hynes, *Chem. Phys. Lett.* **101**, 367 (1983); *J. Phys. Chem.* **89**, 4181 (1985).
7. L. D. Zusman, *Chem. Phys.* **49**, 295 (1980).
8. J. R. Miller, L. T. Calcaterra, and G. L. Closs, *J. Am. Chem. Soc.* **106**, 3047 (1984).
9. Z. R. Grabowski, K. Rotkiewicz, A. Siemiarczuk, D. J. Cowley, and W. Baumann, *Nouv. J. Chim.* **3**, 443 (1979).
10. (a) J. M. Hicks, M. Vandersall, Z. Babarogic, and K. B. Eisenthal, *Chem. Phys. Lett.* **116**, 18 (1985). (b) J. M. Hicks, M. Vandersall, E. V. Sitzmann, and K. B. Eisenthal, *Chem. Phys. Lett.* **135**, 413 (1987).
11. D. Huppert, S. D. Rand, P. M. Rentzepis, P. F. Barbara, W. S. Struve, and Z. R. Grabowski, *J. Chem. Phys.* **75**, 5714 (1981).
12. Y. Wang, and K. B. Eisenthal, *J. Chem. Phys.* **77**, 6076 (1982).
13. K. Rotkiewicz and W. Rubaszewska, *J. Lumin.* **27**, 221 (1982).
14. E. M. Kosower, *J. Am. Chem. Soc.*, **107**, 1114 (1985). R. Giniger, D. Huppert, and E. M. Kosower, *Chem. Phys. Lett.* **118**, 240 (1985).
15. J. R. Miller, *Springer Ser. Chem. Phys.* **42**, 234 (1985).
16. M. McGuire and G. McLendon, *J. Phys. Chem.* **90**, 2549 (1986).
17. W. Harrer, G. Grampp, and W. Jaenicke, *Chem. Phys. Lett.* **112**, 263 (1984).
18. J. Frank and E. Rabinowitch, *Trans. Faraday Soc.* **30**, 120 (1934).
19. N. A. Abul-Haj and D. F. Kelley, *J. Phys. Chem.* **91**, 5903-5 (1987).
20. M. Berg, A. L. Harris, and C. B. Harris, *Phys. Rev. Lett.* **54**, 951 (1985).

21. P. M. Felker and A. H. Zewail, *J. Chem. Phys.* **77**, 5266 (1983); *Chem. Phys. Lett.* **94**, 448 and 454 (1983).
22. Z. R. Grabowski, K. Rotkiewicz, W. Rubaszewska, and E. Kirkor-Kaminska, *Acta Phys. Pol. A* **A54**, 767 (1978).
23. W. Baumann, personal communication.
24. Y. Wang, M. McAuliffe, F. Novak, and K. B. Eisenthal, *J. Phys. Chem.* **85**, 3736 (1981).
25. J. Lee and G. W. Robinson, *J. Am. Chem. Soc.* **107**, 6153 (1985); *J. Chem. Phys.* **81**, 1203 (1984).
26. P. M. Hierl, A. F. Ahrens, M. J. Henchman, A. A. Viggiano, and J. F. Paulson, *J. Am. Chem. Soc.* **108**, 3140-42 (1986).
27. R. J. Visser, P. C. M. Weisenborn, J. Konijnenberg, B. Huizer, and C. A. G. O. Varma, *J. Photochem.*, **32**, 217 (1986). R. J. Visser, P. C. M. Weisenborn, C. A. G. O. Varma, M. P. deHaas, and J. M. Warman, *Chem. Phys. Lett.* **104**, 38 (1984). R. J. Visser, C. A. G. O. Varma, J. Konijnenberg, and P. Bergwerf, *J. Chem. Soc., Faraday Trans. 2*, **79**, 347 (1983).
28. E. A. Chandross, *The Exciplex*; edited by M. Gordon and W. R. Ware (Academic, New York, 1975) p. 187.
29. N. Nakashima and N. Mataga, *Bull. Chem. Soc. Jpn.* **46**, 3016 (1973).
30. Y. Wang, *Chem. Phys. Lett.* **116**, 286 (1985).
31. P. M. Felker, J. A. Syage, W. R. Lambert, and A. H. Zewail, *Chem. Phys. Lett.* **92**, 1 (1982).
32. J. A. Syage, P. M. Felker, and A. H. Zewail, *J. Chem. Phys.* **81**, 2233 (1984).
33. H. Bischof, W. Baumann, N. Detzer, and K. Rotkiewicz, *Chem. Phys. Lett.* **116**, 180 (1985).
34. L. R. Khundkar and A. H. Zewail, *J. Chem. Phys.* **84**, 1302 (1986).
35. O. Kajimoto, K. Yamasaki, K. Arita, and K. Hara, *Chem. Phys. Lett.* **125**, 184 (1986).
36. W. R. Lambert, P. M. Felker, and A. H. Zewail, *J. Chem. Phys.* **81**, 2217 (1984). P. M. Felker and A. H. Zewail, *J. Chem. Phys.* **82**, 2975 (1985).
37. B. W. Keelan, J. A. Syage, J. F. Shepanski, and A. H. Zewail, *Proceedings of the International Conference on Lasers 1983*, San Francisco, CA; Society for Optical and Quantum Electronics, STS Press: McLean, VA, 1985; p. 718.
40. M. Ito, *J. Phys. Chem.* **91**, 517 (1987).

41. J. L. Knee, L. R. Khundkar, and A. H. Zewail, *J. Chem. Phys.* **82**, 4715 (1985); *J. Chem. Phys.* **87**, 115 (1987).
42. G. W. Kenney-Wallace and C. D. Jonah, *Chem. Phys. Lett.* **47**, 362 (1977).
43. L. Kevan, *Acc. Chem. Res.* **14**, 138 (1981).
44. U. Even and J. Jortner, *J. Chem. Phys.* **78**, 3445 (1983).
45. In the evacuated cell containing DMABN crystals at 90°C, we observe UV emission that is due to the monomer with a lifetime of 3.0 ns. When this cell is opened to the air, the lifetime is reduced to 0.4 ns, as observed in the open vapor system.
46. The lifetime of the red-shifted band was also studied in an evacuated cell containing DMABN crystals, and it was found to be the same as in the open system. See Reference 24 for discussion of the kinetic equations used to extract the rate constants for the various relaxation processes.
47. T. Kobayashi, M. Futakami, and O. Kajimoto, *Chem. Phys. Lett.* **130**, 63 (1986).
48. E. M. Gibson, A. C. Jones, and D. Phillips, *Chem. Phys. Lett.*, **136**, 454 (1987).
49. J. A. Warren, E. R. Bernstein, and J. I. Seeman, *J. Chem. Phys.*, **88**, 871 (1988).
50. E. M. Gibson, A. C. Jones, and D. Phillips, *Chem. Phys. Lett.*, **146**, 270-74 (1988).
51. V. H. Grassian, J. A. Warren, E. R. Bernstein, and H. V. Secor, *J. Chem. Phys.*, **90**, 3994-99 (1989).

FIGURE CAPTIONS

- Figure 1. (Top) Portion of the fluorescence excitation spectrum of jet-cooled 4-DMABN. Intensity is not corrected for the laser system response. Nozzle temperature was 160°C, and laser-to-nozzle distance was 3 mm. He backing pressure was 40 psi. The resolution is limited by the laser bandwidth (about 1.5 cm^{-1}). (Bottom) Portion of the fluorescence excitation spectrum of jet-cooled 4-DEABN. Note that the two spectra are lined up with each other, using the first observed line as a marker. The actual assignment of the 0,0 band cannot be made without careful Franck-Condon analysis (see text).
- Figure 2. (Top) Dispersed fluorescence resulting from excitation of jet-cooled 4-DMABN to the first band at 3099Å. Resolution is low in this spectrum (3.2Å) because of the low intensity of this band. Nozzle temperature was 160°C, and laser-to-nozzle distance was 3 mm. He backing pressure was 40 psi. (Middle) Dispersed fluorescence resulting from excitation of jet-cooled 4-DMABN to the 308.7Å band. Resolution was 0.8Å, and nozzle conditions were similar to those mentioned above. (Bottom) Dispersed fluorescence resulting from excitation of jet-cooled 4-DEABN to the 3143Å band. Resolution was 0.8Å, and nozzle conditions were similar to those mentioned above. (Note that the spectra are plotted relative to the excitation energy.)
- Figure 3. Portion of the fluorescence excitation spectrum of jet-cooled 4-DMABN, showing the effect of increasing water partial pressure on the formation of the 1:1 complex (noted with an arrow). In each case the water partial pressure was varied. For case (A) 0, (B) 2, (C) 4, (D) 12, and (E) 24 Torr. Nozzle conditions were kept the same for all cases: temperature 160°C, laser-to-nozzle distance 3 mm, and He backing pressure 40 psi. Laser bandwidth was 2-3 cm^{-1} .
- Figure 4. Fluorescence excitation spectra of jet-cooled complexes containing 4-DMABN. The peaks of the complexes are indicated by an *. The peak at 308.2 nm contains contribution from both the bare molecule and the complex. The nozzle temperature was 150°C, the laser-to-nozzle distance was 10 mm, and the helium backing pressure was 70 psi. Note that the scale and wavelength scan direction are different from Figure 3.
- Figure 5. (Top) Dispersed fluorescence resulting from excitation of the 3085Å band of jet-cooled water/4-DMABN, 1:1 complex. Resolution was 0.8Å. Nozzle temperature was 160°C, water partial pressure 24 Torr, He backing pressure 40 psi, and laser-to-nozzle distance 3mm. Laser bandwidth was 2-3 cm^{-1} . (Bottom) Dispersed fluorescence resulting from excitation of the 3087Å band of jet-cooled 4-DMABN. Resolution was 0.5Å. Nozzle conditions were similar to above. Both spectra are shifted to coincide in order to allow for inspection of the effect of complexation.
- Figure 6. Dependence of the 4-DMABN aggregate of He backing pressure while exciting at 309.9 nm. At high pressure, the "monomer" signal is nearly gone. At low pressure, the signal is that of the monomer under low resolution (24Å). The monomer intensity is 3X that of the aggregate. The laser-to-nozzle distance was 10 mm.

Figure 7. Fluorescence spectra of 4-DMABN vapor in open cell at $\lambda_{\text{ex}} = 310$ nm (solid line), 90°C; (dashed line) $\lambda_{\text{ex}} = 322$ nm, 66°C.

Figure 8. SCHEME I: Photophysical Processes in 4-DMABN Vapor at 60°C in an open cell.

Figure 9. Formation and decay kinetics of fluorescence of 4-DMABN vapor in open cell at 66°C. The solid line represents the best fit of a rise time of 60 ps and decay of 1000 ps.

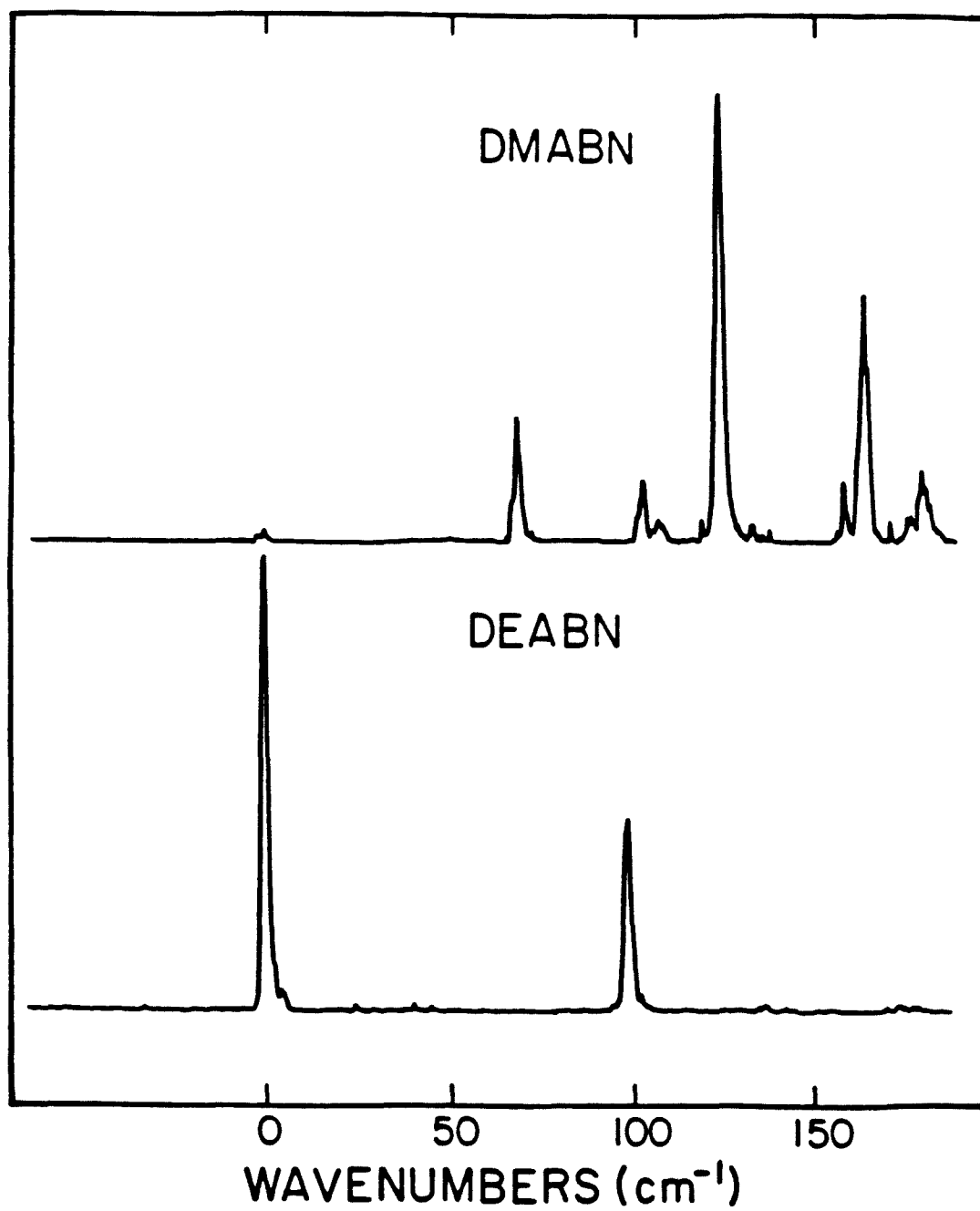


Figure 1

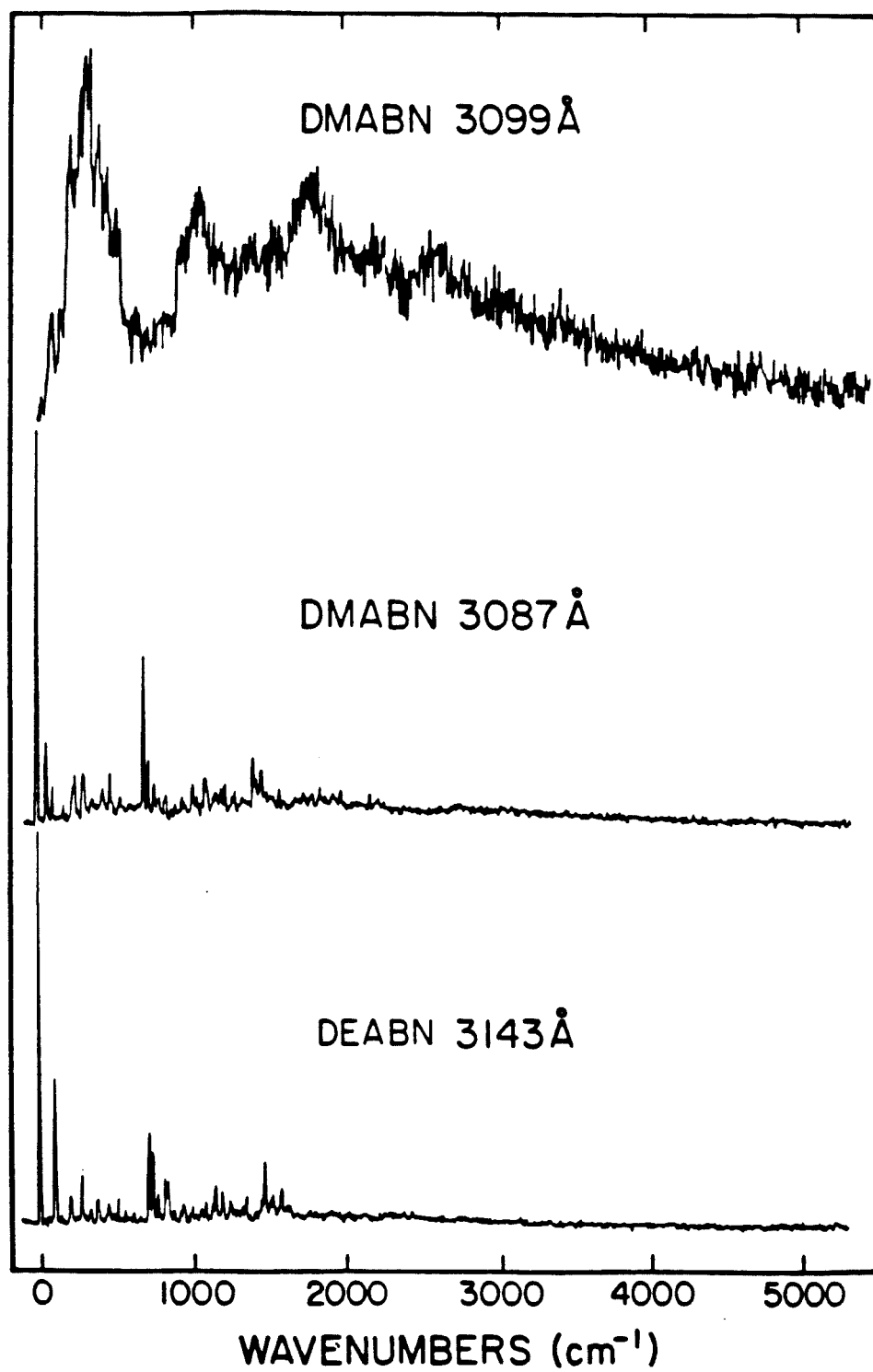


Figure 2

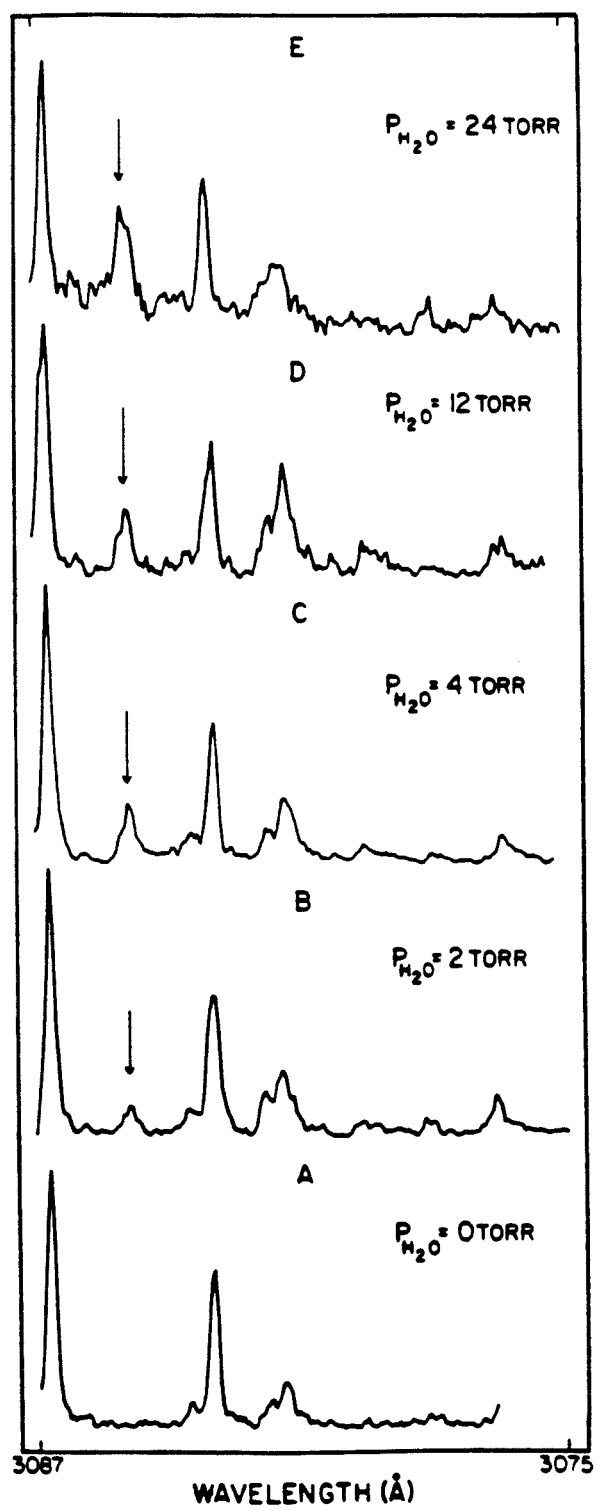


Figure 3

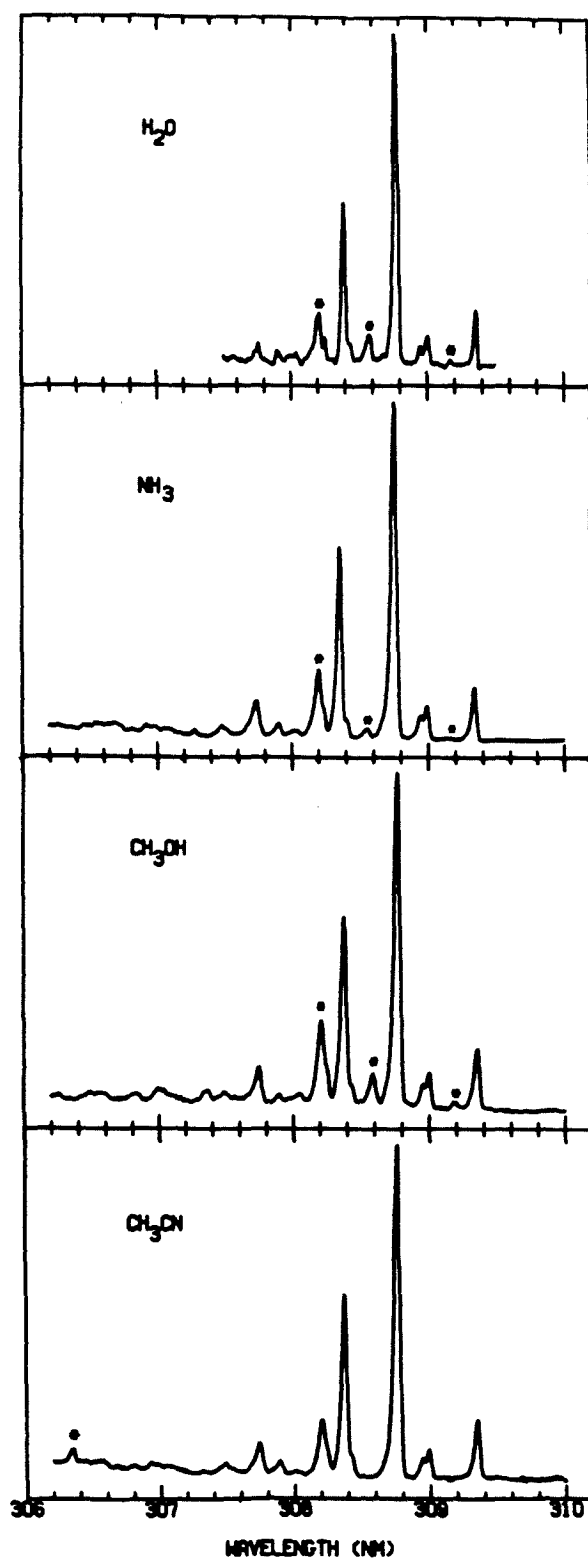


Figure 4

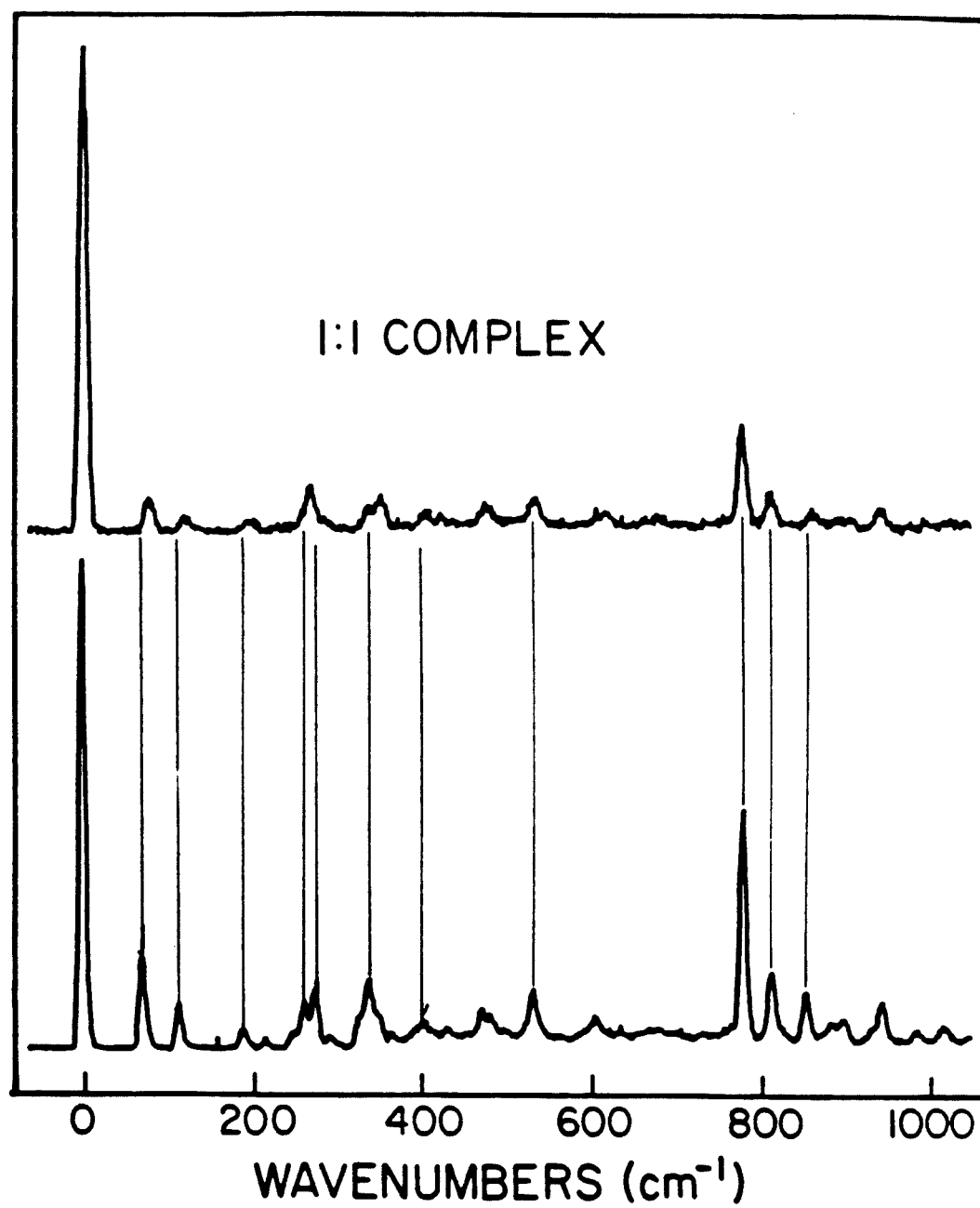


Figure 5

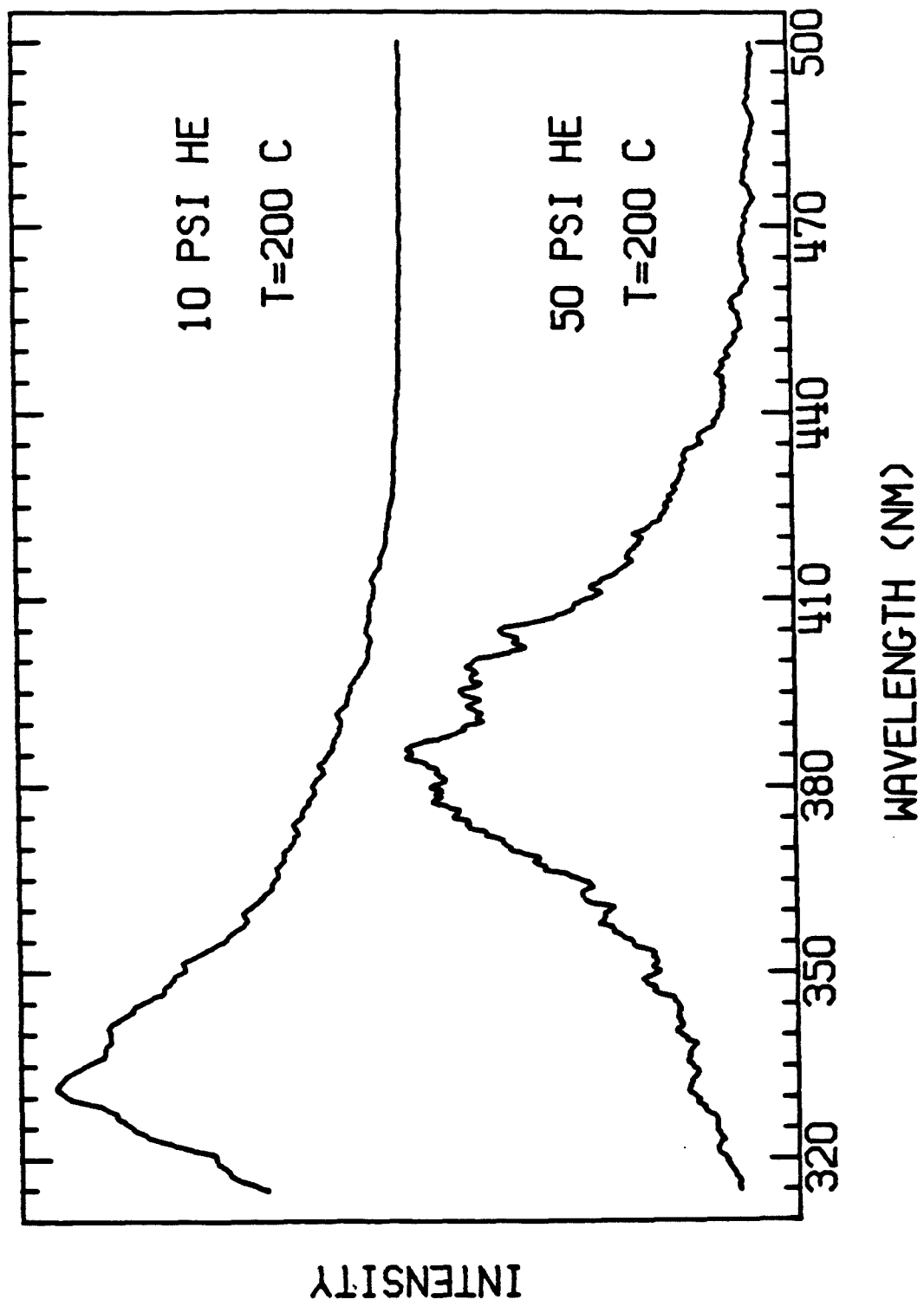


Figure 6

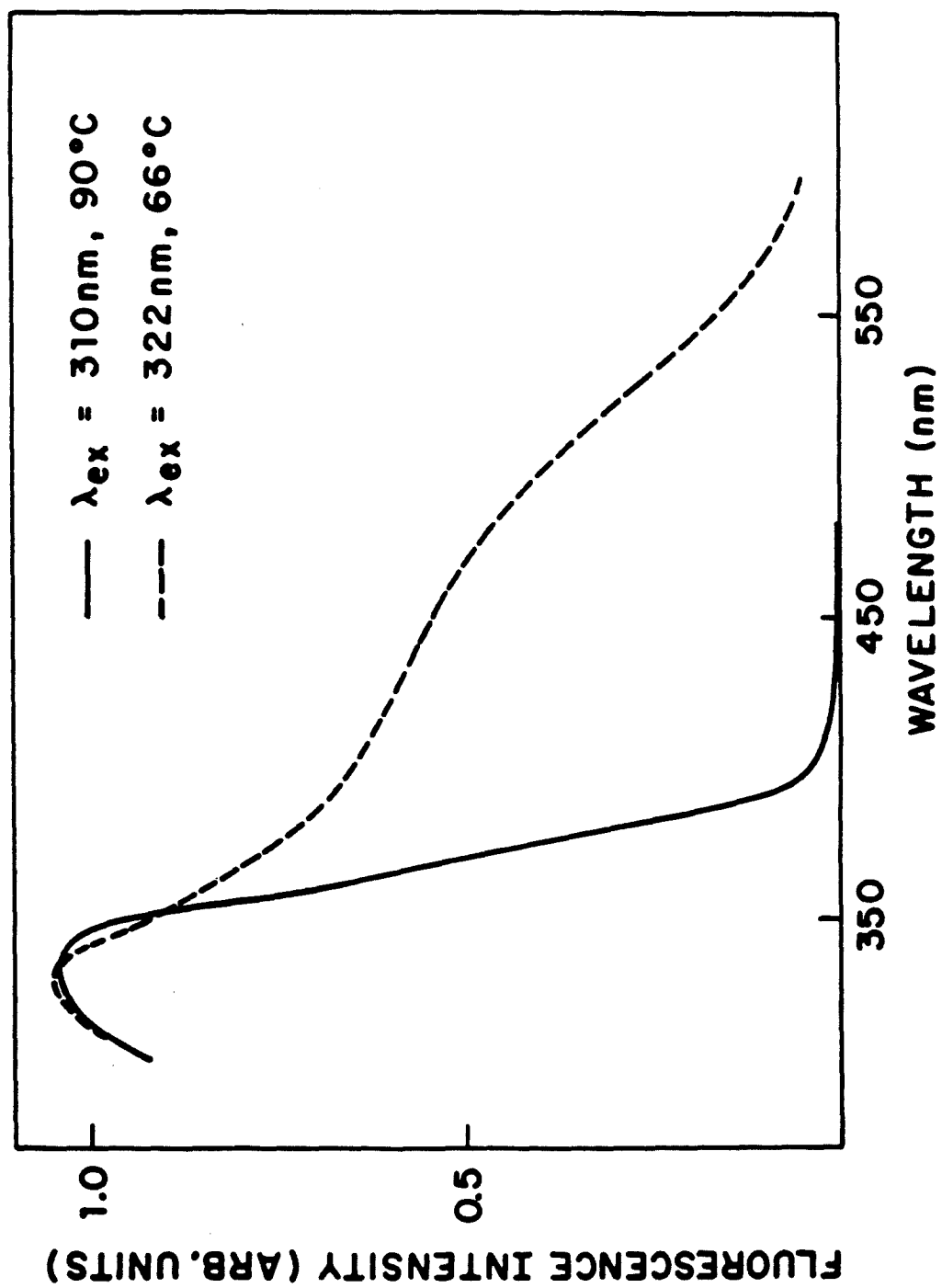
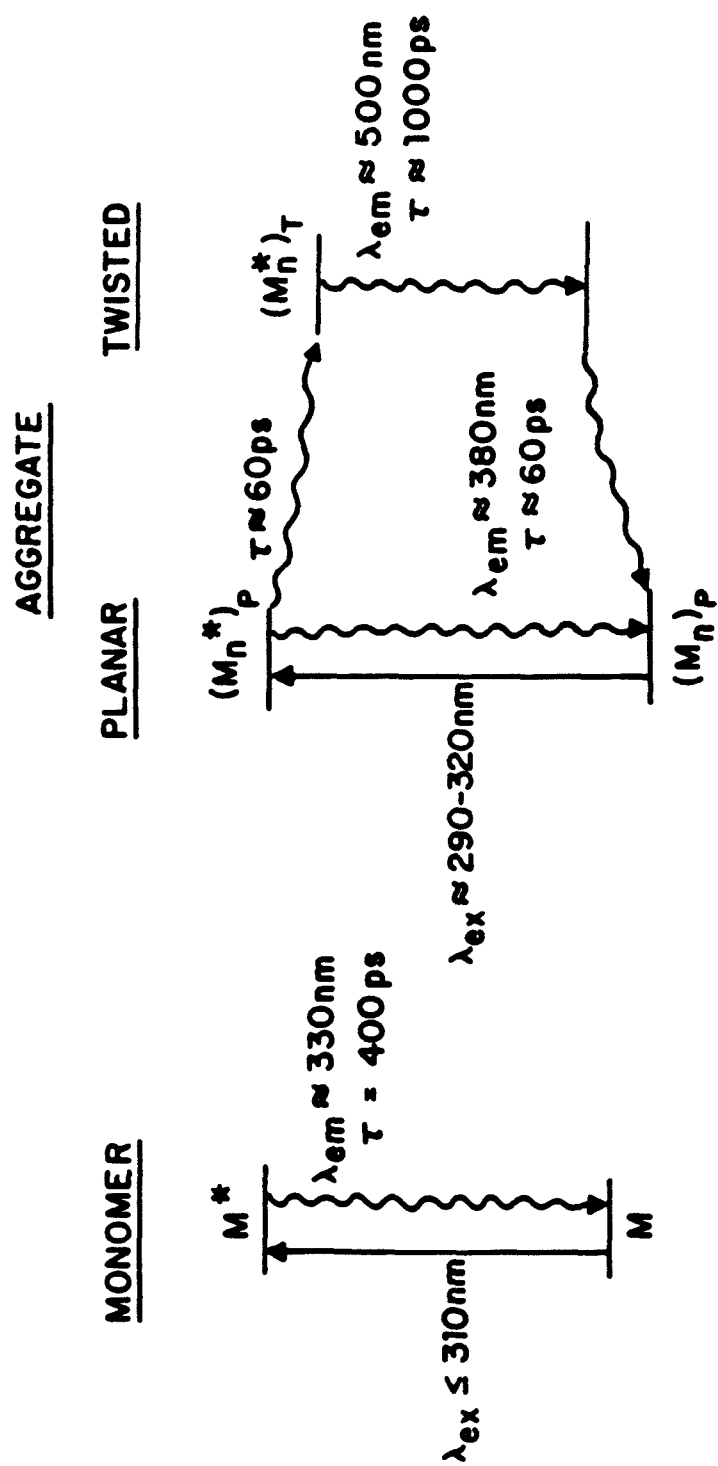


Figure 7



SCHEME 1

Figure 8

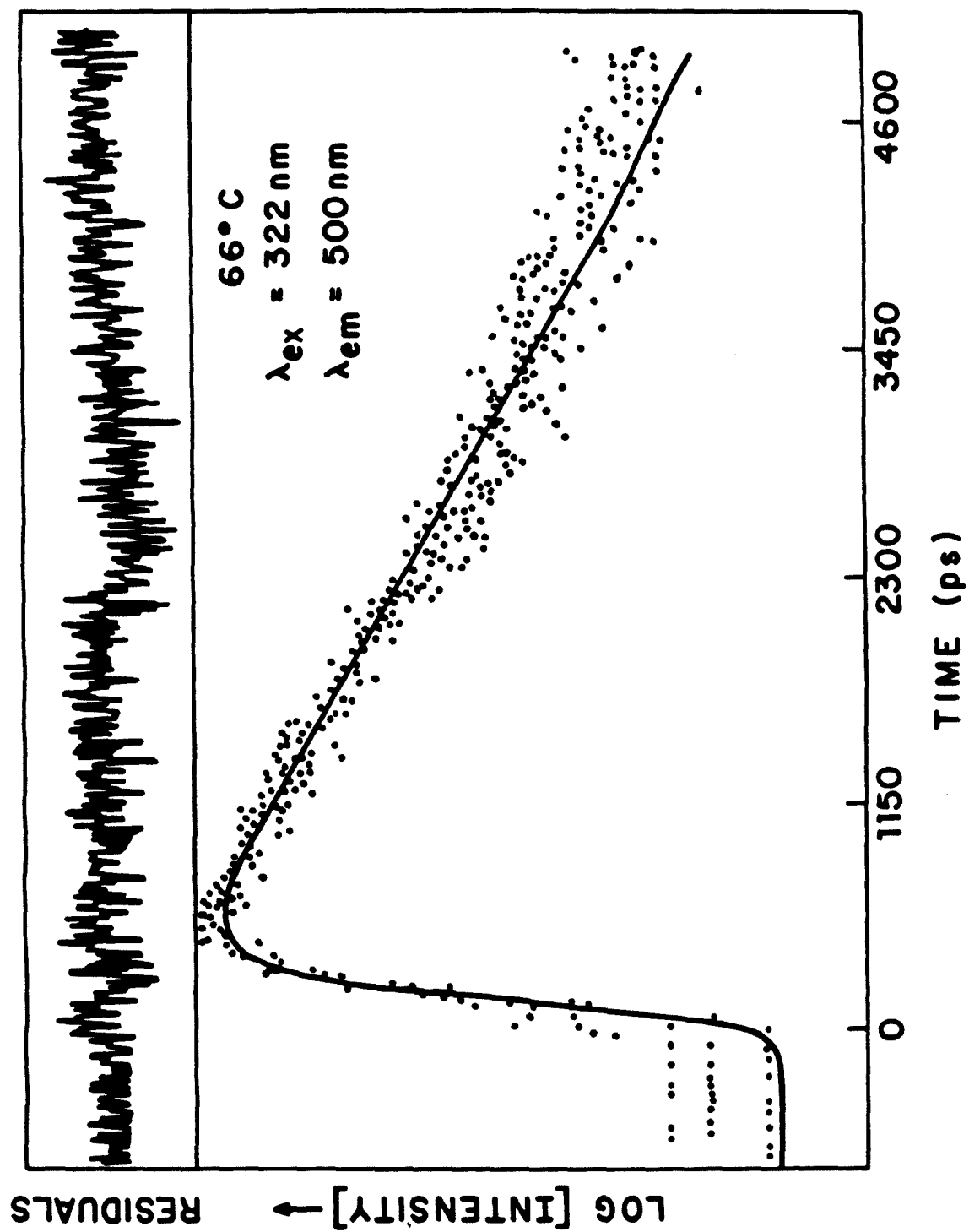


Figure 9

CHAPTER 5

REAL-TIME PROBING OF REACTIONS IN CLUSTERS I: α -NAPHTHOL WITH AMMONIA

This chapter was adapted from the publication:
J.J. Breen, L. W. Peng, D.M. Willberg, A. Heikal, P. Cong and A.H. Zewail, "Real-time Probing of Reactions in Clusters," *Journal of Chemical Physics* **92**, 805-807 (1990)

In this chapter we report our first study of real-time reaction dynamics in finite-sized clusters. The reaction is of the type $AH + S_n$, where the proton transfer (bimolecular) dynamics is examined as the acid AH is solvated with a different number of molecules, $n = 1, 2, \dots$ etc.. This is in continuation of our effort to study reaction dynamics in real-time [1], but now extending the scope of the previous collisionless (solvent-free) condition to a range where condensed phase effects can play a role. Of particular interest to us is the condition at which solvation induces vibrational relaxation and modifies IVR. Real-time studies of reactions in clusters offer great opportunities for obtaining the rates directly [2] and for examining these solvation processes under controlled conditions in molecular beams. Such stepwise solvation by beam methods has been advanced for a variety of systems spanning small molecules [3], large molecules [4], hydrogen-bonded systems [5] and electrons [6]. The focus of this chapter is on our initial results. In Chapter 6, a more complete experimental account of this work will be given. In addition, in Chapter 6 the results described here will be related to both other cluster studies and to the solution studies of similar systems.

Here, we use a new molecular beam machine in combination with two picosecond lasers. As before [1], the time resolution is achieved by delaying the pump-pulse relative to the probe-pulse in a Michelson interferometer arrangement, just before the two pulses enter the molecular beam zone (Figure 1). The mass selection of the skimmed beam is determined by MPI in a time-of-flight spectrometer. Care was taken to lower the pump-laser power to a minimum, and the probe wavelength was chosen to create the ions close to threshold ionization. In addition to these pump-probe experiments, picosecond fluorescence measurements were performed using a time-correlated single-photon counting apparatus [7], similar to earlier studies of isoquinoline-water clusters [5b].

The system of interest here involves the following proton-transfer reaction: $AH^+ \cdot S_n \rightarrow [A^- \cdots S_n H^+] \rightarrow A^- + S_n H^+$, where AH stands for α -naphthol and S_n for n -

ammonia molecules. For this system, we report results only for $n = 1, 2, 3$ and 4, although the cluster distribution is up to $n = 30$.

The real-time study reported here shows a critical dependence for the reaction dynamics on the number of solvent molecules involved in the reaction: For $n = 1$ and 2 we observe nanosecond dynamics and no evidence for proton transfer; for $n = 3$ and 4 the dynamics take place on the picosecond time scale. Our findings should now be relevant to theoretical studies like those by the group of Robinson [8], and complement previous time-integrated studies of gas-phase ion chemistry [9], photoemission and picosecond studies in fluid media [10], and intracluster ion chemistry [11].

Proton-transfer reactions specific to naphthols have been the subject of many studies in solutions [8,10] and matrices [12]. In clusters, the thorough spectroscopic work of the Leutwyler group [13] has provided both the spectral shifts for the different clusters and the spectral changes expected under proton-transfer conditions. We have used their spectral assignments of bands in our study. More recently, the dynamics of IVR [14] has been characterized for α -naphthol by Lakshminarayan and Knee[15].

In our study reported here the bare molecule lifetime is measured to be 60 ± 2 nsec. which is in agreement with earlier measurements [13d,15]. The $n = 1$ cluster has a lifetime of 38 ± 1 nsec. Two isomers have been reported for the cluster with $n = 2$ [13a,13b]; for the spectrally bluer isomer lifetime we measure 43 ± 2 nsec., while for the spectrally redder isomer a lifetime of 39 ± 1 nsec is observed. In addition, the emission that is due to the reacted system, emanating predominantly from clusters with $n \geq 4$, was monitored at 435 nm. and found to have a lifetime of 38 ± 2 nsec.

For the clusters $n = 3$ and 4, the transients measured in the pump-probe experiments reveal a fast-decay component of 100 ± 30 psec. as well as a long, many nanoseconds, decay component [16]. The cluster-size dependence of the onset of the fast dynamics is depicted in Figure 2 for the clusters $n = 1$ and 3.

For this reaction, which takes place on an electronically excited potential energy surface, the dynamics is dependent on the solvent stabilization of the proton transfer and is therefore cluster-size dependent. In a simple description it involves first the IVR among the modes of α -naphthol, followed by the proton transfer to the solvent. The fast 100 psec. component is therefore a measure of the IVR/reaction rate taking place in the clusters while the long time component is the lifetime of the equilibrated system. It is interesting that the 100 psec. time measured in the cluster is longer than the solution-phase reaction time of 33 ± 5 psec [10a].

In conclusion, the proton transfer reaction of α -naphthol in ammonia clusters is indicative of the size-dependent phenomena which time-resolved pump-probe spectroscopy is capable of monitoring directly. Recently, we have extended these studies to clusters of α -naphthol with piperidine and water. Fast decay components, similar to that depicted in Figure 2, were observed for the clusters with piperidine ($n = 2$ or 3) but were not observed for the clusters containing water ($n \leq 21$), on the same timescale. More measurements on this system and other cluster systems will be forthcoming. The hope is to characterize IVR and reaction dynamics as n reaches very large numbers.

Acknowledgements

This work was supported by the AFOSR and by the National Science Foundation.

REFERENCES

- 1) For recent reviews see:
 - (a) A.H. Zewail, *Science*, **242**, 1645 (1988).
 - (b) J.L. Knee and A.H. Zewail, *Spectroscopy*, **5**, 44 (1988).
 - (c) A.H. Zewail and R.B. Bernstein, *Chem. and Eng. News* **66**, 24 (1988).
- 2) J.S. Baskin, M.Dantus and A.H. Zewail, *Chem. Phys. Lett.* **130**, 473 (1986)
- 3)
 - (a) D.H. Levy, *Adv. Chem. Phys.*, **47** (Part 1), 323 (1981).
 - (b) R.E. Miller, *Science*, **240**, 447 (1988).
- 4)
 - (a) A. Amirav, U. Even, and J. Jortner, *J. Chem. Phys.* **74**, 3725 (1981).
 - (b) A. Amirav, U. Even, and J. Jortner, *J. Chem. Phys.*, **75**, 2489 (1981)
 - (c) A. Amirav, U. Even, and J. Jortner, *J. Chem. Phys.*, **86**, 3345 (1986)
- 5)
 - (a) P. M. Felker, W.R. Lambert and A.H. Zewail, *J. Chem. Phys.*, **77**, 1603 (1982); *ibid.* **78**, 5266 (1983).
 - (b) P.M. Felker and A.H. Zewail, *Chem. Phys. Lett.*, **94**, 448 and 454 (1983).
 - (c) K. Fuke and K. Kaya, *Chem. Phys. Lett.*, **94**, 97 (1983).
 - (d) R. Bombach, E. Honegger, and S. Leutwyler, *Chem. Phys. Lett.*, **118**, 449 (1985).
 - (e) E. Honegger, R. Bombach, and S. Leutwyler, *J. Chem. Phys.*, **85**, 1234 (1986).
 - (f) K.Fuke, H Yoshiuchi and K.Kaya, *J. Phys. Chem.*, **88**, 5840 (1984).
 - (g) N.P. Ernsting, *J. Phys. Chem.*, **89**, 4932 (1985).
- 6)
 - (a) H. Haberland, H. Langush, H.G. Schindler and D.R. Worsnop, *Surf. Sci.* **156**, 157 (1985).
 - (b) H. Haberland, H.G. Schindler and D.R. Worsnop, *J. Chem. Phys.*, **81**, 3342 (1984).
 - (c) J.V. Coe, J.T. Snodgrass, C.B. Freidhoff, K.M. McHugh and K.H. Bowen, *J. Chem. Phys.*, **83**, 3169 (1985).

- (d) M. Knapp, O. Echt, D. Kreisle and E.Recknagle, *J. Chem. Phys.*, **85**, 636 (1986).
- (e) M. Knapp, O. Echt, D. Kreisle and E.Recknagle, *J. Phys. Chem.*, **88**, 270 (1984).
- 7) (a) W. R. Lambert, P.M. Felker and A.H. Zewail, *J. Chem. Phys.*, **81**, 2217 (1984).
- (b) P.M. Felker and A.H. Zewail, *J. Chem. Phys.*, **82**, 2975 (1983).
- 8) G.W. Robinson, P.J. Thistlethwaite and J.Lee, *J. Phys. Chem.*, **90**, 4224 (1986).
- 9) (a) P. Kebarle, *Ann. Rev. Phys Chem.*, **28**, 445 (1977).
- (b) A.W. Castleman, Jr. and R.G. Keesee, *Ann. Rev. Phys Chem.*, **37**, 525 (1986).
- 10) (a) S.P.Webb, L.A. Philips, S.W. Yeh, L.M. Tolbert and J.H. Clark, *J. Phys. Chem.*, **90**, 5154 (1986).
- (b) E.W. Kosower and D. Huppert, *Ann. Rev. Phys Chem.*, **37**, 127 (1986).
- (c) D.Huppert, M. Gutman, K.J. Kaufmann, *Adv. Chem. Phys.*, **47** (Part 2), 323 (1981).
- 11) (a) J.F. Garvey and R.B. Bernstein, *J. Phys. Chem.*, **90**, 3577 (1988).
- (b) B.Brutschy, C. Janes and J. Eggert, *Ber. Bunsenges. Phys. Chem.* **92**, 74 and 437 (1988).
- 12) G.A. Brucker and D.F. Kelley, *J. Chem. Phys.*, **90**, 5243 (1989).
- 13) (a) O. Cheshnovsky and S. Leutwyler, *Chem. Phys. Lett.*, **121**, 1 (1985).
- (b) O. Cheshnovsky and S. Leutwyler, *J. Chem. Phys.*, **88**, 4127 (1988).
- (c) R. Knochenmuss, O. Cheshnovsky and S. Leutwyler, *Chem. Phys. Lett.*, **144**, 317 (1985).
- (d) R. Knochenmuss and S. Leutwyler, *J. Chem. Phys.*, **91**, 1268 (1989).
- 14) P.M. Felker and A.H. Zewail, *Adv. Chem. Phys.*, **70**, 265 (1988).

- 15) C. Lakshminarayan and J.L. Knee, *J. Phys. Chem.* **94**, 2637-2643 (1990).
- 16) In the pump-probe experiments transients are recorded over only a temporal range of < 4 nsec., so it is difficult to measure long lifetimes accurately. For the clusters $n = 0, 1$ and 2, transients give evidence for long lifetimes, which are consistent with the picosecond fluorescence measurements (see Figure 2).

FIGURE CAPTIONS

- Figure 1. Schematic of the experimental arrangement depicting the picosecond laser system and cluster-beam apparatus.
- Figure 2. Shown are the decays and fits for the $n = 1$ and the $n = 3$ clusters. For the $n = 1$ cluster, the pump and probe wavelengths are: pump $\lambda = 320.4$ nm, probe $\lambda = 337.1$ nm. For the $n = 3$, cluster the wavelengths are: pump $\lambda = 322.1$ nm, and probe $\lambda = 337.1$ nm. Note that for $n = 3$ there is a fast component (100 ± 30 psec.) and a slow component. The insert is a nonresonant photoionization mass spectrum of $\alpha\text{-NpOH}(\text{NH}_3)_n$ clusters showing a typical cluster distribution.

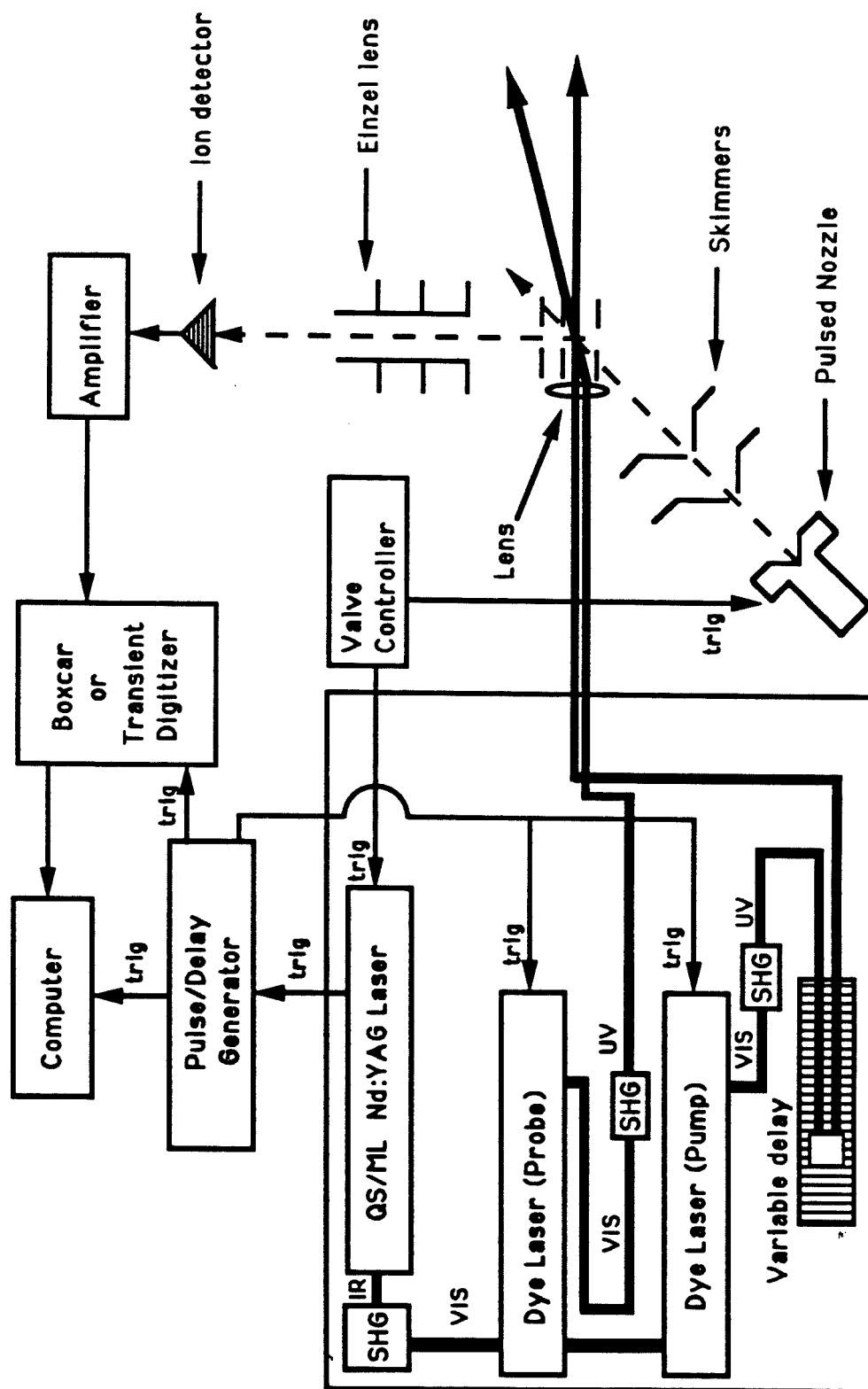


Figure 1

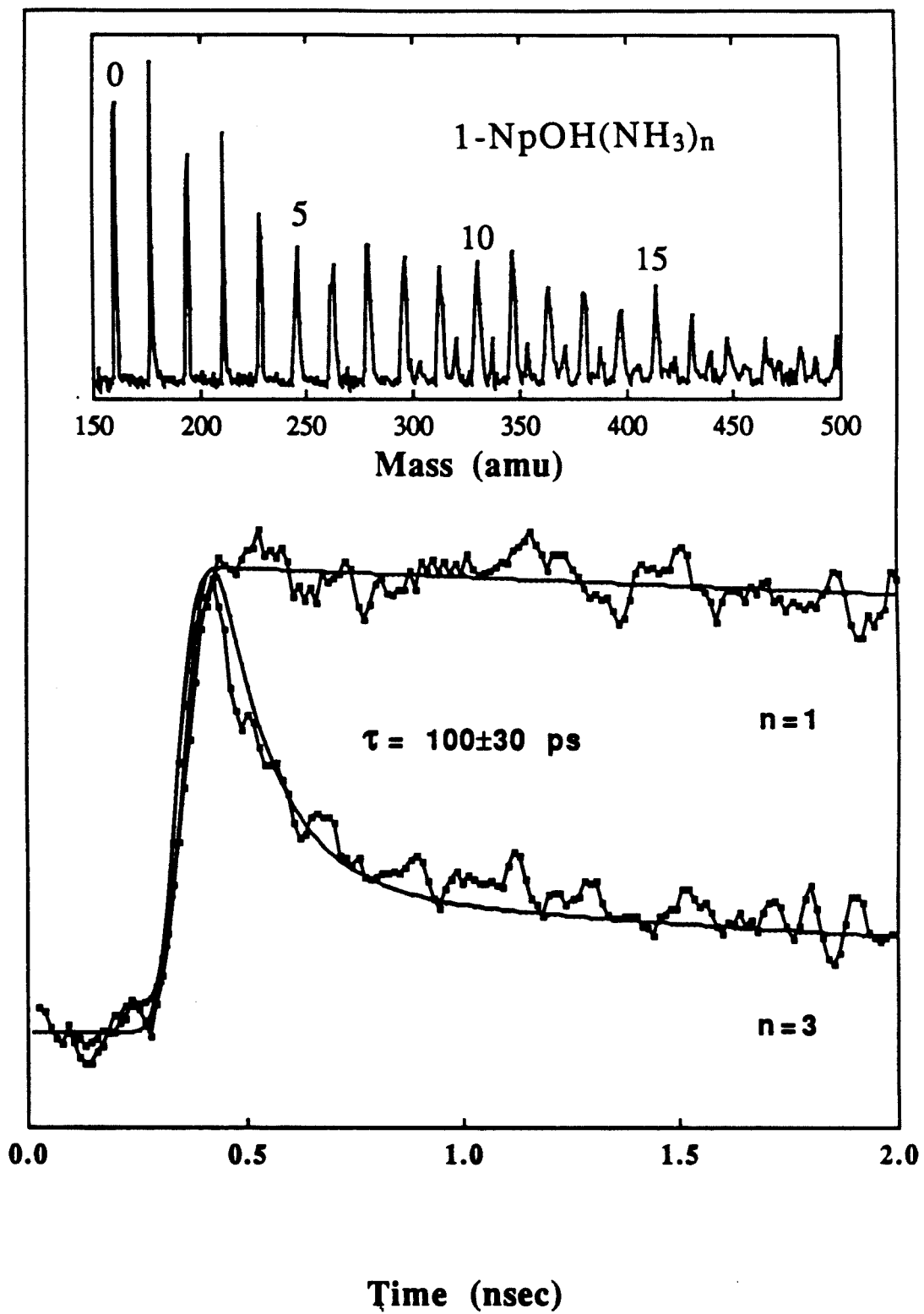


Figure 2

CHAPTER 6

REAL-TIME PROBING OF REACTIONS IN CLUSTERS II: α -NAPHTHOL WITH AMMONIA, PIPERIDINE AND WATER

Abstract

Picosecond pump-probe spectroscopy is applied to the study of the S_1 excited state dynamics of the gas-phase clusters of α -naphthol with ammonia, piperidine and water. These measurements reveal only nanosecond timescale dynamics for the clusters α -NpOH \cdot (NH₃)_{n=1,2}, α -NpOH \cdot (C₅H₁₁N)_{n=1} and α -NpOH \cdot (H₂O)_{n=1-21}. Dynamics on the picosecond timescale are observed for the clusters α -NpOH \cdot (NH₃)_{n=3,4} and α -NpOH \cdot (C₅H₁₁N)_{n=2,3}. These fast-time dynamics, 100 ± 30 ps for the ammonia clusters and 65 ± 10 ps for the clusters with piperidine, indicate the occurrence of proton-transfer reactions in these small solute/solvent clusters. The cluster size and solvent dependence and the timescale for the reaction serve to emphasize the importance of the local solvent for the reaction.

I. INTRODUCTION

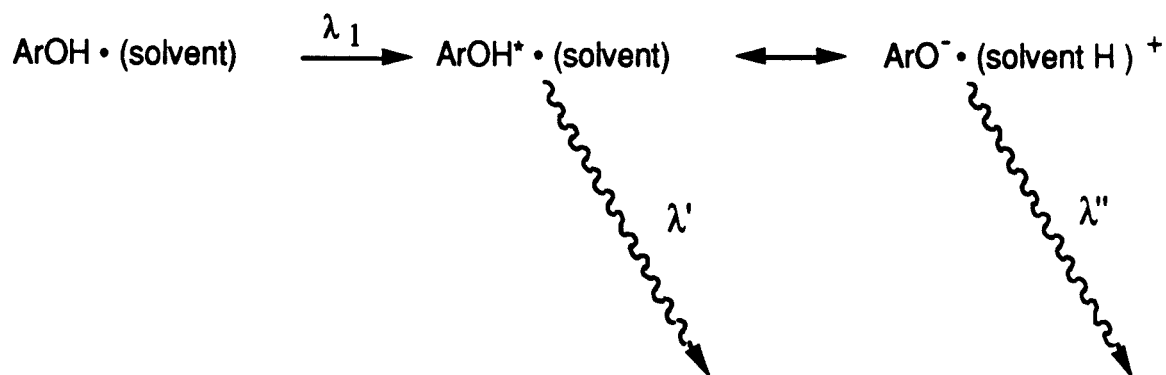
The study of gas-phase clusters and cluster ions has progressed rapidly. This is due both to the interesting chemistry and physics that can occur for individual clusters and to the expectation that these finite-sized systems will provide insights into condensed phase phenomena. Gas-phase clusters can be described as weakly bound collections of atoms, molecules and ions in which the cluster constituents are held together by forces weaker than typical intramolecular bonds. An attractive consequence of the weak bonding in clusters and the small perturbations that the individual molecules experience in the clusters is the retention of individual molecular character. This allows many small clusters to be studied at a level of detail similar to that possible for isolated molecules.

One particular type of clusters that are being actively studied are solute/solvent clusters. In these clusters a single molecule solvated by a number of atoms or molecules is used as a probe of the bonding, structure and chemical dynamics of the cluster. Studies of this type have been performed using atoms, large and small molecules, ions and electrons solvated by either rare gas atoms or other small molecules [1-7]. By controlling the conditions leading to the formation of these clusters and using experimental techniques sensitive to the small perturbations that the probe species experiences, individual clusters can often be interrogated, and the dependence on the cluster size can be observed. Thus the early stages of the transition from the gas phase towards condensed phase systems can be studied in a stepwise and detailed manner. Our interest in this type of cluster is the insight these systems may provide for a better understanding of condensed-phase reaction dynamics. In particular, experimental studies of these systems should highlight the effect of the solvent on vibrational relaxation and intramolecular vibrational redistribution (IVR).

Studies of reactions in gas-phase clusters are becoming increasingly common. There is a large body of work concerned with ion molecule reactions occurring within clusters [7-12]. A primary driving force behind these studies is the need to understand the

dynamics that occurs upon ionization of a neutral cluster and that are observed in subsequent mass analysis. In the case of reactions within neutral clusters, a much smaller number of experiments have been reported. Many of these reactions have been termed as orientated bimolecular reactions and can be considered as "hot-atom chemistry" in structurally well-defined gas phase dimer complexes [13-30]. In these experiments, an energetic atom (*e.g.*, H [13, 21-23,25-30], D [24], O [14,15], Ca [19,20], Hg [16-18,20], and Xe [18]) is produced from one species in the complex and reacts with the other species leading to the formation of a product species that can subsequently be analyzed. Other reactions that have been reported in neutral clusters include a complex-forming reaction between HCl and CH₃F in large rare gas clusters [31,32], electron-transfer reactions [33-37], vibrational predissociation half reactions [2,4,38-54], the formation of iodine from methyl iodide dimers [55-57] and intermolecular proton transfer reactions [56,58-68].

Proton-transfer reactions are clearly important in chemistry [69,70] and have been studied in both intramolecular and intermolecular systems. Among the most extensively studied of these systems are the excited state proton transfer reactions from aromatic alcohols to the surrounding solvent. The general reaction is indicated below ($\lambda' \leq \lambda''$).



One such molecule is α -naphthol which, like many other aromatic alcohols, undergoes a large increase in its acidity upon excitation to the S₁ state and belongs to a class of

compounds exhibiting "dual fluorescence." Emission studies demonstrate that the deprotonation of the acid is observed as blue-green fluorescence, whereas the neutral alcohol emits only blue light [71]. In addition, time-resolved studies of the proton transfer reaction from both α - and β -naphthol in aqueous solution reveal that the rate of formation of the anion is controlled by solvent dynamics [71-78]. More specifically, the rate is limited by the formation of a local solvent structure that can accept and stabilize the proton [72-74]. Time-resolved studies of this reaction in small gas-phase clusters may provide information pertaining to the intrinsic reaction rate for the proton transfer between the electronically excited acid and the solvent consisting of a critical number of solvent molecules.

The coupling of time-resolved spectroscopies with gas-phase clusters, in particular pump-probe techniques, have only recently been applied to cluster studies [29,30,39,51,54,56,67,68,78]. In an earlier communication we briefly reported our results for time-resolved measurements of intermolecular proton-transfer reactions occurring in small clusters of α -naphthol with ammonia, piperidine and water molecules [68]. Our experiments are guided by the extensive spectroscopic work on these cluster systems by Leutwyler and co-workers [58-61]. In these laser-induced fluorescence and resonance enhanced two-photon ionization experiments, the spectral shifts for the various different clusters are reported and both a solvent and cluster-size threshold dependence were observed for the proton-transfer reaction. Similar behavior has been reported in time-resolved emission experiments of matrix-isolated clusters of α - and β -naphthol with ammonia molecules [62,63], in fluorescence experiments of gas-phase clusters of 2-hydroxypyridine with ammonia molecules [65] and in both resonance-enhanced ionization experiments [64] and some very recent time-resolved pump-probe measurements of gas phase clusters of phenol with ammonia molecules [56,67]. In this chapter a more complete account of our previously reported work will be given. In addition, our results will be related both to these other cluster studies and to the solution studies of similar systems.

II. EXPERIMENTAL

Two sets of supersonic beam apparatus were used for this study: one for pump-probe experiments, and the other for picosecond fluorescence measurements. In general, α -naphthol was seeded into a mixture of He and a small percentage of solvent. For ammonia, a gas mixture of 0.5-2% ammonia in He (by pressure) was used. To form solvent/solute complexes with water or piperidine, the partial pressure of solvent in the expansion was set by controlling the temperature of a wet-line reservoir using a water/ice/sodium chloride bath. The experimental conditions were set to maximize the desired signal while minimizing interferences from other clusters. The α -naphthol (Aldrich; 99+%) and piperidine (Aldrich; 99%), helium (Big 3 Industries, 99.99%), and ammonia (Matheson, 99.99%) were used without further purification.

II.A. THE PUMP-PROBE APPARATUS

Pump-probe experiments were done using a newly constructed apparatus designed for the formation and study of clusters. The apparatus is a two-color picosecond pump-probe laser system coupled with a molecular beam machine. The molecular beam is a three-chamber system consisting of an expansion chamber, a buffer chamber, and a time-of-flight (TOF) chamber. The expansion chamber contains the nozzle source, and is used for laser-induced fluorescence (LIF) experiments. The buffer chamber is used for differential pumping. The TOF chamber houses the TOF mass spectrometer. The beam apparatus is schematically illustrated in Figure 1. High-throughput diffusion pumps and a pulsed nozzle are used to allow for the highest possible stagnation pressure and cross section. Unless otherwise noted, the apparatus is constructed out of stainless steel and aluminum. Pressure inside the vacuum chambers is monitored using standard thermocouple and ion gauges, and a pressure-gauge controller (Granville-Phillips Series 307). The laser system, based on a design from Stanford University [79] and

schematically illustrated in Figure 2, is capable of producing 20 ps pulses with up to 10 mJ of visible light per pulse out of each of the two dye lasers. The laser repetition rate can easily be up to a kilohertz, but the experimental repetition rate may be less due to constraints from other equipment.

The pump-probe apparatus has been described in detail in Chapter 3. Here the apparatus is summarized with attention given to the experimental conditions relevant to the α -naphthol experiments. The description is broken down into 7 parts. Parts 1 and 2 describe the three vacuum chambers. The TOF mass spectrometer is discussed in part 3. Part 4 is concerned with the electronics for the pulsed valve. Parts 5 and 6 deal with the laser system. Finally, part 7 outlines data acquisition methods and analysis.

II.A.1. Expansion and Buffer Chambers

The cylindrical expansion and buffer chambers are 16 inches in diameter, and are made of stainless steel (0.250 inch wall) to insure mechanical stability for the alignment of the molecular beam. Both chambers have eight main ports, arranged in two crosses, and are separated by a central flange. The crosses closer to the central flange are used to conduct the experiment, whereas the other crosses are used for the pumps and other utilities. For each chamber, 2.75 inch utility ports are attached where convenient. The expansion chamber is pumped by a 10 inch diffusion pump (Varian VHS-10), while the buffer chamber is pumped by a 6 inch diffusion pump (Varian VHS-6). Both diffusion pumps are equipped with liquid-nitrogen cold traps, and pneumatic gate valves. The diffusion pumps are backed by mechanical pumps (a Leybold D90A for the VHS-10 pump, and a Leybold D60A for the VHS-6 pump).

The expansion and buffer chambers are separated by a central flange assembly. The assembly consists of three stainless steel flanges. The main flange is a 20 inch diameter flange, with a 9 inch diameter hole bored through the center. Into the 9 inch hole goes a 9.5

inch diameter (with a 5.5 inch diameter hole bored through its center) mounting plate. Into the 5.5 inch diameter hole goes a 6 inch diameter plate on which is mounted the first skimmer. Mounted to the 9.5 inch diameter flange is the TOF mass-spectrometer ionizer cube, cube mounts, and four 18 inch long guiding rods (Thomson Industries, Case 60L AISI C-1060 steel-hardened to Rockwell 58-63C, 0.5 inch nominal diameter) for the nozzle assembly. The ionizer cube and cube mounts are on the buffer chamber side of the flange, and the guiding rods are on the expansion chamber side. For LIF experiments, optical baffles are used for the laser entrance and exit ports of the expansion chamber to reduce scattered light. Further scattered light reduction is achieved by painting the inside of the expansion chamber and the front of the nozzle assembly with Xylan 1010, a black fluoropolymer paint (Whitford Corporation).

The nozzle assembly contains the nozzle, pulsed valve, and sample reservoir. It is mounted on two aluminum plates held 6.5 inches apart. The nozzle and valve, mounted on the front plate, are a single unit manufactured by General Valve Corporation (Series 9). The valve is solenoid-driven, and typically operates at 100 Hz with a pulsewidth of less than 500 ms. A conical (30° cone) nozzle with a 150 μ diameter aperture is used. The sample reservoir is mounted on the rear plate. The nozzle and the sample reservoir are independently heated, and the nozzle is kept about 10°C hotter than the sample reservoir to reduce clogging of the nozzle aperture by sample condensation. For the sample holder, a cartridge heater (Chromolax CIR-2012) is used, and a heating tape is used for the nozzle assembly. Temperature is regulated by two temperature controllers (Omega Engineering CN310KC). The nozzle assembly moves on the guiding rods using ball bushings (Thomson Industries A-81420-SS). A ball-nut and ball-screw combination (Warner Electric R-0308) is used to drive the nozzle assembly. The ball screw is rotated from the outside using a rotary motion feedthrough (MDC model BRM-275).

II.A.2. The TOF Chamber

The TOF chamber is composed of a 26 inch long and 6 inch diameter tube, a tee, a 5.125 inch long and 4 inch inner diameter transition tube, and the ionizer cube. The wall thickness of both the 6 inch diameter tube and the tee is 0.125 inches. The ionizer cube and transition tube extend into the buffer chamber, and the tee is attached to the buffer chamber. On the end opposite to the ionizer cube is attached a microchannel plate (MCP) (Galileo FTD 2003) for detecting ions. The TOF chamber is pumped through the tee by a 6 inch diffusion pump (Varian VHS-6), which is equipped with a liquid nitrogen cold trap and pneumatic gate valve. The diffusion pump is pumped by the same mechanical pump used for the buffer chamber VHS-6 pump.

The cube, cube mounts, and the nozzle assembly guiding rods are all attached to the 9.5 inch diameter stainless steel plate mounted onto the 20 inch diameter central flange. The orientation of the cube and mounting pieces is fixed with respect to the laser, molecular beam and MCP detector by mechanically aligning the assembly with pins. The cube is constrained to have its center coincident with both the centerline of the TOF drift tube and the molecular beam axis, and 4 of its faces parallel to the main ports. Since all the critical components are mounted on a single flange, the entire experimental assembly is removable intact (through the back of the buffer chamber) from the main chambers.

II.A.3. Time-of-Flight mass spectrometer

The molecular beam formed in the expansion chamber passes through a nickel skimmer (Beam Dynamics, Model 2, 1.5 mm aperture) on the central flange when entering the buffer chamber, and passes through a second nickel skimmer (Beam Dynamics, Model 2, 2 mm aperture) as it enters the ionizer cube. The beam exits the cube through a 2 mm hole on the face opposite the second skimmer. The lasers enter the cube vertically and perpendicular to the molecular beam, and intersect the beam at the cube center. The ionizer

assembly, ion optics, and pulsed electron gun [80,81] for electron-impact ionization (EI) are mounted on the cover flange for the cube face farthest from the MCP. A short focal length lens focuses the lasers onto the beam. The lens is mounted in a vertical motion translation stage so that the focal point can be adjusted.

The two-stage TOF mass spectrometer is based on the original Wiley-McLaren design [82]. Ions are accelerated through two stages of electric field, and collimated by an Einzel lens [83]. The drift tube is 1.2 m long and the ions are detected with the MCP. The ion signal is immediately amplified 25X with a Stanford Research Systems 300 MHz preamplifier (Model SR440). This minimizes both transmission losses, and interferences from the RF noise generated by the modelocker. When taking a mass spectrum, a waveform analyzer is used to collect, digitize, and signal average the amplified MCP analog signal. The analyzer consists of a 100 MHz transient digitizer (LeCroy 8818A), a LeCroy MM8103A memory module, and a LeCroy 6010 Magic controller unit. It is based in a CAMAC crate (LeCroy 8013A), and triggered by a digital delay generator (Stanford Research Systems model DG535) to coordinate its collection time with the laser pulse. Data transfer to and from the computer is performed via an IEEE DMA interface (NB-DMA-8-G). We have achieved a mass resolution of approximately $m/\Delta m=1000$ with this system. Figure 3 depicts a nonresonant photoionization mass spectrum of α -NpOH \cdot (NH₃)_n clusters showing a typical cluster distribution.

II.A.4. Electronics

The electronics controlling the actuation of the pulsed-valve solenoid and the triggering of the laser were built in our laboratory. Schematics of the circuitry are given in Chapter 3. The control box is a dual pulse generator. The two pulsed outputs are independently adjustable for pulse duration and pulse delay. The repetition rate may be set

in the range 1-200 Hz. These quantities, as well as the total number of pulses, may be displayed on a digital read-out with a variable sampling time.

The first pulsed output triggers a Wavetek pulse generator (Model 802) which in turn triggers the Q-switch driver box for the Nd:YAG and the voltage pulses on the TOF ionizer. The laser then triggers the Stanford delay generator, which triggers the Pockels cell electronics, a boxcar (EG&G 162 mainframe/165 integrator) and A/D board (NB-MIO-16H-9), or the CAMAC crate.

The second pulsed output is sent to a valve driver circuit which amplifies the pulse to 105V. This amplified pulse drives the valve. It is delayed, relative to the first pulsed output, to synchronize the gas pulse with the arrival of the laser pulses.

II.A.5. The Mode-Locked Q-Switched Nd:YAG Laser

The Nd:YAG laser is a homebuilt system assembled from the laser head, mirrors, and power supply components of a Quantronix 416 CW Nd:YAG laser. For optimal thermal stability the resonator cavity is supported by Invar rods, and all the critical mounts are made of stainless steel (Klinger). The Nd:YAG performance is monitored by using the IR leakage through the high-reflecting mirror ($\approx 0.1\%$).

The Nd:YAG is modelocked at 78 MHz, giving a train of pulses, each with a FWHM of ≈ 100 ps and separated by 13 ns peak-to-peak. The Q-switch repetition rate is variable. The combined action of the Q-switch and modelocker results in a train of modelocked pulses inside a Q-switched envelope. This train of IR pulses (1064 nm) is frequency-doubled with a 3 x 3 x 5 mm KTP crystal (Airtron) to 532 nm. The Nd:YAG laser energy output is about 640 mJ per Q-switched envelope at 532 nm. The 532 nm green light is then split by a 50/50 beamsplitter in order to pump the two independent dye lasers.

II.A.6. The Cavity-Dumped Dye Lasers

The cavity of the synchronously pumped dye lasers consists of a dye cuvette with a 1 mm pathlength, two flat broad band high reflecting mirrors, a 25 cm plano-convex lens as the focusing element, and an iris for transverse mode selection. The dye cuvette is set near the Brewster angle to maintain polarized light in the cavity, and is located as close as possible to the rear mirror. The focal point of the intracavity lens lies very close to the rear mirror. The dye solution concentration is optimized by starting with a 100 mg-per-liter solution, and then adding a concentrated solution of the same dye until maximum power is reached. Two intracavity etalons (a 5 m airgap and a 100 m solid etalon, Virgo Optics ET-3 and ET-100, respectively) are used for wavelength selection, and together give a resolution on the order of 3 cm^{-1} .

The dye laser is cavity-dumped electro-optically. The cavity dumper consists of a Pockels cell (Quantum Technology QK-10-1) coupled with a Glan laser escape window (Karl Lambrecht MGLA-SW-8). The Pockels cell is essentially a KDP crystal, which acts as a quarter-wave plate when a specified voltage, approximately 2.4 kV for 600 nm light, is applied axially. The Glan laser escape window is a calcite polarizer that allows light of one linear polarization to pass through, but will reflect light of the opposite polarization out of the cavity. When the pulse in the cavity reaches its maximum intensity, a VFET switching circuit with a rise time of a few nanoseconds is triggered to place 2.4 kV across the Pockels cell [84]. After two passes through the Pockels cell, the pulse is of the opposite linear polarization, and is dumped out of the cavity by the Glan laser window. The Pockels cell is triggered by a photodiode monitoring leakage from the high reflector of the Nd:YAG laser. The Stanford DG535 delay generator is used to optimize the dump time (Figure 2). After cavity dumping, the visible pulses are frequency-doubled, using a LiIO_4 or BBO crystal, and sent to the molecular beam. Pulses from the dye lasers are characterized by taking their autocorrelations, and were typically 30-40 ps in duration.

II.A.7. Data Acquisition and Analysis

Two-color resonance-enhanced multiphoton ionization (REMPI) is used to ionize the clusters selectively, followed by time-of-flight mass spectrometry to detect the resultant cluster ions. The experimental configuration is shown in Figure 4. The conical nozzle is positioned close to the first skimmer. The backing pressure (4 to 20 psig), pulsewidth, delay time, carrier-gas composition, and sample temperature (typically 90°C) were set to maximize the desired signal while minimizing interferences from other clusters. Since the S_1 state is greater than 50% of the ionization energy, one-color two-photon ionization is used as a diagnostic. The pump-laser dye was DCM in methanol, and the probe laser dye was DCM in DMSO. Care was taken to lower the pump-laser power to a minimum, and the probe wavelength was chosen to create the ions close to threshold ionization. Under normal operating conditions, the pressure in the expansion chamber is approximately 5×10^{-5} torr and the pressure in the TOF chamber is 7×10^{-7} torr. The Nd:YAG laser Q-switch is triggered by the pulsed valve driver during an experiment, and the repetition rate is typically 100 Hz. At 500 Hz, the measured 532 nm power is between 300 and 350 mW, corresponding to 600 to 700 mJ per pulse train.

The time resolution of the experiments is achieved by delaying the probe pulse relative to the pump pulse using Michelson interferometry techniques. The pump laser is sent down a static delay line before being directed into the molecular beam, and the probe laser is sent down a variable delay line. The variable delay line consists of a corner cube (Precision Lapping, 1 sec. accuracy w/MgF₂ coating) mounted on a stepper-motor driven translation stage. The translation stage is an Aerotech ATS224 linear positioning stage with a programmable Unidex I driver. The stage provides up to 4 ns of delay time per pass. The laser beams are then recombined on a mirror after which they are propagated collinearly and focused onto the sample.

An Apple Macintosh II computer is used to control data acquisition and to perform data analysis. A typical transient is obtained by averaging the signal, using either the boxcar or transient digitizer, for each position of the optical delay line. Typically, a scan takes about 6 minutes, and 50-100 scans were required for an acceptable signal-to-noise ratio. When cluster sizes are small, single cluster sizes can be excited. Thus, only one mass peak is of interest, and the signal from the MCP is directed toward a boxcar integrator. For larger clusters, a distribution of cluster sizes is seen. In this case single-cluster transients are obtained either using the boxcar, or alternatively using data from experiments in which the signal for all clusters is averaged by the transient digitizer at each delay line position. In the latter case, individual transients are constructed from the averaged mass spectra.

The system response function is approximately Gaussian with an autocorrelation FWHM of about 40 ps. The autocorrelation pulsewidth is used to obtain rate constants from the measured transients. A standard nonlinear least-squares analysis based on the Marquardt algorithm is used [85]. Typically, the rising edge of the transients is best fit by a 60 ps response. The quality of the fit is judged by the value of χ^2 between the real and fitted data.

II.B. PICOSECOND FLUORESCENCE APPARATUS

Picosecond fluorescence measurements were performed using a time correlated single-photon counting apparatus, which has been described previously in detail [86,87]. The present studies are conducted in a manner similar to earlier studies of isoquinoline-water clusters [88]. Lifetime measurements and dispersed fluorescence spectra were obtained by using the frequency-doubled output of a synchronously pumped, cavity dumped dye laser with 0.5m monochromator (SPEX w/Amperex XP2020Q PMT) and assorted electronics common to photon counting apparatuses. DCM (2.1 mM) in a mixture of 30% benzyl alcohol and 70% ethylene glycol were used as the dye solution. A

stagnation pressure of 30 to 70 psig of the ammonia-helium mixture or argon was used. The nozzle diameter was 100 μ , and the α -naphthol sample was heated from 90 to 120°C.

III. RESULTS AND DISCUSSION

III.A. Preliminaries and Spectroscopy

Leutwyler and co-workers have reported extensive time-integrated spectroscopic results for the solute/solvent cluster systems of α -naphthol with ammonia, methanol, piperidine ($C_5H_{11}N$) and water [58-61]. In the experiments involving both α -NpOH $\cdot(NH_3)_n$ and α -NpOH $\cdot(C_5H_{11}N)_n$ clusters a large red shift and substantial broadening in the excitation spectrum were observed as well as a very large Stokes shift and total broadening of the fluorescence for clusters larger than a critical size. In the ammonia clusters the critical cluster size reported is $n = 4$ and for piperidine $n = 2$. In both cases the position and width of the broadened emission were similar to that of the α -naphtholate anion in basic aqueous solution. Experiments with α -NpOH $\cdot(H_2O)_n$ fail to show any evidence of the Stokes shifted and broadened emission indicative of proton transfer until $n \geq 20$. The strength of this emission continues to increase as a function of the cluster size but even for $n \geq 30$ the position and width fail to converge to that of α -naphthol in bulk water.

Important for this work are the results of the cluster size dependent spectral shifts in the resonance-enhanced two-photon ionization spectra for the various small clusters investigated in this chapter. These spectral shifts gathered from the published results of Leutwyler and co-workers are reproduced in Table 1. By using these results with time-of-flight mass analysis, time-resolved experiments on individual clusters were possible without significant interference from other clusters for the cases of α -NpOH $\cdot(NH_3)_{n=1-3}$, α -NpOH $\cdot(C_5H_{11}N)_1$ and α -NpOH $\cdot(H_2O)_{n=1-4}$. In the other cases, especially for the α -NpOH $\cdot(H_2O)_{n=8-20}$ clusters, spectral overlap in the excitation spectrum prevented single-

cluster experiments and care was taken to set the clustering conditions (backing pressure and solvent partial pressure) and temporal overlap of the gas pulse and laser pulses to skew the cluster-size distribution.

Emission lifetime measurements for the small clusters $\alpha\text{-NpOH}\cdot(\text{H}_2\text{O})_{n=1-4}$, excited to the S_1 origin have also been reported and for the blue-green emission, indicative of the α -naphtholate anion, from experiments in which the conditions are set to create large solute/solvent clusters, $n \geq 50$ [61]. These measurements vary significantly over the range of 47-72 ns and nonmonotonically as a function of increasing cluster size. The emission lifetime for the blue-green emission which is averaged over a distribution of large clusters is 28 ± 1 nanoseconds. The emission lifetime measurements for the small clusters $\alpha\text{-NpOH}\cdot(\text{NH}_3)_{n=1-3}$, excited to the S_1 origin and for the blue-green emission observed when the excitation wavelength and conditions are chosen to excite clusters with $n \geq 4$, have also been reported [58-60]. Results of these measurements obtained with the picosecond fluorescence apparatus described in the experimental section are listed in Table 2.

Recently Lakshminarayan and Knee have reported fluorescence lifetime measurements for the bare α -naphthol molecule excited to the S_1 state [89]. Experiments were performed to characterize the intramolecular dynamics as a function of excess vibrational energy above the S_1 origin. Quantum-interference effects, which are manifested as modulations in the fluorescence decays, are observed for only a few isolated excitation levels. No evidence for rapid IVR at high excess energies is observed. In time-domain studies such as these, this rapid energy distribution is observed as an initial rapid dephasing from the prepared superposition followed by the expected exponential decay.

III.B. Picosecond Pump-Probe Studies: $\alpha\text{-NpOH}\cdot(\text{NH}_3)_n$

Figure 5 is a composite figure of our results of the S_1 excited-state dynamics for the clusters $\alpha\text{-NpOH}\cdot(\text{NH}_3)_{n=1-4}$. For each of the transients displayed, a cluster is excited to

its S_1 vibrationless origin by a UV laser pulse (λ_1) and is probed, at some delay relative to this pump pulse, by a second UV laser pulse (λ_2). Probe-laser wavelengths are chosen to be as red as possible with the laser system and to insure a usable signal-to-noise level. Individual experiments for each of the clusters were performed to obtain the transients. The cluster-beam conditions were set to maximize the signal for each cluster while minimizing possible interferences from the other clusters. An exception to this method is the cluster $\alpha\text{-NpOH}\cdot(\text{NH}_3)_4$, which has a broad and ill-defined cluster origin and is excited at 323.8 nm. This wavelength is not strictly the reported cluster origin listed in Table 1 but it is within 150 cm^{-1} of this value. No significant difference in the transients for this cluster are observed when the excitation wavelength is 322.1 nm. Two transients are presented for the $\alpha\text{-NpOH}\cdot(\text{NH}_3)_2$ and are identified as A and B. In the reported spectroscopy work for this system two isomers and two different cluster origins have been identified [58,60].

For each of the clusters $\alpha\text{-NpOH}\cdot(\text{NH}_3)_{n=1}$ and 2(A&B), only nanosecond timescale behavior is observed. As was reported in the Preliminaries and Spectroscopy section of this chapter, the fluorescence-emission lifetimes of the S_1 state for these clusters are of the order of tens of nanoseconds. The delay line used in these experiments has a useful temporal range of four nanoseconds. Therefore, accurate measurements of such long lifetimes are not possible. For the clusters $\alpha\text{-NpOH}\cdot(\text{NH}_3)_{n=3,4}$, the transients reveal dynamics on the picosecond timescale. Each of these transients has a fast component, $100 \pm 30\text{ ps}$, followed by a long nanosecond type decay. The smooth curves that are drawn through the data are the result of a least-squares fitting program based on the Marquardt algorithm and the convolution of a 40 ps Gaussian instrument function representing the cross correlation of the pump- and probe-laser pulses. The time-axis value of zero is set to be at the half maximum of the initial rise of the signal.

III.C. Picosecond Pump-Probe Studies: $\alpha\text{-NpOH}\cdot(\text{C}_5\text{H}_{11}\text{N})_n$ and $\alpha\text{-NpOH}\cdot(\text{H}_2\text{O})_n$

Figure 6 is composite of our time-resolved measurements of the S_1 excited state dynamics for the clusters $\alpha\text{-NpOH}\cdot(\text{C}_5\text{H}_{11}\text{N})_{n=1-3}$. In these reported excitation spectra only the $\alpha\text{-NpOH}\cdot(\text{C}_5\text{H}_{11}\text{N})_1$ cluster has a sharp absorption spectrum and well-defined cluster origin [59]. For the clusters $\alpha\text{-NpOH}\cdot(\text{C}_5\text{H}_{11}\text{N})_{n=1-3}$, the same excitation wavelength, 320.9 nm, was used in each of the experiments. This wavelength is the origin of the $\alpha\text{-NpOH}\cdot(\text{C}_5\text{H}_{11}\text{N})_1$ cluster and is within one of the broad bands reported in the two-photon ionization spectrum for $\alpha\text{-NpOH}\cdot(\text{C}_5\text{H}_{11}\text{N})_2$ cluster. Again, each transient is recorded individually with the cluster conditions set to maximize signal for a particular cluster and the probe wavelength is to the red of the excitation wavelength.

As in the $\alpha\text{-NpOH}\cdot(\text{NH}_3)_n$ cluster transients, a significant difference in the transients is observed as the cluster size increases. For the cluster $\alpha\text{-NpOH}\cdot(\text{C}_5\text{H}_{11}\text{N})_1$ only a long-time, nanosecond type, decay is observed. Both the $\alpha\text{-NpOH}\cdot(\text{C}_5\text{H}_{11}\text{N})_2$ and the $\alpha\text{-NpOH}\cdot(\text{C}_5\text{H}_{11}\text{N})_3$ clusters reveal dynamics on the picosecond timescale. Each of the transients exhibits a fast 65 ± 10 ps decay. The long nanosecond timescale decay evident in both the $\alpha\text{-NpOH}\cdot(\text{NH}_3)_2$ and $\alpha\text{-NpOH}\cdot(\text{NH}_3)_3$ cluster transients is observed only in the $\alpha\text{-NpOH}\cdot(\text{C}_5\text{H}_{11}\text{N})_2$ cluster transient.

Figure 7 is a composite of a representative sample of our time-resolved measurements of the excited-state dynamics for the clusters $\alpha\text{-NpOH}\cdot(\text{H}_2\text{O})_{n=1-21}$. Individual experiments were performed for the clusters $n = 1$ to 4, using the reported cluster origins. The remaining cluster transients were recorded using a transient digitizer with signal-averaging capabilities that allowed the transient for a number of clusters to be recorded in a single experiment. For these multiple-cluster experiments the excitation wavelength is chosen to excite a range of clusters with overlapping two-photon ionization spectra. Two different experiments were used to cover the remaining range of cluster

transients recorded. The excitation wavelength is 320 nm and the nozzle backing pressure is varied from 15 psig to 30 psig in the two experiments in order to shift the cluster distribution to larger n . In all $\alpha\text{-NpOH}\cdot(\text{H}_2\text{O})_n$ cluster transients recorded, no evidence for proton transfer is observed on the timescale of this experiment.

III.D. Discussion

The experiments described in this chapter reveal some of the excited state dynamics in the cluster systems of α -naphthol with ammonia, piperidine and water. The results confirm the presence of proton-transfer dynamics in size-specific clusters of α -naphthol with strong basic solvents. In addition, both the time-integrated spectroscopy results and the time-resolved measurements are consistent with the concepts concerning proton-transfer reactions garnered from condensed phase work. In order to present clearly the time-resolved measurements in proper context, this discussion section will be concerned largely with the $\alpha\text{-NpOH}\cdot(\text{NH}_3)_n$ clusters.

Figure 8 is a qualitative view of the potential energy surfaces important for describing the dynamics of these cluster systems. As the cluster size increases, the stability of the ionic form of the cluster in the excited state also increases. For the cluster $\alpha\text{-NpOH}\cdot(\text{NH}_3)_3$ the ionic form becomes more stable than the neutral form in the excited state of the cluster. Subsequently, electronic excitation of this and larger $\alpha\text{-NpOH}\cdot(\text{NH}_3)_n$ clusters leads to a shift in the population from one form to the other. In the picosecond pump-probe ionization experiments, this change in the cluster form becomes manifested as a loss in two-photon signal. The ionization transition in a two-photon process is known to be a vertical transition and thus the ionization of the ionic form, even though expected with a lower ionization potential [64], should be discriminated against in our experiment. Thus, the 100 ps decay observed in the transient for the $\alpha\text{-NpOH}\cdot(\text{NH}_3)_3$ and $\alpha\text{-NpOH}\cdot(\text{NH}_3)_4$ clusters is a measurement of the population shift or reaction time in these small clusters.

As has been noted in condensed-phase work, the proton-transfer reaction rate from an electronically excited aromatic alcohol to the surrounding solvent is determined by the solvent dynamics [71-77]. The timescale of the reaction will reflect the timescale for the rearrangement of the solvent molecules to stabilize the evolving ionic species. This should also be true in a small solute/solvent cluster. In addition, since each small cluster is composed of a fixed number of solvent molecules and isolated in the molecular beam, an energetic constraint exists for the reaction. In order for the proton transfer to occur in a particular size cluster, the proton affinity of the solvent must be larger than the acid dissociation energy, implying that the reaction is exothermic. This is revealed as the threshold dependence as a function of cluster size for the appearance of a picosecond timescale decay in a cluster.

A significant difference between this time-resolved work and the time-integrated spectroscopy work of Leutwyler and co-workers concerns this threshold size [58-60]. In the reported spectroscopy work, the threshold for the appearance of a broad excitation spectrum and a large Stokes shifted emission is the cluster $\alpha\text{-NpOH}\cdot(\text{NH}_3)_4$. In the time-resolved measurements, this threshold is the cluster $\alpha\text{-NpOH}\cdot(\text{NH}_3)_3$. Attempts to reproduce the sharp emission spectrum exciting over the region of the origin of the $\alpha\text{-NpOH}\cdot(\text{NH}_3)_3$ cluster were unsuccessful. These experiments were conducted in the picosecond fluorescence apparatus with a variety of glass nozzles (sizes and shapes), gas mixtures (0.5% to 5% in helium of argon buffer gas) and backing pressures that often revealed the Stokes shifted emission indicative of large $\alpha\text{-NpOH}\cdot(\text{NH}_3)_n$ clusters. Pertinent to this issue are the spectroscopy and time-resolved measurements of Brucker and Kelley on matrix isolated clusters of α - and β -naphthol with ammonia [62,63]. Their measurements also indicate that the excited-state intermolecular proton transfer occurs at $n = 3$ for both alcohols. Also, no temperature dependence for the reaction rate, equal to 22 ± 5 ps for α -naphthol and 23 ± 5 for β -naphthol, is observed for the clusters with $n=3$

over the temperature range 10-24 K. It is possible that the clusters detected in our two-color picosecond pump-probe measurements suffer from cluster evaporation. However, no broadening is observed in the time-of-flight mass peaks until $n = 5$ (Figure 3) so it is felt that the measurements are correct with regard to cluster size.

In the time-resolved experiments for the other cluster systems, α -NpOH \cdot (C₅H₁₁N)_n and α -NpOH \cdot (H₂O)_n, our results agree completely with the time-integrated spectroscopy results. The cluster-size threshold for the intermolecular proton transfer reaction is α -NpOH \cdot (C₅H₁₁N)_{n=2} clusters and no evidence for the reaction is observed in the cluster transients for α -NpOH \cdot (H₂O)_{n=1-21} clusters.

Recently Steadman, Fournier, and Syage have reported similar time-resolved measurements for excited-state proton-transfer reactions in gas phase clusters of phenol with ammonia, C₆H₆O \cdot (NH₃)_{n=1-7} [56,67]. A cluster-size threshold, $n = 5$, is reported for the appearance of a picosecond timescale decay of 60 ± 10 ps and no evidence of the proton transfer is observed with less basic cluster solvents (methanol and water). In addition, two other significant findings are reported. Protonated ammonia clusters are observed in the mass spectrum with an appearance rate equal to the fast decay in the C₆H₆O \cdot (NH₃)_n clusters where $n \geq 5$ and a competitive recombination rate equal to 350 ± 100 ps is reported for $n \geq 5$. These experiments are conducted without selective cluster excitation ($\lambda_1 = 266$ nm) and with both one photon ($\lambda_2 = 355$ nm) and two-photons ($\lambda_2 = 532$ nm) used for the transition to the ionization continuum. The recombination rate is derived from the signal at long delay time after deconvolution of both the fast decay and the instrument function.

This signal at long delay times is present in both the phenol cluster work and the α -naphthol cluster work. Generally, for the clusters that undergo the proton transfer, the ratio of the magnitude of the long-time signal to the magnitude of the peak signal, near $t = 0$, decreases as the cluster size increases. In the model adopted by Steadman and Syage, which involves a fast acid-base equilibrium, this ratio is a measure of the equilibrium

constant $K = k_1/k_2$. A complementary interpretation is that the magnitude of the signal at long delay time is a reflection of the Franck-Condon probability for ionization from the excited ionic potential energy surface. The decreasing ratio is then a reflection of the completeness of the reaction in terms of the structural changes of the cluster and reduction of the ionization probability.

Overall, the time-resolved cluster measurements are consistent with the description of excited-state proton transfer in condensed media and the importance of the solvent on the energetics and dynamics of the process. Detailed picosecond kinetic studies of the excited state reaction of α - and β -naphthol in aqueous media have been reported [73-75]. In experiments with α -naphthol the rate of appearance of the characteristic emission that is due to the anion (550 nm) and the disappearance of emission that is due to the neutral naphthols (350 nm) is measured at room temperature as a function of solution pH. For H_2O solutions at a pH equal to 7, where the neutral is directly excited and the anion formed in the proton transfer reaction, both the rise and fall times show the same response of 33 ± 5 ps. For solutions with D_2O at the same pH, the response is 105 ± 5 ps [75]. In addition, other experimental studies, coupled with Markov random-walk calculations, for the naphthols in methanol/water solutions lead to the conclusion that a water cluster with $n = 4 \pm 1$ is the proton acceptor and that the reaction rate is controlled by the time necessary to form this specific structure [73,74]. The excited-state proton-transfer is known not to occur for the naphthols in neat methanol [90].

The failure to observe the excited-state proton-transfer reaction in small gas-phase clusters of water is common to both the α -naphthol and the phenol system. In the spectroscopic studies of Leutwyler and co-workers, the evidence for the reaction is not as clear as in the ammonia and piperidine clusters. Although the fluorescence emission does shift towards the red (below 400 nm) as the cluster size increases, at $n \geq 30$ the emission does not match well with that of the naphtholate anion in aqueous media. In the cluster

there are two necessary conditions for the reaction to occur. The proton affinity of the collection of solvent molecules must exceed the dissociation energy of the proton, and the solvent molecules must be able to relax and stabilize the ion pair. Thermodynamic calculations of a cluster's proton affinity, which make use of ion-molecule experimental data, indicate that the proton affinity should be large enough for a cluster when $n \approx 15$ [61]. Since clusters are efficiently cooled in the expansion, they probably resemble amorphous ice and are therefore quite rigid. The solid nature of the clusters is corroborated by electron-diffraction studies of water clusters $n \approx 20$ to a few hundred generated from a neat water expansion [91]. Thus the reaction is probably hindered by the slow dielectric relaxation of the "ice-like" water molecules, which could be longer than the excited state lifetime of the naphthol. In the condensed phase, the excited-state proton-transfer reaction is not observed for the naphthols in ice [61]. This concept of solvent rigidity, preventing proton transfer reactions, in low-temperature glasses has been postulated [92,93].

Another difference between the cluster results and condensed-phase studies is the difference in the proton-transfer rate. In the picosecond fluorescence studies of α -naphthol in aqueous media, the rate ranges from 8 to 33 ± 5 ps in water and from 43 to 105 ± 10 ps in deuterated water as a function of the solution pH [75]. A more directly comparable set of experiments are the picosecond fluorescence measurements of α - and β -NpOH \cdot (NH₃)₃ in argon matrices [62,63]. In these low temperature experiments, the rate for the proton transfer is 22 ± 5 ps for α -naphthol and 23 ± 5 for β -naphthol [62,63]. The observed rates for the gas-phase clusters of α -NpOH \cdot (NH₃)_{n = 3,4} are 100 ± 30 ps.

Quantitative modeling of proton transfer in these cluster systems is difficult at present. Experimental structural determination of small clusters ($n \geq 2$) is not yet commonplace. In addition, in these solute/solvent systems it will be important to characterize the cluster both before the reaction and after the transfer when the solvent has restructured to accommodate the ion pair. However, one can make some qualitative

statements. Brucker and Kelley concluded that the magnitude of the observed proton-transfer rates in the argon-matrix studies [62,63] indicate the existence of an energetic barrier, and that the proton transfer is not an activated process (since the rate was not sensitive to temperature from 10 to 24K) but proceeds via a tunneling mechanism. By invoking this mechanism, and assuming that the potential surface can be approximated as consisting of two bound wells of equal depth [62], the proton-transfer rate (equivalent to the tunneling frequency) is given by:

$$\nu_t = \frac{2\nu}{\pi} \cdot \exp \left[\frac{-2\pi (2m)^{1/2}}{h} \int_{-a}^a V(x) dx \right]. \quad (6.1)$$

Using the simplifying assumption that the barrier is parabolic in shape,

$$V(x) = E(1-x^2/a^2). \quad (6.2)$$

In the above equations, ν is the vibrational frequency, m is the mass of the proton, and a is the distance from the center of the barrier to the classical turning points. Since the actual proton-transfer reaction is exothermic and irreversible, an unsymmetrical potential curve that is bound-free on one side is likely to be more realistic. In this case, the rate of proton-transfer [62] is given by

$$k = \nu \cdot \exp \left[\frac{-4\pi (2m)^{1/2}}{h} \int_{-a}^a V(x) dx \right] \quad (6.3)$$

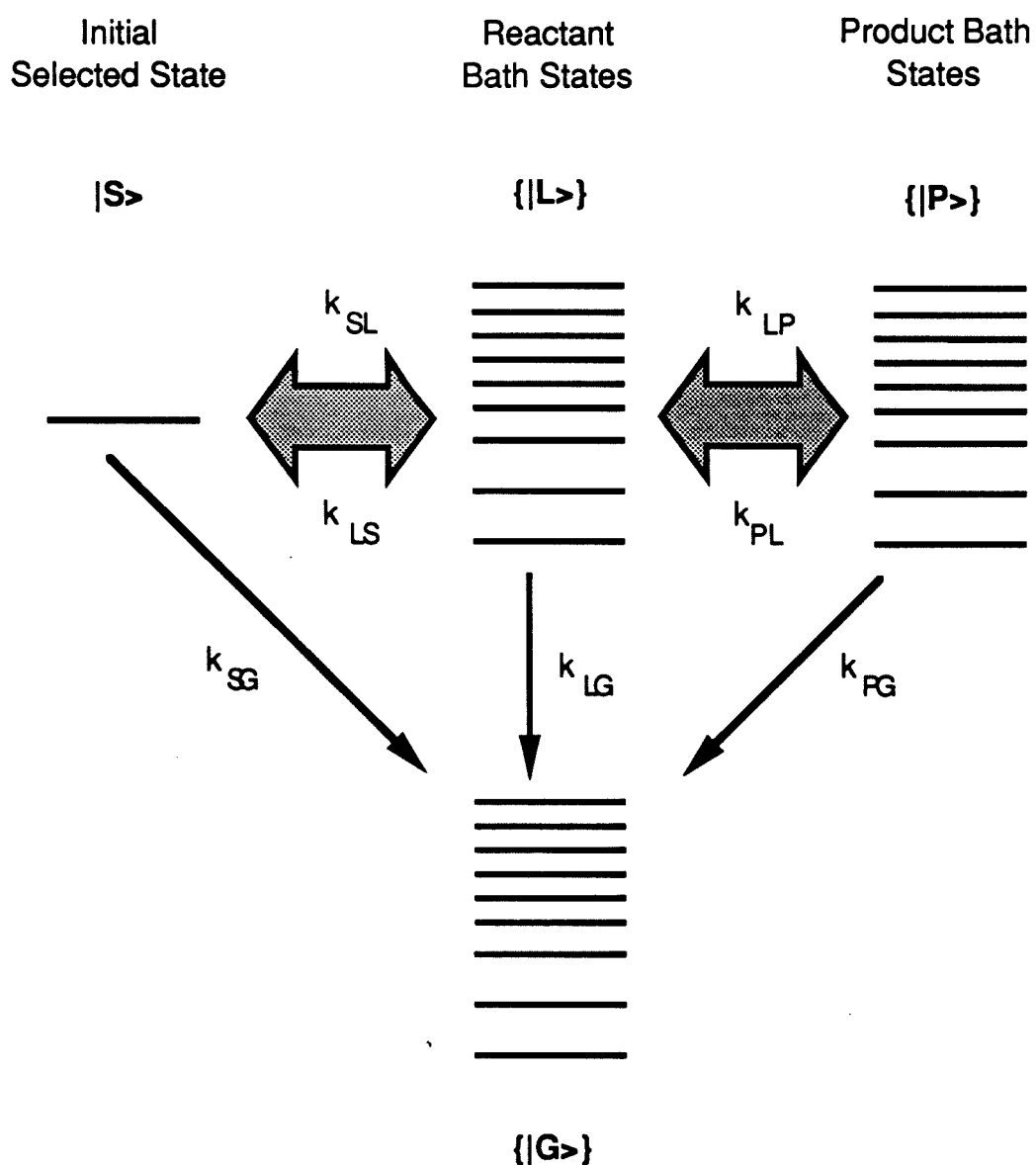
Regardless of the potential curve used, the two parameters that will control the proton-transfer rate are the barrier height and the tunneling distance (Figure 8).

Calculations using the lifetime measurements obtained in the matrix studies, assuming that the proton transfer distance can be estimated from the average O-H...N and O...H-N hydrogen bond distances (about 0.75Å), give barrier estimates of 12.6 and 3.6 kcal/mol from Equations 6.1 and 6.3, respectively, for the zero-point energy vibration of a proton [62,63]. The small barrier heights suggest that small changes in the proton-transfer energetics could have large effects on the proton-transfer rates. Our calculations, similar to those of References 62 and 63 and using the same barrier height, indicate that a change in the tunneling distance of 20% can account for a factor of four in the proton-transfer rate. It seems likely that the clusters in the matrix would be structurally different from the gas-phase clusters and this would subsequently be reflected in the rate of proton-transfer. Furthermore, in the supersonic beam one does not have to consider possible interactions of the cluster with the matrix itself. Studies of different alcohol/solvent systems may shed insights into how sensitive the proton-transfer rates are to the alcohol/solvent energetics.

It would be of interest to investigate the proton transfer dynamics as a function of excess vibrational energy for a specific cluster size. In both these and the matrix studies, the excess vibrational energy is essentially zero. In the matrix, extra energy was added by heating the matrix block. Laser excitation in supersonic beams differs from conventional thermal reactions in two fundamental ways: First, single vibrational levels in the excited electronic states may be excited; and second, the molecules are collision-free during the experiment and subject to intramolecular interactions only. Such experiments may further reveal the nature of the barrier and its sensitivity to the local solvent environment.

The overall kinetics of the proton transfer process, including the possibility of IVR, can be modeled in a phenomenological manner analogous to that of t-stilbene [94]. The microscopic model, which allows the kinetics from specifically prepared vibrational states to be described, is based on the quantum mechanical solution to a similar problem worked out in the context of radiationless transition theory [95]. Quantum interference effects are

ignored. A laser pulse excites the solute molecule to a given vibrational state, which may undergo IVR into a manifold of states. These manifold states then undergo proton transfer along the proton-transfer coordinate to form the product states. Thus the fast component of the experimental decays are due to the IVR/reaction taking place in the clusters, while the long-time component reflects lifetime of the equilibrated system. The general kinetic scheme is illustrated below.



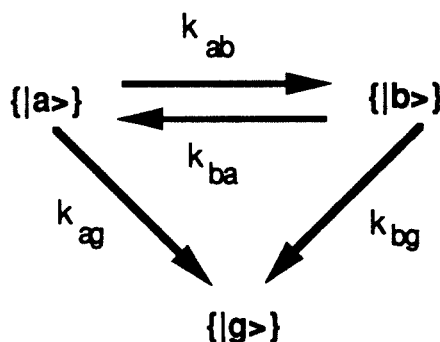
Note that the model permits reversibility in the excited state, but relaxation to the ground state is irreversible. The relevant kinetic equations [94] are

$$\dot{N}_s = - (k_{sg} + k_{sl}) N_s + k_{ls} N_l \quad 6.4$$

$$\dot{N}_l = - (k_{lg} + k_{ls} + k_{lp}) N_l + k_{sl} N_s + k_{pl} N_p \quad 6.5$$

$$\dot{N}_p = - (k_{pg} + k_{pl}) N_p + k_{lp} N_l \quad 6.6$$

If the rate of IVR is much faster than the proton-transfer rate, or vice-versa, then the kinetic scheme can be shown to reduce to the three-state problem [94] described by



Here, state ensembles $\{|a\rangle\}$ and $\{|b\rangle\}$ represent either a combination of $|S\rangle$ and $|L\rangle$ or $|L\rangle$ and $|P\rangle$. Implicit in this three-state formalism is the assumption that states within a manifold have very similar decay rates because of equilibration or similar Franck-Condon factors. The assumption, while not necessarily correct, greatly simplifies the analysis. Solving Equations 6.4 through 6.6 for the populations is straightforward, and the solutions for either combination of $\{|a\rangle\}$ and $\{|b\rangle\}$ are given below.

$$N_a(t) = K \{ \exp(-\lambda_a t) + m \exp(-\lambda_b t) \} N_a(0)$$

$$N_b(t) = F \{ \exp(-\lambda_b t) - \exp(-\lambda_a t) \} N_a(0)$$

where the various constants are given by the expressions

$$K = \frac{\Lambda_a - \lambda_b}{\lambda_a - \lambda_b} \quad F = \frac{k_{ab}}{\lambda_a - \lambda_b} \quad m = \frac{\lambda_a - \Lambda_a}{\Lambda_a - \lambda_b}$$

$$\Lambda_a = k_{ag} + k_{ab}$$

$$\Lambda_b = k_{bg} + k_{ba}$$

$$\lambda_{a,b} = \frac{1}{2} \{ (\Lambda_a + \Lambda_b) \pm [(\Lambda_a - \Lambda_b)^2 + 4k_{ab}k_{ba}]^{1/2} \}$$

If the rate of IVR from the initially excited vibrational state is much faster than all other rate constants, then the latter will be mode-independent.

Figure 9 shows simulated population decays, assuming that the IVR rate is much faster than all other rate constants. The decays are calculated for a series of back-reaction rate constants, represented by k_{ba} in the three-state formalism of the previous paragraph. The expected populations of the α -NpOH \cdot (NH₃)_n and the $(\alpha$ -NpO⁻) \cdot [H⁺(NH₃)_n] are shown. The time axis is the same as for the experimental decays. Data from the α -NpOH \cdot (NH₃)_{n=3,4} clusters are used for the proton transfer rate k_{ab} (100 ps), the decay from the initial excited state back to the ground state (60 ns), and for the decay of the equilibrated system (40 ns) to the ground state. Although the plotted curves are not meant to simulate the experimental data quantitatively, they do suggest that the experimentally observed biexponential decays are influenced by the balance between the back-reaction rate versus the proton transfer rate.

IV. Conclusions

Picosecond time-resolved pump-probe spectroscopy has been applied to excited-state proton-transfer reactions in small clusters. The investigation of the clusters α -naphthol with ammonia, piperidine and water indicates the occurrence of the proton transfer on the picosecond timescale in the clusters α -NpOH \cdot (NH₃)_{n=3,4} and α -NpOH \cdot (C₅H₁₁N)_{n=2,3}. The measured rates of 100 ± 30 ps for the ammonia clusters and 65 ± 10 ps for the clusters with piperidine compare well with proton-transfer studies of other gas-phase clusters, phenol with ammonia, matrix-isolated clusters, α -naphthol with ammonia and α - and β -naphthol in aqueous media. Future application of these techniques to other cluster systems will possibly provide insights into condensed-phase solvent dynamics and the solvent's role in reaction dynamics.

REFERENCES

1. A.W.Castleman, Jr. and R.G. Keesee, *Ann. Rev. Phys. Chem.* **37**, 525 (1986).
2. D.H. Levy, *Adv. Chem Phys.* **47** (Part 1), 323 (1981).
3. R. Miller, *Science* **240**, 447 (1988).
4. F.G. Celii and K.C. Janda, *Chem. Rev.* **86**, 507 (1986).
5. S. Leutwyler and Jürg Bösiger, *Chem. Rev.* **90**, 489 (1990).
6. *Atomic and Molecular Clusters*, edited by E. R. Bernstein, (Elsevier, Amsterdam,1987).
7. C.E. Klots and R.N. Compton, *J. Chem. Phys.* **69**, 1644 (1978).
8. T.D. Mark and A.W. Castleman, Jr., *Adv. Atomic Mol. Phys.* **20** (1985), edited by B. Bederson (Academic Press, Orlando).
9. M. T. Coolbaugh, W.R. Peifer and J.F. Garvey, *J. Phys. Chem.* **94**, 1619 (1990).
10. M. T. Coolbaugh, W.R. Peifer and J.F. Garvey, *J. Am. Chem. Soc.* **112**, 3692 (1990).
11. J. J. Breen W.B. Tzeng, K. Kilgore R.G. Keesee and A.W. Castleman, Jr., *J. Chem. Phys.* **90**, 19 (1989).
12. W.-B. Tzeng, S. Wei, R.G. Keesee and A.W. Castleman, Jr., *Chem. Phys. Lett.* **168**, 31 (1990).
13. H. Ohoyama, M. Takayanagi, T. Nishiya and I. Hanazaki, *Chem. Phys. Lett.* **162**, 1 (1989).
14. K. Honma and O. Kajimoto, *Chem.Phys. Lett.* **117**, 123 (1985).
15. K. Honma Y.Fujumura, O. Kajimoto and G.Inoue, *J. Chem. Phys.* **88**, 4739 (1988).
16. C. Jouvét and B. Soep, *Laser Chem.* **5**, 157 (1985).
17. W.H. Breckenridge, C. Jouvét and B. Soep, *J. Chem. Phys.* **84**(3) 1443 (1986).
18. C. Jouvét, M. Boivineau, M.C. Duval and B. Soep, *J. Phys. Chem.* **91**, 5416 (1987).
19. J.P. Visticot, B. Soep and C.J. Whitham, *J. Phys. Chem.* **92**, 4574 (1988).

20. C. Jouvet, M.C. Duval, B. Soep, W.H. Breckenridge and C. Whitham and J.P. Visticot, *J. Chem. Soc. Faraday Trans. 2* **85**(8), 1133 (1989).
21. S. Buelow, G. Radhakrishnan, J. Catanzarite and C. Wittig, *J. Chem. Phys.* **83**, 444 (1985).
22. G. Radhakrishnan, S. Buelow and C. Wittig, *J. Chem. Phys.* **84**, 727 (1986)
23. S. Buelow, M. Noble, G. Radhakrishnan, H. Reisler, C. Wittig and G. Hancock, *J. Phys. Chem.* **90**, 1015 (1986).
24. S. Buelow, G. Radhakrishnan and C. Wittig, *J. Phys. Chem.* **91**, 5409 (1987).
25. C.Wittig, S. Sharpe and R.A. Beaudet, *Accounts Chem. Res.* **21**, 341 (1988).
26. G.Hoffmann, D. Oh, H. Iams and C. Wittig, *Chem. Phys. Lett.* **155**, 356 (1989).
27. Y.Chen, G. Hoffmann, D.Oh and C.Wittig, *Chem. Phys. Lett.* **159**, 426 (1989).
28. Y. Chen, G. Hoffmann, S.K. Shin, D.Oh, S. Sharpe, Y.P. Zeng, R.A. Beaudet and C.Wittig, *Photoinitiated Reaction in Weakly-Bonded Complexes: Entrance Channel Specificity*, to be published (1990).
29. N.F. Scherer, L. R. Khundkar, R.B. Bernstein and A. H. Zewail, *J. Chem. Phys.* **87**, 1451 (1987)
30. N.F. Scherer, C. Sipes, R.B. Bernstein and A. H. Zewail, *J. Chem. Phys.* **92**(9) 5239 (1990).
31. D.J. Levander, M.Mengel, R. Pursel, J. McCombie and G. Scoles, *J. Chem. Phys.* **86**, 7239 (1987)
32. D.J. Levander, M.Mengel, R. Pursel, J. McCombie and G. Scoles, *Z. Physik. D* **10**, 7239 (1988).
33. J.A. Warren, E.R. Bernstein and J.I. Seeman, *J. Chem. Phys.* **88**, 871 (1988).
34. M. Castella, J. Prochorow and A. Tramer., *J. Chem. Phys.* **81**, 2511 (1984).
35. M. Castella, F. PiuZZi and A. Tramer, *Chem. Phys. Lett.* **129**, 105 and 113 (1986).
36. A. Amirav, M. Castella, F. PiuZZi, and A.Tramer, *J. Phys. Chem.* **92**, 5200 (1988).
37. M.Castella, P.Millie, F.PiuZZi, J. Caillet, J.Langlet, P. Claverie and A.Tramer, *J. Phys. Chem.* **93**, 3941 and 3949 (1989).
38. J. C. Drobbits and M.I. Lester, *J. Chem. Phys.* **86**, 1662 (1987).
39. J. C. Drobbits, J. M. Skene and M.I. Lester, *J. Chem. Phys.* **84**, 2896 (1986).

40. J. M. Skene, J. C. Drobbits and M.I. Lester, *J. Chem. Phys.* **85**, 2329 (1986).
41. K.C. Janda, *Adv. Chem. Phys.* **60**, 201 (1985).
42. J.I. Cline, N. Sivakumar, D.D. Evard and K.C. Janda, *J. Chem. Phys.* **86**, 1636 (1987).
43. A. Mitchell, M. J. McAuliffe, C.F. Giese and W.R. Gentry, *J. Chem. Phys.* **83**, 4271 (1985).
44. M.P. Casassa, A.M. Woodward, J.C. Stephenson and D.S. King, *J. Chem. Phys.* **85**, 6235 (1986).
45. G.E. Ewing, *Faraday Discuss. Chem. Soc.* **73**, 325 (1982).
46. G.E. Ewing, *Chem. Phys.* **63**, 411 (1981).
47. J. A. Beswick and J. Jortner, *Adv. Chem. Phys.* **47**, 363 (1981).
48. P.M. Felker, Wm. R. Lambert and A.H. Zewail, *J. Chem. Phys.* **72**, 1603 (1982).
49. P.M. Felker and A.H. Zewail, *J. Chem. Phys.* **78**, 5266 (1983).
50. A.H. Zewail, *Faraday Discuss. Chem. Soc.* **75**, 315 (1983).
51. J.L. Knee, L.R. Khundkar and A.H. Zewail, *J. Chem. Phys.* **87**, 115 (1987).
52. D.H. Semmes, J.S. Baskin and A.H. Zewail, *J. Am. Chem. Soc.* **109**, 4101 (1987).
53. D. H. Semmes, J. S. Baskin and A.H. Zewail, *J. Chem. Phys.* **92**, 5239 (1990).
54. J.J. Breen, D. M. Willberg and A.H. Zewail, to be published (1990).
55. J.A. Syage and J. Steadman, *Chem. Phys. Lett.* **166**, 159 (1990).
56. J. Steadman, E.W. Fournier and J.A. Syage, *Applied Optics*, to be published (1990).
57. P.G. Wang, Y.P. Zhang, C.G. Ruggles and L.D. Ziegler, *J. Chem. Phys.* **92**, 2806 (1990).
58. O. Cheshnovsky and S. Leutwyler, *Chem. Phys. Lett.*, **121**, 1 (1985).
59. R. Knochenmuss, O. Cheshnovsky and S. Leutwyler, *Chem. Phys. Lett.* **144**, 317 (1988).
60. O. Cheshnovsky and S. Leutwyler, *J. Chem. Phys.* **88**, 4127 (1988).
61. R. Knochenmuss and S. Leutwyler, *J. Chem. Phys.* **91**, 1268 (1989).

62. G.A. Brucker and D.F. Kelley, *J. Chem. Phys.* **90**, 5243 (1989)
63. G.A. Brucker and D.F. Kelley, *Chem. Phys.* **136**, 213 (1989).
64. D.Solgadi, C. Jouvét and A. Tramer, *J. Phys. Chem.* **92**, 3313 (1988).
65. M.R. Nimlos, D.F. Kelley and E.R. Bernstein, *J. Phys. Chem.* **93**, 643 (1989).
66. H.S. Im, V.H. Grassian and E.R. Bernstein, *J. Phys. Chem.* **94**, 222 (1990).
67. J. Steadman and J. A. Syage, *J. Chem. Phys.* **92** (7), 4630 (1990).
68. J.J. Breen, L. W. Peng, D.M. Willberg, A.H. Heikal, P.Cong and A.H. Zewail, *J. Chem. Phys.* **92**, 805 (1990).
69. R.P. Bell, *The Proton in Chemistry* (Cornell Univ. Press, Ithaca, 1973).
70. R.P. Bell, *The Tunnel Effect in Chemistry* (Chapman and Hall, New York, 1980).
71. E.M. Kosower and D.Huppert, *Ann Rev. Phys. Chem.* **37**,127 (1986).
72. D.Huppert, E. Kolodney, M. Gutman and E. Nachiel, *J. Am. Chem. Soc.* **104**, 6949 (1982).
73. J.Lee, R.D. Griffin and G.W. Robinson, *J. Chem. Phys.* **82**, 2572 (1982).
74. J.Lee, G.W. Robinson, S.P.Webb, L.A. Philips and J.H.Clark, *J. Am. Chem. Soc.* **108**, 6538(1986).
75. S.P.Webb, L.A.Philips, S.W. Yeh, L.M. Tolbert and J.H. Clark, *J. Phys. Chem.* **90**, 5154 (1986).
76. D.C. Borgis, S.Lee and J.T. Hynes, *Chem. Phys. Lett.* **162**, 19 (1989).
77. M.Morillo and R. I. Cukier, *J. Chem. Phys.* **92**, 4833 (1990).
78. D. Ray, N.E. Levinger, J. M. Papanikolas and W.C.Lineberger, *J. Chem. Phys.* **91**, 6533 (1989).
79. F. G. Patterson, *Ph.D. Thesis*, Stanford University, 1985.
80. J. E. Pollard and R. Cohen, *Rev. Sci. Instr.* **58**, 32 (1987).
81. L. R. Khundkar, *Ph.D. Thesis*, California Institute of Technology, 1989.
82. W. C. Wiley, I. H. McLaren, *Rev. Sci. Instr.* **26**, 1150 (1955).
83. E. Carrasquillo, T.S. Zwier and D.H. Levy, *J. Chem. Phys.* **83**, 4990 (1985).
84. J. C. Postelwaite, J.B. Miers, C. C. Reiner, D. D. Dlott, *IEEE J. Quantum Electronics* **24**, 411 (1988).

85. W. H. Press, B. P. Flannery, S. A. Teukolsky, and W. T. Vetterling, *Numerical Recipes in C* (Cambridge Univ. Press, Cambridge, 1988).
86. W. R. Lambert, P.M. Felker and A.H. Zewail, *J. Chem. Phys.* **81**, 2217 (1984).
87. P.M. Felker and A.H. Zewail, *J. Chem. Phys.* **82**, 2975 (1983).
88. P.M. Felker and A.H. Zewail, *Chem. Phys. Lett.* **94**, 448 and 454 (1983).
89. C. Lakshminarayan and J.L. Knee, *J. Phys. Chem.* **94**, 2637-2643 (1990).
90. N.M. Trieff and B.R. Sundheim, *J. Phys. Chem.* **69**, 2044 (1965).
91. G. Torchet, P. Schwartz, J. Farges, M. F. deFeraudy and B. Raoult, *J. Chem. Phys.* **79**, 6196 (1983).
92. D.M. Hercules and L.B. Rodgers, *J. Phys. Chem.* **64**, 397 (1960).
93. J.T. Hynes, *J. Stat. Phys.* **42**, 149 (1986).
94. J. A. Syage, P. M. Felker, and A. H. Zewail, *J. Chem. Phys.* **81**(11), 4706-4723 (1984).
95. F. Lahmani, A. Tramer, and C. Tric, *J. Chem. Phys.* **60**, 4431 (1974) and references therein.

TABLE 1**Cluster-Size Dependent Spectral Shifts**

<u>Cluster</u>	<u>Spectral Shift (cm⁻¹)</u>	<u>Pump λ (nm)</u>	<u>Probe λ (nm)</u>
$\alpha\text{-NpOH} \cdot (\text{NH}_3)_n^{\text{a}}$			
n = 0	0	317.9	
1	- 236	320.4	324.0
2 (A)	- 276	320.7	324.0
2 (B)	- 352	321.6	324.0
3	- 409	322.3	337.5
4	- 710 \pm 50	323.3	337.5
$\alpha\text{-NpOH} \cdot (\text{H}_2\text{O})_n^{\text{b}}$			
n = 1	- 143 \pm 10	319.4	337.5
2	- 81	318.7	"
3	- 136	319.1	"
4	- 164	319.6	"
5	- 155 / - 113 ^c	319.9	"
6	/ - 107	"	"
7	/ - 111	"	"
8	- 105 / - 208	"	"
9	/ - 175	"	"
10	/ - 161	"	"
11	/ - 142	"	"
12	/ - 209	"	"
13	/ - 207	"	"
14	/ - 200	"	"
15	/ - 215	"	"
16	/ - 238	"	"
17	/ - 233	"	"
18	/ - 247	"	"
19	/ - 238	"	"
20	/ - 200	"	"

TABLE 1 (continued) $\alpha\text{-NpOH} \cdot (\text{C}_6\text{H}_{11}\text{N})_n^{\text{d}}$

n = 1	- 307 \pm 25	320.9	337.5
2	\approx - 750	320.9	"
3		320.9	"

a = Reference 60

b = Reference 61

c = sharp band position/broad band position

d = Reference 59

TABLE 2**Picosecond Fluorescence Measurements of α -NpOH \cdot (NH₃)_n**

<u>Cluster</u>	<u>Lifetime(nsec)</u>	<u>Excitation λ(nm)</u>	<u>Detection λ(nm)</u>
α -NpOH \cdot (NH ₃) ₀	60 ± 2	318.1	332.8
α -NpOH \cdot (NH ₃) ₁	38 ± 1	320.6	335.5
α -NpOH \cdot (NH ₃) ₂	43 ± 2	320.9	335.8
α -NpOH \cdot (NH ₃) ₂	39 ± 1	321.8	336.7
α -NpOH \cdot (NH ₃) _{n\geq4}	38 ± 1	322.7	428.0

FIGURE CAPTIONS

- Figure 1. Schematic of the molecular beam apparatus.
- Figure 2. Schematic of the picosecond laser system.
- Figure 3. A nonresonant photoionization time-of-flight mass spectrum of α -NpOH(NH₃)_n clusters showing a typical cluster distribution.
- Figure 4. Schematic of the experimental arrangement depicting the picosecond laser system and cluster-beam apparatus.
- Figure 5. Pump-probe transients obtained for the clusters α -NpOH(NH₃)_{n=1-4}. Details for each of the experiments are contained in the text and in Table 1. The solid lines through the transients for α -NpOH•(NH₃)_{n=3,4} are numerical fits to the data depicting a fast decay of 100 ± 30 ps.
- Figure 6. Pump-probe transients obtained for the clusters α -NpOH•(C₅H₁₁N)_{n=1-3}. Details for each of the experiments are contained in the text and in Table 1. The solid lines through the transients for α -NpOH•(C₅H₁₁N)_{n=2,3} are numerical fits to the data, depicting a fast decay of 65 ± 10 ps.
- Figure 7. Pump-probe transients obtained for α -NpOH•(H₂O)_{n=1,3,9,13,19} clusters. Details for each of the experiments are contained in the text and in Table 1.
- Figure 8. A schematic view of the potential energy surfaces involved in the proton-transfer reactions of α -NpOH(NH₃)_n.
- Figure 9. Calculated time dependence of α -NpOH(NH₃)_n and α -(NpO⁻)[H⁺(NH₃)_n] over the period of the pump-probe transients for $n = 3,4$. Rate constants correspond to the three-state model depicted on page 202. It is assumed that the IVR rate is much faster than all other rate constants. The decays are calculated for reverse proton-transfer rate constants (k_{ba}) equaling 1×10^7 , 1×10^8 , 1×10^9 , 5×10^9 , 1×10^{10} , 5×10^{10} , and 1×10^{11} sec. Additional parameters are the lifetimes of 100 ps for the forward proton-transfer rate (k_{ab}), 60 ns for the decay from the initial excited state back to the ground state (k_{ag}), and 40 ns for the decay of the equilibrated system to the ground state (k_{bg}). The decays correspond to increasing reverse proton-transfer rate constants from top to bottom for the α -(NpO⁻)[H⁺(NH₃)_n] curves, and from bottom to top for the α -NpOH(NH₃)_n curves.

Molecular Beam Apparatus Schematic. Top View.

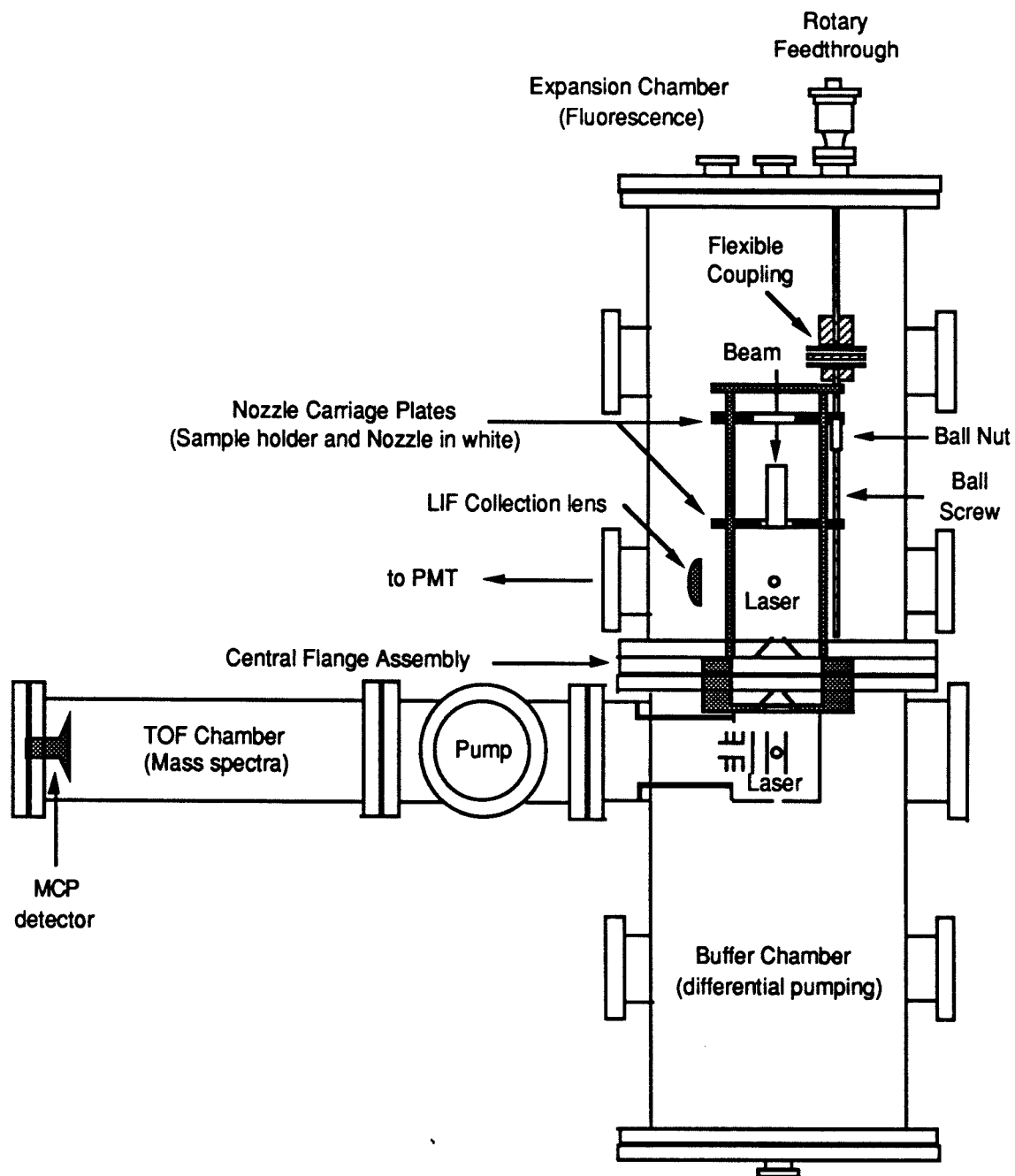


Figure 1

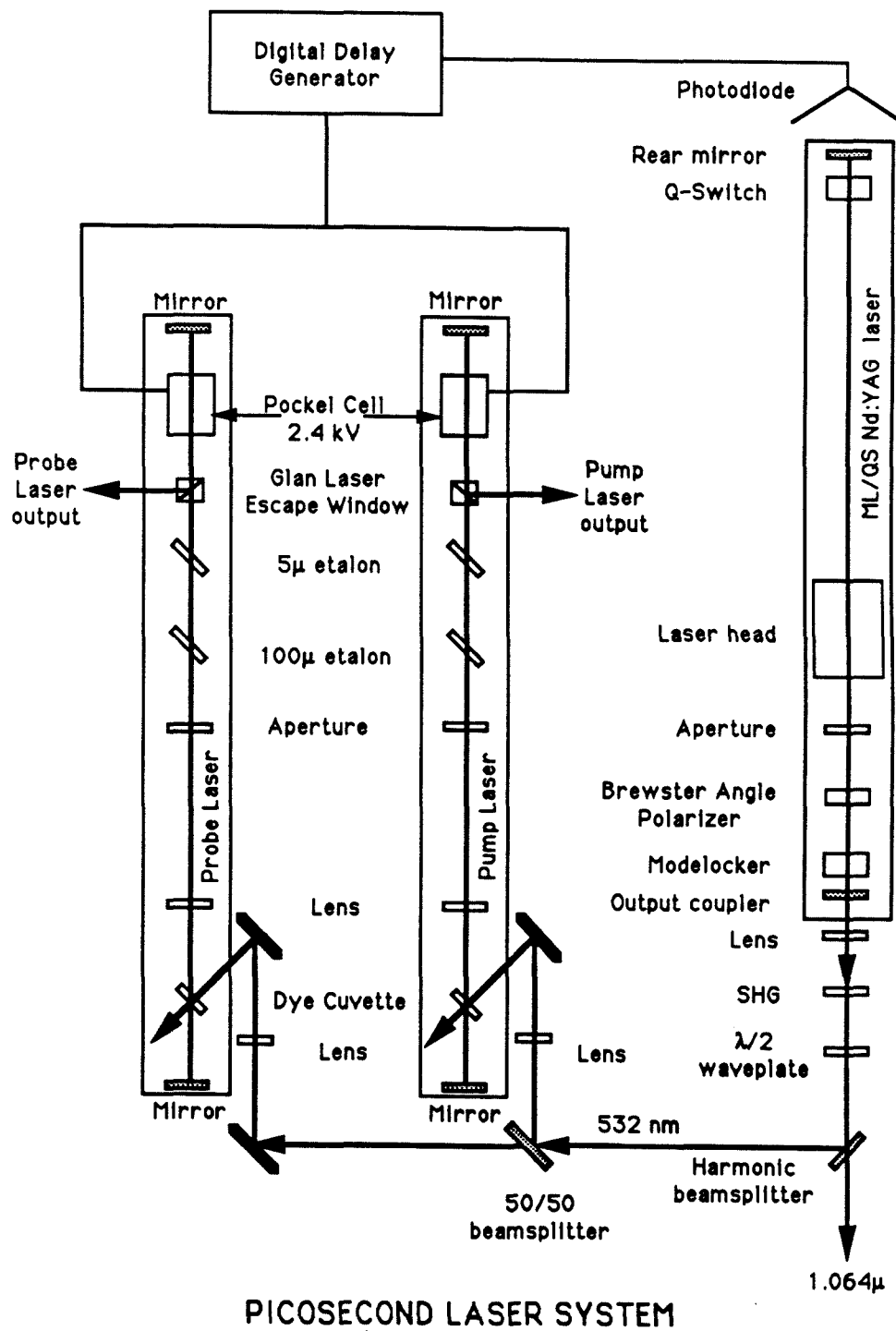


Figure 2

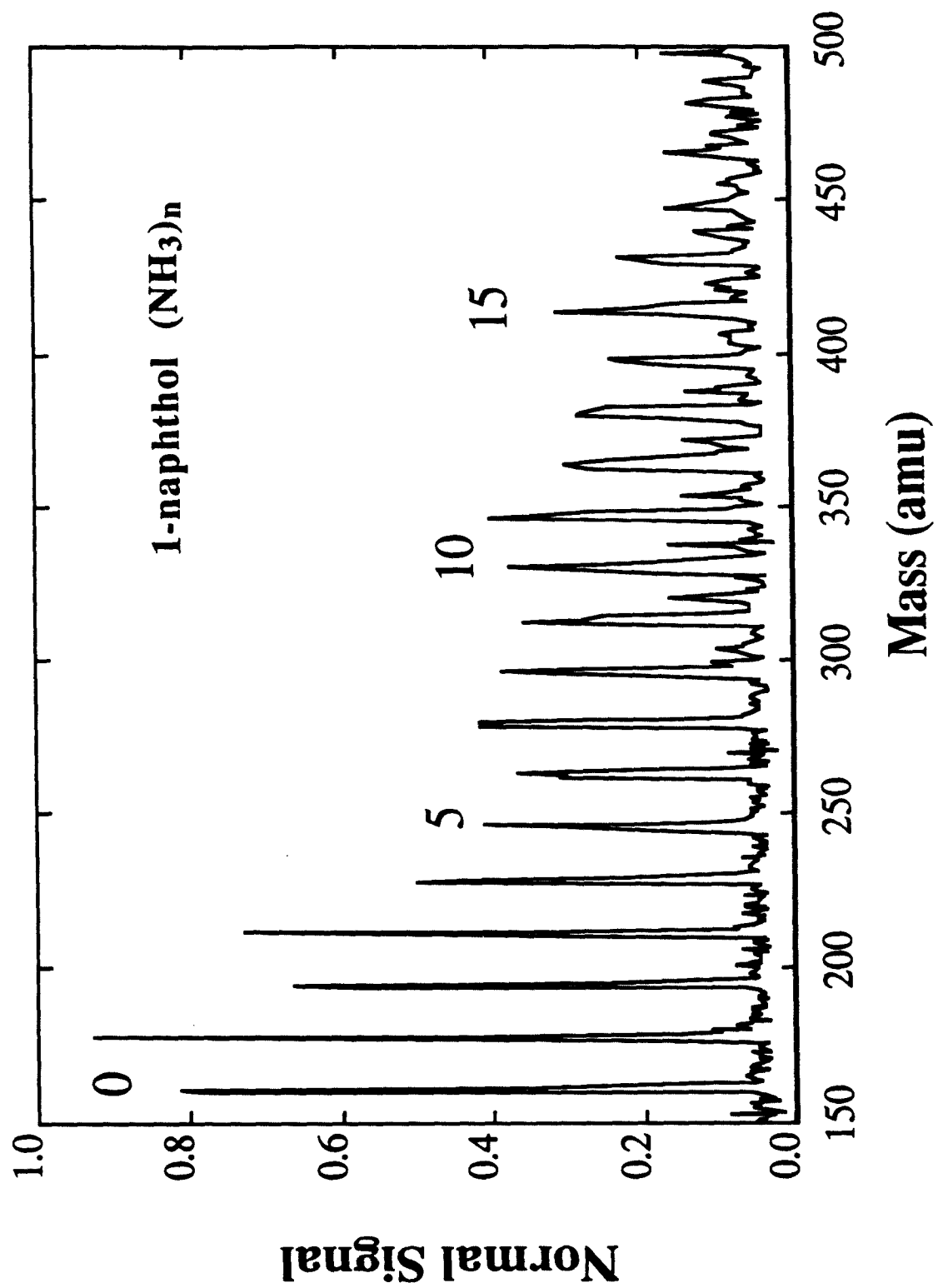


Figure 3

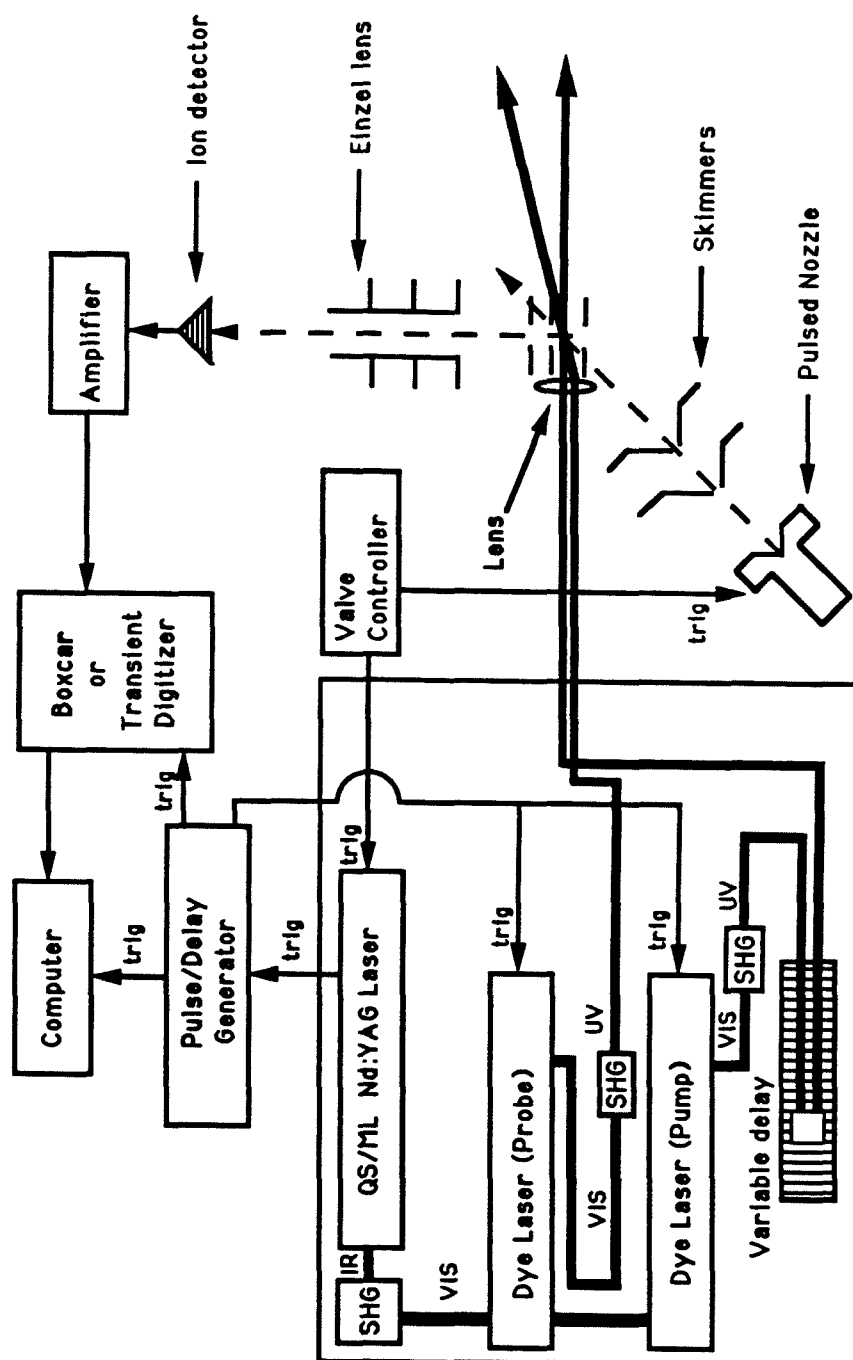


Figure 4

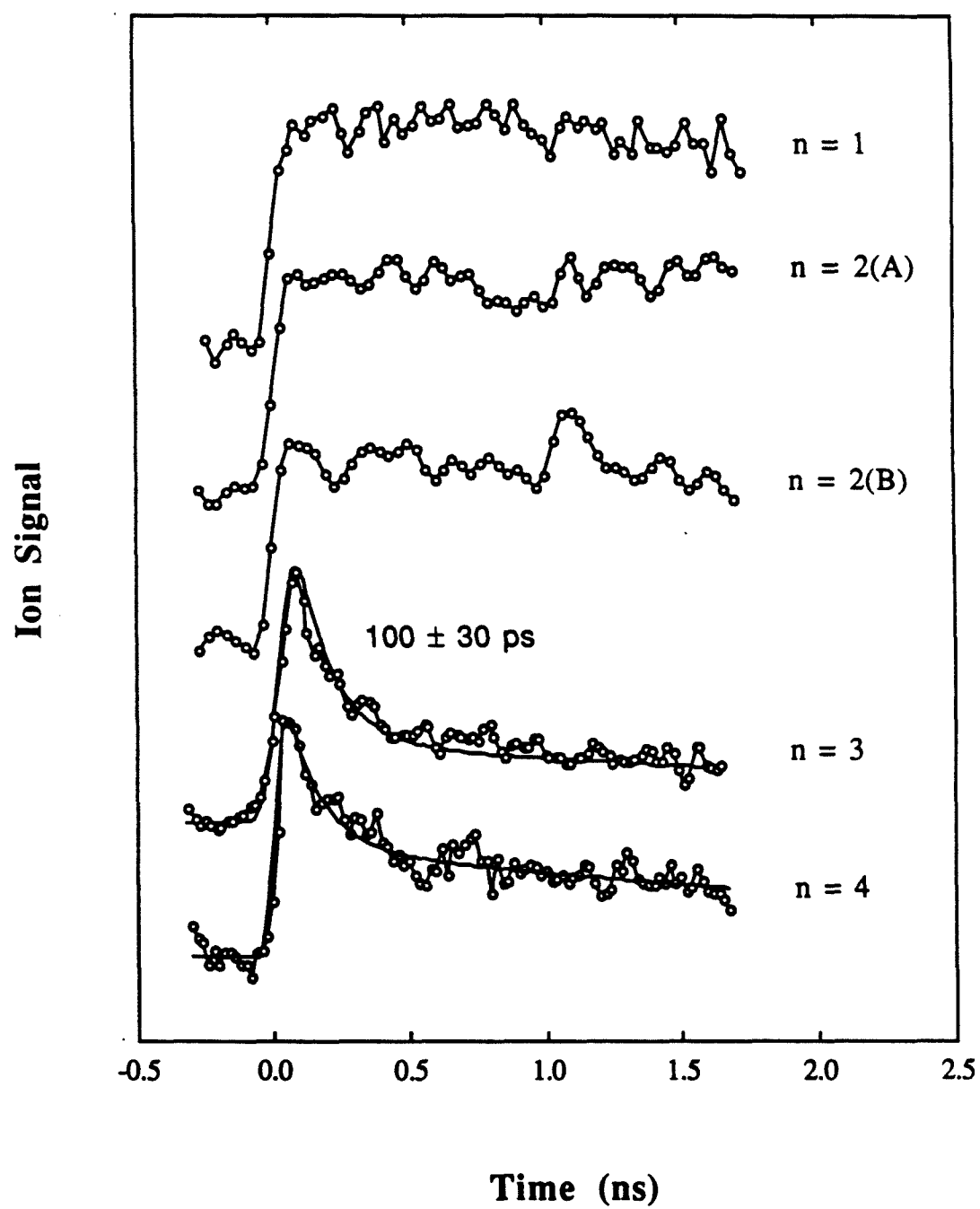


Figure 5

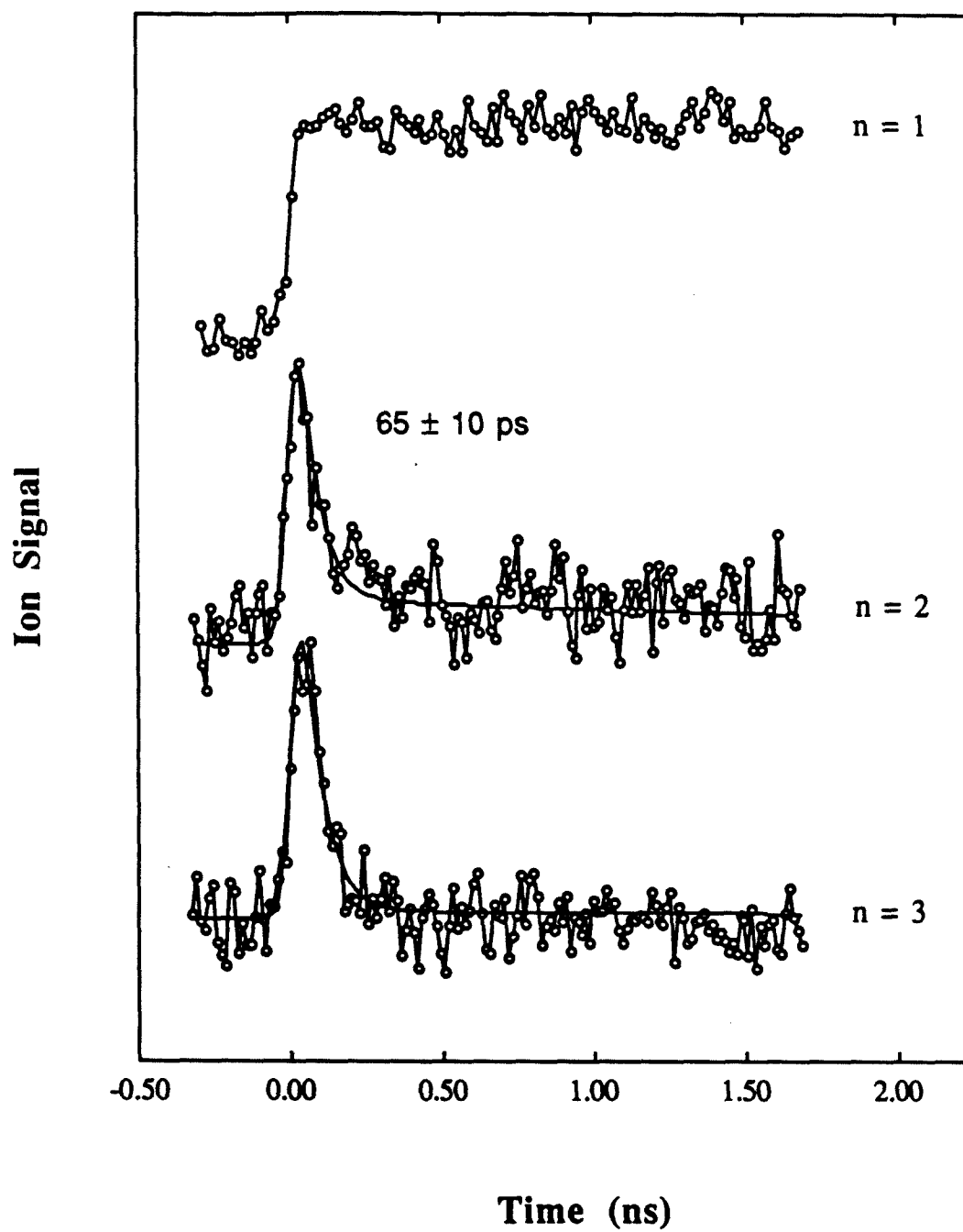


Figure 6

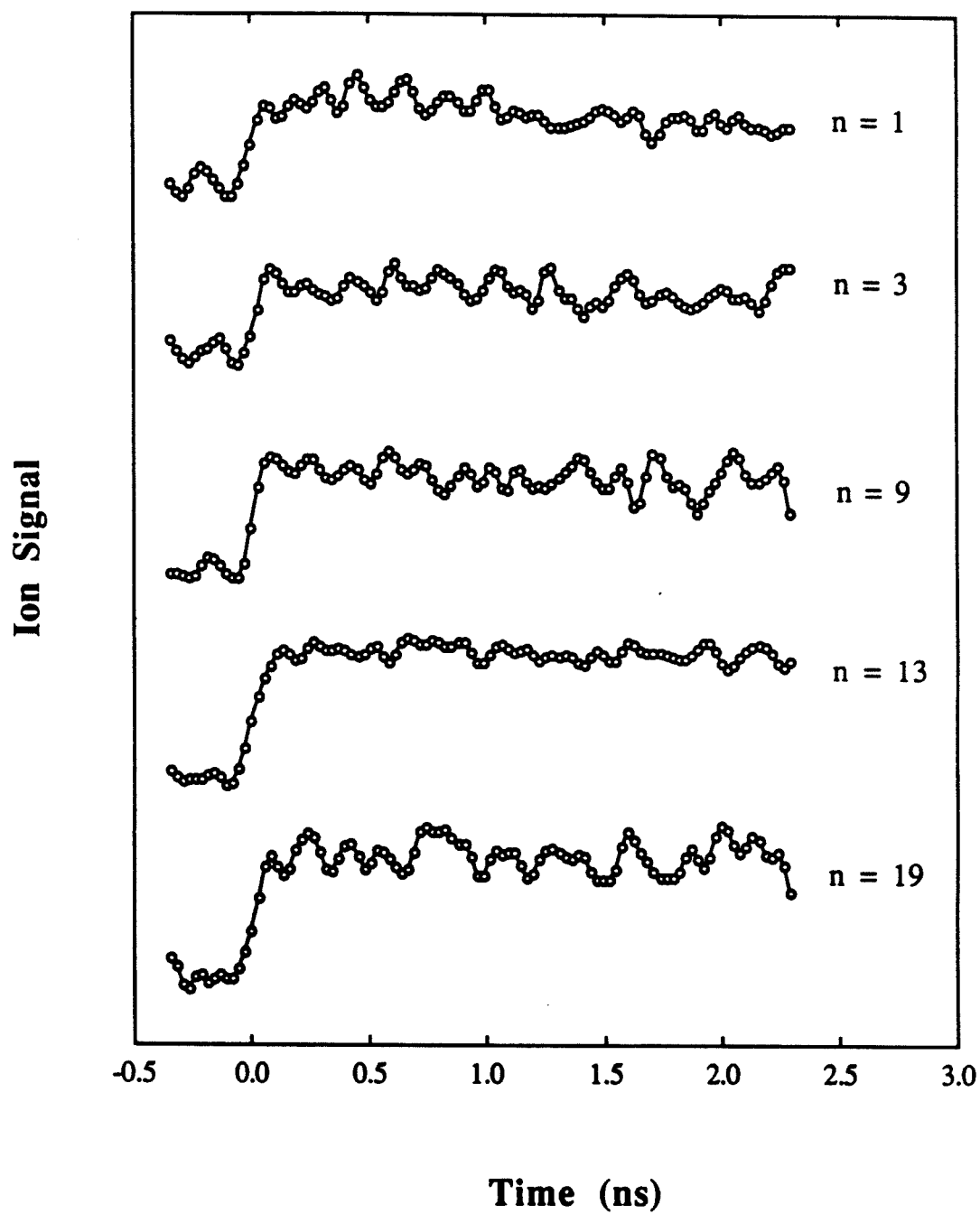


Figure 7

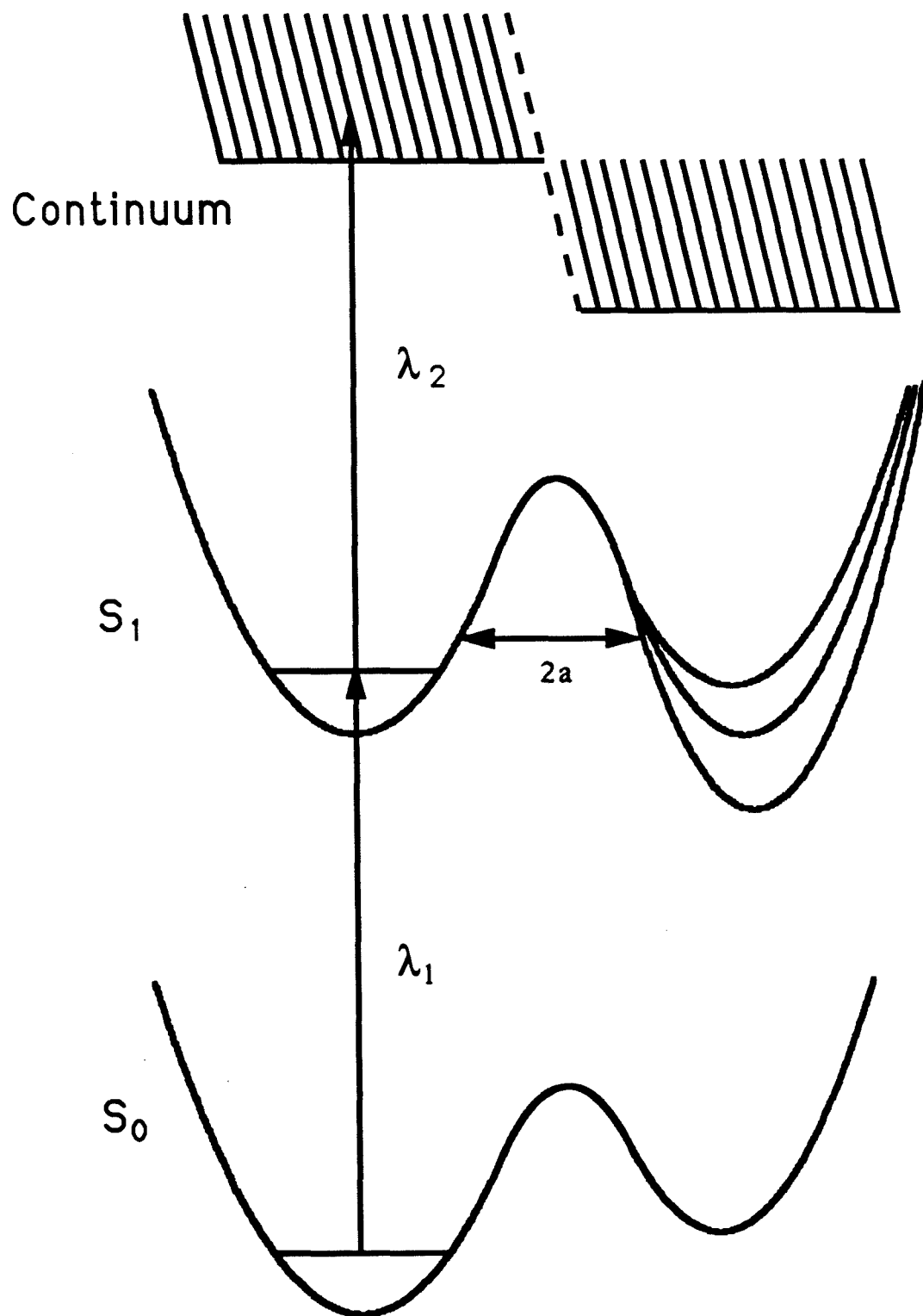


Figure 8

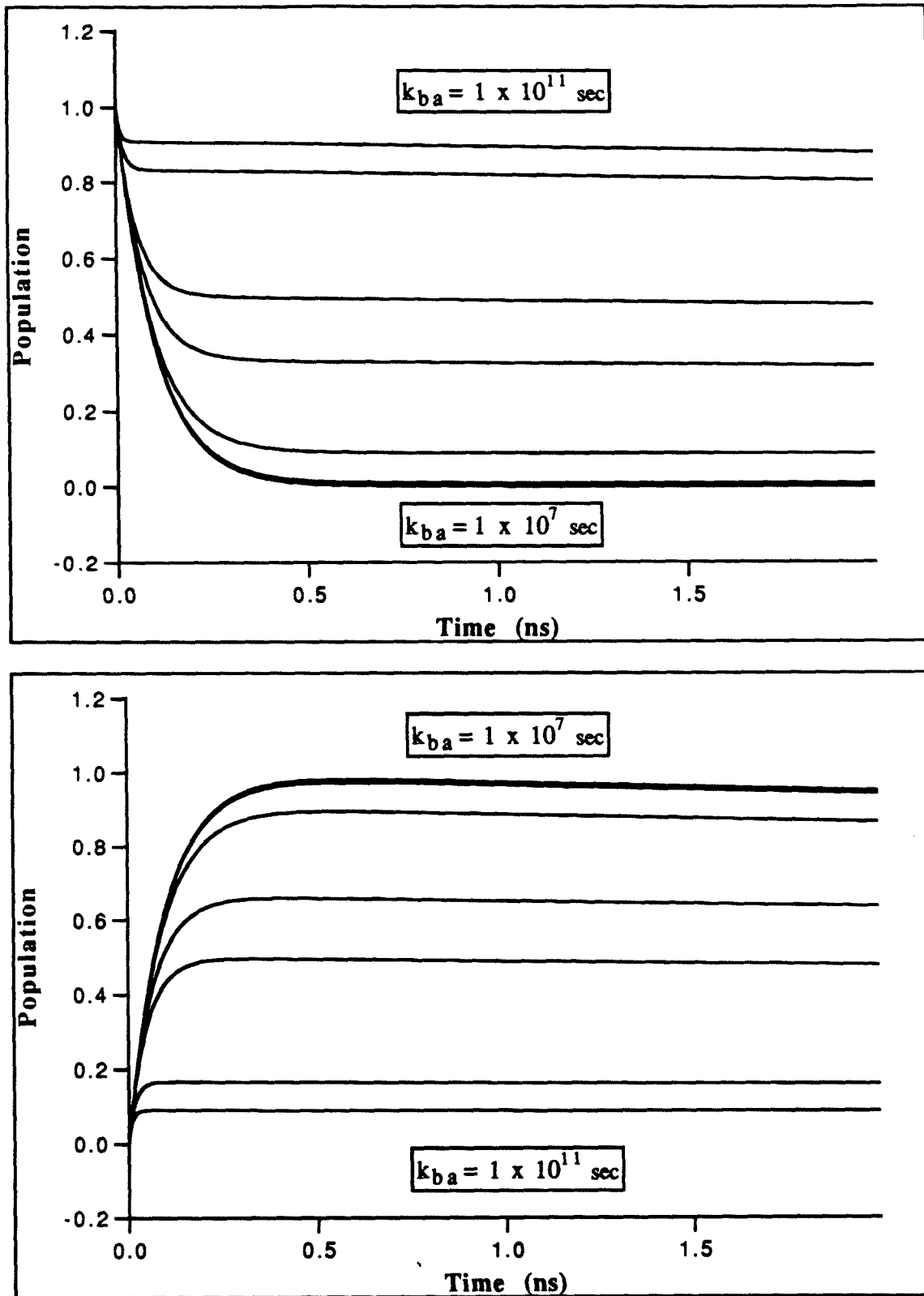


Figure 9

CHAPTER 7

SUMMARY AND CONCLUSIONS

The separation of charges is one of the more pervasive processes in nature. In this thesis, the molecules p-(Dimethylamino)benzonitrile (DMABN) and α -naphthol (α -NpOH) have been used as model systems for studying the charge-transfer process. The molecules were studied in neutral molecular clusters composed of the molecule plus some number of solvent molecules. Molecular clusters, defined as chemical species held together by forces weaker than the average chemical bond, provide an environment to study the solvation process as a function of specific solvent-cluster size. Being larger than ordinary molecules but smaller than bulk objects, clusters represent a state of matter that is intermediate between molecules and the condensed phase. Therefore, the use of clusters offers the opportunity to investigate solvation effects on the reaction dynamics of a system as it evolves from the gas phase to the condensed phase. The extent of solvation is often critical since reaction intermediates and products can be stabilized by the solvent, or react with the solvent itself. In solution, the charge-transfer behavior of DMABN and α -NpOH is dependent on the nature of the solvent.

Electronic absorption and emission spectra studies of size-selected clusters have shown that the major effects of solvent clusters on the solute electronic absorption spectra are to shift the peak locations, to broaden the width of the bands, and to change the band shapes. The changes may be very specific and highly dependent on cluster size. Furthermore, the trends in the band shifts, bandwidths, and band shapes can be very nonmonotonic. However, these experiments were sensitive only to the equilibria between reactant and product. Since inhomogeneous broadening of the linewidths occurs in clusters, temporal resolution is essential for measuring and understanding the dynamics that occurs in these clusters.

Given this motivation, a new apparatus for making real-time measurements of large neutral clusters was constructed. It consists of a molecular beam interrogated by two picosecond lasers, accompanied by fluorescence and ion detection. The size of the solvent-

solute system is selected by adjusting the molecular beam conditions. This opens the possibility for studying the role of solvation on the physical, chemical, and dynamical behavior of the system from the solvent-solute van der Waals complex to the solution bulk limit. Two types of experiments for studying the dynamics of clusters may be performed with the apparatus: laser-induced fluorescence (LIF) and resonance-enhanced multi-photon ionization (REMPI). REMPI has an advantage over LIF in being more species-specific, and is able to resolve species with overlapping absorption spectra. Additionally, electron-impact (EI) ionization is available for characterizing the cluster beam. The combination of the laser and molecular beam allows for investigation of the effect of solvent on the excited electronic state dynamics of the solute molecule for a specific cluster size.

The DMABN molecule presents a case where the charge-transfer (electron-transfer) is intramolecular. The solvent may stabilize the twisted internal-charge-transfer (TICT) state, but is not a direct participant in the charge-transfer reaction. The experimental data indicate that in a thermalized vapor self-complexes of DMABN (dimer or n-mer) can undergo an excited-state isomerization, given the observed visible emission characteristic of this polar state. Self-complexes were also formed in the beam, as evidenced by a red-shift in the neutral form emission, but charge-transfer was not observed. This reflects the differences in the internal temperature and/or size of the self-complexes formed in the jet versus those formed in the vapor. In contrast, the beam studies reveal that the isolated molecule and the 1:1 complex with water, methanol, acetonitrile, or ammonia do not undergo a charge-transfer isomerization. These results can be understood in terms of the argument that a sufficiently polar solvent molecule or molecules are required before excited-state charge-transfer and structural twist can occur. One solvent molecule is insufficient to stabilize the charge-separated form.

The influence of the solvent on the formation of the TICT state is also of interest. In the molecular beam, the solvent configuration about the solute is frozen out. However,

it is not clear what effect, if any, freezing the solvent configuration has since liquid-state studies suggest that solvent dielectric relaxation does not control TICT state formation. Also of importance is the possible role of specific interactions between the solute and solvent. In protic solutions, hydrogen bonding is thought to oppose the charge transfer in DMABN by withdrawing electron density from the amino nitrogen. In order to make any statements about the effects of hydrogen bonding on the dynamics of CT formation, the geometry of the DMABN-solvent complex must be determined.

A further complication in the DMABN experiments is that they were done before the apparatus possessed mass resolution capability. This makes it impossible to evaluate the size distribution of the self-complexes in the molecular beam or in the vapor. In addition, this prevented the study of solute-solvent complexes larger than a 1:1 complex in the molecular beam experiments. For the molecular beam, conditions were set to optimize the 1:1 solute-solvent complex while keeping the signal response linear with respect to solvent vapor pressure. This minimizes possible interferences from larger clusters.

The intracuster proton transfer between α -NpOH and surrounding solvent molecules is an example of a reaction directly involving the solvent. The radical change in its acidity upon optical excitation to the first excited singlet electronic state makes it useful to investigate the dynamics of proton transfer and of chemical reaction induced by a rapid pH jump. The investigation of the clusters α -NpOH with ammonia, piperidine and water indicate the occurrence of the proton-transfer on the picosecond timescale in the clusters α -NpOH \cdot (NH₃)_{n=3,4} and α -NpOH \cdot (C₅H₁₁N)_{n=2,3}. The measured rates of 100 \pm 30 ps for the ammonia clusters and 65 \pm 10 ps for the clusters with piperidine compare well with proton-transfer studies of other gas-phase clusters: phenol with ammonia, matrix-isolated clusters, α -naphthol with ammonia and α - and β -naphthol in aqueous media. A significant difference between this time-resolved work and previous time-integrated spectroscopy work concerns the threshold size for the α -NpOH \cdot (NH₃)_n system. In the frequency

domain, the threshold for the appearance of a broad excitation spectrum and a large Stokes shifted emission is the cluster $\alpha\text{-NpOH}\cdot(\text{NH}_3)_4$. In the time-resolved measurements this threshold is the cluster $\alpha\text{-NpOH}\cdot(\text{NH}_3)_3$. In the case of water, no proton transfer was observed for up to $n=21$. The cluster-size thresholds have been rationalized in terms of a threshold proton affinity of the solvent. The proton affinity of the solvent must be larger than the acid dissociation energy, which implies that the reaction is exothermic. In the case of water, over 30 solvent molecules are believed to be required before proton-transfer can occur.

It is thought that clusters will serve as finite, microscopic models of the condensed phase. Studies of their properties will shed light on the microscopic events that occur in bulk systems. However, on the basis of the behavior of $\alpha\text{-NpOH}$, it seems that the extrapolation of properties from the isolated molecule to the condensed phase is not direct. There appears to be a critical number, below which cluster behavior is discrete and cluster size dependent, and above which there is an asymptotic approach to the bulk behavior.

Measurement of other relaxation rates in clusters would be a feasible experiment to help understand the effects of the solvent on the reaction at a microscopic level. Of particular interest is the influence of the solvent on intramolecular vibrational energy redistribution (IVR). The upper limit on the amount of excess vibrational energy that can be deposited in a cluster is limited by fragmentation. In the DMABN experiments, charge-transfer was found for the vapor cell self-complexes under certain excitation conditions. It would be of interest to investigate the excess vibrational energy dependence of these self-complexes, as well as of higher order DMABN-solvent clusters. Such studies might identify the differences between the clusters formed by the molecular beam and the vapor cell, and explain why charge-transfer fluorescence is observed in one case but not the other. In the $\alpha\text{-NpOH}$ experiments, excitation was conducted with essentially no excess vibrational energy. Work in matrices suggests that the reaction rate is governed by

tunneling through a barrier, rather than being an activated process. Qualitative calculations indicate that the reaction barrier is not too large, so that deuteration or excess vibrational energy might have a profound influence on the measured reaction rate. Studies of the excess vibrational energy dependence of the proton-transfer rate in α -NpOH clusters, as well as in different alcohol/solvent systems, may shed insights into understanding how the rates are influenced by the alcohol/solvent energetics. Furthermore, such experiments may further reveal the nature of the barrier and its sensitivity to the local solvent environment.

In conclusion, time-resolved picosecond studies hold great promise for studying complex reaction mechanisms in size-specific neutral clusters. The proton-transfer reaction of α -NpOH in various basic solvent clusters is indicative of the size-dependent phenomena which time-resolved pump-probe spectroscopy is capable of monitoring directly. Future application to other cluster systems may provide insights into condensed-phase solvent dynamics and the role of the solvent in reaction dynamics. Relaxation processes such as intramolecular vibrational energy redistribution (IVR) can be characterized as the number of solvent molecules becomes very large. Although the techniques are now well established for studying stepwise solvation, the work reported here shows that picosecond measurements of rapid intra- and intermolecular photochemistry in clusters offer a new domain for studying the molecular basis of solvation in molecular systems.

APPENDIX

DYNAMICS OF INTRAMOLECULAR VIBRATIONAL ENERGY REDISTRIBUTION IN DEUTERIATED ANTHRACENES: ROTATIONAL BAND CONTOUR ANALYSIS AND TIME-RESOLVED MEASUREMENTS

This appendix was previously published as:
L.W. Peng, B.W. Keelan, D.H. Semmes, and A.H. Zewail, "Dynamics of Intramolecular
Vibrational Energy Redistribution in Deuteriated Anthracenes: Rotational Band Contour
Analysis and Time-Resolved Measurements,"
Journal of Physical Chemistry, **92**, 5540-5549 (1988).

ABSTRACT

The nature of intramolecular vibrational energy redistribution (IVR) in jet-cooled anthracene-9-d₁ and anthracene-d₁₀ has been investigated in both the frequency and time domains. Comparison with anthracene-h₁₀ is made, with particular emphasis on the role of vibrational density of states and molecular symmetry. The general regions of IVR (nonexistent, restrictive, and dissipative) have been identified, as in anthracene-h₁₀, in all molecules studied.

I. INTRODUCTION:

In a recent series of papers from this laboratory [1,2], the dynamics of intramolecular vibrational energy redistribution (IVR) was investigated in jet-cooled anthracene- h_{10} and trans-stilbene. This was accomplished by spectrally and temporally resolving the fluorescence as a function of excess vibrational energy. From the spectral data [2] for anthracene- h_{10} , it was possible to assign the vibrational symmetries (a_g or b_{1g}) of levels below 1100 cm^{-1} and other higher energy levels. In addition, the distinctiveness of the P-(Q)-R structure of the contours served as a basis for evaluating the spectral purity of levels, i.e., whether a level had major contributions from one (spectrally pure) or more than one (spectrally impure) vibronic state. The temporal data [1] revealed the dynamic nature of the redistribution as a function of excess energy. Single-exponential, quantum beats, and biexponential fluorescence decays have been measured for both anthracene- h_{10} and trans-stilbene. The relationship of the decays to the nature of dynamic IVR (nonexistent to restrictive to dissipative with increasing vibrational energy) has been discussed in detail [1,3,4]. Single-exponential decays indicate the absence of dynamic IVR in the excited single vibronic level (SVL), while quantum beats are the result of IVR among a few vibrational levels. Biexponential decays indicate dissipative IVR among approximately 10 or more levels [5].

In an attempt to generalize these findings to deuteriated analogues and to understand the effect of chemical structure of IVR, we have undertaken studies of IVR in partially and fully deuteriated anthracenes. In this paper we will focus on the simplest aspects of molecular symmetry and vibrational-state density. These effects on IVR can be potentially investigated by spectrally and temporally studying the fluorescence as a function of excess vibrational energy in two of anthracene's isotopes: anthracene-9- d_1 (point-group symmetry C_{2v}) and anthracene- d_{10} (point-group symmetry D_{2h}). The fluorescence excitation spectra, dispersed fluorescence spectra, and temporal data for the three anthracene isotopes are

compared. From these data, the vibrational assignments and purity and IVR dynamics are presented. An exhaustive rotational band contour analysis of 65 levels in anthracene-9-d₁ and 71 levels in anthracene-d₁₀ is made, and the results are compared with 61 levels in anthracene-h₁₀.

II. EXPERIMENTAL SECTION

To study the IVR in the two anthracene isotopes, we measured the frequency- and time-resolved fluorescence intensity from many single vibronic levels observed in their excitation spectra. Two sets of laser/supersonic jet apparatus were used for this study. The experimental arrangements are the same as for most of the earlier work done on anthracene-h₁₀.

The spectroscopy of the deuteriated anthracenes was obtained by using a Nd:YAG pumped pulsed dye laser system (10 Hz, 5-ns pulse width), with the dye laser output frequency-doubled by a KDP crystal to produce UV light. The dyes used in this study were 25% normal concentration LDS 750 in normal concentration methanolic LDS 698 (lower energies) and normal concentration ethanolic LDS 698 (higher energies). Spectra were taken with the sample temperature held at 443K with 50 psi of carrier gas (nitrogen or neon) backing pressure. Optimal cooling was achieved at a laser-to-nozzle distance of 10 mm, with the nozzle diameter being 0.5 mm. When the emission was not resolved with the monochromator, it was passed through a UV band-pass filter (Schott UG-11 filter) to remove stray visible light and through a cutoff filter (Schott GG-395 filter) to remove scattered laser light. Pressure tuning was done with nitrogen, which gives a full-scan range of 20 cm⁻¹ at 360 nm. The pulsed dye laser was frequency-calibrated by using an iron-neon lamp and the optogalvanic method [7]. Vibrational frequencies are reproducible to ± 1 cm⁻¹ below 1000 cm⁻¹ and ± 2 cm⁻¹ above 1000 cm⁻¹.

Temporal data were obtained by using a modelocked, synchronously pumped, cavity-dumped dye laser. The red dye laser output was doubled with a lithium iodate second-harmonic generation crystal producing nanojoule pulses in the ultraviolet (UV) region of a 15-ps duration. Dispersed fluorescence spectra were recorded by using a three-plate birefringent filter as a tuning element, which gives a 5 cm^{-1} bandwidth in the UV output. Temporal decays of dispersed fluorescence were recorded with an etalon as an additional tuning element to narrow the laser bandwidth to 2 cm^{-1} . These near-ultraviolet laser beam pulses illuminated molecules in a free-jet molecular beam expansion that was produced by expanding 30 psi of helium over the isotope of anthracene in a reservoir held at 438K (about 5 torr of vapor pressure) and expanded through a 70 micron pinhole. Fluorescence was dispersed by a 0.5m monochromator and collected by one of three photomultiplier tubes (PMT's), depending on the relative importance of a short system response time and absolute sensitivity. Dispersed fluorescence spectra were recorded with a 1.6Å resolution by counting the pulses from an Amperex XP2020Q photomultiplier tube with a multichannel analyzer. Temporal decays of spectrally resolved emission were recorded by using time-correlated single-photon-counting electronics and either a Hamamatsu R1564U or a Hamamatsu R2287U-01 multichannel plate photomultiplier tube. The system response function was measured after each decay by detecting scattered laser light when the molecular beam nozzle was moved in the laser beam and typically had a full width at half maximum (FWHM) of 80 ps. The measured decays were deconvoluted from the system response function and fit to a single exponential, were Fourier analyzed to obtain quantum beat frequencies, or were deconvoluted from the system response function and fit to a double-exponential decay depending on the nature of the decay. Data were stored and analyzed with a PDP 11/23 computer. The monochromator was calibrated by recording the spectrum of a hollow cathode iron-neon lamp under normal experimental conditions.

Anthracene- h_{10} (Aldrich 99.9+%) and anthracene- d_{10} (Aldrich 98+%) were used without further purification. Anthracene-9- d_1 was synthesized from 9-bromoanthracene (Aldrich 98%) by lithiation with *n*-butyllithium followed by hydrolysis in D_2O [8]. Following recrystallization in benzene, the purity of the product was found to be >99% chemically by gas chromatography and >95% isotopically by mass spectrometry (the balance being anthracene- h_{10}). The excitation spectrum of anthracene-9- d_1 showed minor anthracene- h_{10} impurity lines; these were readily identified by absolute frequency and relative intensity.

III. VIBRATIONAL-STATE DENSITIES

A. Anthracene- h_{10} .

Vibrational-state densities were calculated between 0 and 2000 cm^{-1} by using the direct-counting computer program reported in the paper by Khundkar et al. [9]. Vibrational frequencies for the normal modes of the ground electronic state were taken from the valence-field calculations of Cyvin and Cyvin [10] for the in-plane vibrations and from the calculations of Evans and Scully [11] for the out-of-plane vibrational frequencies. The force fields used in these calculations were based on infrared absorption frequencies and a force field transferred from benzene, respectively. All of these calculated frequencies are close to the experimentally determined values [12,13] for both the in-plane and out-of-plane vibrational frequencies.

In the excited state, however, there is a dearth of information on the values of the vibrational frequencies. From spectroscopic experiments on isolated molecules in a molecular beam, 15 vibrational frequencies are known in both the ground and the first excited singlet electronic states, all for in-plane modes [3]. Vibrational frequencies have not been calculated for the excited-state force field. The only quantitative indication of how the vibrational frequencies and therefore the density of vibrational states change for

anthracene- h_{10} when it is excited into the first singlet from ground singlet comes from data on benzene, where there is good agreement between calculated and measured vibrational frequencies for almost all the vibrational modes in the ground and excited electronic states [14,15].

Our approximate calculations for the vibrational-state densities of the three isotopes in the first excited singlet are based on the valence field normal frequencies for the ground singlet [10,11]. The difference between values for S_0 and S_1 are roughly accounted for by considering data for benzene. Benzene's in-plane vibrational frequencies are 4% lower in S_1 than in S_0 on the average (known S_1 anthracene in-plane vibrational frequencies are 6% lower than the average in S_0), and out-of-plane vibrational frequencies are 32% lower on the average. To calculate the vibrational-state density for anthracene in the excited singlet, we therefore made the approximation that the average difference between the in-plane and out-of-plane vibrational frequencies in the ground and first excited singlet of anthracene is the same as the average difference for benzene, 4% for in-plane and 32% for out-of-plane vibrations.

The approximate S_1 vibrational frequencies for anthracene calculated by using this benzene-like approximation were used with the computer algorithm mentioned to directly count the number and density of vibrational levels at various energies of interest. To estimate the uncertainty in this approximation, we repeated the calculation with the out-of-plane frequencies decreased by 5% more and 5% less than the average in benzene. The results are listed in Table I and plotted in Figure 1.

B. State Densities of the Isotopes.

A detailed normal-coordinate calculation of the S_0 anthracene- d_{10} frequencies is given in the literature [10,11]. The vibrational density of states (labeled as curve B for anthracene- d_{10} in Figure 2) is then calculated in the same manner as is done for

anthracene- h_{10} . Curve A for anthracene- d_{10} is an approximate calculation based on the well-known Teller-Redlich rule for isotopic substitution [16]. Similarly, the vibrational frequencies for anthracene-9- d_1 in S_1 were calculated by using the Teller-Redlich rule and the approximate S_1 anthracene- h_{10} frequencies. The Teller-Redlich rule, in the harmonic oscillator limit, relates products of vibrational frequencies for an unsubstituted molecule to those of the substituted molecule for each symmetry species of the lower symmetry point group (only C_{2v} in the case of anthracene-9- d_1). For use of the equation to calculate explicitly the frequencies for the substituted molecule, an approximation must be made relating each of the frequencies in each symmetry class to the anthracene- h_{10} frequencies of that class. Since it is impossible to estimate frequency changes for specific vibrations without a more involved normal-coordinate analysis, it is assumed that all frequencies change by the same factor or, equivalently, that the ratios of vibrational frequencies of the same symmetry species are the same for the two isotopically related molecules [17]. Again, the direct-counting computer algorithm was used to calculate state densities from these vibrational frequencies. The results are listed in Table I and plotted in Figure 2 [18].

IV. RESULTS AND DISCUSSION

A. Fluorescence Excitation Spectra.

Although the power-normalized S_1 fluorescence-excitation spectra of anthracene-9- d_1 (point-group symmetry C_{2v}) and anthracene- d_{10} (point-group symmetry D_{2h}) in supersonic beams have been reported previously [19], these spectra were not analyzed in any great detail.

The S_1 fluorescence excitation spectra of anthracene-9- d_1 and anthracene- d_{10} are compared with that of anthracene- h_{10} in Figure 3. Each spectrum is plotted against vibrational (excess) energy, i.e., energy above the electronic origin. By obtaining the spectrum of a mixture of all three analogues, we determined the relative positions of the

anthracene-9-d₁ and anthracene-d₁₀ origins to be 12 and 71 cm⁻¹, respectively, to the blue of the anthracene-h₁₀ origin (27695 cm⁻¹) [19]. Origin blue-shifts upon deuteration are expected since excited-state vibrational frequencies are usually lower than ground-state frequencies and so have smaller absolute deuterium (zero-point) shifts.

The vibrational energies (cm⁻¹) and relative intensities (origin = 100%) of the more intense levels in each isotopic species are listed in Table II. The intensities above which the table is complete for each species are as follows: anthracene-h₁₀, 0.05%; anthracene-9-d₁, 0.1%; anthracene-d₁₀, 1%. Analogous levels in the different isotopic species are placed on the same line of the table. The assignments involved many points (and sometimes speculations), and the criteria used for the assignments have been detailed in Reference 20.

It is shown in section IV.D that the a_g and b_{1g} modes can be easily distinguished by contour shapes. The small number of non-totally symmetric modes simplified the determination of analogous bands and thus provided a check on the isotopic shifts and intensity changes of nearby symmetric levels. Levels of different isotopes were not considered analogous and placed on the same line of Table II unless this assignment was consistent with most or all of the different criteria.

The excitation spectra of these three analogues are qualitatively very similar, but they differ quantitatively in the variation of average intensity with vibrational energy. In anthracene-h₁₀, the intensity of levels drops precipitously with increasing vibrational energy: e.g., the strongest level in the C-C stretching region (1380 cm⁻¹) is only ~1.4% as strong as the origin. The average level intensity drops off less rapidly in anthracene-9-d₁; the strongest C-C stretch at 1409 cm⁻¹ is ~5.3% as intense as the origin. In anthracene-d₁₀, average intensity decreases slowly with E_{vib}; the 1382 cm⁻¹ C-C stretch is ~40.8% as strong as the origin. The trend is especially clear when one considers the multipliers in Figure 3 (1, 10, 100 in anthracene-h₁₀; 1, 10, 20 in anthracene-9-d₁; 1, 1, 3 in anthracene-d₁₀). In an electronic transition involving little geometry change, most of the intensity is

concentrated in the origin. It would thus appear that vibronic activity plays an important role [14,15].

One other difference was noted in the excitation behavior of the three analogues: While anthracene- h_{10} was efficiently vibrationally cooled by neon carrier gas (the spectrum in Figure 3 was obtained with 50 psi of neon), anthracene-9- d_1 and anthracene- d_{10} showed slight and severe apparent sequence congestion, respectively, in neon. Both deuteriated anthracenes cooled well in 50 psi of nitrogen (see Figure 3). The origin of this difference in cooling behavior between the isotopic analogues is not clear.

B. Dispersed Fluorescence Spectra.

The dispersed fluorescence spectra of some of the SVLs investigated are presented in Figure 4 for anthracene- h_{10} and for the two deuteriated isotopes studied. As was observed in the earlier studies of anthracene- h_{10} , the spectra from the deuteriated isotopes fall into three general categories of description: (1) Assignable, sharp spectra are observed at "low" excitation energies. (2) Slightly broadened spectra that still have some sharp, resolvable structure are observed at "intermediate" excitation energies. Some of this sharp structure is assignable as originating from the initially excited level and some is not. (3) Broad, unresolvable spectra with very little resonance fluorescence are observed at "high" excitation energies. It must be noted, however, that there is not necessarily a clear division between the three types of behavior. Additionally, as discussed before [1,2], spectral congestion is not a direct measure of the nature of the dynamic IVR [5].

Table III has explicit spectral assignments for the bands observed in the fluorescence from the levels at $S_1 + 751 \text{ cm}^{-1}$ and $S_1 + 1409 \text{ cm}^{-1}$ in anthracene-9- d_1 , exemplifying how the bands in the spectra from the different energy regions can be assigned.

C. Temporal Behavior.

The temporal behavior of both "relaxed" (where possible) and "unrelaxed" fluorescence bands was recorded from the same SVLs as in Figure 4, as some are presented in Figure 5 for anthracene- h_{10} and anthracene-9- d_1 . Similar results (not shown) were obtained for anthracene- d_{10} . The difference between the single-exponential decays (convoluted with the system response function), the beating decays, and the double-exponential decays of the fluorescence is clear.

The anthracene- h_{10} data in this section have been published previously and are repeated here for the purpose of comparison with data from the deuteriated isotopes.

D. Rotational Band Contour Analysis: Medium Resolution.

At lower vibrational energies ($<1100\text{cm}^{-1}$) in both deuteriated anthracenes, nearly all of the rotational band contours conformed to one of two distinct types. The much commoner contour type, exemplified by the electronic origins, exhibited well-separated P and R branches, but no Q branch, and had FWHM near 3.2 cm^{-1} . The rare contour type (e.g., at 231 cm^{-1} in anthracene-9- d_1) showed a sharp Q branch and was narrower than the prevalent contour type (FWHM of 2.5 cm^{-1}). This situation is identical with that found in anthracene- h_{10} (prevalent contour type, FWHM of 2.3 cm^{-1}) [2]. The two types of contours of each of the three isotopic species are compared in Figure 6 (commoner labeled a_g , rare labeled b_{1g}); the similarity of each contour type for the different analogues is evident. In the previous anthracene- h_{10} study, the prevalent contour type was associated with symmetric (a_g) vibrations, while the rare type was due to antisymmetric (b_{1g}) vibrations. Although the same conclusion can be reached for the deuteriated compounds strictly by analogy, the arguments of the previous study, suitably modified, are given below.

Assuming anthracene to be planar, anthracene-d₁₀ belongs to the point group D_{2h}. The similarity of the contours of anthracene-9-d₁ suggests that it is reasonable to use D_{2h} nomenclature to describe this species, despite the fact that it belongs to point-group C_{2v}. We shall follow this convention in this paper so that the symmetry descriptors are consistent throughout. As C_{2v} is a subgroup of D_{2h}, this does not result in the loss of useful information, and C_{2v} nomenclature can be recovered from the D_{2h} designations. In D_{2h}, the x, y, and z axes transform like B_{3u}, B_{2u}, and B_{1u}, respectively. With the convention $I_x < I_y < I_z$ (so that x is the a rotational axis, y the b, and z the c, where $A > B > C$), the S₁ state is B_{2u} in symmetry.

With lower-case letters to denote vibrational symmetries and capital letter for electronic symmetries, the ground vibronic state (which is the only one appreciably populated in the free jet with nitrogen carrier gas) is |A_ga_g>. Hence one may specify the symmetry of a vibronic transition to S₁ simply by specifying the symmetry of the vibrational level in S₁. An a_g transition will be fully (electric dipole and Franck-Condon) allowed and will be y-polarized, since $\langle B_{2u}a_g | y | A_ga_g \rangle$ does not equal zero. The b_{1g} levels will be vibronically (Herzberg-Teller) allowed by coupling with a B_{3u} state [20,21]. In the following section, our assignment of transition symmetries is supported by computer simulation of contour shapes as a function of transition-moment orientation. Anticipating this, a brief description of higher energy behavior and an explanation of the symmetry assignments in Table II are appropriate. At higher vibrational energies, there is a tendency for contours to be broader and less clearly structured; above approximately 1700 cm⁻¹ virtually no contours are noticeably structured (within our resolution). Such contours are termed "spectrally impure," meaning that more than one vibronic level contributes significantly to the contour (Figure 7).

E. Computer Simulation of Contours.

Computer simulations were generated by a FORTRAN program developed by Schlag's group in Munich [22]. Distortion in S_0 and S_1 was assumed to be negligible. Sufficiently large J values were included in the calculations so that a doubling of the maximum included J value had an insignificant effect on the calculated contour shape (typically $J_{\max} = 30$ was satisfactory). The resolution was taken to be 0.1 cm^{-1} , twice the nominal laser bandwidth-limited resolution of the system, as in the anthracene- h_{10} study.

The rotational constants of the deuteriated anthracenes in S_0 were calculated by using the same structural data [10] as were used in the anthracene- h_{10} study. The results (in cm^{-1}) for anthracene-9- d_1 are $A = 0.06824$, $B = 0.01520$, and $C = 0.01243$; for anthracene- d_{10} , $A = 0.05915$, $B = 0.01385$, and $C = 0.01249$. All three molecules are close to being prolate symmetric tops, with asymmetry parameters, of $\kappa = -0.9007$ (anthracene-9- d_1), -0.8903 (anthracene- d_{10}), -0.9058 (anthracene- h_{10}). All three molecules are close to "case 7" in Ueda and Shimanouchi's study of rotational band contour shapes in asymmetric tops [23], as all are planar (thus $1 - C/A - C/B = 0$, since $C^{-1} = A^{-1} + B^{-1}$), and all have $2C/B$ approximately equal to 1.6 (anthracene-9- d_1 , 1.636; anthracene- d_{10} , 1.620; anthracene- h_{10} , 1.643).

In anthracene-9- d_1 , there are four pairs of equivalent protons that transform similarly. Character analysis [20] yields $\Gamma_{\text{pair}} = 3A + B$ (using C_{2v} rotational subgroup nomenclature), so $\Sigma_{\text{tot}} = (3A + B)^4 = 136A + 120B$. Note that $136 + 120 = 256 = 2^8$, as is expected for eight fermions with two possible spin states each. Anthracene- d_{10} has one set of two and two sets of four deuterons (spin equal to 1 in units of $\hbar/2\pi$). The two sets of four deuterons transform identically, so only one set need be analyzed. Character analysis, analogous to that done for anthracene- h_{10} [20], yields $\Sigma_{\text{tot}} = 15066A + 14580(B_1 + B_3) + 14823B_2$. Note that $15066 + (2 \times 14580) + 14823 = 3^{10}$, as is expected for 10 deuterons with three possible spin states each. The variation in statistical weights in these molecules

can be compared to that found in anthracene- h_{10} ($\Sigma_{tot} = 288A + 240(B_1 + B_3) + 256B_2$) [2].

Two parameters were fit by hand to reproduce the experimental contours: rotational temperature and excited-state rotational constants. As rotational temperature is increased, simulations become broader and the P-R branch gap increases. The dependence is weak, and the temperature can be estimated from previous studies, so fitting to the nearest kelvin (as evaluated the P-R branch gap values) is straightforward. The temperatures in nitrogen carrier gas were found for the two classes of vibrations to be $a_g = 23\text{K}$, $b_{1g} = 23\text{K}$ for anthracene-9- d_1 , and $a_g = 21\text{K}$, $b_{1g} = 26\text{K}$ for anthracene- d_{10} , compared to $a_g = 15\text{K}$, $b_{1g} = 8\text{K}$ for anthracene- h_{10} . This increase in rotational temperatures upon deuteration may be significant as it parallels the poorer vibrational cooling of these compounds in neon, as was discussed in Section IV.A.

Variation of the excited-state rotational constants affects the relative intensities of the P, Q, and R branches. Since rotational constants are not expected to change appreciably upon excitation (they usually decrease slightly because of slightly increased bond lengths), fitting them to the nearest 0.25% is feasible if one assumes that the three constants change by the same amount upon excitation; i.e., $A^*/A = B^*/B = C^*/C$. Although this assumption is not necessarily correct, it greatly simplifies the fitting procedure. The reductions of rotational constants upon excitation to S_1 were found to be 0.5% for anthracene-9- d_1 , and 0.75% for anthracene- d_{10} , compared to 1% for anthracene- h_{10} .

It should be emphasized that neither of the two fitted parameters had a profound influence on the contour shapes of the simulations; e.g., a_g contours always lacked Q branches, while b_{1g} contours always exhibited them. This is important as polarization (symmetry) assignments might otherwise be ambiguous. The agreement of the simulations and experimental contours, depicted in Figures 8 (anthracene-9- d_1) and 9 (anthracene- d_{10}),

provides evidence that the commoner and rarer contour types correspond to a_g and b_{1g} levels in S_1 , respectively.

Simulations of b_{3g} vibrational contours, using the derived average temperature and S_1 rotational constants found above, are very broad, with exceptionally intense Q branches. As in the case of anthracene- h_{10} , no such contours were observed for the deuteriated anthracenes. We conclude that vibronic coupling to B_{1u} states is less important than the observed vibronic coupling to B_{3u} states in the first excited states of the three anthracenes studied.

F. The Restricted IVR Region: An Example.

1. Frequency-Resolved Spectra.

Following excitation to, for example, $S_1 + 1380 \text{ cm}^{-1}$ in anthracene- h_{10} , quantum-beat modulations have been observed in the fluorescence decays under selective detection conditions [1,6,24]. Both the in-phase and out-of-phase beats have been observed at a number of wavelengths. Detection of emission to the $S_0 + 390 \text{ cm}^{-1}$ level results in a distinctively modulated decay (390 cm^{-1} is ν_{12} , a prominent a_g fundamental in the S_1 excitation spectrum). To probe the coupling mechanism responsible for these quantum beats (and hence implicated in the process of restricted vibrational redistribution), we performed the frequency analogues of the temporal experiments [2,6]. The rotational band contour of $S_1 + 1380 \text{ cm}^{-1}$ is normal (i.e., similar to other a_g contours observed in S_1 when emission to the $S_0 + 1460 \text{ cm}^{-1}$ region is detected). In contrast, detection of emission to $S_0 + 390 \text{ cm}^{-1}$ yields a unique contour, which differs from the other a_g contours in having the R branch much more intense than the P branch, in having a greater FWHM, and in having a wider, deeper P-R branch gap. The coupling mechanism in this case could involve Coriolis interactions or special anharmonic forces, as was discussed by us [1,5,6] and by Amirav [25].

In anthracene-9-d₁, the $S_1 + 1409 \text{ cm}^{-1}$ level is suitable for a similar study, since (1) it is an intense, spectrally pure level, exhibiting distinct P-R structure, and (2) two types of quantum beat modulations (in-phase and out-of-phase) are observed in the fluorescence decays under certain detection conditions. Specifically, detection of emission to $S_0 + 390 \text{ cm}^{-1}$ yields in-phase quantum beats that are due to emission from a state that is initially populated by the laser pulse (as in the case of the previously discussed anthracene-h₁₀ quantum beats). In contrast, detection of emission from a state populated indirectly through coupling to a laser-populated state, e.g., emission to $S_0 + 1499 \text{ cm}^{-1}$, yields out-of-phase quantum beats. These two types of quantum beats differ in phase by 180° , since the population oscillates between the states producing the two types of modulation. Total detection of emission (i.e., detection of all emission except that absorbed by a laser cutoff filter) yields a typical single-exponential decay with no (or very weak) quantum-beat modulations.

The frequency analogues of these temporal experiments are depicted in Figure 10. The resolved emission (=dispersed fluorescence) spectrum is shown in the upper half of the figure, trace A. The rotational band contour obtained with total detection is shown in trace B in the lower half of the figure. Detection of emission to the range $S_0 + 390 (\pm 100) \text{ cm}^{-1}$, shown by the interval labeled 1 in trace A, yields the contour in trace C, corresponding to in-phase quantum beats. Contour D, corresponding to out-of-phase quantum beats, was obtained through detection of interval 2 in trace A ($S_0 + 1499 (\pm 25) \text{ cm}^{-1}$). These three contours are somewhat similar in appearance, the differences being within the range of experimental uncertainty (as judged by spectral reproducibility). Certainly there are no dramatic differences in contour shapes as in anthracene-h₁₀ $S_1 + 1380 \text{ cm}^{-1}$. It would therefore appear that anharmonic coupling is responsible for the quantum beats in this system, consistent with the dominant extent of anharmonic coupling in S_1 anthracene-h₁₀ [1,5,6]. However, we cannot rule out completely the presence of

some Coriolis interactions [5,6,25]. It is important to note that even though the spectra are similar, the time-resolved data reflect entirely distinct IVR dynamics [5].

2. Temporal Behavior.

The fact that anthracene- h_{10} excited to $S_1 + 1420\text{ cm}^{-1}$ exhibits restrictive IVR among four levels, while dissipative IVR involving approximately 20 levels is observed at 1792 cm^{-1} , has been justified qualitatively by a calculation of vibrational density of states for the ground singlet electronic state: the density at 1792 cm^{-1} is 5 times the density at 1420 cm^{-1} , which could account for the observation of 5 times the number of coupled levels [1b].

More information is necessary, however, to account for the redistribution more quantitatively. This is apparent when one notes that the actual number of observed coupled levels in anthracene- h_{10} is larger than the calculated ground-state density would suggest. For example, in the excitation of anthracene- h_{10} to $S_1 + 1420\text{ cm}^{-1}$, the molecular symmetry of the observed four coupled levels must be the same if the coupling is anharmonic. Since there are eight symmetry species for D_{2h} anthracene, there must be 32 levels in the energy region that is under investigation. Although our laser bandwidth is 2 cm^{-1} , we can detect beat frequencies only in our temporal measurements of $<10\text{GHz}$. This reasoning leads to a total density of 96 states/cm^{-1} for anthracene- h_{10} , which is far different from the ground-state calculation of 25 states/cm^{-1} . The state density we calculated for S_1 agrees more closely with the number of experimentally observed coupled levels, but is higher than the observed state density (see Table I). At 1420 cm^{-1} the calculated density of a_g states in S_1 is about twice that observed; at 1792 cm^{-1} it is about 4 times that observed (the number of observed coupled levels at 1792 cm^{-1} is a lower limit calculated from the ratio of the amplitudes of the fast and slow components in the biexponential decay of the unrelaxed fluorescence). This comparison of observed and calculated vibrational-state

densities suggests that the number of levels participating in the IVR dynamics in anthracene- h_{10} is approximately equal, within a factor of 2, to the number of levels of the proper symmetry to be anharmonically coupled and that are studied experimentally (i.e., prepared coherently and resolved temporally).

Overall, the observed IVR in anthracene-9- d_1 is similar to the observed IVR in anthracene- h_{10} . There are, however, exceptions. The level at $S_1 + 1173 \text{ cm}^{-1}$ in anthracene-9- d_1 is involved in restricted redistribution, while a level at very nearly the same excess vibrational energy in anthracene- h_{10} ($S_1 + 1168 \text{ cm}^{-1}$) undergoes no dynamic IVR. This difference in the IVR in anthracene-9- d_1 compared to anthracene- h_{10} can be understood in terms of the effects of symmetry reduction by monodeuteration as discussed in the Introduction. By comparing the IVR in anthracene- h_{10} with the IVR in anthracene-9- d_1 that occurs at the energy where the calculated state densities are the same, one is able to compare IVR in the two molecules. This method would circumvent the major uncertainty in all the S_1 vibrational-state density calculations: the uncertainty in all the S_1 vibrational frequencies compared to those of S_0 . For example, no IVR is observed when anthracene- h_{10} is excited to $S_1 + 1168 \text{ cm}^{-1}$ or less (within our time resolution). The calculated vibrational-state density for anthracene- h_{10} at 1168 cm^{-1} in S_1 is 61 cm^{-1} . From Figure 2, anthracene-9- d_1 and anthracene- h_{10} have nearly the same total state densities at this energy. If, however, anthracene-9- d_1 is effectively C_{2v} rather than D_{2h} , the density of totally symmetric modes is $61/4$ per cm^{-1} instead of $61/8 \text{ cm}^{-1}$. Therefore, no IVR is expected in anthracene-9- d_1 below 1030 cm^{-1} (where the density of totally symmetric modes is equal to that of anthracene- h_{10} at 1168 cm^{-1}) if the IVR is statistical. Listed in Table IV are the calculated vibrational-state densities for the energies where no, restricted, and dissipative IVR were observed in anthracene- h_{10} . Also listed are the energies where these vibrational-state densities occur in the deuteriated isotopes. This table indicates how the redistribution might be expected to change because of isotopic substitution.

The experimental observation of restricted IVR at $S_1 + 1173\text{ cm}^{-1}$ in anthracene-9-d₁ is in accord with these predictions. At this vibrational-state density, beats are seen in the fluorescence decay of D_{2h} anthracene-h₁₀ and in the fluorescence decay of C_{2v} anthracene-9-d₁. The energies where IVR is first observed in the two molecules, however, are different. Similar results regarding the different regions of IVR were also found in anthracene-d₁₀.

V. CONCLUSIONS

The highly analogous rovibronic nature of three anthracene isotopes can be seen from the spectroscopic data. The data clearly show the similarity of the excitation spectra and rotational band contour shapes, as well as the correlation of the observed vibrational levels. Qualitatively, we can relate the comparative dynamics of IVR to the relative state density and symmetry of the molecule. But the most important finding here is that the regions of IVR identified previously for anthracene-h₁₀ and *trans*-stilbene (nonexistent, restrictive, and dissipative IVR) [1,5] have also been found in all deuteriated anthracenes studied here. These regions of IVR have also been observed recently in azulene by Wallace and co-workers [26]. Both spectral and temporal studies of these molecules confirm this picture. It seems that this "division" of IVR regions in large molecules is general.

Acknowledgements. We gratefully acknowledge funding of this work by the National Science Foundation. When we started this work several years ago, Professor E. Lee was very helpful in teaching us the details of the computer program for the rotational contours. This article is dedicated, in memory of a great colleague and scholar, to Professor Ed Lee.

Registry No.

Anthracene-9-d₁, 4485-03-4; anthracene-d₁₀, 1719-06-8; anthracene-h₁₀, 120-12-7.

VI. REFERENCES

1. (a) P. M. Felker and A. H. Zewail, *J. Chem. Phys.* **82**, 2961 (1985); (b) *Ibid.* 2975; (c) *Ibid.* 2994; (d) *Ibid.* 3003.
2. B. W. Keelan and A. H. Zewail, *J. Chem. Phys.* **82**, 3011 (1985); *J. Phys. Chem.* **89**, 4939 (1985).
3. W. R. Lambert, P. M. Felker, and A. H. Zewail, *J. Chem. Phys.* **81**, 2209 (1984).
4. S. Mukamel, *J. Chem. Phys.* **82**, 2867 (1985).
5. For a review, see: P. M. Felker and A. H. Zewail, *Adv. Chem. Phys.* **70**, 265 (1988).
6. W. R. Lambert, P. M. Felker, and A. H. Zewail, *J. Chem. Phys.* **81**, 2217 (1984).
7. E. F. Zalewski, R. A. Kellar, and R. Engleman, Jr., *J. Chem. Phys.* **70**, 1015 (1979) and references therein.
8. J. L. Charlton and R. Agagnier, *Can. J. Chem.* **51**, 1852 (1973).
9. L. R. Khundkar, R. A. Marcus, and A. H. Zewail, *J. Phys. Chem.* **87**, 2473 (1983).
10. B. N. Cyvin and S. J. Cyvin, *J. Phys. Chem.* **73**, 1430 (1969).
11. D. J. Evans and D. B. Scully, *Spectrochim. Acta* **20**, 891 (1964).
12. J. G. Radziszewski and J. Michl, *J. Chem. Phys.* **82**, 3527 (1985). See also A. Bree, *Chem. Phys. Lett.* **131**, 65 (1986).
13. W. R. Lambert, P. M. Felker, and A. H. Zewail, *J. Chem. Phys.* **81**, 2195 (1984).
14. M. J. Robey and E. W. Schlag, *J. Chem. Phys.* **67**, 2775 (1977).
15. K. Krogh-Jespersen, R. P. Rava, and L. Goodman, *J. Phys. Chem.* **88**, 5503 (1984).
16. E. B. Wilson, J. C. Decuis, and P. C. Cross, *Molecular Vibrations*; Dover: New York, 1955.

17. A single chemical substitution on a polyatomic molecule generally affects only a few vibrational frequencies (see, for example: G. Herzberg, *Infrared and Raman Spectra of Polyatomic Molecules*; Van Nostrand: Princeton, 1945). Comparing Cyvin and Cyvin's and Evans and Scully's calculated frequencies for anthracene- h_{10} and 9,10- d_2 , it is clear that only some of the frequencies are affected by this substitution; more than 70% are within 30 cm^{-1} of their values in anthracene- h_{10} and most of those are within only 5 cm^{-1} . For anthracene-9- d_1 , therefore, it was assumed that only the frequencies that change substantially upon 9,10- d_2 substitution are changed for 9- d_1 substitution. The Teller-Redlich rule was used to calculate the remaining 20 frequencies.
18. Cyvin and Cyvin and Evans and Scully [10,11] also calculated all the normal frequencies for anthracene- d_{10} . The difference in the vibrational-state density calculated by using their vibrational frequencies and the density calculated by using the Teller-Redlich rule and their anthracene- h_{10} frequencies is not too significant, although some specific frequencies differ by as much as 20%.
19. W. R. Lambert, P. M. Felker, J. A. Syage, and A. H. Zewail, *J. Chem. Phys.* **81**, 2195 (1984).
20. B. W. Keelan, *Ph.D. Thesis*, California Institute of Technology, 1986.
21. G. Herzberg, *Electronic Spectra and Electronic Structure of Polyatomic Molecules*; Van Nostrand Reinhold: New York, 1966; pp. 66-8, 137-41.
22. H. Selzle, W. E. Howard, and E. W. Schlag, *Rotational Band Contour Program*, from Technische Universitat Munchen.
23. T. Ueda and T. Shimanouchi, *J. Mol. Spectrosc.* **28**, 350 (1968).
24. P. M. Felker and A. H. Zewail, *Phys. Rev. Lett.* **53**, 501 (1984).
25. A. Amirav, *J. Chem. Phys.* **86**, 4706 (1987).
26. D. R. Demmer, J. W. Hager, G. W. Leach, S. C. Wallace, *Chem. Phys. Lett.* **136**, 329 (1987).

TABLE I

APPROXIMATE DENSITIES AT RELEVANT ENERGIES^a

	<u>770 cm⁻¹</u>	<u>1420 cm⁻¹</u>	<u>1790 cm⁻¹</u>
S ₀ , anthracene-h ₁₀	1	25	123
S ₁ , anthracene-h ₁₀	6	233	1443
S ₁ , anthracene-h ₁₀ (+5%)	4	151	887
S ₁ , anthracene-h ₁₀ (-5%)	8	388	2497
S ₁ , anthracene-d ₁	6	257	1609
S ₁ , anthracene-d ₁₀ ^b	12	691	5059
S ₁ , anthracene-d ₁₀ ^c	15	901	6680

^aPer wavenumber^bLiterature^cTeller-Redlich rule

TABLE II

COMPARISON OF S₁ VIBRATIONAL LEVELS IN
ANTHRACENE-H₁₀, -9D₁, AND -D₁₀

Anthracene-h ₁₀			Anthracene-9d ₁			Anthracene-d ₁₀		
Energy ^a	Intensity ^b	Assign ^c	Energy ^a	Intensity	Sym ^d	Energy ^a	Intensity	Sym
0	100.0	0 ₀ ⁰	0	100.0	ag	0	100.0	ag
209	0.17	ag	210	0.1	ag	-	-	-
232	0.74	1 ₁₀ ⁻¹	231	1.4	b _{1g}	229	11.2	b _{1g}
385	13.51	12 ₀ ¹	385	11.8	ag ⁺	370	58.9	ag
390	0.45	2x209?	396	0.2	=	-	-	-
-	-	-	-	-	-	392	1.1	b _{1g}
-	-	-	421	0.2	ag	-	-	-
444	0.08	ag	449	0.3	ag	430	1.6	ag
473	0.19	ag	460	0.7	ag	418	4.5	ag
541	0.71	2 ₁₀ ⁻²	542	1.6	ag	525	10.2	ag
583	0.24	1 ₁₀ ¹	583	0.8	ag	567	3.5	ag
623	0.06	ag	614	0.6	ag	561	2.1	ag
630	0.05	b _{1g}	634	0.2	b _{1g}	619	1.4	b _{1g}
678	0.03	ag	673	0.1	ag	649	5.7	ag
-	-	-	694	0.1	ag	-	-	-
748	0.19	ag	742	0.5	ag	690	2.6	ag
755	0.45	1 ₀ ¹ ag	751	1.5	ag	720	11.8	ag
766	0.91	2 ₀ ²	769	2.3	ag	743	14.5	ag

TABLE II (continued)

Anthracene-h ₁₀			Anthracene-9d ₁			Anthracene-d ₁₀		
<u>Energy</u>	<u>Intensity</u>	<u>Assign</u>	<u>Energy</u>	<u>Intensity</u>	<u>Sym</u>	<u>Energy</u>	<u>Intensity</u>	<u>Sym</u>
775	0.04	a _g	778	0.1	a _g	—	—	—
—	—	—	832	0.2	2a _g	—	—	—
—	—	418+370	—	—	—	788	1.7	a _g
889	0.22	$\bar{9}_0^1$	880	0.5	b _{1g}	791	6.7	2b _{1g}
895	0.08	b _{1g}	864	0.2	b _{1g}	764	1.1	b _{1g}
—	—	—	884	0.5	b _{1g}	—	—	—
905	0.09	a _g	899	0.1	+	804	1.7	a _g
910	0.05	a _g	904	0.2	a _g	809	2.4	a _g
—	—	—	913	0.1	a _g	—	—	—
—	—	—	948	0.1	a _g ?	917	2.1	a _g
961	0.04	a _g	959	0.1	a _g	928	0.7	=
966	0.03	a _g	966	0.2	a _g	937	1.5	+
—	—	—	995	0.1	a _g +	—	—	—
1019	0.24	9_0^1	1012	0.2	a _g	—	—	—
—	—	—	1028	0.1	a _g	—	—	—
1042	0.21	a _g	1037	0.6	a _g	829	16.5	a _g
—	—	—	1073	0.1	3b _{1g}	—	—	—
1094	0.14	a _g	1089	0.5	a _g	845	3.4	+
—	—	—	1101	0.1	b _{1g} +	—	—	—

TABLE II (continued)

Anthracene-h ₁₀			Anthracene-9d ₁			Anthracene-d ₁₀		
Energy	Intensity	Assign	Energy	Intensity	Sym	Energy	Intensity	Sym
1142	0.07	$10_0^1 12_0^1$	1135	0.3	+	1092	2.9	a _g
1146	0.19	12_0^3				1114	1.6	a _g
1158	0.08	a _g	-	-	-	-	-	-
-	-	-	1160	0.7	b _{1g}	864	1.0	b _{1g}
1168	0.56	$7_0^1 8_0^1$	1167	1.1	a _g	874	5.4	a _g
			1173	1.3	+	882	8.8	a _g
-	-	-	1183	0.3	+	-	-	-
1184	0.15	$\bar{7}_0^1$	1189	0.4	b _{1g} ⁺	-	-	-
-	-	-	1269	0.1	+	-	-	-
-	-	-	1278	0.1	+	-	-	-
-	-	-	1297	0.2	+	-	-	-
-	-	-	1304	0.2	a _g	-	-	-
-	-	-	1319	0.2	a _g	-	-	-
1291	0.19	a _g	-	-	-	-	-	-
-	-	-	-	-	-	1039	1.9	a _g
-	-	-	-	-	-	1136	1.0	+
-	-	-	-	-	-	1162	1.2	+
-	-	829+370	-	-	-	1197	3.8	a _g
-	-	-	-	-	-	1235	1.5	a _g

TABLE II (continued)

Anthracene-h ₁₀			Anthracene-9d ₁			Anthracene-d ₁₀		
Energy	Intensity	Assign	Energy	Intensity	Sym	Energy	Intensity	Sym
-	-	-	-	-	-	1307	3.5	a _g
-	-	-	-	-	-	1339	8.6	+
-	-	-	-	-	-	1359	1.7	a _g
-	-	-	-	-	-	1364	3.5	+
1380	1.39	$6_0^1 a_g$	1375	3.0	a _g +	1382	40.8	a _g
1389	0.27	a _g	-	-	-	-	-	-
1409	0.80	2a _g ?	1409	5.3	a _g	1450	33.2	a _g +
1414	0.13	+	1418	0.3	+	1419	2.4	a _g
1418	0.35	+				1425	2.4	a _g +
1420	0.73	5_0^1	1435	1.5	a _g	1440	15.2	+
-	-	-	1454	0.3	a _g +	-	-	-
1469	0.09	1094+385	1469	0.2	+	1215	1.1	+
-	-	-	1480	0.2	2b _{1g}	1465	2.5	b _{1g} ?
1501	1.03	4_0^1	1499	3.4	a _g +	1484	17.7	+
1506	0.20	b _{1g}	-	-	-	-	-	-
1508	0.24	b _{1g}	-	-	-	-	-	-
1514	0.56	$4_0^{-1}+$	1509	2.2	+	1475	9.6	+
1516	0.24	b _{1g}	1520	0.3	b _{1g}	1497	3.9	b _{1g} +b _{1g} ?

TABLE II (continued)

Anthracene-h ₁₀			Anthracene-9d ₁			Anthracene-d ₁₀		
<u>Energy</u>	<u>Intensity</u>	<u>Assign</u>	<u>Energy</u>	<u>Intensity</u>	<u>Sym</u>	<u>Energy</u>	<u>Intensity</u>	<u>Sym</u>
1543	0.06	+	1532	0.2	+	1510	2.5	+
1545	0.08	+						
1548	0.09	ag						
1550	0.14	$7/8_0^1 12_0^1$	1550	0.2	+	1241	2.7	ag
						1249	1.6	ag
1577	0.06	=	1573	0.3	+	1546	4.6	ag
1590	0.07	=	1582	0.3	ag+	1554	4.8	+
1635	0.25	ag+	1629	0.4	+	1592	6.5	ag+
1640	0.09	+	-	-	-	1587	3.7	ag
-	-	-	-	-	-	1608	1.9	ag+
1715	0.07	=	1705	0.1	+	1641	6.3	ag+
-	-	2 x 829	-	-	-	1658	2.8	ag+
-	-	1307+370	-	-	-	1679	1.0	ag
-	-	-	-	-	-	1690	2.0	ag+
-	-	1339+370	-	-	-	1712	2.5	+
-	-	1359+370	-	-	-	1729	1.4	+
1767	0.23	$6_0^1 12_0^1$	1765	0.7	+	1751	7.6	+
1771	0.11	+	-	-	-	-	-	-
1773	0.13	1389+385	-	-	-	-	-	-
-	-	-	-	-	-	1778	4.2	+
1792	0.28	1409+385	1792	1.2	+	1811	8.9	+

TABLE II (continued)

Anthracene-h ₁₀			Anthracene-9d ₁			Anthracene-d ₁₀		
Energy	Intensity	Assign	Energy	Intensity	Sym	Energy	Intensity	Sym
1795	0.05	1414+385	1803	0.1	=	1793	1.1	+
1798	0.05	1418+385						
1801	0.14	$5_0^1 1_2^1$	1820	0.1	=	1821	6.4	+
1883	0.04	+	-	-	-	-	-	-
1885	0.12	$4_0^1 1_2^1$	1886	0.6	+	1852	3.6	+
1890	0.04	1506+385	-	-	-	-	-	-
1895	0.04	$4_0^{-1} 1_2^1$	-	-	-	1846	3.6	+
1897	0.04	1516+385	-	-	-	1866	0.6	=
-	-	-	1926	0.1	=	1920	1.5	+
-	-	-	-	-	-	1952	1.7	+
-	-	1592+370	-	-	-	1961	1.7	+

TABLE II (continued)

^a Vibrational energy in cm^{-1} . The -h₁₀ data are primarily from Refs. 2 and 13. The -h₁₀ origin is 27695 cm^{-1} (from Ref. 13); in this study the -9d₁ and -d₁₀ origins were found to be shifted 12 and 71 cm^{-1} , respectively, to higher energy.

^b Percent intensity relative to the origin of each molecule (100%), which is the most intense transition in each molecule. The -h₁₀ data are primarily from Refs. 2 and 13.

^c A_n^m denotes the transition of mode number A from n quanta in the ground electronic state to m quanta in the excited state S₁; combination bands are $A_n^m B_j^i \dots$. A bar over a mode number indicates a non-totally symmetric (*e.g.*, b_{1g}) vibration. Where mode numbers have not been assigned in Ref. 13, combination bands are denoted by a + b, where a and b are the -h₁₀ vibrational frequencies in cm^{-1} (in a few cases, combination bands in -d₁₀ have no observed -h₁₀ analog; the -d₁₀ frequencies are then given in this column). For levels not assigned in Ref. 13, vibrational symmetries from Ref. 2 are given (see note d for designations; superpositions of levels are also denoted with a comma; *e.g.*, 10₀,a_g¹ indicates that mode number 10 and another a_g vibration overlap).

^d Vibrational symmetries found in this study from rotational band contour analysis. Superpositions of levels are denoted variously, *e.g.* 2a_g (two a_g vibrations overlap), a_g+ (one or more vibrations of indeterminate symmetry overlap with an a_g vibrations), or just + (two or more vibrations of indeterminate symmetry overlap). The designation == indicates that no symmetry analysis has been performed for that level.

TABLE III
SPECTRAL ANALYSIS

<u>E_{vib}</u>	<u>Assignment</u>	<u>Intensity</u>
	$S_1 + 1409 \text{ cm}^{-1}$	
0	1409_0^1	22
390	$1409_0^1 12_1^0$	8
1164	$1409_0^1 8_1^0$	13
1411	1409_1^1	34
1457	?	55
1499	?	93
1556	$1409_0^1 8_1^0 12_1^0$	100
1587	?	51
1692	?	26
1883	?	47
1942	$1409_0^1 8_1^0 12_2^0$	46

TABLE III (continued)

SPECTRAL ANALYSIS

<u>E_{vib}</u>	<u>Assignment</u>	<u>Intensity</u>
	$S_1 + 751\text{ cm}^{-1}$	
0	10_0^1	54
390	$10_0^1 12_1^0$	24
753	10_1^1	100
905	?	38
1033	?	39
1138	$10_1^1 12_1^0$	46
1914	$10_1^1 8_1^0$	20
2005	(753 + 1252)	20
2158	$10_1^1 6_1^0$	60
2313	$10_1^1 8_1^0 12_1^0$	33
2546	$10_1^1 6_1^0 12_1^0$	29

TABLE IV^a

	<u>Vibrational State Density</u>	<u>E(-h₁₀)</u>	<u>E(-9-d₁)</u>	<u>E(-d₁₀)</u>
no IVR	61	1170	1030	960
restricted IVR	120-700	1290-1640	1160-1480	1080-1380
dissipative IVR	1500	1800	1670	1530

^aThe densities are per wavenumber, and the energies are in wavenumbers.

FIGURE CAPTIONS

- Figure 1:** Calculated vibrational density of states versus excess vibrational energy for the S_0 and S_1 electronic states in anthracene- h_{10} .
- Figure 2:** Calculated vibrational density of states versus excess vibrational energy for the S_1 electronic state of the three anthracene analogues.
- Figure 3:** S_1 fluorescence excitation spectra of anthracene- h_{10} (50 psig of neon, 415K, $X/D = 24$), anthracene-9- d_1 , and anthracene- d_{10} (both 50 psi of nitrogen, 443 K, $X/D = 20$). Energy references are the electronic origins (anthracene- $h_{10} = 27695 \text{ cm}^{-1}$, anthracene-9- $d_1 = 27707 \text{ cm}^{-1}$, anthracene- $d_{10} = 27766 \text{ cm}^{-1}$). Note that the multiplicative factors for the intensities differ in the three spectra.
- Figure 4:** Dispersed fluorescence spectra (anthracene- h_{10} , top; anthracene-9- d_1 , middle; anthracene- d_{10} , bottom) taken for selected bands in the excitation spectra of the three anthracene analogues. Resolution is 1.6\AA .
- Figure 5:** In-phase fluorescence decays (anthracene- h_{10} , left column; anthracene-9- d_1 , right column) of the initially excited state for selected bands in the excitation spectra of the three anthracene analogues. All decays are for detection 390 cm^{-1} to the red of the excitation wavelength.
- Figure 6:** Comparison of experimental rotational band contours for the origin (a_g symmetry) and $\tilde{\nu}_{11}$ (b_{1g} symmetry) for each of the three isotopic species. Experimental conditions were 50 psig of nitrogen, 443 K, $X/D = 20$.
- Figure 7:** Variation of spectral purity of rotational contours with vibrational energy in anthracene- d_{10} . The three contours shown are $S_1 + 1039$, 1450 , and 1751 cm^{-1} , which are assigned as a_g , a_g+ , and $+$, respectively. Note the decrease of the distinctiveness of the P-R rotational structure and the increase in FWHM as vibrational energy increases.
- Figure 8:** Comparison of experimental rotational band contours (EXP) and computer simulations (SIM) for anthracene-9- d_1 . Experimental conditions were as in Figure 6. The contours were best reproduced by using excited-state rotational constant reduced 1/2% from the ground-state values and taking the rotational temperature to be 23 K.
- Figure 9:** Comparison of experimental contours (EXP, conditions as in Figure 6) and computer simulations (SIM) for anthracene- d_{10} . The experimental contours were best reproduced by using excited-state rotational constants reduced 3/4% from S_0 values and taking the rotational temperature to be 21 (a_g) or 26 K (b_{1g}).

Figure 10: Selective detection study of the $S_1 + 1409 \text{ cm}^{-1}$ level in anthracene-9-d₁. The resolved emission (=dispersed fluorescence) spectrum is shown in trace A. Total detection (i.e., detection of all emission except that absorbed by a laser cutoff filter) yields the typical rotational band contour B. Detection of emission to $S_0 + 390 (\pm 100) \text{ cm}^{-1}$ (this interval being labeled 1 in trace A) gives contour C. Detection in the interval labeled 2 in trace A ($S_0 + 1499 (\pm 25) \text{ cm}^{-1}$) produces contour D.

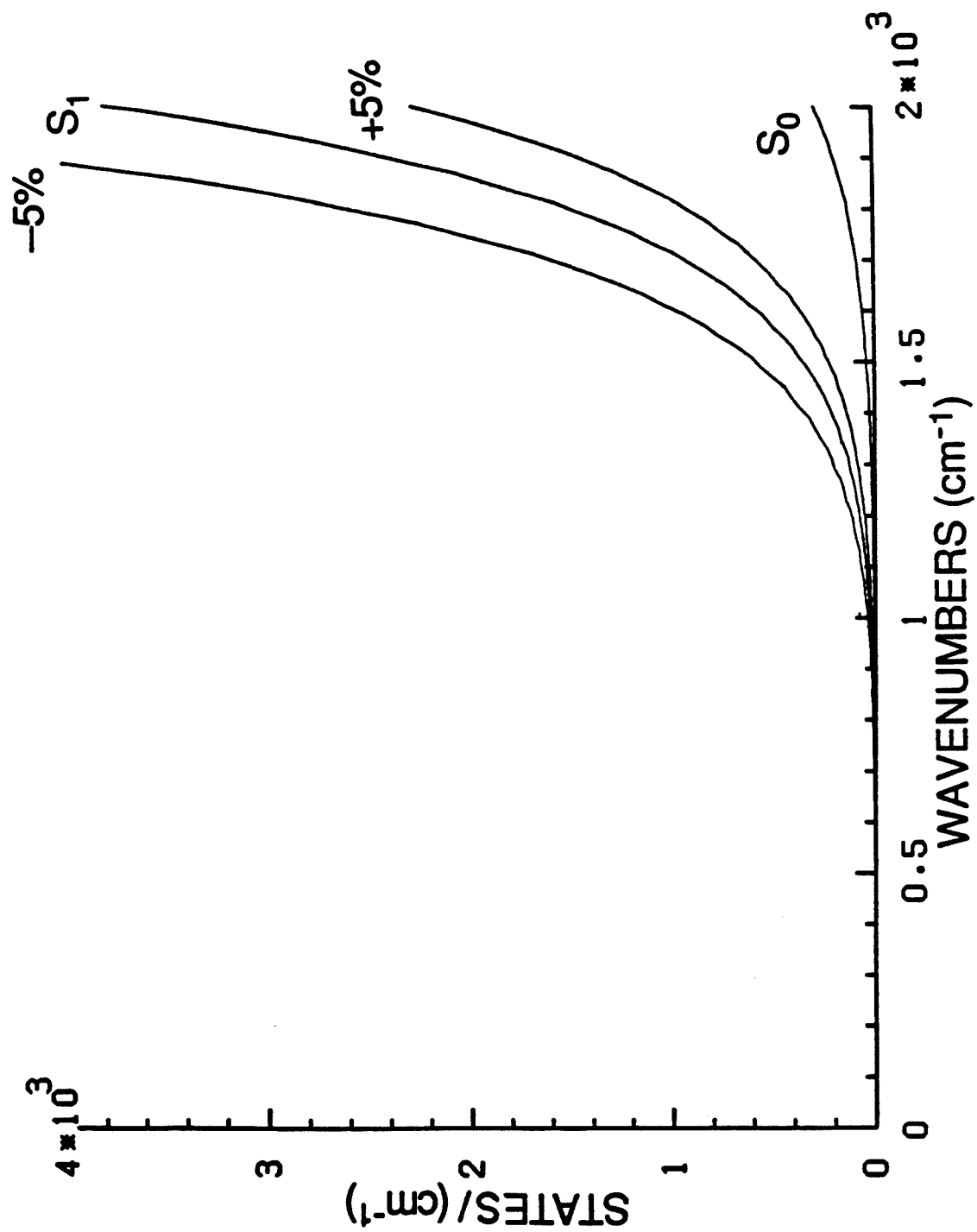


Figure 1

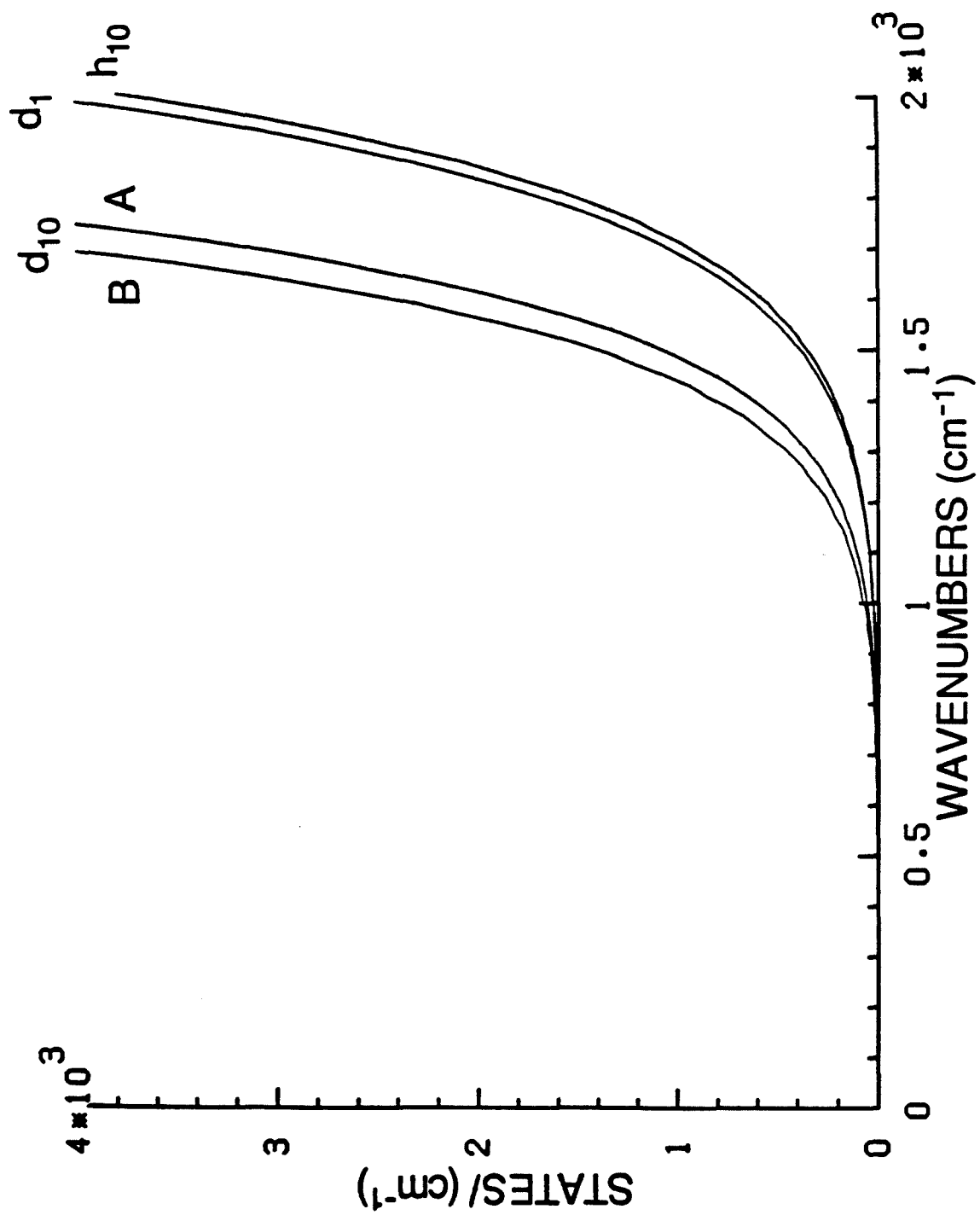


Figure 2

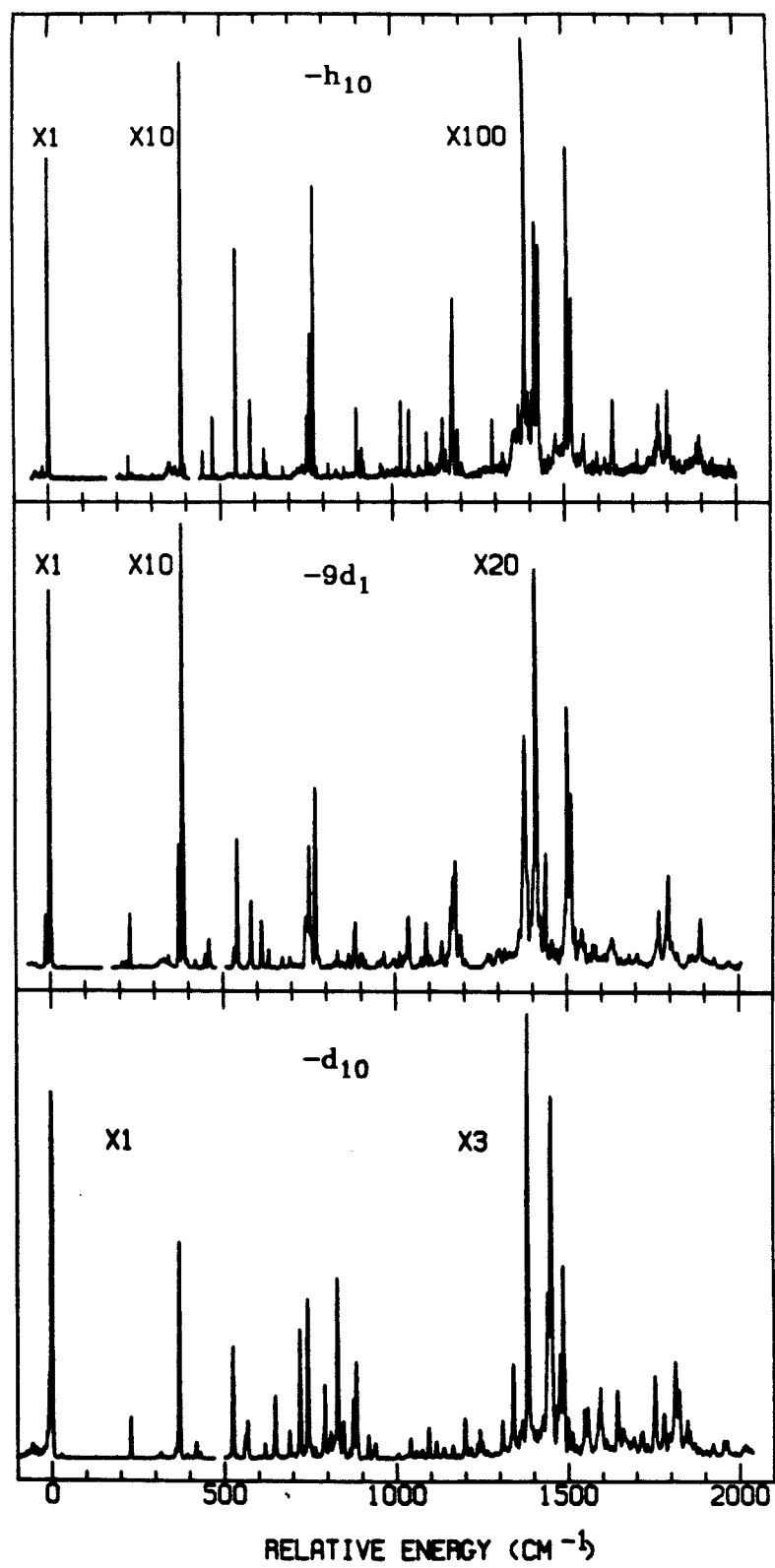


Figure 3

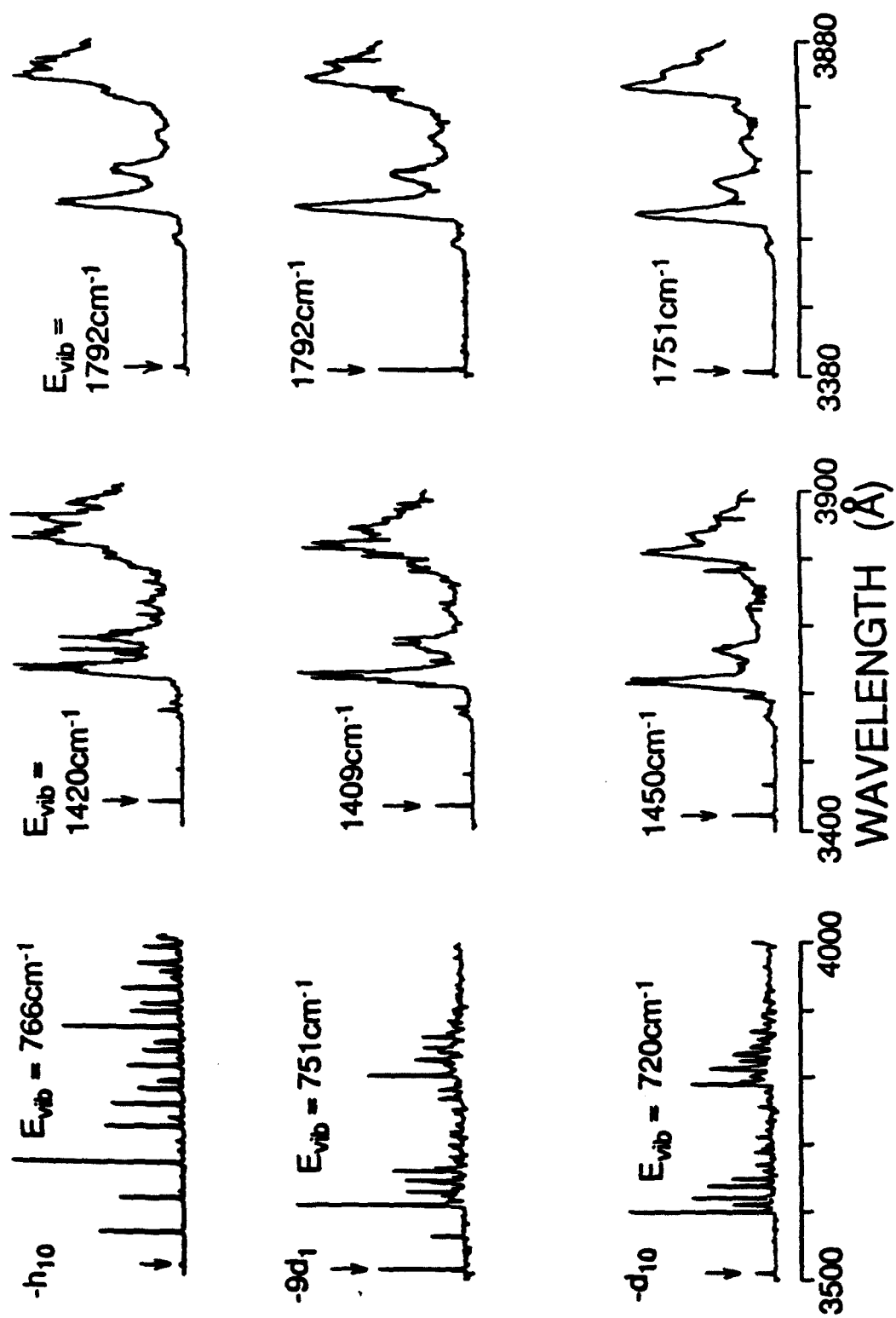


Figure 4

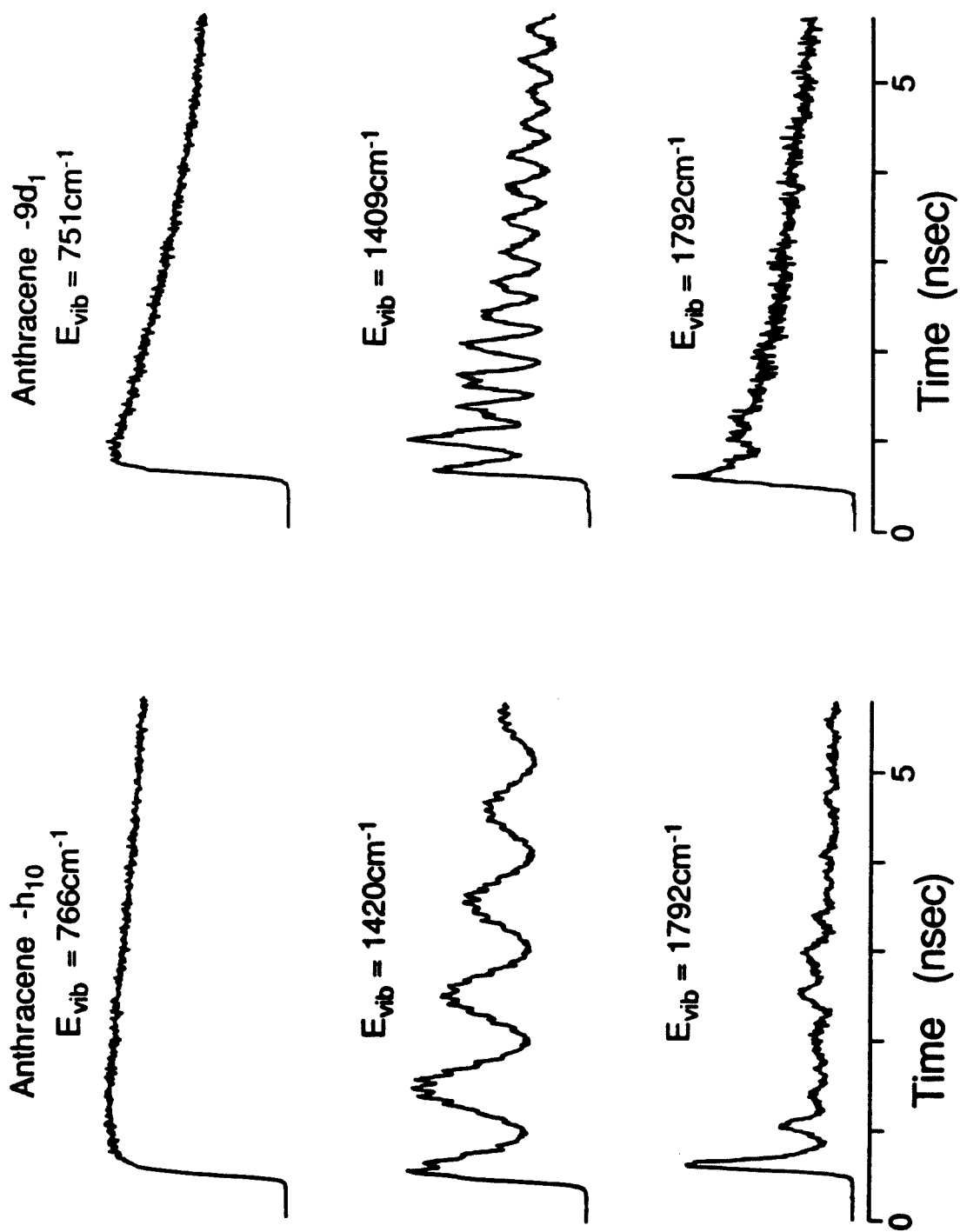


Figure 5

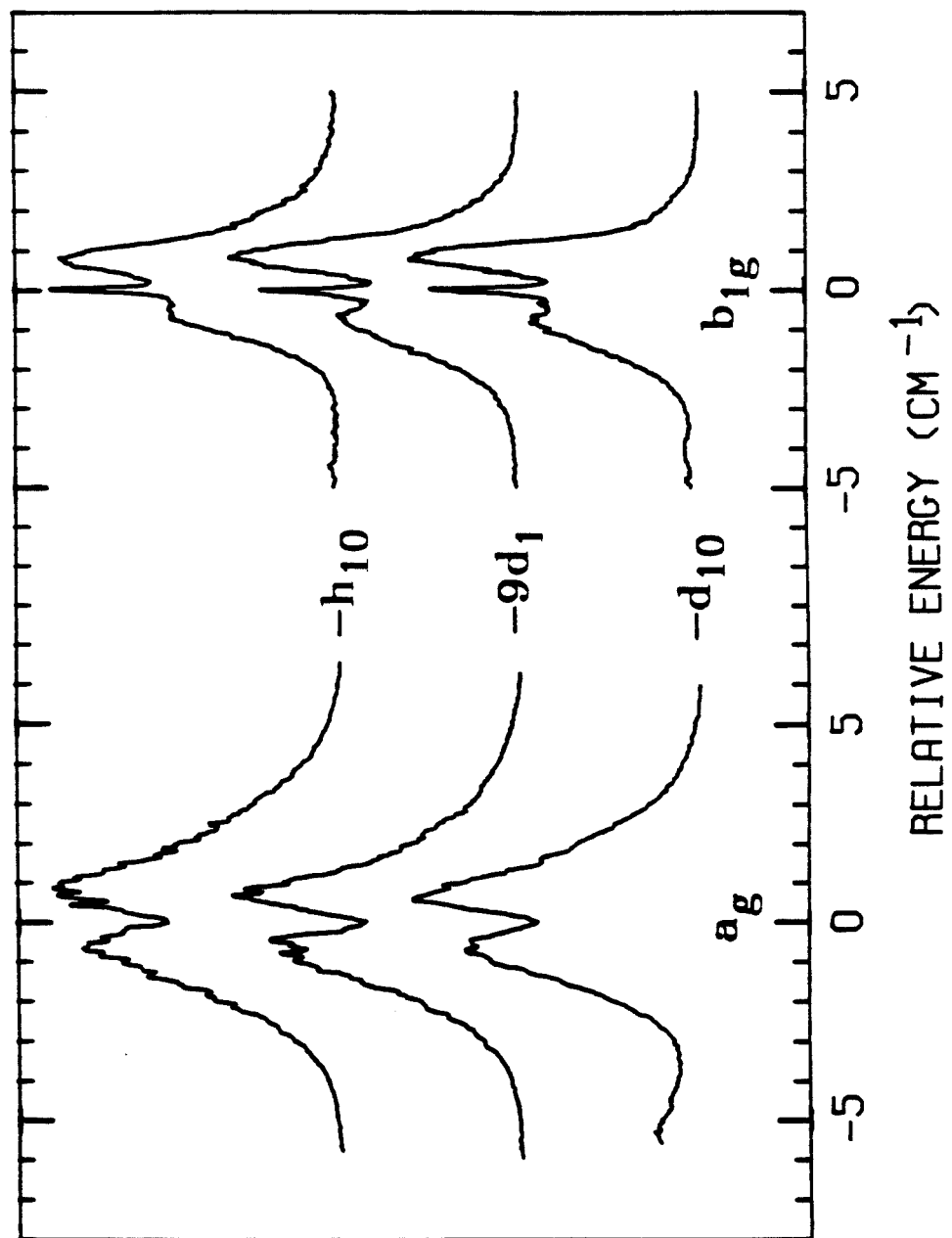


Figure 6

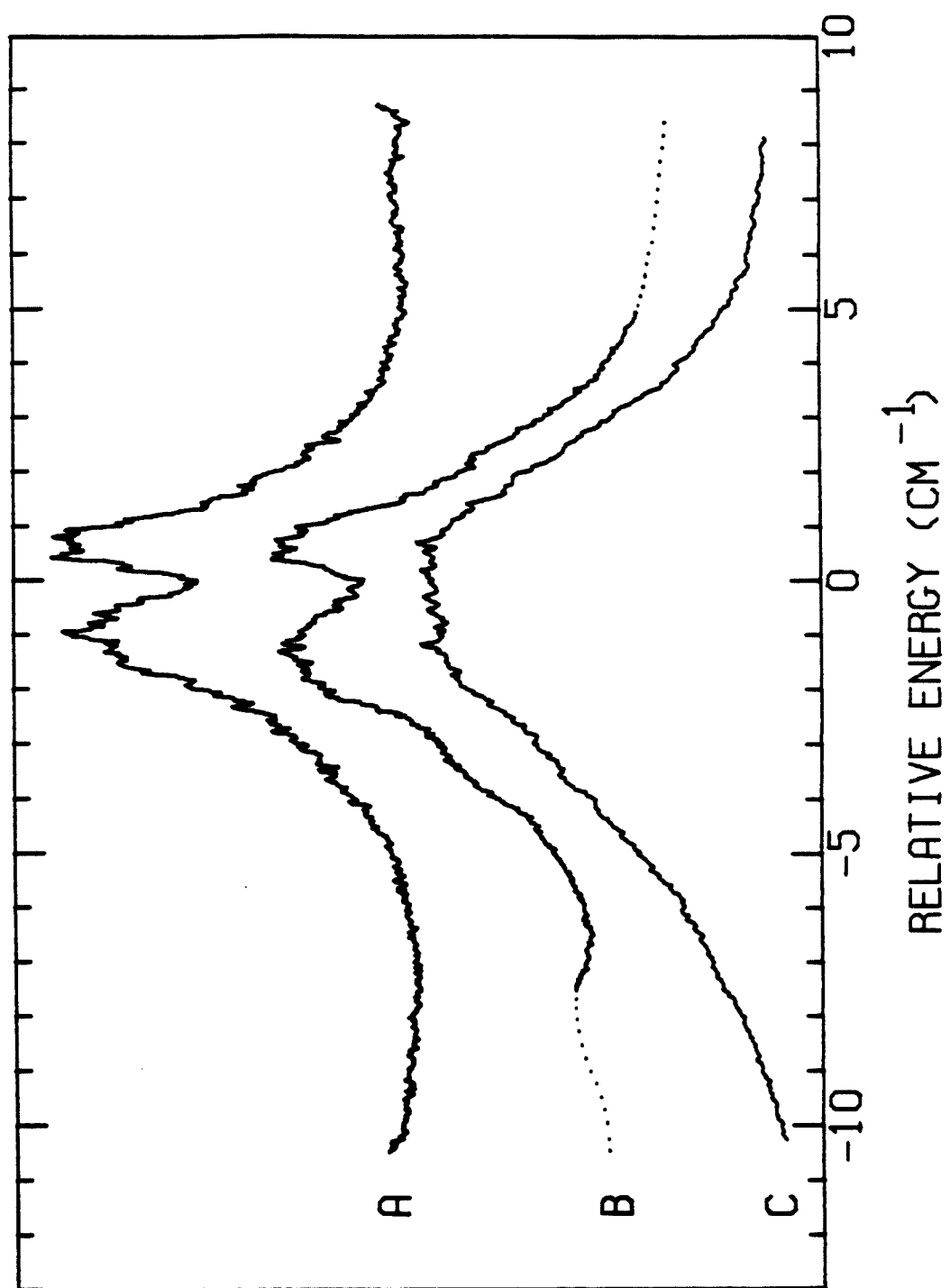


Figure 7

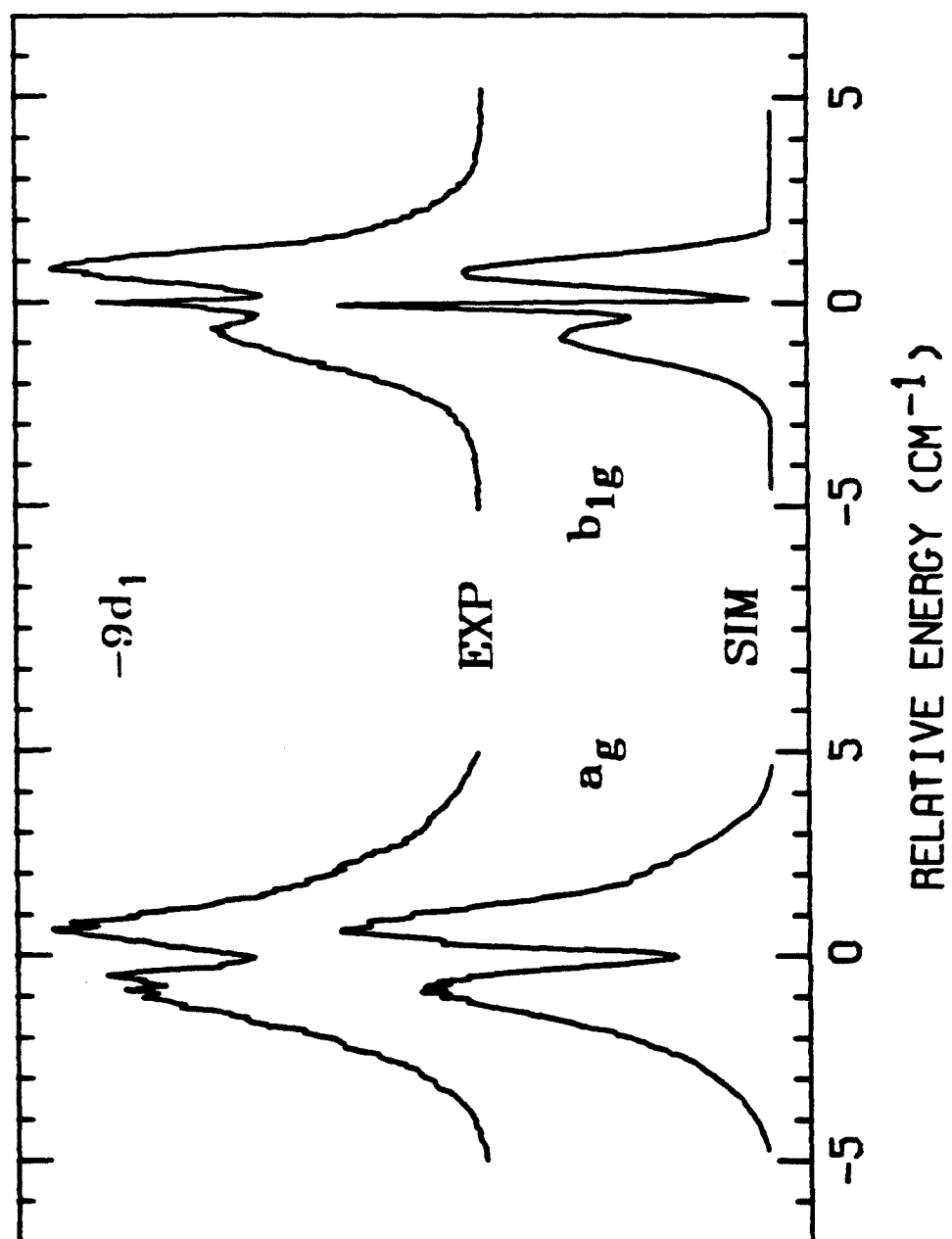


Figure 8

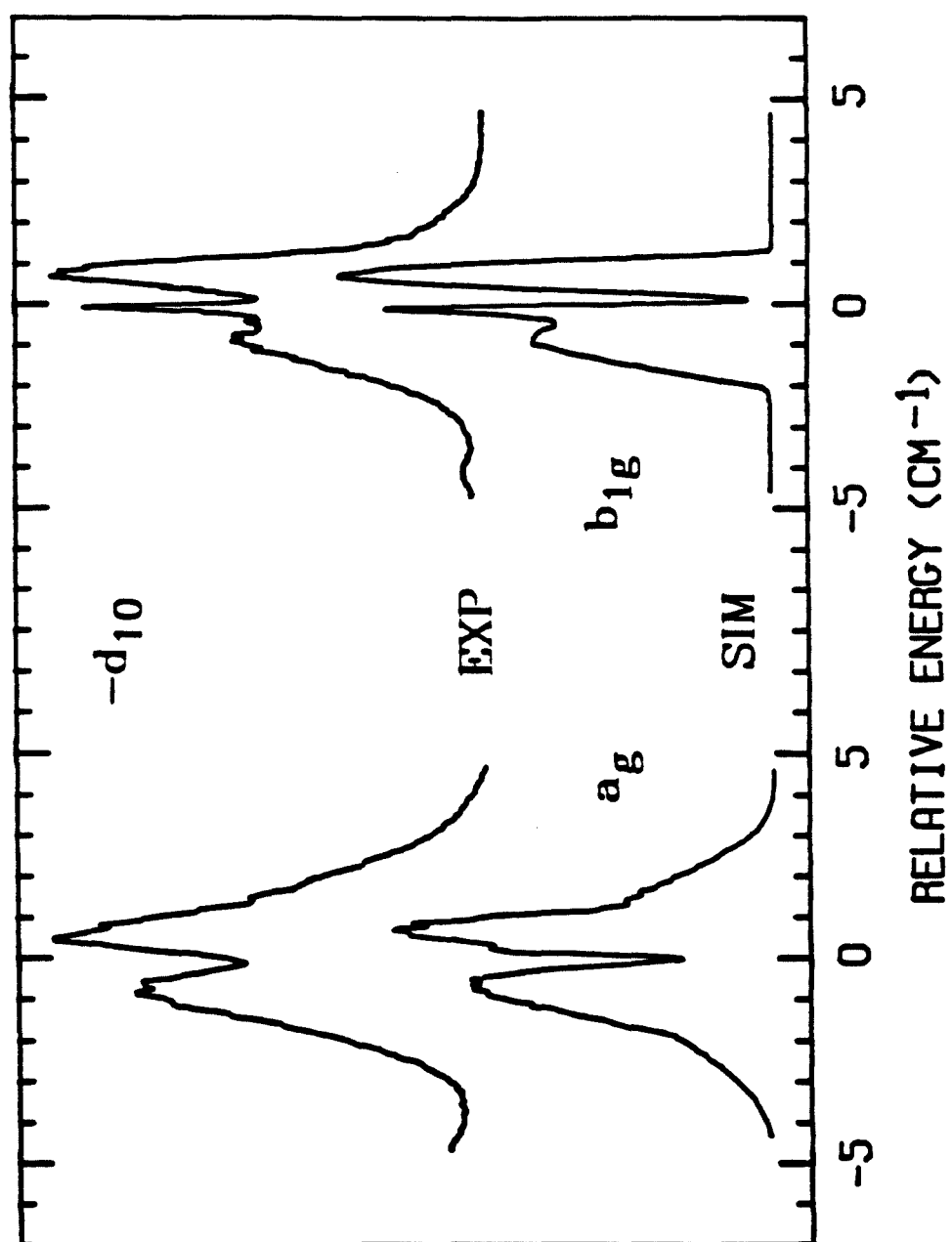


Figure 9

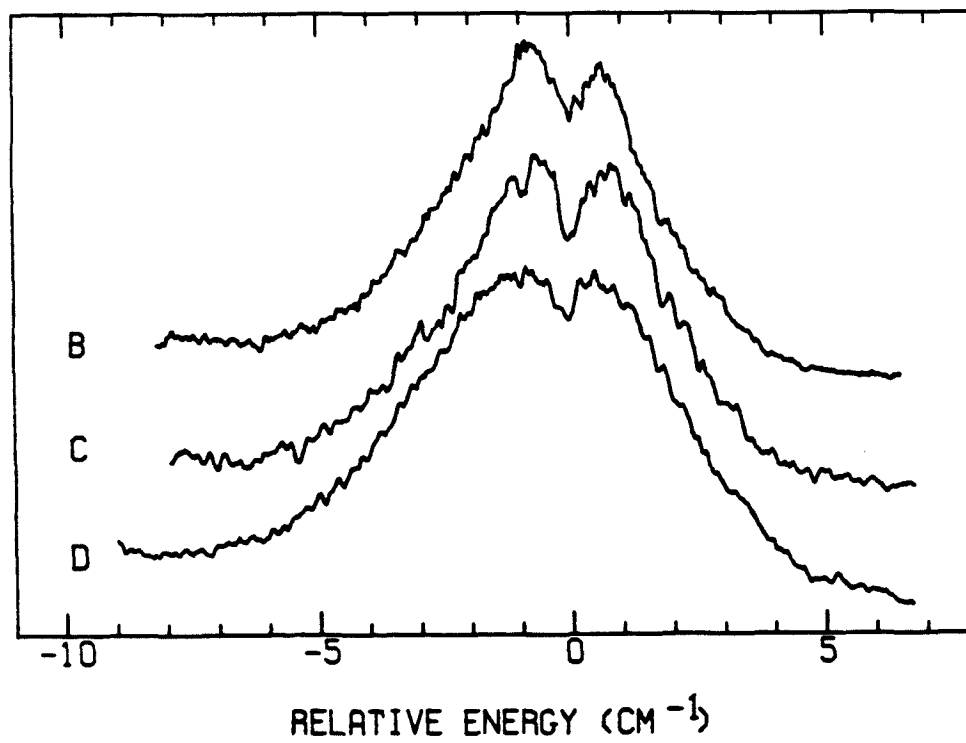
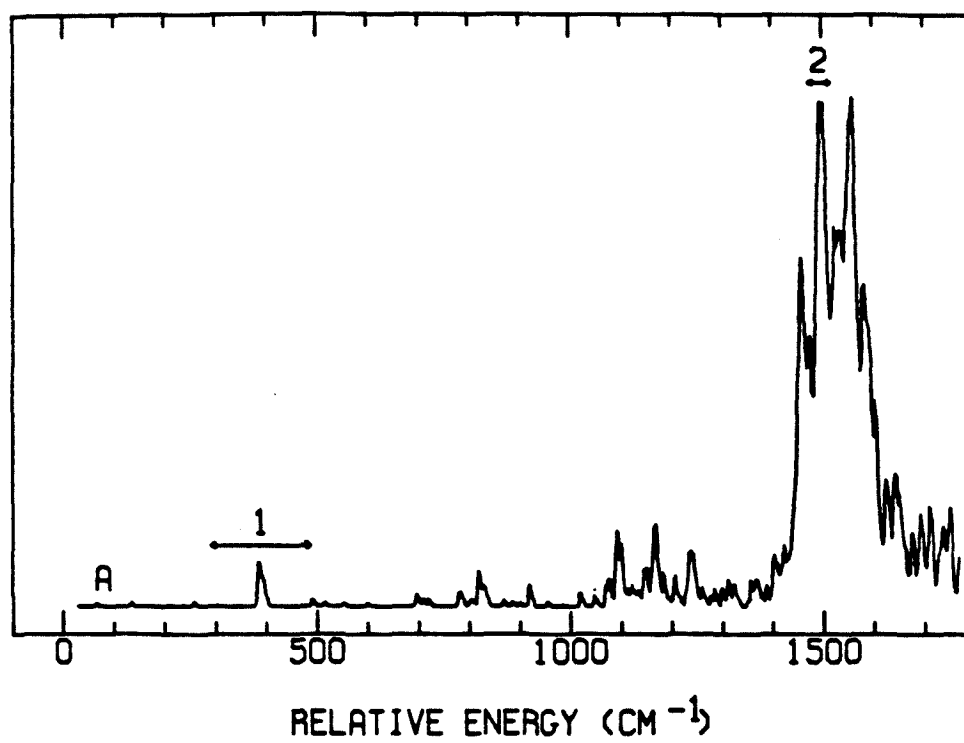


Figure 10

**REACTIONS IN SMALL CLUSTERS
STUDIED BY
TIME-RESOLVED LASER SPECTROSCOPY**

VOLUME TWO

Thesis by
Lawrence Weimin Peng

*In Partial Fulfillment of the Requirements
for the Degree of
Doctor of Philosophy*

California Institute of Technology
Pasadena, California

1991

(submitted 1 October 1990)

ABSTRACT

The data acquisition and data analysis software used to acquire and analyze the data presented in Volume One are described in exhaustive detail. The software consists of two independent custom applications, called **Data Analysis (version 2)** and **Data Acquire (version 13.5)**, and was developed for use on the Apple Macintosh II platform. The applications are complete and integrated packages controlling all facets of the user interface, laboratory equipment interface, plotting, file creation, printing, etc. Extensive use is made of the Macintosh Toolbox, and the software conforms to the Macintosh User Interface guidelines. **Data Analysis** is a general data analysis program, and **Data Acquire** is for data acquisition and some data analysis. The programs will be discussed from the point of view of both the user and the programmer, however particular emphasis is placed on the programs' structure and internal operation from a programmer's viewpoint. Included is a fully worked out example illustrating how to modify the programs.

TABLE OF CONTENTS

VOLUME TWO

1. Introduction to the Data Acquisition and Data Analysis Programs .	1
References	5
 2. System and Hardware Requirements	 6
2.1. Introduction	7
2.2. System and Hardware	7
2.3. NI-488 Software Installation	8
2.4. References	12
 3. Overview of the Data Acquisition and Data Analysis Programs. . .	 13
3.1. Introduction	14
3.2. General Overview	14
3.3. Menu Summary	16
1. APPLE	16
2. FILE and EDIT	16
3. COMMUNICATIONS (<i>Data Acquire</i>)	16
4. COLLECTION	17
5. FITTING.	18
6. DISPLAY	18
7. TRANSFORM	18
8. FUNCTIONS (<i>Data Analysis</i>)	19
9. WINDOWS	19
3.4. Use of special features	19
1. Communication Menu Dialog Boxes (<i>Data Acquire</i>)	19
1. The Unidex Dialog Box	20
2. The CAMAC Crate Dialog Box	21
3. The Boxcar Dialog Box	23
4. The Spex CD2A Dialog Box	23
2. Selective Plotting	25
3. Data Acquisition Control	26
4. Fitting and Convolution	28
1. Nonlinear Least Squares Fitting	28
2. Convolution	30
3. Nonlinear Least Squares Convolution	32
5. Data Manipulation	33
6. Using the Second Plot Window	34
7. Reconstructing Transients from Mass Spectra	35
8. Saving Data to Files	36
3.5. References	37
Tables	38
Figure Captions	40
Figures	43

4. Global Structure of the Data Acquisition and Data Analysis Programs	65
4.1. Introduction	66
4.2. Overview of Program Operation	67
4.3. Program Segmentation	69
4.4. Program Resources	70
1. Menu Resources	72
2. Dialog Resources	72
3. Window Resources	73
4. Icon Resources	73
5. Version Resources	74
4.5. Data Arrays and Memory Allocation	75
4.6. Notes about Numerical Recipes Routines	76
4.7. Filenames and Data File Creation	77
4.8. Variable Type Conversions	78
4.9. Plotting on the Plot Window	79
4.10. References	81
Figure Captions	82
Figures	83
 5. Source Files and Libraries Description	 87
5.1. Introduction	88
5.2. Macintosh Interface	92
5.3. Memory Allocation	98
5.4. Plotting	99
5.5. File Management	100
5.6. Data Analysis	102
5.7. Data Acquisition	106
5.8. Project Name and Resources	109
5.9. C Programming Environment Libraries	109
5.10. References	111
 6. Program Modification: A Tutorial	 112
6.1. Introduction	113
6.2. Creating the Resources	114
6.3. Modifying the Code to Use the New Resources	115
6.4. Code for Calculation and Plotting	119
6.5. Testing and Final Comments	120
Figure Captions	122
Figures	123

7. Troubleshooting	131
7.1. Introduction	132
7.2. Loss of Communication between the Computer and Data Acquisition Boards	132
7.3. Crashes due to a Bad Trigger	133
7.4. Crashes that are due to the Delay Line Unidex Controller	133
7.5. Crashes that are due to the Data Acquisition Boards or Bad Data Acquisition System Files	134
7.6. Crashes that are due to a Bad Data File	135
7.7. Crashes due to the Development Environment	136
7.8. References	137
 8. Development Environment Parameters	138
Reference	141
Table	142
 Appendix	
Update Notes for National Instruments NI-488 and LabDriver Software	144

CHAPTER 1

INTRODUCTION TO THE DATA AQUISITION AND DATA ANALYSIS PROGRAMS

1.1 INTRODUCTION

In the present volume of this thesis, the data acquisition and data analysis programs used to acquire and analyze the data presented in volume one are described in exhaustive detail. The programs are named **Data Analysis (version 2)** and **Data Acquire (version 13.5)**. **Data Analysis** is a general data analysis program, and **Data Acquire** is for data acquisition and some data analysis. In addition to their data analysis and acquisition features, both programs contain capabilities for generating, editing, plotting, and printing data files. The programs will be discussed from the point of view of both the user and the programmer; however, particular emphasis is placed on the programs' structure and internal operation from a programmer's viewpoint. The discussion is sufficiently complete so that one may feel secure about making any desired changes or additions. A list of the source files which comprise the programs, and a complete source code listing for both programs, are available (Professor Ahmed H. Zewail, California Institute of Technology).

The basic structure of **Data Analysis** and **Data Acquire** is the same, so much of the material in this volume is common to both programs. Therefore, in subsequent chapters, the discussion is often in terms of one program. Details unique to either program are noted when relevant. The programs were written in the C programming language (Think C v3, Symantec Corporation), and developed for use on an Apple Macintosh II computer. Throughout this volume, it is assumed that the reader is familiar with the basic skills required to use the Macintosh and the Think C environment. Details about Think C which are important to the programs are given in Reference 1. Both programs make extensive use of the Macintosh Toolbox, follow the standard Macintosh guidelines, and utilize the math coprocessor. Although originally written on a 68020 processor/68881 math-coprocessor based machine, the programs have been used successfully on 68030 processor/68882 math-coprocessor platforms. Early versions of **Data Acquire** have been

modified for use with the femtosecond apparatus in the **Caltech Femtosecond Facility** [2]. The primary differences are that there is little data analysis capability, reduced window handling capabilities, reduced plotting capabilities, and necessary changes have been made in the data acquisition schemes as required by the femtosecond apparatus.

The programs are based on the program **MiniEdit** (provided by Think C). **MiniEdit** is a C version of the sample Pascal application in Reference 4. **MiniEdit** is too simple to be practical, but it is a very convenient shell to use as a prototype for developing useful applications. Under MultiFinder, each program receives 512K of RAM unless otherwise specified by the user. The user can increase the amount of memory allocated by using the **Get Info** box. Reducing the amount of allocated memory is not recommended, but can be done if the amount of memory available is a serious issue.

This volume is intended to serve several important purposes. First, it is the user's manual for both programs illustrating the use of their various features. Second, it is a troubleshooting manual for solving commonly encountered problems. Third, the discussion provides instruction, hints, and warnings about how the programs work internally. This should be useful since the programs may serve as a basis for programs used in the future. Fourth, it will provide a foundation for understanding how the Macintosh Toolbox is used in these programs. Finally, a discussion is given concerning the issues of portability to other Macintosh platforms and upgrades in the development environment. As of this writing, Think C v4 is the most recent version. This volume is not designed to be a manual for learning the C programming language, or for detailed discussions about how the Macintosh Toolbox is constructed. Excellent references for the C language [3,4] and for the Macintosh Toolbox [5-8] already exist.

The remainder of this volume is comprised of seven chapters and an appendix. The necessary system and hardware requirements, as well as the procedures for installing the IEEE-488 driver software used by the data acquisition NuBus boards, are outlined in

Chapter 2. In Chapter 3, an overview of the programs is given. The various menus and features are summarized and discussed from a user's point of view. The internal structure of the programs is reviewed from a global perspective in Chapter 4, and Chapter 5 provides more specific descriptions about the source files and libraries. Files are discussed in terms of their major function in the programs. Chapter 6 documents the procedure for making changes or additions to the programs. A fully worked out example is given illustrating how to alter a menu, construct a dialog box, and plot data on the plotting windows. Troubleshooting procedures are given in Chapter 7. Chapter 8 describes the settings for the development environment used to write the programs. Finally, the Appendix contains update notes concerning the data acquisition NuBus boards and associated driver software.

REFERENCES

1. (a) Symantec, *Think C User's Manual*, version 3 (1988).
(b) Symantec, *Think C Standard Libraries Reference*, version 3 (1988).
2. M. Dantus, *Ph.D. Thesis*, California Institute of Technology, to be submitted.
3. B. W. Kernighan and D. M. Ritchie, *The C Programming Language*, 2nd Edition (Prentice-Hall, Englewood Cliffs, 1988).
4. S. G. Kochan, *Programming in ANSI C*, 2nd Edition (Hayden, Indianapolis, 1988).
5. Apple Computer, Inc., *Inside Macintosh*, volumes 1-5 (Addison-Wesley, Reading 1988).
6. S. Chernicoff, *Macintosh Revealed*, volumes 1-3 (Hayden, Indianapolis, 1987-89).
7. D. Mark and C. Reed, *Macintosh Programming Primer* (Addison-Wesley, Reading, 1989).
8. S. Knaster, *How to Write Macintosh Software*, 2nd Edition (Hayden, Indianapolis, 1988).

CHAPTER 2

SYSTEM AND HARDWARE REQUIREMENTS

2.1 INTRODUCTION

In this chapter, an outline of the system and hardware requirements is given. **Data Analysis** is designed to be independent of any given laboratory. **Data Acquire** was written for the laboratory described in this thesis (see Volume one, Chapter three). Therefore, some of the communication routines, particularly those for RS-232 communication, are unique to a given piece of laboratory equipment. Only the data analysis aspects of **Data Acquire** are laboratory independent. Also included in this chapter are the procedures for installing the needed driver software used by the NuBus data acquisition boards. The driver software and associated hardware described herein for IEEE-488 are also pertinent to the femtosecond apparatus [1]. If the reader's hardware is significantly different, then driver software section may not be applicable.

2.2 SYSTEM AND HARDWARE

The program requires a Macintosh II with a math coprocessor and at least a 12 inch monitor. It has been run with System 5 and System 6 (up to 6.0.4). The program has been written to utilize the math coprocessor, and will crash if the coprocessor is absent. It is possible to adjust the program, without changing any user written program code, to run without the math coprocessor. One must change the development environment settings and make appropriate substitutions for the pertinent C libraries. The procedure is outlined in Chapter 8.

In addition to the NuBus video card for the monitor, the Macintosh has been equipped with two NuBus data acquisition boards. The boards are the NB-M10-16H-9 [2a] and the NB-DMA-8-G [2b]. The NB-DMA-8-G is an IEEE-488 board with Direct Memory Access (DMA) capability, and is used for data acquisition through the LeCroy Waveform analyzer or the NB-M10-16H-9. The NB-M10-16H-9 is a multifunction input and output board, and is presently used as an analog-to-digital converter when acquiring

data through the boxcar averager. In addition, the NB-M10-16H-9 has the National Instruments Real-Time System Integration (RTSI) bus that transmits control signals to the NB-DMA-8-G to make high-speed data acquisition operations with DMA possible. Up to eight differential channels are available on the NB-M10-16H-9, although only one channel is currently in use. LabDriver software [3a] is used to program the NB-M10-16H-9, and the board averages the incoming analog signal when triggered from an external source. NI-488 driver software is used to program the NB-DMA-8-G [3b].

2.3 NI-488 SOFTWARE INSTALLATION

If the system file is replaced or damaged, the NB-DMA-8-G board software (National Instruments) must be reinstalled and the board reconfigured. This must be done even if system backups show the NI-488 Init and the NB-DMA-8-G board. There are two versions of the NI-488 driver software currently in use. Version 1 (August 1988) is being used by the laboratory described in this thesis, and version 2.3 (1989) is being used by the femtosecond apparatus [1]. One should note that updates in the driver software may require the use of specific versions of the Macintosh System (see the Appendix).

Below is given the instruction for installing version 1 of the NI-488 software. Since both Macintoshes in the **Caltech Femtosecond Laser Facility** use the same NB-DMA-8-G board, device and bus numbers for both are given. The installation procedure is given below. The installation software is on the **NI-488 for Macintosh** diskette (hereafter called **NI-488**) provided by National Instruments.

- A) Reboot the Macintosh from the **NI-488** diskette.
- B) Copy the NI-488 Init to the system folder on the hard disk.
- C) Restart computer from the **NI-488** diskette.

- D) Run the installer from the **NI-488** diskette and select the Macintosh II installation script.
- E) Reboot the Macintosh from the hard disk.
- F) Check the NB Boards control panel init for the NB-DMA-8-G board slot number to make sure the board is recognized. The check boxes are meaningless.
- G) Disconnect the GPIB connections on the back of the Macintosh. Test the installed software with the NB-DMA-8-G hardware by running the application **NI-488Test** from the **NI-488** diskette.
- H) Run **IBCONF** from the **NI-488** diskette to configure the NB-DMA-8-G board.
- I) For 047A, choose dev1 from the Devices menu and change the device name to **camctr**.
- J) For 047 there are 2 devices. From the Devices menu choose dev7 and change the device name to **boxcar**. Then choose dev13 and change the device name to **oma**.
- L) For 047A use the Buses menu to select bus4 and click the checkbox for **camctr**.
- M) For 047 use the Buses menu to select bus4 and click the checkboxes for **boxcar** and **oma**.
- N) Quit **IBCONF** and save the changes made.
- O) Reboot the computer to implement the changes.

The software for version 2.3 is on a disk entitled "NI-488 Distribution Disk for NB-DMA-8-G, NB-GPIB & GPIB-SE" (National Instruments). The differences between version 2.3 and previous incarnations is given in the update notes on the distribution disk. Included in the update notes are instructions for the removal of version 1 from the Macintosh System file. These notes are reproduced in the Appendix. The major point of concern is that a single init, NB Handler Init, now replaces both the NI-488 and LabDriver inits of version 1. At the present level of sophistication for IEEE-488 employed in Data

Acquire, the driver software update has not required any corresponding updates in the program code. The installation procedure for version 2.3 is given below. The distribution diskette is called **NI-488**.

- A) Reboot the Macintosh from the **NI-488** diskette.
- B) Copy the NB Handler Init and NB Boards control panel init to the system folder on the hard disk.
- C) Reboot the Macintosh from the hard disk.
- D) Check the NB Boards control panel init for the NB-DMA-8-G board slot number to make sure the board is recognized. The check boxes are meaningless.
- E) Disconnect the GPIB connections on the back of the Macintosh. Test the installed software with the NB-DMA-8-G hardware by running the application **NI-488Test** from the **NI-488** diskette.
- F) Run **IBCONF** from the **NI-488** diskette to configure the NB-DMA-8-G board.
- G) For 047A, choose dev1 from the Devices menu and change the device name to **camctr**.
- H) For 047 there are 2 devices. From the Devices menu choose dev7 and change the device name to **boxcar**. Then choose dev13 and change the device name to **oma**.
- I) For 047A use the Buses menu to select bus4 and click the checkbox for **camctr**.
- J) For 047 use the Buses menu to select bus4 and click the checkboxes for **boxcar** and **oma**.
- K) Quit **IBCONF** and save the changes made.
- L) Reboot the computer to implement the changes.

Finally, a few additional steps may be required for the Macintosh associated with the femtosecond apparatus. These steps are relevant to the data acquisition program parameter files, and often need to be done after a system upgrade, or if a catastrophic computer crash occurs. Problems are indicated if opening the parameter files give nonsense or error messages. The corrective procedure, which seems to work regularly, is given below.

- A) Make sure a copy of the DA param folder is in the System folder.
- B) Run the current version of the Data Acquisition program
- C) Select a parameter file. This may give an error message. Clicking the mouse gets rid of the error message and opens the parameter window. Fix each of the requested numbers.
- D) Save the changes to the parameter file. Next time the parameter file is opened, there should be no problem.

2.4 REFERENCES

1. M. Dantus, *Ph.D. Thesis*, California Institute of Technology, to be submitted.
2. (a) National Instruments, NB-M10-16 User Manual, February 1988.
(b) National Instruments, NB-DMA-8-G User Manual, 1988.
3. (a) National Instruments, LabDriver Software Reference Manual, January 1988.
(b) National Instruments, NI-488 Software Manual for the Macintosh, August 1988.

CHAPTER 3

OVERVIEW OF THE DATA ACQUISITION AND DATA ANALYSIS PROGRAMS

3.1 INTRODUCTION

In this chapter, **Data Acquire** and **Data Analysis** are described from the user point of view. Therefore, the focus is on the features available in the programs, and on what the user must do to use a particular feature. Information about what is happening with the programs internally via their code is reserved for Chapters 4 through 6. This chapter is divided into three parts. In Section 3.2, an overview of the programs is given. The overview discusses the program in the broadest sense. The various menus are described in Section 3.3. Section 3.4 provides more specific information on special features of the programs.

3.2 GENERAL OVERVIEW

The program makes extensive use of the Macintosh Toolbox and tries to abide by the Macintosh interface guidelines whenever possible. Windows are used to display and list the data, menus list the choices available to the user, dialog boxes are used to enter necessary parameters, and alert boxes post helpful hints and warnings.

The program initially displays two windows (the **Data Window** and **Plot Window**), but has the capacity for four (Figure 1). All windows are document windows with zooming capability. The **Data Window** is used to list the data points of a data file. The program recognizes unlinked text files and text files linked to **CricketGraph** or **Excel**. The plotting windows (**Plot Window** and **Plot Window Two**) display old or new data in graphical form. The **Help Window** is used to open a file for viewing, but not for text editing. If the **Help Window** is the front window, only the **File** menu is active.

If data acquisition is in progress, the data are plotted on the **Plot Window** as data acquisition proceeds. During data acquisition, the new data are not listed in the **Data Window**. Data are collected using a boxcar averager, a CAMAC crate based transient

digitizer, or by reconstructing data from previously saved mass spectra. For boxcar data, the **Plot Window** shows the current data scan as a series of dots on the screen. For multiple scans, the screen also shows the average of all previous scans as a solid line. In contrast, the **Plot Window** shows a solid line for each CAMAC data point since, unlike the boxcar, the crate is multiple-shot averaging over some number of channels (rather than some number of data points). When using a second boxcar channel, or averaging a second mass peak through the transient digitizer, those data are displayed in **Plot Window Two**. When rebuilding a decay from previously saved mass spectra, the rebuilt data are shown point by point in both the **Plot Window** and **Plot Window Two**.

Several data analysis features are available. This include Fourier transforms, convolution, NLS fitting, smoothing, selective editing, simple data manipulations, etc. A more complete list is given in Section 3.3. The data are plotted on the **Plot Window** as data analysis proceeds. When fitting or convolving data, the data scatter is displayed in **Plot Window Two**.

Except for NLS fitting and NLS convolution, the newly analyzed data can be viewed without disturbing the original data by using the **PREVIEW** button. The modified data are displayed for examination or comparison with the original data. In addition, the dialog box is redisplayed so that the current analysis parameters can be viewed or changed. Using the **PREVIEW** button also allows the user to examine the effects of different types of data analysis on a data file without having constantly to retrieve the original data. If an analysis button is pressed, *e.g.*, **CONVOLVE** in the Convolution dialog box, then the modified data will replace the raw data. In this case, the dialog box is not redisplayed. The modified data can then be analyzed further or saved to a file through the **Collection** menu. In the cases of NLS fitting and NLS convolution, a **PREVIEW** button is not used since the respective dialog boxes cover the screen. In the case of the NLS routines, the fits can be directly saved to a file by using the **SAVE FIT** button.

3.3 MENU SUMMARY

3.3.1 APPLE

The **Apple** menu is the standard one described in Reference 1. Choosing **About Data Acquire** or **About Data Analysis** in the Apple menu gives an entertaining display showing the program name and version number (*e.g.*, Figure 2). Choosing **Program Help** brings up a file-opening dialog box so that files can be opened to the **Help Window**.

3.3.2 FILE and EDIT

The **File** and **Edit** menus are the standard ones described in Reference 1. However, it must be kept in mind that the **File** menu items **New**, **Close**, **Save**, **Save As** and **Revert** operate only on the **Data Window**. Data files displayed on the **Plot Window** should be saved through the **Collection** menu (Section 3.3.4). All **Edit** menu items operate on the **Data Window** only.

2.3.3 COMMUNICATIONS (Data Acquire)

This menu brings up dialog boxes that are used to set the laboratory equipment data acquisition parameters. Choose **Unidex Port** for the optical delay line, **Boxcar Port** for the analog-to-digital board which digitizes the incoming boxcar signal, **LeCroy Port** for the CAMAC crate-based waveform analyzer, or **Spex CD2A** for the Spex 1870C monochromator Compudrive. The allowed values for an instrument's parameters are given in its dialog box. The delay line dialog box can be used to set the delay line position independent of data acquisition. Additionally, some auxiliary scan parameters (*e.g.*, the number of data points per scan, the number of scans, etc.) may be present in more than one dialog box. More details about the dialog boxes are given in Section 3.4.1.

As of this writing, both IEEE-488 and RS-232 commands are used. The boxcar utilizes routines from National Instruments LabDriver, version 1. The IEEE-488 interface installed in the Macintosh system file is also from National Instruments (NI-488, version 1). The Unidex driver and Spex CD2A Compudrive are powered using RS-232.

2.3.4 COLLECTION

This menu is divided into several groups of options. The first group (**Start and Pause**) starts, stops, and pauses data acquisition (Section 3.4.3). The second group (**DYE LASER 1 AC, DYE LASER 2 AC, E-Impact, Probe Spectrum, Pump Spectrum, MPI, and X Correlation**), relevant only to **Data Acquire**, is a set of labels to identify the type of data in a file. To activate a label, choose its menu item. Only one label may be active at a time. The active label is automatically included in the default filename when a new data file is saved. The third group (**Run Boxcar, Run CAMAC, Build CAMAC Decay**) identifies the source of the data, *i.e.*, the CAMAC crate, the Boxcar, or previously saved mass spectra. The menu item chosen identifies which data acquisition routines are to be used. See Section 3.4.7 for notes about the item **Build CAMAC Decay**. Finally, the last group (**Save Data (Text), Save Data (CricketGraph), Save Data (Excel)**) can be used to save a new data file. Files are saved as tab-delimited text, which may be unlinked or linked to **CricketGraph**, or **Excel** (see Chapter 4). The saved file is put into the folder determined by the Macintosh Hierarchical File System. Note that the **File** menu operates on the **Data Window**, not on the **Plot Window**.

To prevent the loss of data during data acquisition because of computer crashes or laboratory equipment failure, the most current averaged data file is automatically saved in text format (see Chapter 4) after every scan. The filename for **Plot Window** data is **Most Current Scan**. If **Plot Window Two** is in use, its contents are saved as **Most**

Current Scan Two. If multiplexing mass spectra, the filename is user specified. Saving every intermediate file means that only the current scan is lost in the event of a catastrophic crash. The files are created in the same folder that the application is in.

3.3.5 FITTING

Data fitting is done via the hierarchical **NLS Convolve (Data Analysis only)**, **NLS Fit** and **Convolve** menus. The menus allow for least-squares fitting of data to the chosen function, or convolution of data with a chosen response function (Section 3.4.4).

3.3.6 DISPLAY

The menu item **Selective Plot** is used to expand a portion of a data file for display on the **Plot Window**. The data range to be expanded is chosen by using the mouse. The program automatically rescales the axes based on the selected data range. The menu item **Selective Edit (Data Analysis only)** is used to edit the data file displayed on the **Plot Window** (Section 3.4.2).

3.3.7 TRANSFORM

The Transform menu provides capabilities for simple data manipulation. Smoothing of data is done by choosing **Smooth**. **Change Data By Constant** allows for multiplication/addition of the X or Y data values by a constant. **Change Data By Function** allows for transformation of the X or Y data values by simple functions. Whether changed by a constant or by a function, the X and Y data pairs remain associated. **Fourier Transform** permits a time-to-frequency Fourier transform, and **Fourier Parameters** displays the dialog box used to set the Fourier transform parameters (resolution and data windowing, Section 3.4.5).

3.3.8 FUNCTIONS (Data Analysis)

This menu is used to generate simple functions. The menu item chosen corresponds to the type of function generated. When a menu item is selected, a dialog box (Figure 3) is used to specify the function parameters, start position, step size, and number of points. The functional forms are given in Table 1.

3.3.9 WINDOWS

This menu lists all visible windows on the screen. The active window menu item is checked. When a window is opened, its name is appended to the end of the menu. If a window is closed, its menu item is removed from the menu. Choosing a window menu item brings that window to the front. The menu is continuously updated when the user clicks on various windows.

3.4 USE OF SPECIAL FEATURES

3.4.1 Communication Menu Dialog Boxes (Data Acquire)

In this section, a more detailed description is given for the settings of the various communication dialog boxes. Communication with the delay line and Spex CD2A Compudrive is done via RS-232 through the modem port. IEEE-488 is used for communication with the LeCroy CAMAC controller. The figures that will be presented attempt to show as many of the dialog box items as possible. However, the reader should note that not all of the items will necessarily be visible at the same time. The dialog box items that are displayed will depend on the mode of data taking employed. Most dialog items are self-explanatory, so this section will focus on items of special interest. Note that the initial default values for the various dialog items are defined in the source file **Data Acquisition.c**.

3.4.1.1 The Unidex Dialog Box

The delay line may be moved regardless of the status of data acquisition. The delay line dialog box is shown in Figure 4. To initiate movement of the delay line from a new or current start position without acquiring data, press the **New Start Position/Set Up For Manual Move** button. The delay line cycles once to the current Start Position, and redisplay the dialog box (with dialog items for manual movement visible). Single increments (up to 128) from the current Start Position are made by clicking the button **Increment Unidex**. The dialog box displays the number of manual increments made, and the position of the delay line (in steps) from the current Start Position. Another set of increments using the same Start Position is made by pressing the **Repeat Increment Cycle** button, and then pressing the **Increment Unidex** button. As long as the delay line is in manual mode, the dialog box always reappears after the delay line has finished moving. Note that the **Repeat Increment Cycle** or **New Start Position/Set Up For Manual Move** buttons reset the increment and step counters to zero. To terminate the manual incrementation, click the **OK** or **CANCEL** buttons.

Because of the way the delay line routines are written, the delay line routines are called in the same order as if one were taking data. This means that whenever a set of increments are started from a new start position, the delay line must first cycle once back to home to be properly initialized for the increment routine.

The delay line position, from the current Start Position, equals the increment number times steps/data point. If steps/data point changes while a set of increments is in progress, the delay line will move forward by a large amount (increasing steps/data point) or may move backwards (decreasing steps/data point). For example, consider 4 increments starting with steps/data point equal to 10,000. The first increment moves the delay line by 10,000, and the second increment positions the delay line at 20,000. If the steps/data point is now increased to 20,000, the third increment positions the delay line at 60,000. If the

steps/data point is now put back to 10,000, the fourth step moves the delay line backwards to 40,000.

3.4.1.2 The CAMAC Crate Dialog Box

The CAMAC crate dialog box is shown in Figure 5. Normally the values for the **Pretrigger Size** (set to 0), **Slot #** (set to 7), **Offset** (set to 0), or **Data Accumulation Type** (set to SUM) need not be changed. The **Slot #** refers to the slot number of the 100 MHz transient digitizer (LeCroy 8818A) in the CAMAC crate, not to a slot in the Macintosh. The setting for the **Memory Size** (default setting of 32K) has been changed in the past, but the 32K setting is normally adequate. The settings for the parameters labelled as **Sampling Period** and **Record Length to Average** define which portion of the mass spectrum is displayed on the **Plot Window**.

The CAMAC crate dialog box can be configured in 3 modes. First, the total mass spectrum (defined by the **Sampling Period** and **Record Length to Average**) may be collected. This is the default setting. When taking a total mass spectrum, make sure that the **Delay Line**, **AutoStore mode**, and **Average a Mass** checkboxes are all unchecked. Second, single mass peaks may be averaged in a manner analogous to using the boxcar. Collect single mass peaks if only a specific part of the total mass spectrum is of interest. Third, the total mass spectra may be collected and automatically saved for future analysis. The latter two modes are often used in conjunction with the optical delay line (see Volume 1, Chapter 3, Section 3.4.3) for obtaining pump-probe transients. If the **Delay Line** checkbox is on, the delay line moves in between taking mass spectra according to the parameters in the Unidex dialog box (Section 3.4.1.1). To collect a single mass peak, make sure that the **Average a Mass** checkbox is checked. If the **Average a Mass** checkbox is unchecked, then the total mass spectrum will be collected.

To set up for a single mass collection, check the **Average a Mass** and **Delay Line** checkboxes. When the **Average a Mass** checkbox is checked, the **SELECT CHANNELS TO AVERAGE** button appears. Clicking the **SELECT CHANNELS TO AVERAGE** button brings up a dialog box titled **Select CAMAC Channels** (Figure 6). The **Select CAMAC Channels** dialog box is used to specify the peak position, in microseconds, of the mass peak to be averaged, the width about the peak position, and the first point of the 10 point background. The peak position of the desired mass, the x-axis value of the peak when acquiring total mass spectra, is entered as the value for **Mass Peak**. The 10 points used for the background calculation start with the input value plus the next 9 points. Although 4 channels are indicated, only 1 channel is presently active. Press the **OK** button to return to the CAMAC crate dialog box.

To save mass spectra automatically in order to build decays later, the **AutoStore mode** and the **Delay Line** checkboxes must be checked. When the **AutoStore mode** checkbox is on, the acquired mass spectra are automatically saved as separate files before going on to the next mass spectra. When data acquisition is started, a standard dialog box for opening files appears requesting the user to specify the global filename (see Chapter 3) to use when saving the mass spectra (Figure 7). If no global filename is provided, then **Most Current Scan** is used by default. Press **SAVE** or **CANCEL** to continue data acquisition. On the first scan, the acquired mass spectra are shown on the **Plot Window**, and the spectra are saved using the global filename provided. On each successive scan the program reopens the previous mass spectra file for the given delay line position, averages the new mass spectra with the old mass spectra, and then saves the newly averaged mass spectra under the same filename. The previously averaged mass spectra are lost. The mass spectra for the current scan is shown in the **Plot Window**, and the averaged mass spectra is displayed in **Plot Window Two**.

3.4.1.3 The Boxcar Dialog Box

The boxcar dialog box, shown in Figure 8, is the simplest of the 4 communication dialog boxes. It is used to set up the parameters for the analog-to-digital board (National Instruments NB-M10-16H-9). This board digitizes the incoming signal from the boxcar. The dialog box has a total capacity for 4 channels. All 4 channels are active with respect to the analog-to-digital board, but only channels 1 and 2 are fully integrated with the rest of the program. Note that the **Gain** value is limited to 1,2,4, or 8 for each active channel, and is normally set at 1. Data can be taken while scanning either the delay line or the Spex 1870C monochromator. The monochromator is controlled by a Spex CD2A Compudrive (Section 3.4.1.4), and the delay line is controlled by a Unidex 1 programmable driver (Section 3.4.1.1). Additionally, the dialog box may be used to set auxiliary scan parameters. These parameters are the number of data points per scan, the number of scans, and the question of whether to scan the delay line or monochromator.

3.4.1.4 The Spex CD2A Dialog Box

The Spex CD2A dialog box (Figure 9) is used to set the scan parameters for the Spex CD2A Compudrive. The CD2A controls the Spex 1870C monochromator. The dialog box has been written to allow the monochromator to be scanned continuously or in increments. However, in order to synchronize the monochromator with data acquisition, one must scan the monochromator in increments.

The dialog items for the CD2A are as follows. **Start Position** is the beginning wavelength of the scan. **Number of Scans** is the number of wavelength scans desired. **Scanning Mode** determines whether the monochromator is to be scanned continuously, or in increments. **Increment** is the wavelength step size when scanning in burst mode, and **Dwell Time** is the time to wait between individual increments. **Rate** indicates the scan speed if scanning in a continuous mode. **Scan Delay** is the time to wait between

individual scans. **CD2A Remote** (not active) is for automatic RS-232 configuration. Note that the maximum end wavelength capability for the CD2A is 6500Å.

Computer control of the Spex during data acquisition is handled as follows. The CD2A sends back messages when it has finished moving to a particular wavelength. The program waits for these messages before averaging data. However, the CD2A RS-232 command list does not allow one to make the CD2A wait for any reply from the Macintosh before continuing to the next wavelength position [1]. The CD2A moves independently of the Macintosh until it completes the requested number of scans, or is sent a stop command by the user stopping the scan. If the scan command is sent again, the CD2A starts scanning at the beginning of the first scan. As a result, no ability to pause in the middle of a scan exists. Thus the pause option in the **Collection** menu is turned off. The **Dwell Time** is used to hold the CD2A at the desired wavelength while data acquisition is in progress. Typically, the **Dwell Time** is set to the time required to average a data point plus at least two seconds. The extra two seconds give the program time to plot the data, update everything and get ready for the next data point.

Finally, the CD2A is configured as follows for two-way RS-232 communication. First, the CD2A configuration parameter number 21 must be set manually to 1010. This parameter also specifies the structure of messages sent by the CD2A to the Macintosh. Second, the **Remote** key on the CD2A keyboard is pressed. If no error messages occur, then configuration for RS-232 is complete. Although provisions have been made in the dialog box to support automatic configuration for RS-232, the CD2A does not currently support that option. Furthermore, for some reason the CD2A RS-232 baud rate, parity, and number of character bits cannot be changed. Thus, just before data acquisition begins, the program sets the RS-232 parameters of the Macintosh serial drivers to match the CD2A. Procedures for examining and setting configuration parameters are given in the Spex CD2A manual.

3.4.2 Selective Plotting

Selective plotting is done by choosing **Selective Plot** or **Selective Edit (Data Analysis only)** from the **Display** menu. **Selective Plot** allows the user to expand selectively a chosen part of a data file, which is displayed on either plotting window. The selected data are replotted and rescaled automatically. **Selective Plot** is also available through the **NLS Fit** menu, and enables the user to fit different portions of a data file. **Selective Edit** allows for editing of data files displayed on the **Plot Window** only.

When **Selective Plot** is chosen, the program waits for the user to select a data range with the mouse. Press the mouse button at the starting X-value, drag the mouse in the positive X direction to the end X-value, and release the mouse button. During the dragging process the data range being selected will be shaded. Once the range is selected, the **Plot Window** is redrawn, and control returned to the main event loop. To select another data range for the same data file, select **Selective Plot** again. The **Plot Window** redisplay the entire data file so that the new data range can be selected.

The routine used by **Selective Plot** is not dependent on the data source. A variable called **NumOfPlotPts** has been defined, and is set equal to the length of an individual data scan or data file. For the boxcar, **NumOfPlotPts** = number of data points, whereas for the CAMAC, **NumOfPlotPts** = record length-10 (the first 10 CAMAC channels are ignored). **NumOfPlotPts** is not used for files fit through the **NLS Fit** menu. In the **NLS Fit** menu, the number of data points in the file is used.

If **Selective Edit** is chosen, the user is asked to specify the start and end X-values for the X-axis (Figure 10). If the entered X-value is not an actual X-value, then the entered value is rounded off to the nearest actual X-value. The start value is always less than or equal to the end value. If the values are entered in reverse order, they are automatically turned around. If the entered values are outside the actual range of X-values, the values are set to the first or last X-value of the file. Clicking the **RELOT** button plots

the selected range of data on the **Plot Window**. Click the **SAVE** button to save the newly edited data file. Like **Selective Plot**, **Selective Edit** first displays the entire data file on the **Plot Window** to facilitate data range selection.

3.4.3 Data Acquisition Control

Depending on how data is being acquired, the X and Y axes on the plotting windows have different meanings. Table 2 summarizes the axis units with respect to the type of data being taken.

A data scan can be interrupted when the program makes a pass through the main event loop. In this program, a pass through the main event loop is made after every data point. This is preferable to making a pass after an individual scan is finished. Since a data point is taken every few hundred laser shots at 100 Hz, it could be a long wait until a scan is finished. If data were taken at a faster rate (e.g., a data point every 3 laser shots at 20 Hz), then one may consider passing through the main event loop after every scan to avoid being limited by the time needed to traverse the event loop.

Data acquisition is controlled using the first two items in the **Collection** menu. The first item starts and stops data acquisition. It is called **Start** prior to data acquisition, and **Stop** during data acquisition. The second item pauses or resumes data acquisition. It is called **Pause** during data acquisition, and **Continue** when data acquisition is paused. Start Data acquisition by choosing **Start**. Choose **Stop** to stop data acquisition, or **Pause** to pause data acquisition. The menu items are accessed through either the keyboard or the mouse. The keyboard commands are **⌘-G** (**Start/Stop**) and **⌘-H** (**Pause/Continue**). To select a menu item with the mouse, put the cursor on the menu bar and hold the mouse button down until the **Collection** menu appears. For either **⌘-G** or **⌘-H**, the data acquisition status flags and menu item names are adjusted, the Macintosh serial drivers opened or closed as necessary, and control is returned to the main event loop. Avoid any

other commands during data acquisition, since other commands have no regard for the status of external equipment.

The effects of **Stop** and **Pause** on data acquisition are as follows. If the boxcar is being used, **Stop** results in the current scan being lost. When using the CAMAC crate, data acquisition stops as soon as the crate is finished with the current data point. If **Pause** is chosen, the current scan stops after taking the current data point. Choose **Continue** to resume data acquisition with the next data point. However, see the discussion on the Spex CD2A dialog box (Section 3.4.1.4) for the one exception regarding the use of **Pause**. If the user decides to stop after pausing, **Stop** should be chosen. Two other cases of data acquisition are important, and for both cases data acquisition control is equivalent to using the boxcar. Case one is when the CAMAC crate is used to monitor a single mass peak. Case two is when a decay is rebuilt from previously saved mass spectra.

The number of data points per scan, represented by the variable **NumOfDataPts**, is set in the boxcar dialog box. If a previously saved data file has been opened to the **Plot Window**, check the value of **NumOfDataPts** before taking another data scan. When a saved data file is opened, **NumOfDataPts** is always set to the number of data points in that data file.

One other important experimental parameter is the time delay between successive scans when acquiring data through the boxcar. The time delay (in seconds) is set through a dialog box, which appears immediately after **%-G** is chosen. The default value is 1 second (Figure 11). In the pump-probe experiment, the signal at the end of a scan is often quite different than it is at the beginning of a scan. The time delay should be sufficiently long to prevent data early in a scan from being biased by data late in a scan. Note that regardless of how data are acquired, the dialog box requests confirmation to start data acquisition.

Under special circumstances the user may pause data acquisition after completing a scan, open a previously saved file, and resume data acquisition with the next scan without

having to start from scratch. To resume with the next scan, be sure to reopen the file **Most Current Scan** just before continuing data acquisition. This luxury exists when using only one boxcar channel or when using the CAMAC crate to monitor one mass peak, and is due to the way memory for data files is allocated. It does not exist for data using **Plot Window Two** (Section 3.4.6).

3.4.4 Fitting and Convolution

The nonlinear least-squares fitting and convolution are driven from the **NLS Fit**, **Convolve**, and **NLS Convolve** menus. The least-squares fitting and convolution routines are taken from Reference 8. The nonlinear least-squares routines are based on Marquardt's algorithm (Section 3.4.4.1). Convolution is done in one of two ways. The **Convolve** menu uses the fast Fourier transform (Section 3.4.4.2), and the **NLS Convolve** menu uses numerical integration coupled with Marquardt's algorithm to do a nonlinear least-squares fit of the convolution data (Section 3.4.4.3). Any preparation of data files must be done beforehand.

3.4.4.1 Nonlinear Least Squares Fitting

The **NLS Fit** menu functions correspond to the functional forms to which the data will be fit. If the **Convolve** menu item **Convolve A File** is chosen, then the file that is currently opened to the **Plot Window** will be convolved with a chosen response function. If one of the functions in the **Convolve** menu is chosen, then that function will be convolved with a chosen response function. The convolution routines have been tested for data files up to 256 points, but the ultimate size of a data file is limited by the RAM.

NLS fitting options are set through the **NLS Fit** dialog box (Figure 12). The user may fit all or part of a data file, show all or part of a data file while fitting, show the scatter of the data about the fit (raw data minus the fit), and regulate the step size that the fitting

routine takes as it searches for the minimum. If the **Fit Entire File** check box is checked, the entire data file is fit. If it is unchecked, the program waits for the user to select what part of the data file to fit. Until the **Fit Entire File** box is rechecked, the routine will continue to fit the last selected data range. Section 3.4.2 explains how to select a portion of a data file. If only a portion of a data file is being fit, the fit may be displayed in two ways. The user may display the fit and the entire data file, or just show the fit and the portion of the data file being fit. The Marquardt Parameter and its multiplier regulate the fitting routine step size. The larger the multiplier, the smaller the step size. The default values are those given in Reference 2.

The Fit dialog box has four buttons: **FIT DATA**, **SAVE FIT**, **RESET**, and **CANCEL**. The **CANCEL** button behaves as usual. The **FIT DATA** button starts the fitting routine, given an initial guess for the fitting parameters, for the range of data selected. The **RESET** button reinitializes the fitting routine back to square one. To fit a new data range (but not the whole file) to the current function, it is easiest to press the **RESET** button and then select the new data range. Otherwise the **Fit Entire File** box must be rechecked, the whole data file refit, the desired fitting function chosen, and then the new data range reselected. The **SAVE** button saves the current fit, and displays the current selected data range of a file plus the current fit on the **Plot Window**.

In the **NLS Fit** dialog box, the check boxes next to the parameter boxes allow the user to freeze the value of a parameter (box unchecked). Table 1 shows the mathematical form for each fitting function. The initial guesses of the parameters are based on the data file and are most accurate for Gaussian, Lorentzian, Hyperbolic secant squared, and line functions. For the exponential step function, only the baseline is considered known. The other three variables are assigned arbitrary values. The single exponential function is more difficult, especially when there are zero or negative data points. The initial guesses are made using a logarithmic transform. If the file has data points that are zero or negative, the

initial guesses for a single exponential fit must be entered manually. Fit the data by unchecking the **Fit Entire File** checkbox and select the entire data file. The double exponential is even more difficult. Only parameters A1, A4, and A6 are estimated, and their reliability is uncertain. Parameters A2, A3, and A5 are assigned an arbitrary value. The best way to fit a double exponential is to fit different parts of the file to lines and single exponentials first to better estimate the fitting parameters.

When fitting a selected portion of a file, the initial guesses are recalculated on the basis of the selected data range. The new initial guesses are not displayed. For the bell shaped functions (Gaussian, Lorentzian, and Hyperbolic secant squared), the guesses are calculated in the same manner as for the entire data file. In the case of the exponential step and double exponential, it is not clear how one would calculate good initial guesses. Therefore, the new values are simply the ones entered by the user. Calculations for a single exponential are straightforward, but there is a problem with the recalculated initial guesses if any data is zero or negative. Since a logarithmic transform is impossible for zero or negative data, the program finds the most negative value in the data range and then adds that value + 0.075 to every point to make the whole file positive. The value 0.075 ensures that the log transform is sufficiently small for a stable fit. Then, using the shifted data file, the fit parameters are estimated and the fit calculated. The data are shifted back to the original values, and everything is plotted on the **Plot Window**. Since the fit parameters are estimated by making a logarithmic transformation on the exponential, shifting the data introduces errors in calculating good initial guesses. Thus the first fit for shifted data is rarely adequate.

There is a final point regarding the fitting routine. If the routine hits a singularity because of a bad initial guess, then a dialog box appears (Figure 13). The dialog box gives the user three options: Continue fitting, terminate fitting, or terminate the program. In practice, the program does not have to be aborted unless the error is in memory allocation.

The user may continue NLS fitting (even though the results are erroneous), or terminate fitting and try a new set of initial guesses. Since the fitting method is sensitive to the input parameters, getting the dialog box is not uncommon.

3.4.4.2 Convolution

When a particular function in the **Convolve** menu is chosen, the function is convolved with a response function (Gaussian, Lorentzian, or Hyperbolic secant squared) to simulate the data file. The **Convolve A File** option convolves, but does not simulate, an existing data file with a chosen response function. Thus, functions whose forms are not explicitly listed in the **Convolve** menu can be convolved.

The operational difference between the two convolution options is simple. Convoluting to a function assumes that one is trying to reproduce a data file as the convolution of a response function with one of the functions listed in the **Convolve** menu. The convolution dialog box allows the user to vary all the function parameters, and the FWHM of the response function. When convoluting, the program generates the function selected (given the given parameters) and convolves the generated function with the chosen response function. The quality of the fit is judged by the value of the chi-square between the real and simulated data. Like the **NLS Fit** dialog box, the user can also display the data scatter (raw data minus convolved data). In contrast, **Convolve A File** assumes that the user wants to convolve the data file itself with a response function. Thus, the only variable parameters are the FWHM of the response function and the baseline of the data file.

Regardless of the convolution option, the convolution routine displays the convolution dialog box (Figure 14). Unlike NLS fitting, initial guesses for the function parameters must be provided by the user. To examine the convolved data, but not override the original data, use the **PREVIEW** button. If a function listed in the menu is being

convolved, both the original data and convolved data are drawn onto the **Plot Window**. When **Convolve A File** is chosen, only the convolved file is displayed. The dialog box is redisplayed after plotting is finished. The chi-square between the convolution file and the real data file is calculated and shown in the dialog box, and the type of fitting function and response function convolved is indicated on the **Plot Window**. Pressing the **CONVOLVE** button performs the same convolution as the **PREVIEW** button, but replaces the original data by the new data. The new data are plotted, but the dialog box is not redisplayed. Pressing the **CANCEL** button will dismiss the dialog box.

3.4.4.3 Nonlinear Least Squares Convolution

When a function in the **NLS Convolve** menu is chosen, the function is convolved with a response function (Gaussian, Lorentzian, or Hyperbolic secant squared) and fit to the experimental data using the nonlinear least-squares (NLS) fitting method described in Section 3.4.4.1. Thus the visual operation of NLS convolution is very similar to that of NLS fitting. Choosing an item in the **NLS Convolve** menu brings up the dialog box shown in Figure 15. Pressing the **Convolve** button initiates the NLS convolution procedure. The dialog box is redisplayed when the calculation is finished. The chi-square between the convolved file and the real data file is calculated and displayed, along with the current best-fit parameters, in the dialog box. Both the real data and convolved data are drawn onto the **Plot Window**. Like the **NLS Fit** dialog box, the user can also display the data scatter (raw data minus convolved data). Pressing either the **SAVE** or **CANCEL** button dismisses the dialog box. If **SAVE** is pressed, then the convolved file can be saved. The **CANCEL** button functions as usual. Currently, all options present in NLS fitting are available for NLS convolution.

There is a critical difference between NLS fitting and NLS convolution. The values of the convolved function and its derivatives are calculated by numerical integration in NLS

convolution. In NLS fitting, the function and its derivatives are calculated analytically. Analytical expressions could be used for NLS convolution, but the expressions are very cumbersome. The additional calculations required by using numerical integration mean that the time required for the overall calculation is significantly longer than for NLS fitting alone. Therefore, during every fitting cycle, the convolved data is plotted as each point is calculated. After each cycle, the current best-fit is drawn through the raw data on the **Plot Window**. In this sense, NLS convolution mimics data acquisition.

Like the NLS fitting routine, a dialog box (Figure 13) appears if an error occurs because of a bad initial guess. In addition, the same dialog box appears if the mouse button is depressed during NLS convolution. Thus, the mouse button serves to pause the program. This feature should be useful since the NLS convolution calculations could take some time to complete.

3.4.5 Data Manipulation

Simple data manipulation is done using the **Transform** menu. The user can smooth data files, add or multiply constants to a data file's X and Y values, take a time-to-frequency Fourier transform, and set the parameters (resolution and type of data window) for the Fourier transform. All of the functions used to smooth data and take the Fourier transform are taken from Reference 2.

As mentioned in Section 3.2, analyzed data can be previewed using the **PREVIEW** button. This option is available for data smoothing, changing data values, and for Fourier Transforms. Previewing the data allows the user to see the analyzed data without losing the original data. The relevant dialog box reappears after plotting is completed to allow the user to examine the current analysis parameters, or to observe the effects of different parameter values easily. The **PREVIEW** button also allows the user to examine the results of different types of data analysis on a data file without having to

retrieve the original data. If an analysis button is pressed, *e.g.*, **SMOOTH** in the Smooth dialog box, then the modified data replaces the raw data. In this case, the dialog box is not redisplayed. The modified data can then be analyzed further or saved to a file through the **Collection** menu.

Data smoothing and changing data values are straightforward. For smoothing, the size of the smoothing window is set using a dialog box (Figure 16). If the smoothed data are previewed, then both the smoothed data and original data are plotted. Data values can be changed either by a constant (Figure 17) or by a function (Figure 18). In either case, the desired parameters are set in the appropriate dialog box. Pressing the **CANCEL** button will dismiss the dialog box.

The Fourier transform is set up in two ways, and both cases involve the input of real data. Both methods are in the Fourier transform dialog box (Figure 19). The first method (called Total transform) uses the routine entitled `four1()` [2]. The method can handle complex numbers, but the imaginary parts are set to zero. The real or imaginary components of the positive frequencies, the transform magnitude, or the phase angle can be displayed. The zero and Nyquist frequencies are not plotted, as they would dominate the plot. The second method (called Real frequency FT) uses the routine `realft()` [2], and can handle only real numbers. In this case, the real data is split into two parts. One of the real parts is used as a pseudo imaginary component of the data. The actual frequencies are extracted after performing additional operations on the transformed data [2].

The parameters for the Fourier transform are set by choosing the menu item **Fourier Parameters**. A dialog box (Figure 20) appears, giving the user various options. To reduce leakage problems in the Fourier transform, the data may be windowed. The program defaults to a square window (equivalent to no windowing) upon startup. The other three alternatives are a Hanning, Parzen, or Welch window [2]. The transform

resolution is defined by the extent of zero padding. The zero padding parameter is also used for the convolution routines, since convolution utilizes the Fourier transform.

3.4.6 Using the Second Plot Window

Plot Window Two is used for both data acquisition and data analysis. It displays newly acquired data, or the scatter between a fit and raw data. Due to the way data is kept in RAM, no data analysis on **Plot Window Two** data is allowed. Except for the **Display** menu, all data analysis routines require that **Plot Window Two** be closed. In order to use the data analysis routines on **Plot Window Two** data, the data must be saved through the **Collection** menu and reopened to the **Plot Window**. This prevents any inadvertent loss of data.

3.4.7 Reconstructing Transients from Mass Spectra

Pump-probe transients can be reconstructed from previously saved mass spectra. All the previous mass spectra must possess the same number of data points. The saved mass spectra must have a filename of a definite form (see Chapter 3)

To set up the parameters for reconstructing decays, choose the **Collection** menu item **BUILD CAMAC DECAY**. When the menu item is chosen, the **Reconstruct CAMAC Decay** dialog box appears (Figure 21). The **Start Position** value is the delay line position, in millimeters from the zero, for the first mass spectrum file. **Increment per file** is equal to the increment taken by the delay line when the mass spectra were originally acquired. **Number of data points/file** is the length of the mass spectra files in data points. **Number of files** is the total number of mass spectrum files to be used for the reconstruction process. The dialog box permits two decays to be reconstructed at a time. The peak position values for the mass peaks of interest are given in microseconds (the x-axis value), and a single peak width and background are used for both peaks. The

background is calculated using the input point plus the next 9 points. The **BUILD DECAY** button saves the parameters, and the **CANCEL** button aborts the reconstruction procedure.

If the **BUILD DECAY** button is chosen, a standard dialog box for opening files appears requesting the global filename (see Chapter 3) to be used (Figure 22). Choose either the **SAVE** or the **CANCEL** button to dismiss the dialog box. If **SAVE** is pressed, then the program is ready to reconstruct decays. Like the **Reconstruct CAMAC Decay** dialog, choosing the **CANCEL** button aborts the reconstruction procedure.

The reconstruction process is initiated in the same way as an ordinary data acquisition scan. Simply choose **%-G**. The decay corresponding to the value input for mass peak one (data point one in the **Reconstruct CAMAC Decay** dialog) appears in the **Plot Window**. **Plot Window Two** displays the decay for mass peak two (data point two in the **Reconstruct CAMAC Decay** dialog). The reconstruction routines respond to **%-G** and **%-H** as if data acquisition were in progress (Section 3.4.3). To reconstruct another set of transients, simply repeat the procedure starting with the **Collection** menu item **BUILD CAMAC DECAY**.

3.4.8 Saving Data to Files

Data on either the **Plot Window** or **Plot Window Two** can be saved using the **Collection** menu. Files can be created that are unlinked, linked to Excel, or linked to CricketGraph. The data on the active window are saved.

3.5 REFERENCES

1. Spex Industries, CD2A Owner's manual (1985).
2. W. H. Press, B. P. Flannery, S. A. Teukolsky, and W. T. Vetterling, *Numerical Recipes in C* (Cambridge Univ. Press, Cambridge, 1988).

TABLE 1
FUNCTIONAL FORMS

Gaussian

$$y = A_1 * \exp[-((x-A_2)/A_3)^2] + A_4$$

$$FWHM = 2 * \sqrt{\ln(2)} * A_3$$

Lorentzian

$$y = A_1 * [1+((x-A_2)/A_3)^2]^{-1} + A_4$$

$$FWHM = 2 * A_3$$

Hyperbolic Secant Squared

$$y = A_1 * \{2/(\exp[((x-A_2)/A_3)] + \exp[-((x-A_2)/A_3)])\}^2 + A_4$$

$$FWHM = 1.7627 * A_3$$

Single Exponential

$$y = A_1 * \exp[-((x-A_2)/A_3)] + A_4$$

Double Exponential

$$y = A_1 * \{\exp[-((x-A_4)/A_2)] + A_5 * \exp[-((x-A_4)/A_3)]\} + A_6$$

Exponential Step

$$y = A_1 * [1-\exp((x-A_2)/A_3)] + A_4 \text{ for } ((x-A_2)/A_3) < 0$$

$$y = A_4 \text{ for } ((x-A_2)/A_3) \geq 0$$

Line

$$y = A_1x + A_2$$

TABLE 2**AXIS UNITS FOR THE DATA ACQUISITION PROGRAM**

<u>Mode</u>	<u>X axis</u>	<u>Y axis</u>
Boxcar (delay line)	Unidex units* (microns)	volts
Boxcar (Spex CD2A)	wavelength (Angstroms)	volts
CAMAC	microseconds	counts
Reconstruct** CAMAC Decay	Unidex units (millimeters)	counts/1000
CAMAC*** Decay (Single Mass)	Unidex units (microns)	counts

***A Unidex unit equals 1 micron per step**

****Building a decay from previously saved mass spectra**

*****Building decay by averaging over a single mass with the CAMAC crate based transient digitizer**

FIGURE CAPTIONS

- Figure 1:** The **Data Analysis** application when it is launched from the Finder desktop. The plotted data file is arbitrary, and is used to make all menus active. The display for **Data Acquire** is very similar, except that the **Functions** menu is deleted and replaced by the **Communications** menu.
- Figure 2:** The credits display for **Data Analysis**. The display for the **Data Acquire** is analogous. Note that the actual display consists of white text on a black background. The white and black colors have been inverted for the sake of clarity.
- Figure 3:** The dialog box for generating functions using the **Functions** menu. In this case, the function being generated is a Gaussian. The functional forms are given in Table 1.
- Figure 4:** The dialog box used to enter the parameters for communication with the Aerotech Unidex 1 controller. The controller regulates the movement of the Aerotech delay line. The delay line can be moved independent of data acquisition.
- Figure 5:** The dialog box used to enter the parameters for communication with the LeCroy CAMAC crate 6010 Magic controller. The CAMAC crate may be used to obtain total mass spectra or to perform single mass peak averaging. Additionally, one may use the dialog box to set the number of scans.
- Figure 6:** The dialog box for setting the parameters for averaging single mass peaks using the LeCroy CAMAC crate. The parameters identify the number of peaks to be averaged, their mass spectrum positions, the peak width to be averaged, and the place to start calculating the signal background.
- Figure 7:** The dialog box for entering the global filename to be used when automatically saving total mass spectra for future use.
- Figure 8:** The dialog box used to enter the parameters for the National Instruments NB-M10-16H-9 analog-to-digital board. The board digitizes the analog signal coming from the EG&G boxcar. Data through the boxcar are taken while scanning either the delay line or the Spex 1870C monochromator. Additionally, the dialog box may be used to set auxiliary scan parameters. These parameters are the number of data points per scan, the number of scans, and the question of whether to scan the delay line or monochromator.
- Figure 9:** The dialog box used to set the parameters for communication with the Spex CD2A CompuDrive. The CD2A controls the Spex 1870C monochromator. Currently, the CD2A must be configured manually for the correct two-way RS-232 communication parameters.
- Figure 10:** The **Selective Edit** dialog box. The dialog box allows the user to edit a data file. If the **REPLOTT** button is chosen, the edited data file is plotted and the original data is lost. If the **PREVIEW** button is chosen, the edited data file is displayed but the original data is not replaced.

- Figure 11:** The dialog box asking the user to confirm or abort data acquisition. When using the boxcar, it also allows you to specify the time delay between successive data scans.
- Figure 12:** The NLS fitting dialog box. If the **FIT DATA** button is chosen, the original data file and each successive NLS fit are displayed for each cycle through the NLS fitting routine. The NLS fit may be saved to a new file using the **SAVE FIT** button. If an error occurs during the calculations, the dialog box shown in Figure 13 appears.
- Figure 13:** The dialog box that appears if calculational errors occur during NLS Fitting (see Figure 12) or NLS Convolution (see Figure 15), or if the user wishes to interrupt NLS Convolution. The dialog box also appears if the user wishes to interrupt NLS Convolution. If the **CONTINUE** button is chosen, the program continues from the point of interruption. If the **STOP PROCEDURE** button is chosen, the calculation stops at the point of interruption, and returns the current results. If the **ABORT PROGRAM** button is chosen, the program quits.
- Figure 14:** The convolution dialog box. One may convolve a response function with a specific functional form, or with an arbitrary data file. The functional forms are given in Table 1. If the **CONVOLVE** button is chosen, the convolved data are displayed and the original data is overridden. The convolved data, if one is convolving a response with a specific functional form, may be compared to the original data (without overriding the original data) by using the **PREVIEW** button. If the **PREVIEW** button is chosen, the original data and the convolved data are displayed simultaneously.
- Figure 15:** The NLS convolution dialog box. One may convolve a response function with a specific functional form, or with an arbitrary data file. The functional forms are given in Table 1. If the **CONVOLVE** button is chosen, the convolved data are displayed and the original data is overridden. The convolved data, if one is convolving a response with a specific functional form, may be compared to the original data (without overriding the original data) by using the **PREVIEW** button. If the **PREVIEW** button is chosen, the original data and the convolved data are displayed simultaneously. If an error occurs during the calculations the dialog box shown in Figure 13 appears. If the mouse button is depressed during the calculations the dialog box shown in Figure 13 appears.
- Figure 16:** The dialog box used for smoothing data over a user-specified data point window. If the **SMOOTH** button is chosen, the smoothed data are displayed and the original data are overridden. The smoothed data may be compared to the original data (without overriding the original data) by using the **PREVIEW** button. If the **PREVIEW** button is chosen, both the smoothed and original data file are displayed.

- Figure 17:** The dialog box for changing the X and Y data values by a constant. The X-Y data pairs remain associated. A constant may be added to the data, or the data may be multiplied by a constant. If the **CHANGE** button is chosen, the changed data are displayed and the original data are overridden. The changed data may be examined (without overriding the original data) by using the **PREVIEW** button. If the **PREVIEW** button is chosen, the changed data are displayed but subsequent data analysis begins with the original data file.
- Figure 18:** The dialog box for changing the X and Y data values by a simple function. The X-Y data pairs remain associated. If the **CHANGE** button is chosen, the changed data are displayed and the original data are overridden. The changed data may be examined (without overriding the original data) by using the **PREVIEW** button. If the **PREVIEW** button is chosen, the changed data are displayed but subsequent data analysis begins with the original data file.
- Figure 19:** The Fourier Transform dialog box. Either the complex or real-valued Fourier transform may be taken. Currently, the transform is from the time-to-frequency domain only. For the complex transform the real, imaginary, magnitude, or phase angle of the transform may be plotted. If the **TRANSFORM** button is chosen, the transformed data are displayed and the original data are overridden. The transformed data may be examined (without overriding the original data) by using the **PREVIEW** button. If the **PREVIEW** button is chosen, the transformed data are displayed but subsequent data analysis begins with the original data file.
- Figure 20:** The Fourier Transform parameters dialog box. The parameters determine the shape of the window to be applied to the data prior to the transform, and the extent of zero padding applied to the original data file.
- Figure 21:** The dialog box used to set the parameters for reconstructing decays from previously saved mass spectra. The decays of two peaks are reconstructed. The parameters identify the mass spectrum positions of the peaks, the peak width to be averaged, and the place to start calculating the signal background.
- Figure 22:** The dialog box for entering the global filename to be searched for when reconstructing decays from previously saved mass spectra.

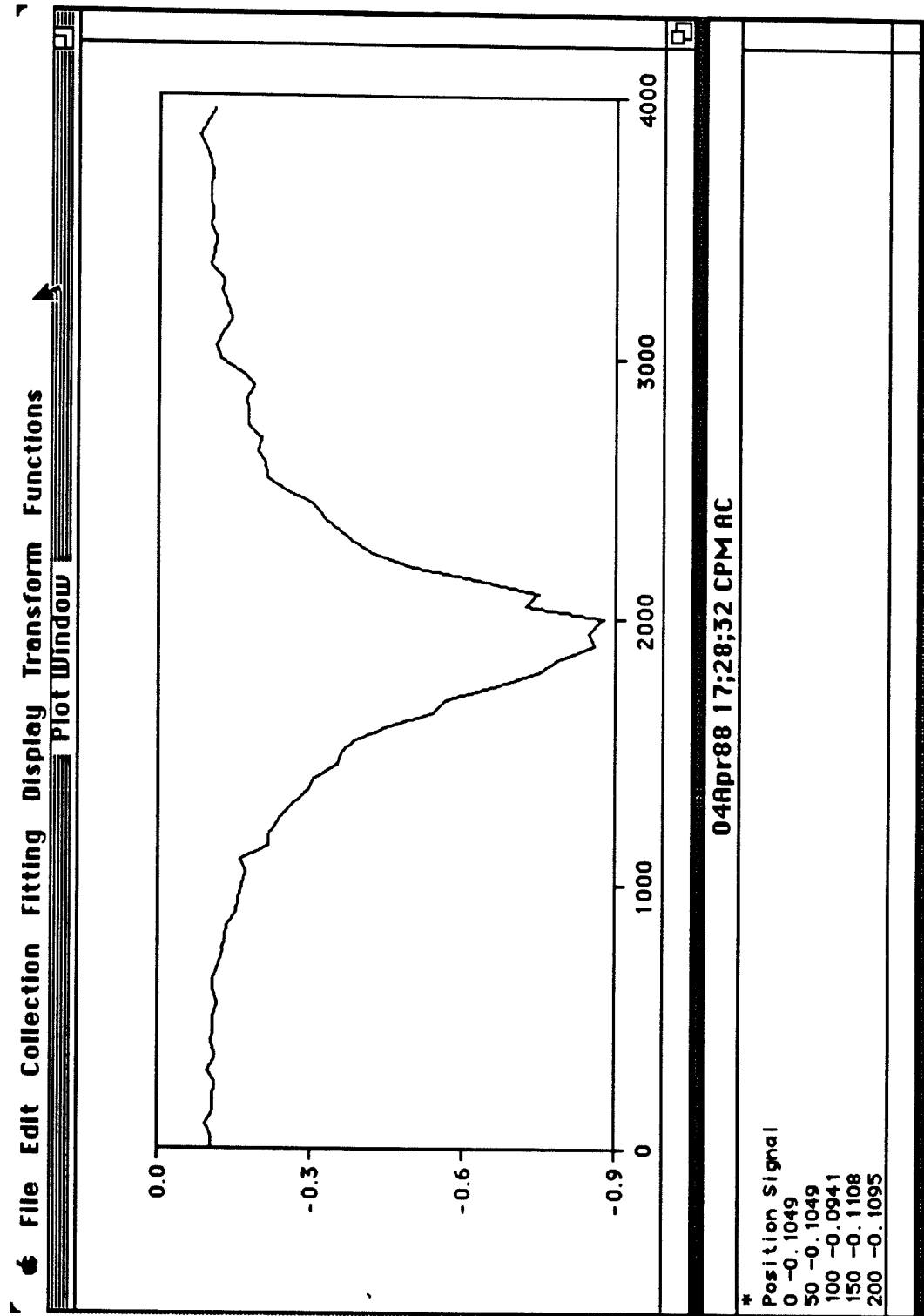


Figure 1

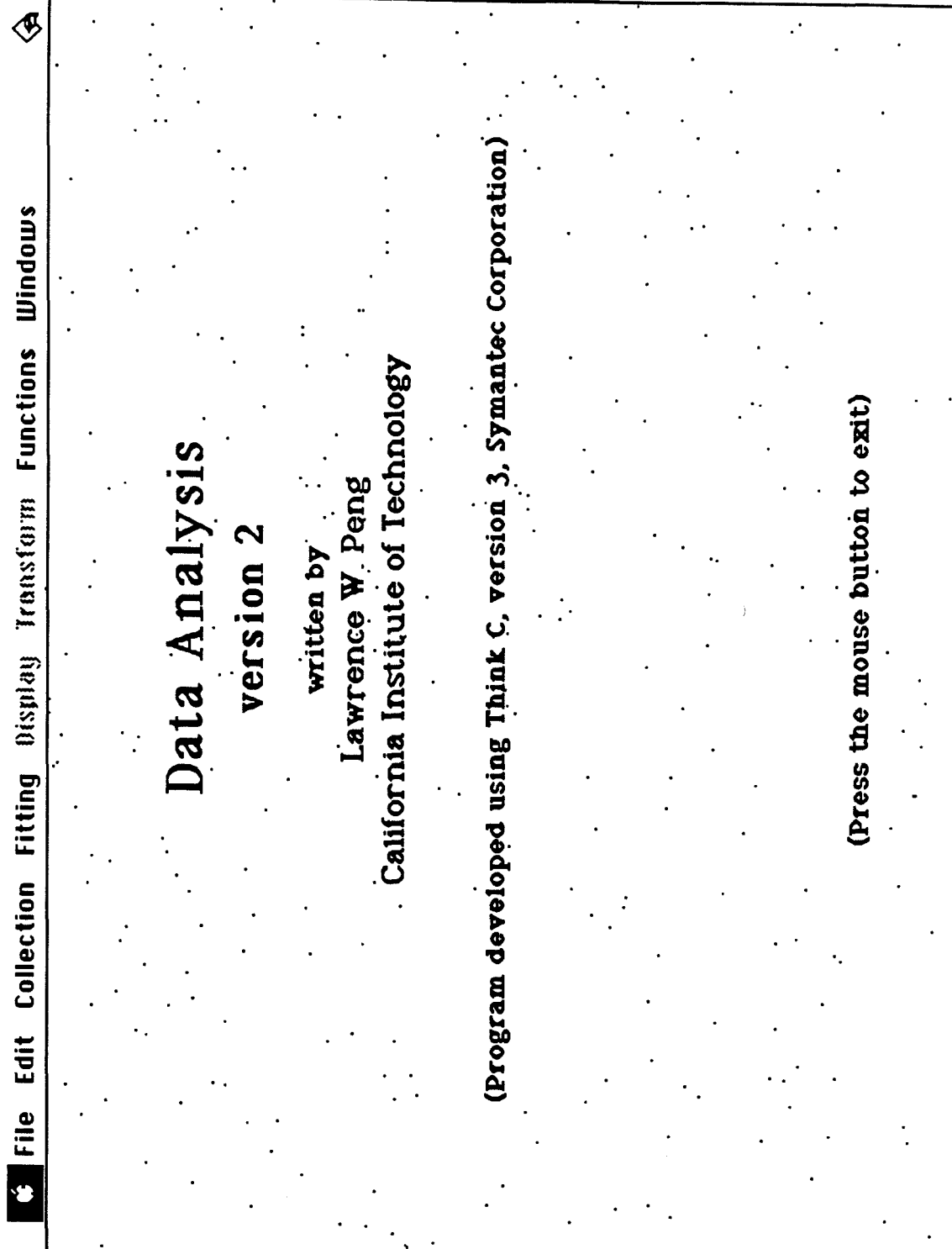


Figure 2

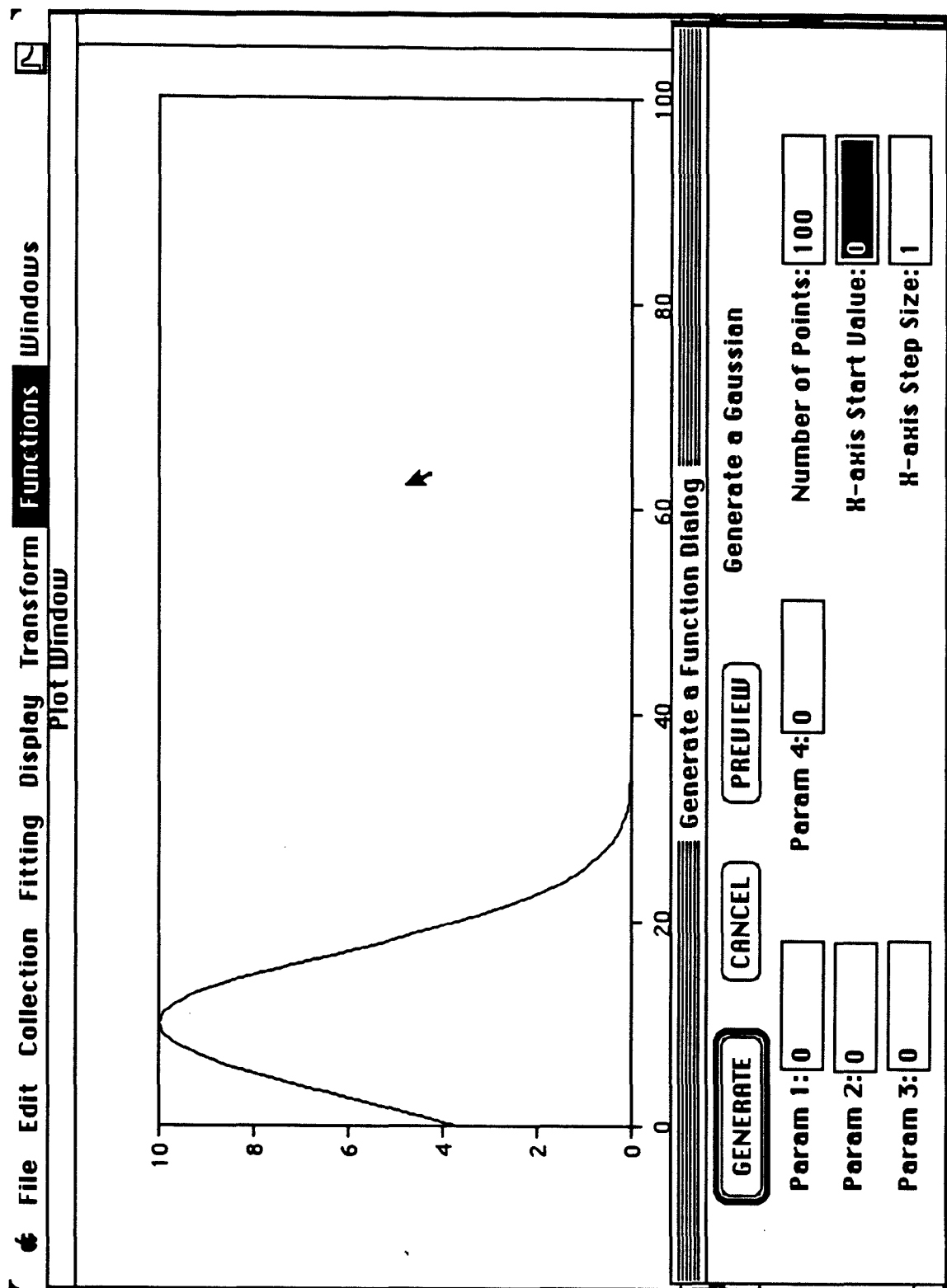



Figure 3

File Edit Communications Collection Fitting Display Transform
 UNIDEX Delay Line

Move steps/data point
 Start position: steps

OK  Cancel

NEW START POSITION/SET UP FOR MANUAL MOVE

Total Steps From Current Start Position: 0
 Total Number of Manual Increments: 0
 (128 maximum)

INCREMENT UNIDEX REPEAT INCREMENT CYCLE

* Position
 50000.0
 50500.0
 51000.0

Figure 4

File Edit **Communications** Collection Fitting Display Transform
 LeCroy CAMAC Parameters

Sampling Period in ns:
 (10,20,40,80,160,320,640 or -1 for EXT) (0,1,2,3,4,5,6,7,8)

Slot # (1,2,...,10): Offset (+/- 0.5):
 (32,64,96,128K)

Data Accumulation Type: ☒ SUM ☐ EHP

of shots/point: Record Length to Average:
 (1-1,000,000) (1-8,192)

of scans:

AutoStore mode: ☐ on/off Delay Line: ☐ on/off

Average a Mass: ☒ on/off

SELECT CHANNELS TO AVERAGE

OK Cancel

Figure 5

File Edit **Communications** Collection Fitting Display Transform

Plot Window

Select CAMAC Channels

of masses to average: ☐ 1 ☐ 2 ☐ 3 ☒ 4

Mass peak (H-axis value):

of points to integrate (odd #):
 (symmetric about mass peak)

Start 10 point background with point (H-axis value):

This dialog box always returns to the "LeCroy CAMAC Parameters" dialog box!
 PRESENTLY ONLY CHANNEL ONE IS ACTIVE!!!!

Figure 6

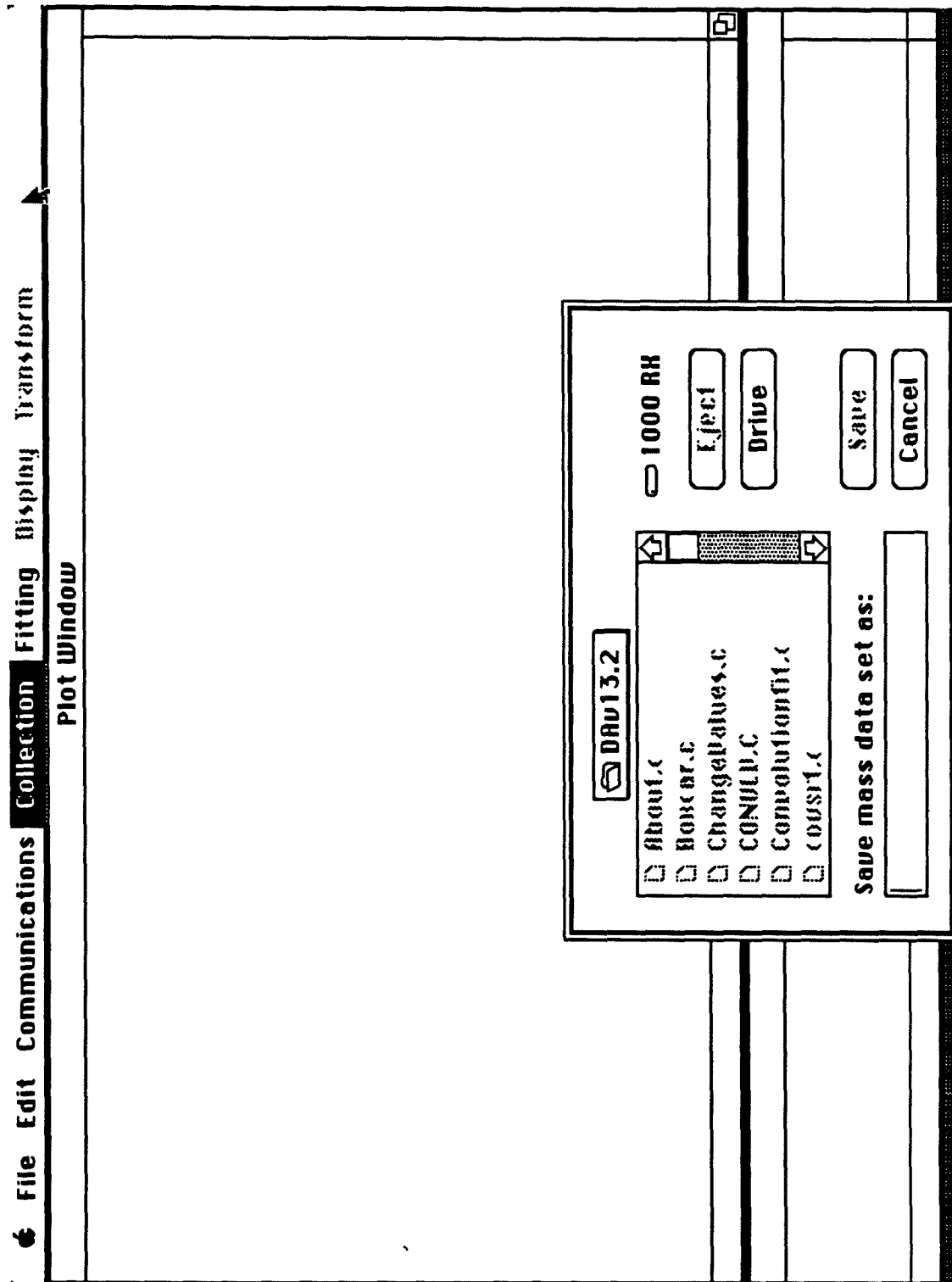


Figure 7

File Edit **Communications** Collection Fitting Display Transform

Boxcar Parameters

of data points: 1

of shots/point (>3): 200
(must be an even #)

of channels: ☐ 1 ☐ 2 ☐ 3 ☒ 4

of scans:

Active Channel Vectors: 1 2 3 4

Gain (1,2,4 or 8):

☒ Use Delay Line ☐ Use SPEX CD2A

OK Cancel

EG&G P.E.

Figure 8

File Edit Communications Collection Fitting Display Transform

Plot Window

Spex CD2A CompuDrive

CD2A Remote: ☒ ON ☐ OFF

Scanning mode: ☐ Continuous ☒ Burst

of scans: Increment (Å): Maximum End Position Is 6500Å!!!

Start Position (Å):

Dwell time (0.01-600 sec): Scan delay (0-600 sec):
(add 2 sec for code cycling)

OK

RS-232 settings (1200 Baud, 1 stop bit, 8 character bits, no parity) match CD2A configuration parameters 15,16, and 17. CD2A must be manually configured for 2-way RS-232 (configuration element 21 - 1010).

CANCEL

CD2A does not allow one to pause a scan!!! Spectrometer backlash is 50Å.

* Po 62 62 62

Figure 9

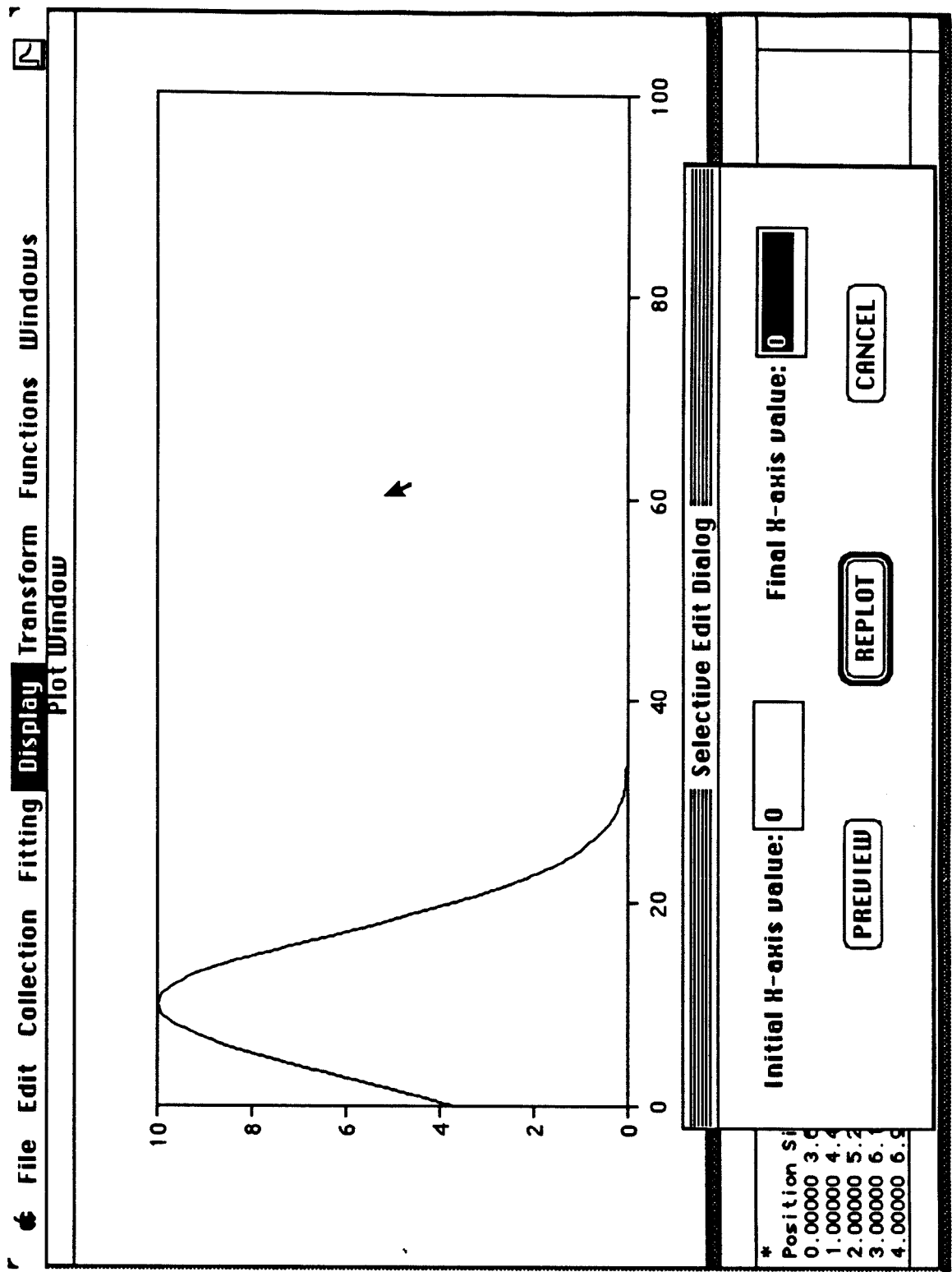


Figure 10

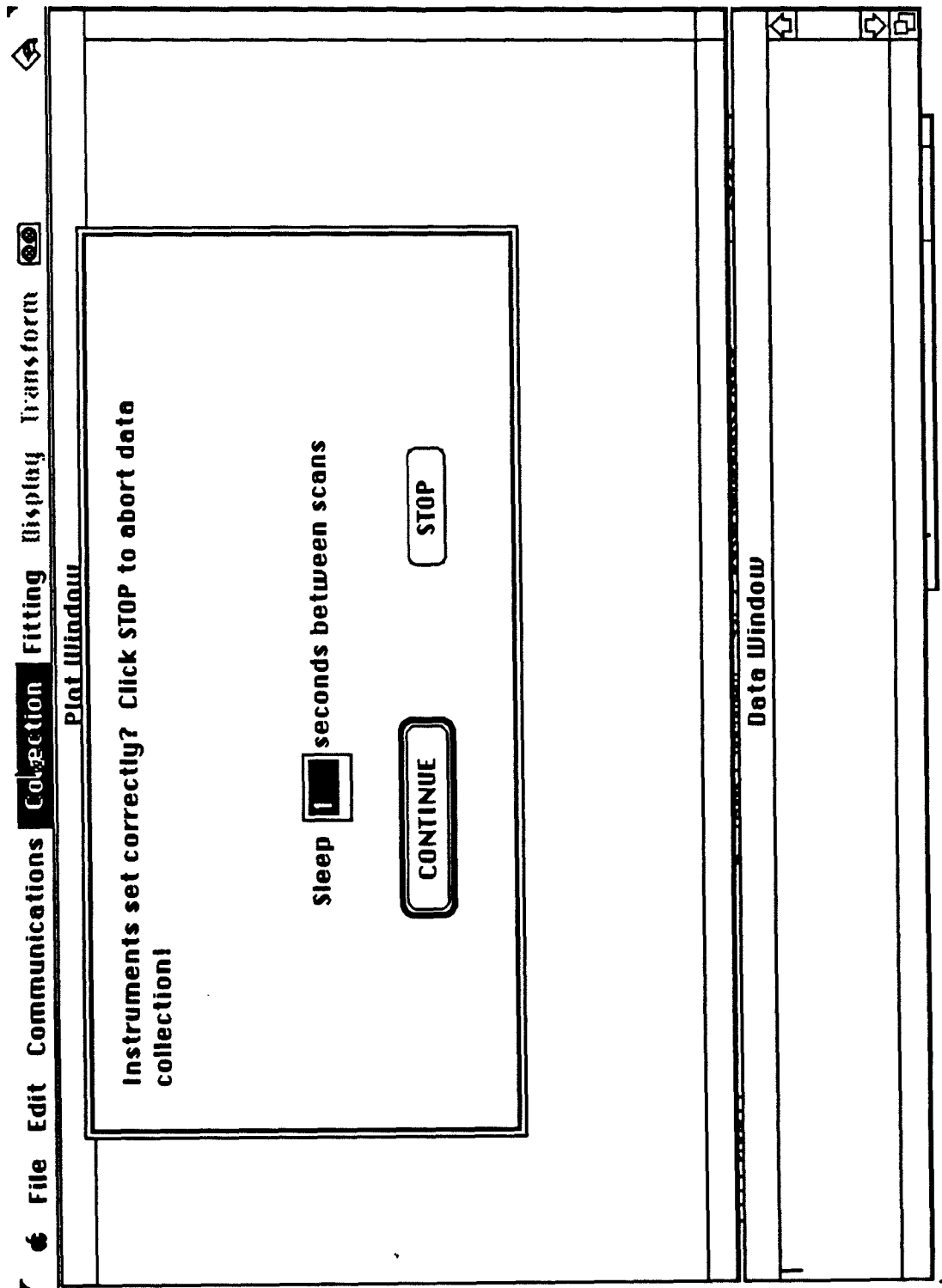


Figure 11

File Edit Collection **Fitting** Display Transform Functions

Plot Window

Enter initial guesses for fit parameters:

<input checked="" type="checkbox"/> Parameter 1	-0.7718562	<input type="button" value="FIT DATA"/> <input type="button" value="RESET"/>
<input checked="" type="checkbox"/> Parameter 2	2000	
<input checked="" type="checkbox"/> Parameter 3	360.3387	
<input checked="" type="checkbox"/> Parameter 4	-0.1026438	

Multiply/Divide Marquardt parameter by (default = 10):

Start fit with Marquardt parameter at (default = 0.001, and not 0!):

FIJHM =
 Chi-Squared =

☐ Fit Entire File? ☒ Display Entire File While Fitting?
☐ Show data scatter
 RESET for new data range!

200 0.1030

4000

Figure 12

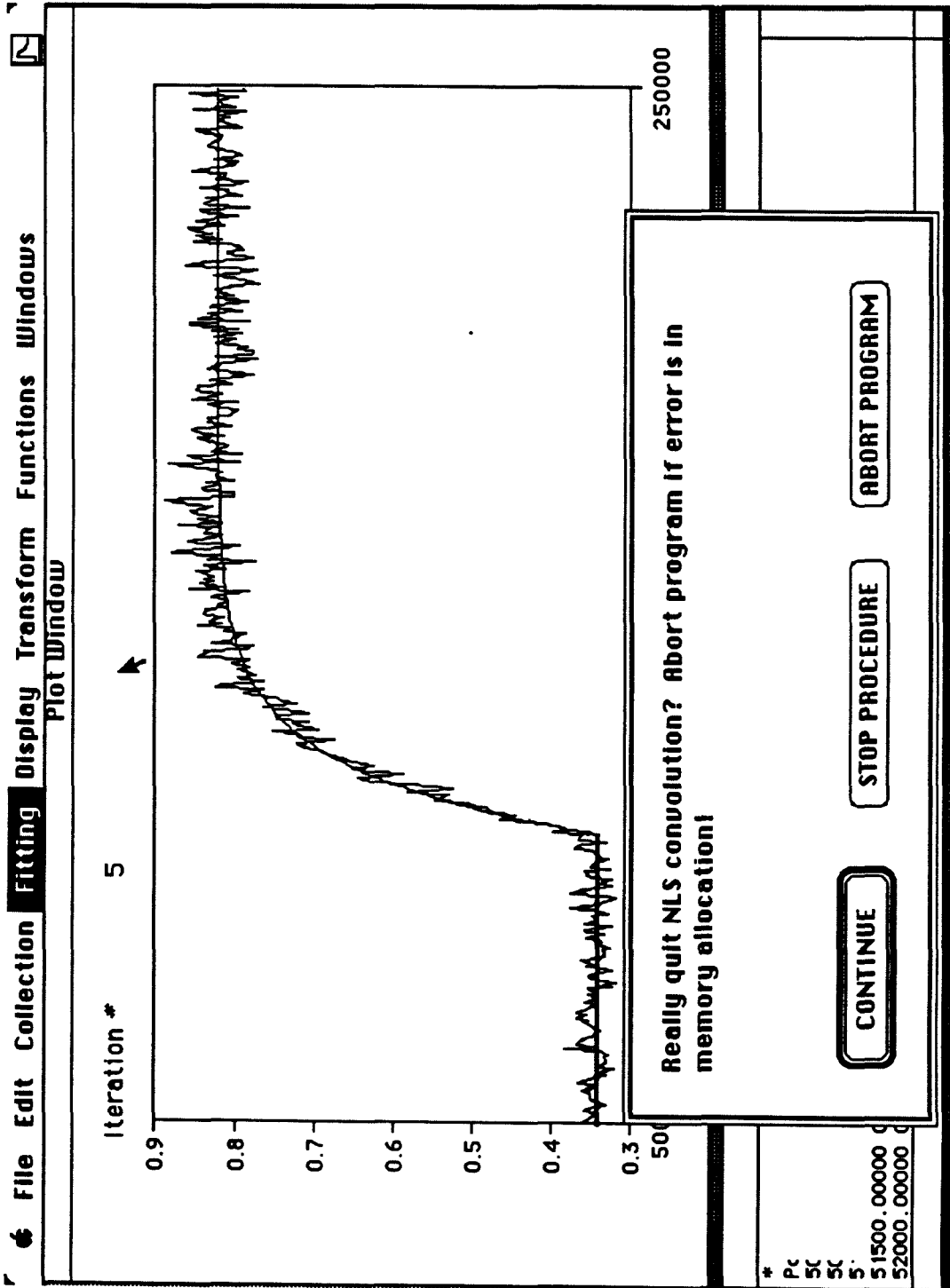


Figure 13

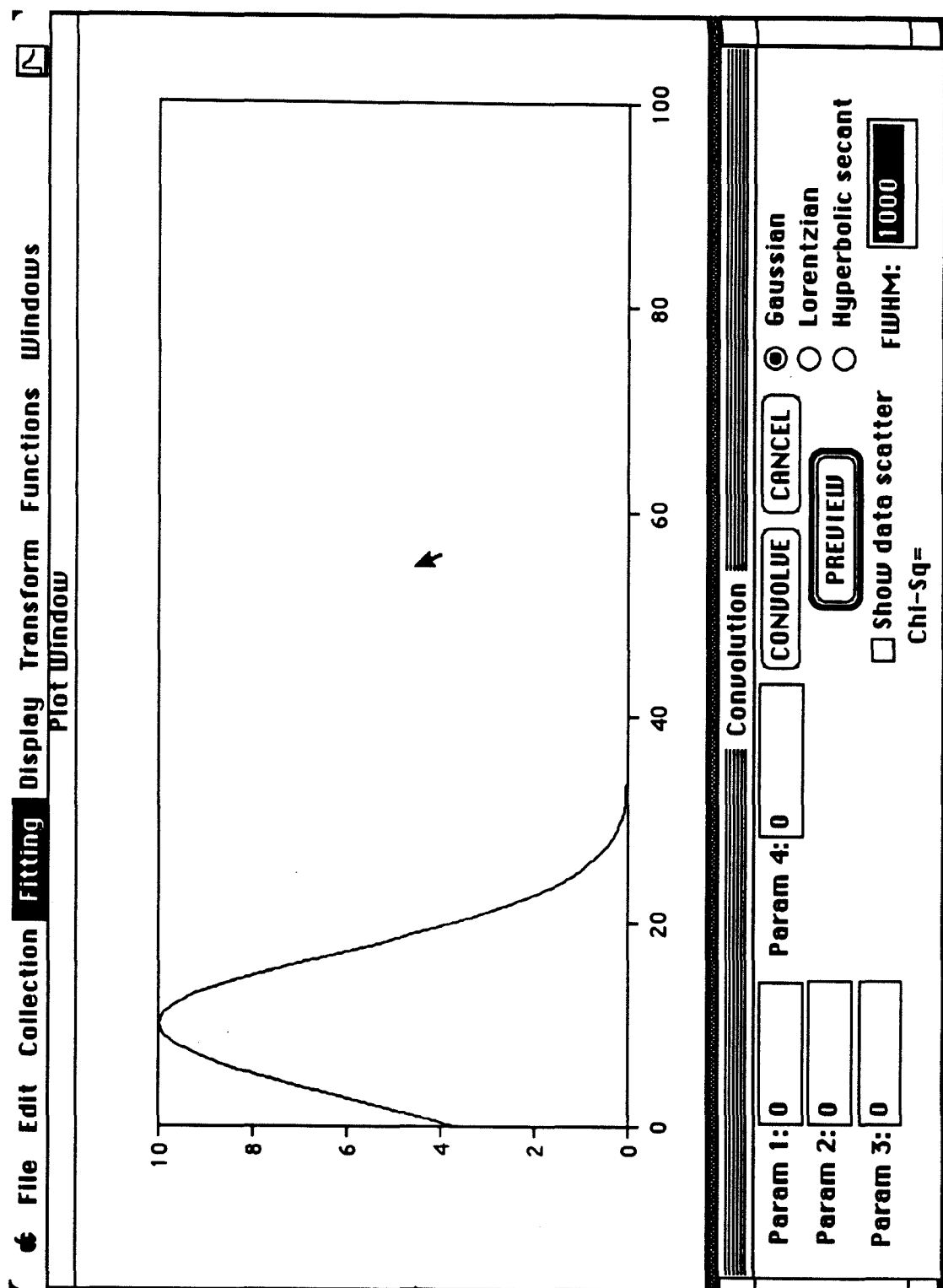


Figure 14

File Edit Collection **Fitting** Display Transform Functions Windows

Enter initial guesses for fit parameters:

☒ Param 1

☒ Param 2

☒ Param 3

☒ Param 4

Type of Response Function

☒ Gaussian
☐ Lorentzian
☐ Sech Squared

Response FWHM:

Multiply/Divide Marquardt parameter by (default = 10):

Start fit with Marquardt parameter at (default = 0.001, and not 0!):

FWHM =
Chi-Squared =

☐ Fit Entire File? ☒ Display Entire File While Fitting? ☐ Show data scatter

RESET for new data range!

3.00000 6.12626
4.00000 6.97676

Figure 15

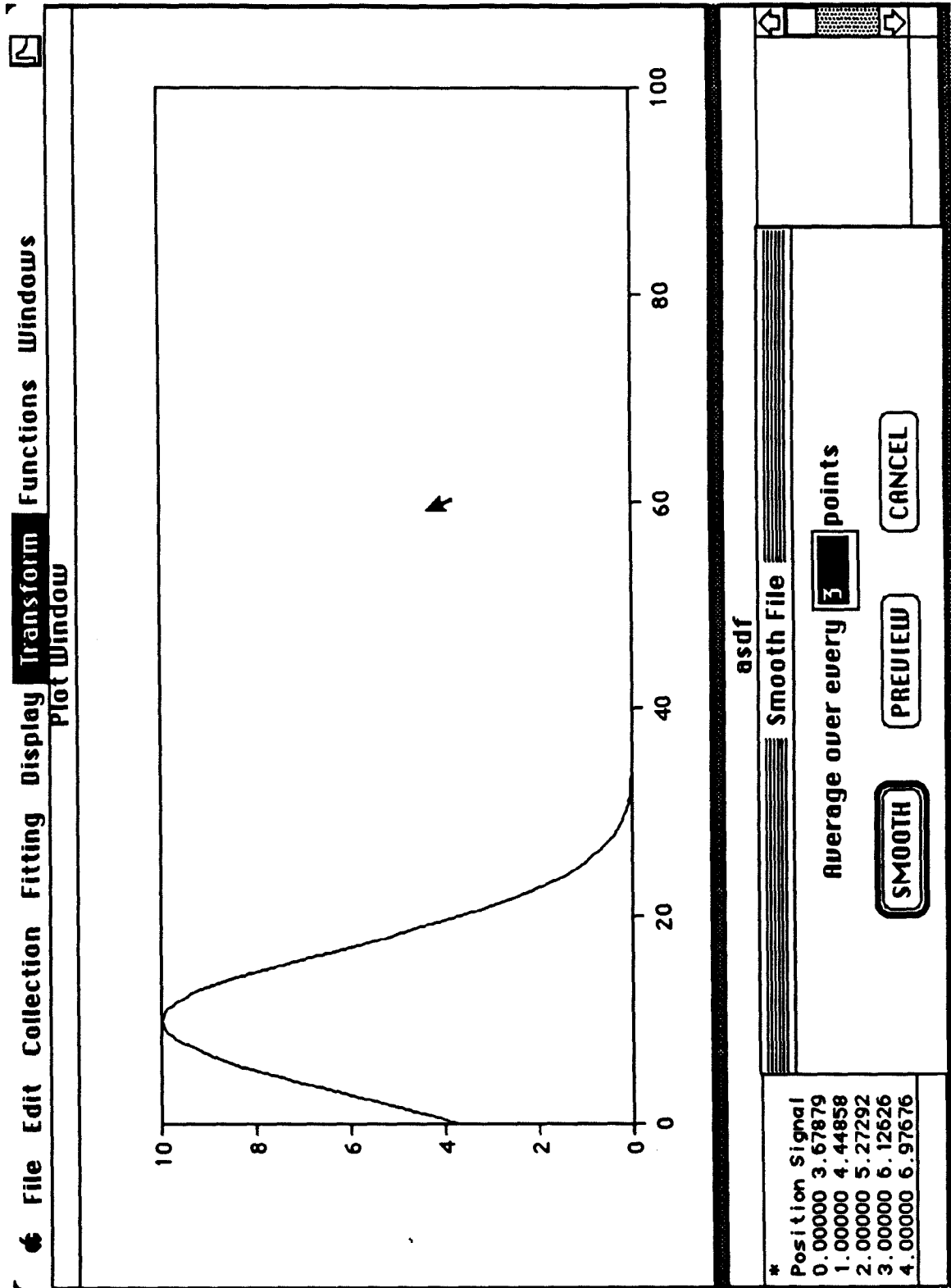


Figure 16

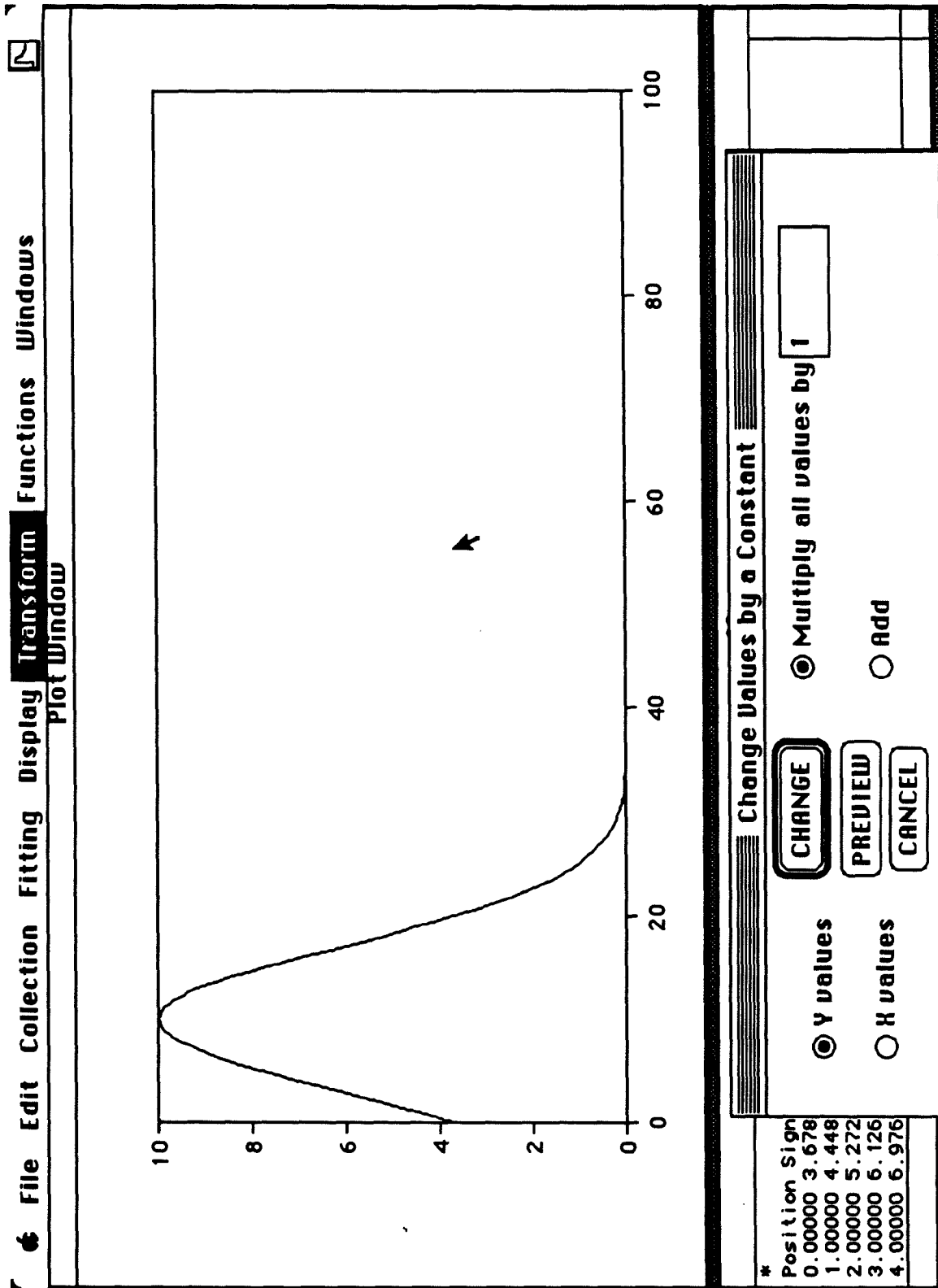


Figure 17

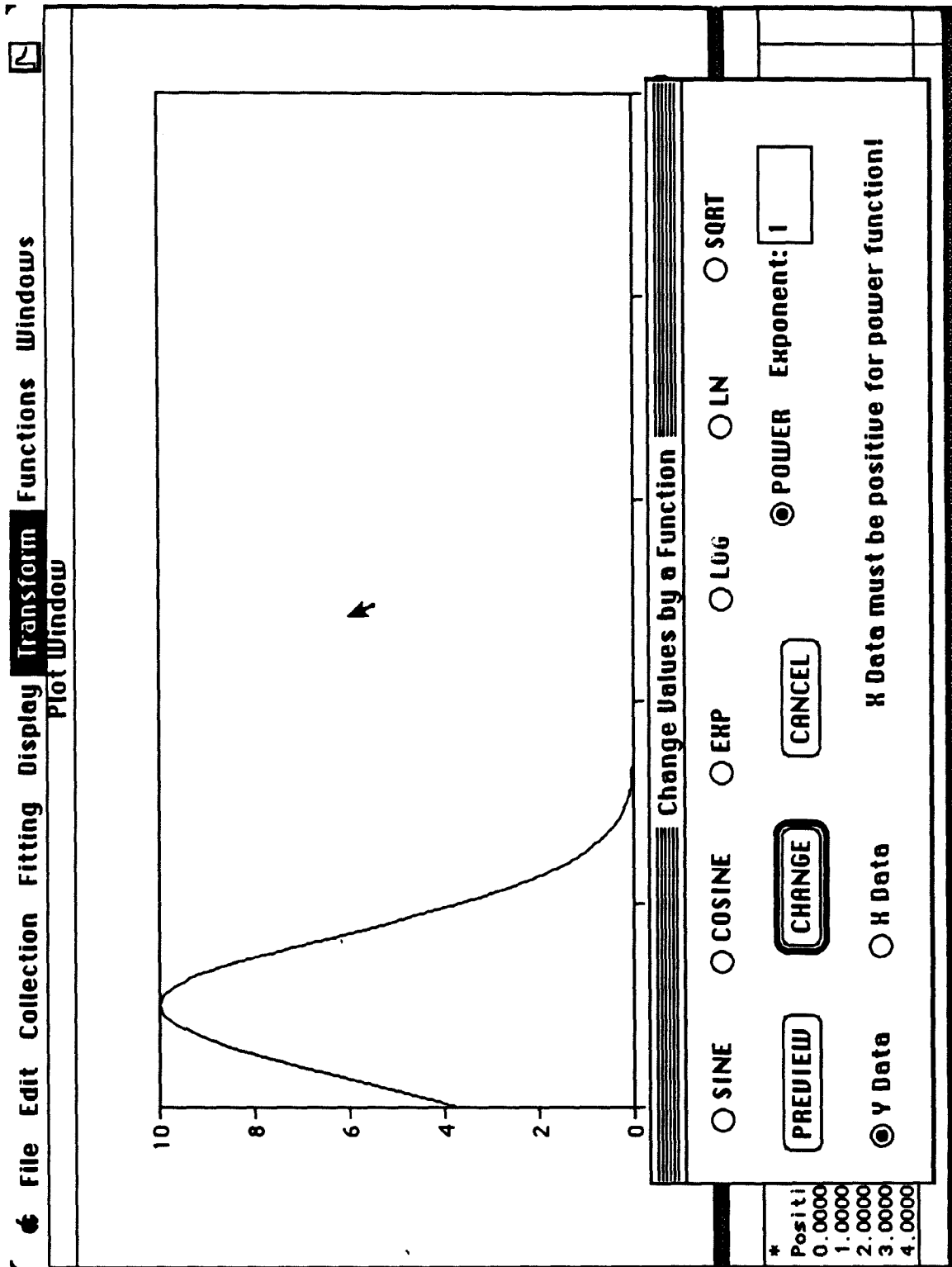


Figure 18

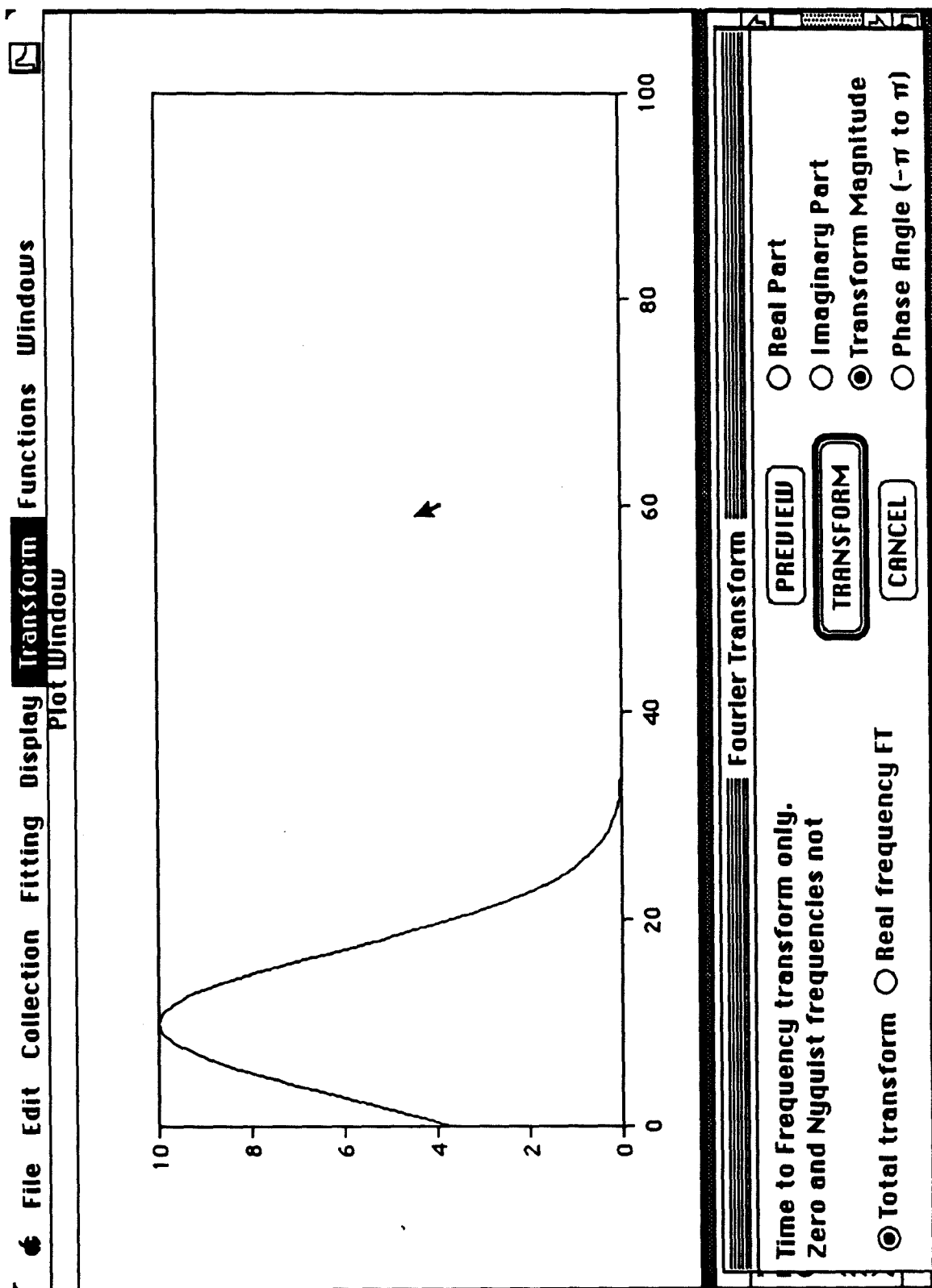


Figure 19

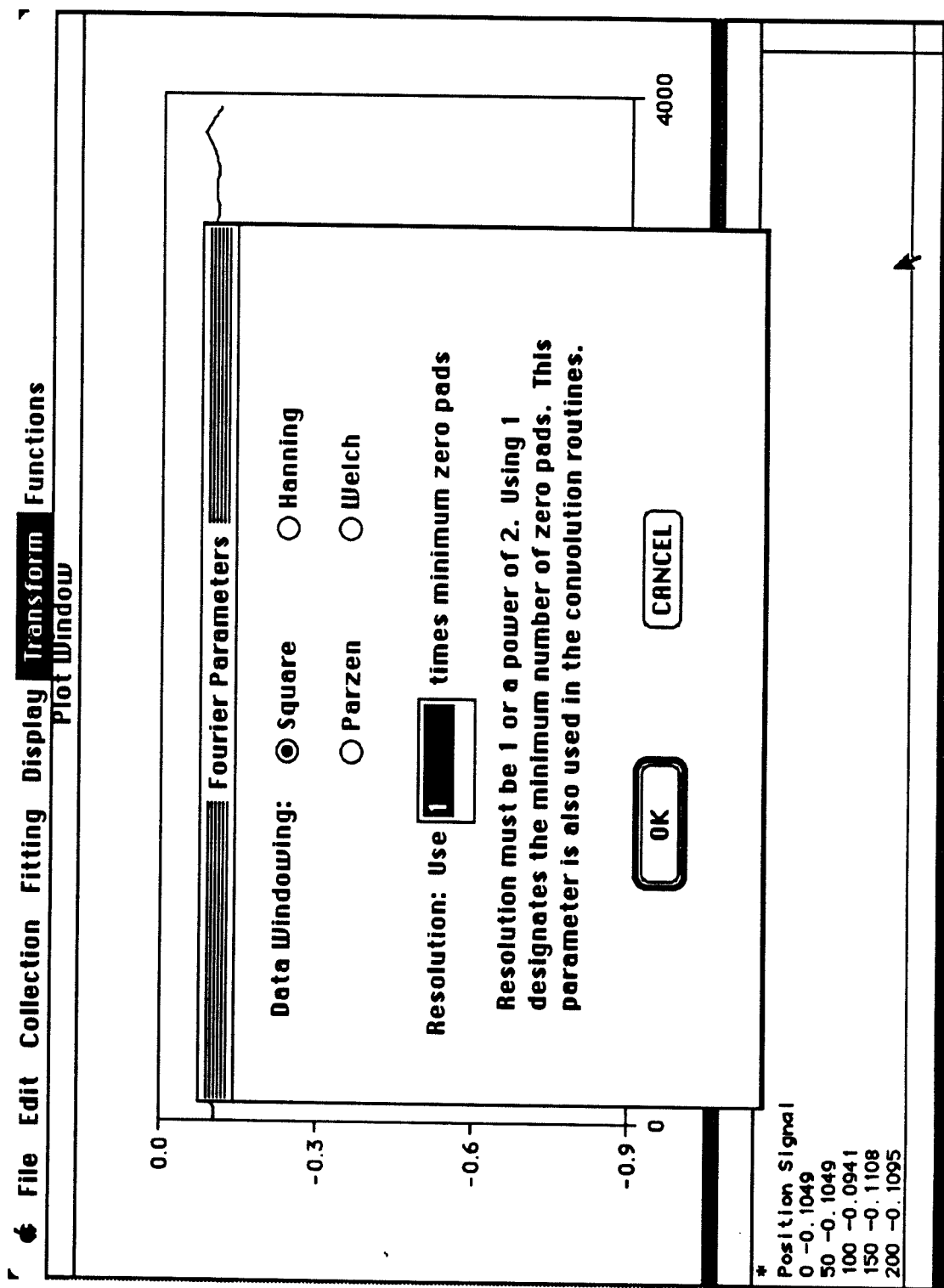


Figure 20

File Edit Collection Fitting Display Transform Functions Plot Window

Reconstruct CAMAC Decay

BUILD DECAY **CANCEL**

Start Position: Increment per file:

of data points/file: Number of files:

Average data point one (X-axis value):

Average data point two (X-axis value):

of points to integrate (3 or 5):
(Symmetric about main point)

Start 10 point background with point (X-axis value):

Position and Increment refer to the Unidex position numbers (mm from home) attached to the filename

Position Sign

0	-0.1049
50	-0.1049
100	-0.0941
150	-0.1108
200	-0.1095

4000

Figure 21

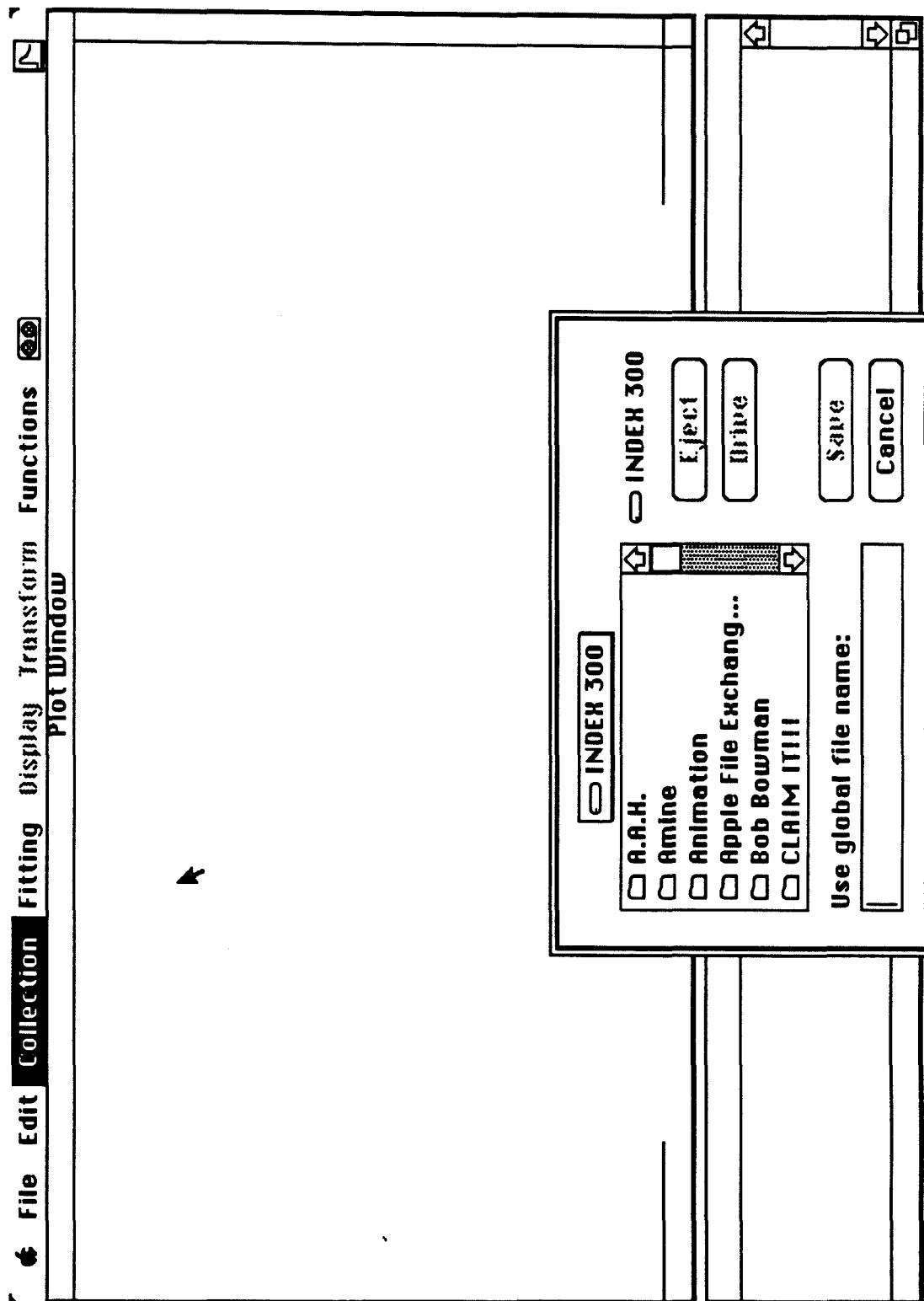


Figure 22

CHAPTER 4

GLOBAL STRUCTURE OF THE DATA ACQUISITION AND DATA ANALYSIS PROGRAMS

4.1 INTRODUCTION

In this chapter, a detailed discussion of the internal structure and operation of **Data Acquire** and **Data Analysis** is given from a global perspective. By global it is meant that the issues covered are common to many source files or are important to the program as a whole. Specific information on single or on small groups of source files and libraries will be deferred to Chapter 5. Figures 1 and 2 are schematic flowcharts showing how the program is structured for data acquisition and data analysis. Figure 1 is for data acquisition, and Figure 2 is for data analysis.

The remainder of the chapter is divided into eight subsections. Section 4.2 provides an overview of how the program is initialized, and gives an example of how the program responds to a user-generated event. The method of response is basically common to all other events that could be generated. Section 4.3 is concerned with the segmentation structure of the program. Proper segmentation allows programs to be larger than the actual memory available and helps to reduce memory fragmentation. Section 4.4 discusses the program resources. In this program, resources are very important for the construction of the user interface. Section 4.5 introduces the global data arrays and memory allocation schemes. Dynamic memory allocation, used extensively in the program, is another means of reducing memory fragmentation and of maximizing the amount of memory available. Proper utilization of the global data arrays enables the user to exploit the full capabilities of the program. Section 4.6 provides information about the Numerical Recipes [1] routines used. Filenames and data file creation are the subject of Section 4.7. Of particular importance is the ability to link files to other applications. Section 4.8 addresses the issue of variable type conversions. This matter is critical for the data acquisition routines, especially where communication to external devices is involved. Finally, Section 4.9 provides a general discussion about plotting data on the plotting windows.

4.2 OVERVIEW OF PROGRAM OPERATION

The program starts by initializing the Macintosh Toolbox (high level toolbox routines, QuickDraw, and low level operating system routines). The initialization code is then made purgeable (Section 4.3), since it is no longer needed. The program resources are opened; and the cursors, menus, windows, and file system are set up. Program control then goes to the main event loop.

The main event loop evaluates the type of event and where it occurred. An event can be defined as a requested action by the user or by the operating system. It is up to the programmer to decide what type of events is important for the program to recognize. Events are normally processed in the order of occurrence, but certain types of events always have priority [2-5]. The main event loop in this program handles all user-generated events: mouse, keyboard, windows, updates, controls, and the status of data acquisition. The operating system ordinarily handles low level miscellaneous events, such as recognizing that a floppy disk has been inserted into the disk drive. The main event loop is composed of three sections: one to handle mouse events, the second to deal with the keyboard and windows (including controls and updates), and the third to monitor the status of data acquisition. The status of data acquisition is **the last item** checked. This ensures that data acquisition will be sensitive to the last processed keyboard or mouse event.

The way the main event loop responds to user actions is basically the same regardless of the event. The following is an example of how a user command is executed, along with the relevant routines involved. The user action is listed followed by the program's internal response. The example is for data acquisition with the boxcar averager. Although this is not the simplest example, other possibilities are no more difficult. It is assumed that all starting parameters are already specified. From the user's point of view, one simply chooses **Start** from the **Collection** menu.

User: No action.

Program: Cycle through MainEvent().

User: Choose **Collection** menu.

Program: Main event loop gets menu bar event. Go to DoCommand() and identify **Collection** menu.

User: Choose **Start**.

Program: Go to DoDataCollectionMenu(). Identify the menu item corresponding to **Start**. Ask user if all is ready to go.

User: Confirm **Start** or cancel data acquisition.

Program: If confirmed, then turn on data acquisition flags and open the Macintosh serial drivers. Return to DoDataCollectionMenu(). Then return to DoCommand(), which returns to MainEvent(). If cancelled, return to DoDataCollectionMenu(). Then return to DoCommand(), which returns to MainEvent().

User: Data Acquisition started.

Program: MainEvent() checks data acquisition flag status and finds them turned on. Go to DoDataBoxcarScan() and take a data point. Return to MainEvent().

User: No action.

Program: MainEvent() continues to check the status of the data acquisition flags. If they are on, do DoDataBoxcarScan() until the required number of data points and scans is taken. During data acquisition plot the averaged data (DrawPlotWind()) on the **Plot Window**, and save it to a file. When finished, DoDataBoxcarScan() turns off the data acquisition flags and closes the Macintosh serial drivers. Signal that the scan is finished.

User: Set up for next scan.

Program: MainEvent() checks status of data acquisition flags and finds them turned off. Since no user events are present, continue to cycle through MainEvent().

Of course, the user could always generate a keyboard or mouse event during data acquisition by using ⌘-G (**Start/Stop**) and ⌘-H (**Pause/Continue**). As previously mentioned (chapter 3, section 4.3), ⌘-G and ⌘-H set the status of the data acquisition flags.

4.3 PROGRAM SEGMENTATION

When the program project is opened by Think C, the program segmentation structure is shown (Figure 3 for **Data Acquire**, Figure 4 for **Data Analysis**). Program segments are handled by the Macintosh segment loader. By default, the program code is locked in memory when loaded. This means that upon program startup, the segment containing the main program (main()) is in **Data Acquisition.c** or **Data Analysis.c** is loaded first. Additional segments are loaded when a routine in them is called. Since the

segments are locked in memory, and need not be loaded in any specific order, it is possible that significant memory fragmentation may result.

In this program, attempts have been made to reduce memory fragmentation by making the segments dynamic. Except for the main program (in **Data Acquisition.c**), code is made purgeable by calling the Toolbox routine `UnloadSeg(routine name)`. The segments that are made purgeable are indicated at the end of the main event loop. The routine name is arbitrary, since a call to any routine in a segment affects the entire segment. Code segments are swapped in and out of memory in whole segments no larger than 32K. A segment should never unload the segment that called it, or unload itself. Since the segment containing the main program is never purgeable, the safest place to put `UnloadSeg()` calls is in the main event loop [5]. For example, if **initialize.c** and **Data Acquisition.c** are in the same segment, the program crashes upon startup when executing `UnloadSeg(Initialize)`. If **Data Acquisition.c** and the fitting routines are in the same segment, the program crashes when fitting a file.

This program project is set up so that routines common to a specific purpose are grouped into the same source file, and source files devoted to a common task are in the same segment. The initialization routines (**initialize.c**) is one segment. Routines for data analysis and communication with external equipment (including the initialization routines for serial communications, **Serial Comm Initialize.c**) are in separate segments. Seldom used routines (*e.g.*, **AboutProgram.c**) are in their own segments. **Data Acquisition.c** and other frequently used routines remain locked.

4.4 PROGRAM RESOURCES

Resources are the building blocks of all Macintosh programs [2-5]. They can include all the descriptive information needed by a program. These might be the menus, the fonts, the icons, the characteristics of a window, or the layout of a dialog box, to

mention just a few. Resources come in various types, and an application may have several resources of a given type. However, there is only one type of a given resource that is identical for all Macintosh applications. To make this point clearer, consider the resource type WIND, which is the window template used to construct a window. This program has a total of four resources of type WIND (since there are four windows), but windows in all Macintosh applications are described by the same WIND resource type. Even code segments (Section 4.3) can be treated as resources. In a sense, a Macintosh program can be thought of as nothing but a collection of resources.

Resources can be built using either of two applications supplied by Think C. The first is **ResEdit**, and the second is **RMaker**. **ResEdit** [3,4] allows the user to create resources graphically, but does not create resource source files. Program resource source files can be created and compiled using **RMaker** [3,4], but this requires knowledge of how to write the **RMaker** code. Thus, using **ResEdit** is often more convenient. Every program resource has its own ID number, which is recognized by the Toolbox resource manager. For compatibility with the Macintosh system software, all programmer created resources must have ID numbers ranging from 128 to 32767 inclusively. For a given resource type, there may be further restrictions. See Reference 2 for the final word. The symbolic constants and identification numbers for the resources used in this program are in **Data Acquisition.h** or in **Data Analysis.h**.

As far as this program is concerned, resources created by the user are employed to separate the "look" of the program from the program code itself. In this way, the visual appearance of the program can be changed without having to recompile, or even worse, actually having to write a new set of code. Manipulating resources (*e.g.*, turning menu items off or on) is done using Toolbox routines. Some resources (*e.g.*, a dialog box to open or write a file) are predefined in the Toolbox [2]. Except for some menus and the Version resource, all other program resources were built using **ResEdit**.

In analogy with code segments, some of the program resources are made purgeable (using **ResEdit**) to reduce memory fragmentation. The remaining resources are left un purgeable as they are expected to be used frequently. The only resources that are never purgeable are menu resources. If menu resources are purgeable and memory has been moved, the program crashes when a menu item is chosen.

4.4.1 Menu Resources

The **File**, **Edit**, **Transform**, **Fitting**, **Communication**, and **Collection** menus were built with **ResEdit**. Except for the **Apple** menu, all other menus are built with code. Although it is not necessary to build menus via code, the menus that were built serve as an illustration of the procedure. The **Apple** menu is a mixture of **ResEdit** and code. **ResEdit** was used to identify the **Apple** menu and add the items **About Data Acquire**, **About Data Analysis**, and **Program Help**. **Apple** menu desk accessories are added in the routine **SetUpMenus()**. Upon startup, **SetUpMenus()** loads all menu resources, builds menus using code, and draws the menu bar. When building menus, note the order in which the menu items are listed. To prevent a menu item from highlighting, disable it when building the menu. The program identifies the menu item chosen by using switch statements. The switch case number must match the item number in the menu.

4.4.2 Dialog Resources

All user dialog boxes in this program are of the modal type. When a modal dialog is called, the user may perform no other function than to work within the dialog box. The dialog box must be dismissed for the program to continue. In contrast, modeless dialogs (*e.g.*, desk accessories) can remain open in the background. Dialog box resources are composed of two resource components: **DLOG** and **DITL**. **DLOG** identifies and sets up the dialog box. **DITL** lists all the dialog items within the dialog box borders. Items are

numbered in the order in which they are created. All dialog box routines (**dialog routines.c**) need to know the dialog item's DITL number. Switch statements are used to identify the dialog item chosen, and the case number must match the DITL number. For a modal dialog, the Toolbox assumes that the first item is the default button and frames the button in bold when the routine `frameOkButton()` is used. The framed button is associated with **return** on the keyboard. When a dialog box is active, it first assigns the value of the external variables to corresponding local variables. The program then enters a loop so that the user can change a local variable value or dismiss the dialog box. If the dialog box is cancelled, the local variable values are ignored. Otherwise, the external variables are assigned the value of the local variables. Alert boxes are dialog boxes, and the Dialog manager normally takes care of any needed housekeeping.

4.4.3 Window Resources

All four windows are defined as resources of type **WIND** and were built using **ResEdit**. When building a window resource, the size, title, and type of window are set. The type of window is defined by the `procID` number (*e.g.*, document window with zooming has `procID = 8`) [2].

4.4.4 Icon Resources

In the **Communication** menu in **Data Acquire**, the dialog boxes (except for the **Spex CD2A**) have icons present in them. The icons (resource type **ICON**) in the dialog boxes are for display only, and serve no other function. Icon resources are added to the dialog resources in the same manner as if one were adding a button. In addition, the application itself is represented by an icon on the Finder desktop. All icons were built with **ResEdit**.

4.4.5 Version Resources and Links with the Finder

The Version resource (LPNH for **Data Acquire** and PENH for **Data Analysis**), coupled with the resource types BNDL (Bundle), FREF (File Reference), and ICN# (icon list), allows an application to have its own identity with the Finder. This also makes it possible to link files to their parent application. When linked files are double-clicked, the creating application is automatically launched. The Version resource for this program was created using **RMaker**. The **RMaker** source file is named **project name.R**. The compiled resource file is called **project name.twosrc** in order to distinguish it from the main resource file. The **project name** is the Think C project name, *e.g.*, **Data Acquire-047A** for the **Data Acquire** program. Once the Version resource is created, **ResEdit** is used to copy it into the main resource file. The Version resource name must be the same as the Think C project's Creator's name, and must be different from all other applications. The Version name for an application can be checked using **ResEdit**. By using **ResEdit**, the reader will note that the resource type BNDL is composed of a list of the resource types FREF and ICN#. There is a direct correspondence between FREF and ICN#, i.e., the first FREF is associated with the first ICN# and so forth. The local ID (localID) numbers always start at zero, and the resource (rsrcID) numbers correspond to the resource number of the given type. As an example, the icon for the application (FREF type APPL) has the local ID of zero, and the resource ID 128 (its ICN# resource number). The ordering of the FREF and ICN# resources is critical and must be adhered to if the link to the Finder is to work properly [2,4]. Resources for the application are always done first, followed by resources for various file linkages. If additional FREF and ICN# resources are created, they should be attached to the end of the current BNDL list.

4.5 DATA ARRAYS AND MEMORY ALLOCATION

The most important data arrays in the program are global ones called XData and YData. XData is a row vector whose size is equal to the number of points in the file. YData is a matrix composed of four rows equal in size to XData. The number of rows is arbitrarily set. These dynamically allocated arrays are used to store new data, and to store data when opening a saved data file. When memory for new XData and YData arrays are allocated, the old XData and YData arrays are erased. Following C conventions, all row numbers are zero offset. Thus, YData row zero corresponds to the first row of Y values in memory. Other data arrays are used when needed. Except for the Display menu, the data analysis routines work on copies of the XData and YData arrays. Using copies serves two purposes: (1) A data file can be worked on as often as desired without having to reopen the file every time; (2) raw and manipulated data can be compared simultaneously on the Plot Window.

The type of data stored in the YData matrix depends on whether data acquisition or data analysis is in progress. When using the boxcar or when CAMAC averaging single mass peaks, the YData matrix is organized so that channel one data are in YData row zero, channel two data are in YData row one, etc. Two boxcar channels and one CAMAC channel for averaging a mass peak are available. For both of these cases, however, provisions have been made for four channels. When rebuilding decays from mass spectra, the YData matrix is organized so that decay data are in YData row zero, decay two data are in YData row one, etc. Currently the limit is two peaks at a time. If the user is taking mass spectra, then the mass spectra are in YData row zero. If the user is averaging mass spectra over successive scans, then the averaged mass spectra are in YData row one. For data analysis there are too many cases to list here, but the organization of the YData matrix for a particular type of analysis is given in the appropriate data analysis source file.

The plotting routine source files (**plot.c**, **plotTwo.c**) and the file writing routine source file (**Write.c**) operate on data stored in **XData** and **YData**. There are a few cases where the raw data must be moved in order to save or plot a data transformation. In these cases, the raw data are stored in a temporary local array. When plotting or writing is done, the raw data are restored into the **XData** and **YData** arrays. The plot routines already allow plotting of a generated function by passing the proper flags to the routine. If the plotting routine **DrawPlotWind()** is called, the data are displayed in the **Plot Window**. If the plotting routine **DrawPlotWindTwo()** is called, the data are displayed in **Plot Window Two**. This scheme is not the best way, but is manageable for a program of this size.

Another important item is the relationship of the **XData** array to the plot and selective plotting routines. The **X** values are always plotted in ascending order. The routines expect the lowest value of **X** to be in **XData[0]**, and the largest **X** value to be in **XData[Number of Data Points-1]**. The Selective Plotting routine uses the **XData[0]** value as a reference to establish which part of the data file (in terms of data points) has been selected. When a constant is added to the **X** values or the **X** values multiplied by a positive number, there is no change in the **X** values' order. However, multiplying by a negative number reverses the order. To rectify this problem, the program immediately sorts the **X** values into ascending order whenever the **X** values are multiplied by a constant.

4.6 NOTES ABOUT NUMERICAL RECIPES ROUTINES

Most of the subroutines used to fit, convolve, smooth, and sort data were taken from the book **Numerical Recipes in C** [1]. The only major change made to these routines are that the data type has been changed from float to double. The final results are converted to type float just before plotting takes place. A few minor changes have been made (as indicated in the source file) in order to accommodate other program features.

Using type-double for calculations instead of type-float requires twice as much memory, but avoids potentially fatal roundoff errors.

One problem with the routines in Reference 1 is that they are set up for unit offset arrays. The program data arrays are zero-offset. To get around this conflict, the routine is called in the main program as Func(AA-1) instead of Func(AA). AA is a zero-offset array in the main program, and unit offset in the Numerical Recipes routine [1]. No changes in the routine from Reference 1 are needed.

4.7 FILENAMES AND DATA FILE CREATION

Data may be saved in three possible formats. Regardless of the format chosen, the data file is saved as tab-delimited text. The possible forms are listed below.

- (A) **Standard document:** Not linked to any particular application and is represented by the default document icon.
- (B) **CricketGraph document:** Represented by the CricketGraph file icon.
- (C) **Excel document:** Represented by an icon labelled as Excel Text.

The text file structure contains 2 lines of headers (an asterisk in the first line, and X and Y data column names in the second) followed by the data in two columns (X being the first column). Data files are composed of one set of X data and one set of Y data, and may be up to 32K in length. Files may be created or modified in a different application, but must be saved in the proper format in order for **Data Analysis** or **Data Acquire** to handle it. Files that are incorrectly structured may lead to a crash if the file is opened.

Filenames are created in three formats, depending on how the data file is acquired. If the file is saved through the **Collection** menu, then the filename is composed of the date, time, plus the active label from the **Collection** menu (**Data Acquire** only). The

temporary files **Most Current Scan** or **Most Current Scan Two** are created using the C language. If mass spectra are being saved so that decays can be reconstructed at a later date, then one is asked to enter a global filename. If the global filename is TEST, the program will create or look for filenames called TEST_#, where # is the delay line position in millimeters from the delay line zero. If no global filename is given, then **Most Current Scan** is used by default. The # parameter values are determined by the **Unidex** dialog box (Figure 3) if acquiring data, and by the **Reconstruct CAMAC Decays** dialog box (Figure 17) if reconstructing data.

3.8 VARIABLE TYPE CONVERSIONS

During the course of data acquisition and data display, there are several variable type conversions made. All variable type conversions must be taken into account when making changes to the program code.

The global arrays to which new data are transferred (XData, YData), so that a data file can be saved or plotted on the **Plot Window**, are type-float. The boxcar and CAMAC crate routines initially store new data in local arrays (**data_channel** for the boxcar, **new_data** for the CAMAC). These local arrays are type-float and type-long-int respectively. The plotting and fitting routines work with XData and YData. Note that although type-long-int allows integer values larger than 32K, a direct conversion to type-float cannot be made without first converting to type-int. There is no problem in directly converting type-int to type-float.

For mass spectra, the XData and YData array bounds are determined by the number of channels (represented by the variable **avglen**) used by the CAMAC crate. When making the XData and YData arrays, the array bounds must equal the integer value of **avglen**. An integer variable called **NumOfCAMACPts** has been declared and assigned the integer value of **avglen** (through the CAMAC dialog box). When **avglen** is used by

the CAMAC crate routine to set up the crate and to set the size of the needed internal data arrays, **avglen** must be type long integer. If there is a mixture of integer and long integer for **avglen**, the program crashes. If **avglen** is always an integer, then the CAMAC crate gives **YData** which is correct up to 255 laser shots. Past 255 laser shots, **YData** becomes a large negative number.

The delay line needs the variable **NumOfDataPts** to be type-long-int. Here **NumOfDataPts** is the total number of increments the delay line takes per scan. If **NumOfDataPts** is not type-long-int, the delay line crashes or adds the sum of the distances travelled by all previous scans to the first increment of the current scan. **NumOfDataPts** must be type-int elsewhere in the program.

4.9 PLOTTING ON THE PLOT WINDOW

Data plotted on the plotting windows are stored in memory as a picture. The picture is associated with a picture record, which is a recording of all **QuickDraw** calls used to construct it [2-4]. A picture record may be up to 4 gigabytes in size.

Pictures speed up the redrawing of a data file on the plotting windows. This is illustrated by considering dialog boxes. If the user calls up a dialog box, the dialog box will usually cover part of the plotting window. When the dialog box is dismissed, the plotting window must be redrawn. If the plot is available as a picture record, then the program will know which part of the plot was affected and how to redraw it. If no picture record is available, then the plot must be recalculated entirely from scratch.

Each cycle through the plotting routine purges the old picture and picture record, and creates the picture and picture record for the new plot. The main plotting routines, **DrawPlotWind()** and **DrawPlotWindTwo()**, both have two **QuickDraw** commands to clear the old plot. **EraseRect()** clears the picture on the window, and the picture record is cleared by calling **KillPicture()**. A picture record remains in memory until explicitly cleared. If

KillPicture() is not called, then the program crashes after about 69 scans of 1500 points each (on a 2 megabyte machine). When KillPicture() is called, at least 1000 scans (the largest number tested) of 2048 points each can be made. The current picture record is not cleared until a call is made for a new plot. Otherwise, any update to the plotting windows causes a crash.

4.10 REFERENCES

1. W. H. Press, B. P. Flannery, S. A. Teukolsky, and W. T. Vetterling, *Numerical Recipes in C* (Cambridge Univ. Press, Cambridge, 1988).
2. Apple Computer, Inc., *Inside Macintosh, volumes 1-5* (Addison-Wesley, Reading, 1988).
3. Stephen Chernicoff, *Macintosh Revealed, volumes 1-3* (Hayden, Indianapolis, 1987-89).
4. David Mark and Cartwright Reed, *Macintosh Programming Primer* (Addison-Wesley, Reading, 1989).
5. Scott Knaster, *How to Write Macintosh Software, 2nd Edition* (Hayden, Indianapolis, 1988).

FIGURE CAPTIONS

Figure 1: A schematic program flowchart for data acquisition.

Figure 2: A schematic program flowchart for data analysis.

Figure 3: The Think C segmentation structure for **Data Acquire**.

Figure 4: The Think C segmentation structure for **Data Analysis**.

Main Event Loop keeps track of the number of scans taken,
as well as Starting/Stopping/Pausing data acquisition!!!

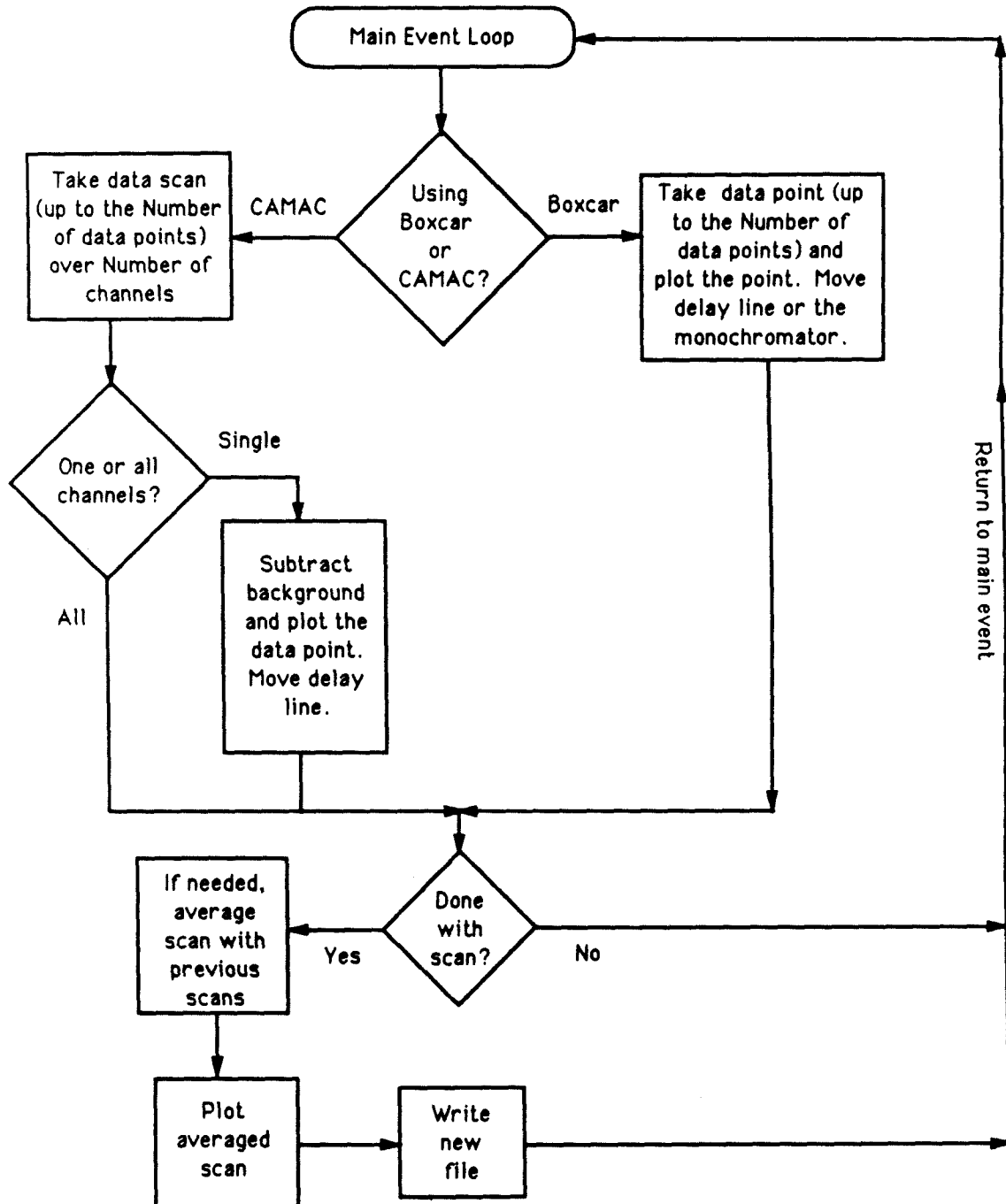


Figure 1

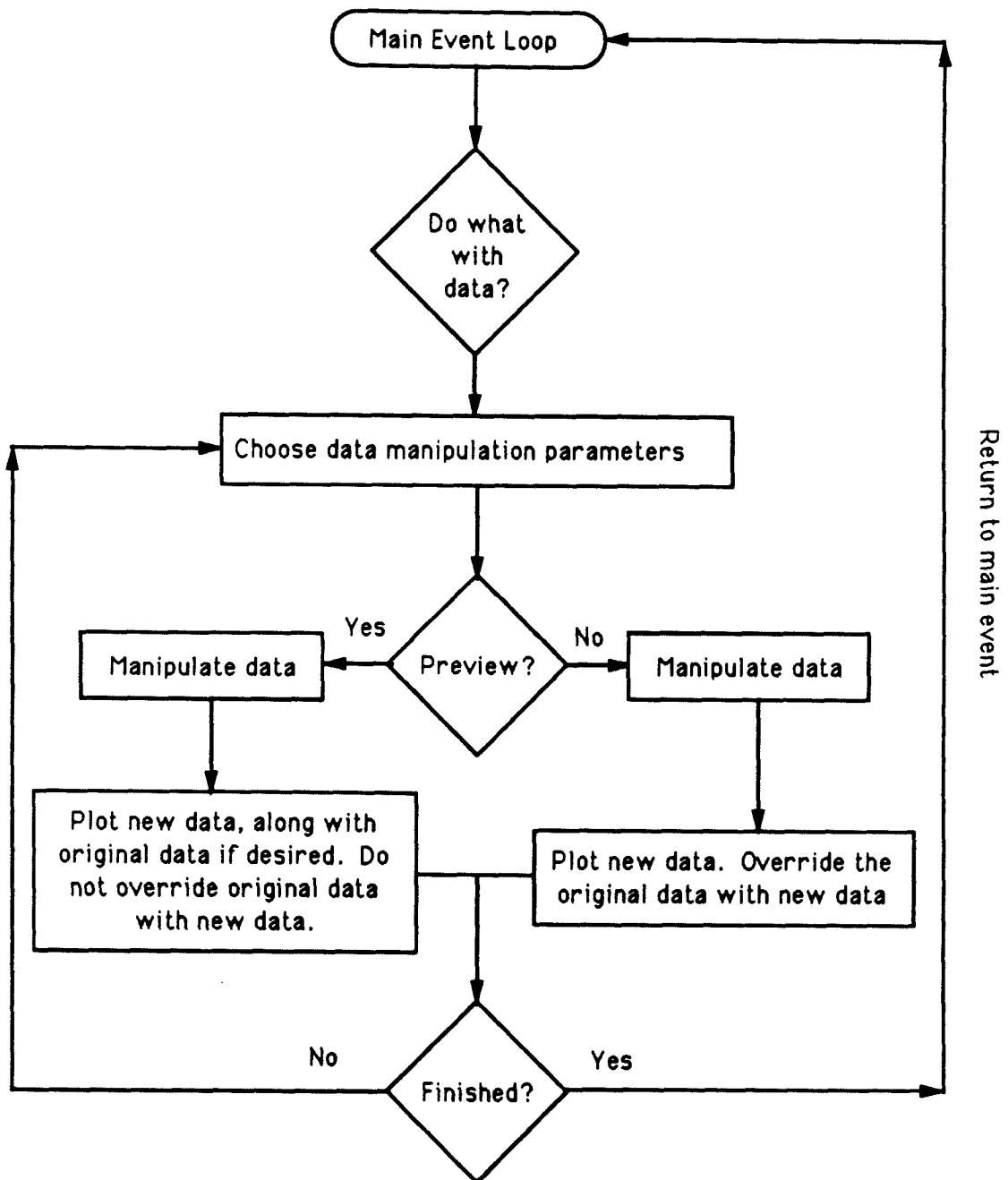


Figure 2

Data Acquire-047A		Data Acquire-047A	
Name	obj size	Name	obj size
Data Acquisition.c	3882	Fourier.c	4486
Decode.c	532	funcs.c	2786
dialogRoutines.c	1036	gaussj.c	1690
file.mini.c	2196	mrqcof.c	680
Help.Windows.c	1608	mrqmin.c	1306
MenusAndArrays.c	2348	REALFT.C	1042
mini.Windows.c	2048	SM00FT.C	856
MousePaint.c	242	Smoothfit.c	898
nrutil_fixed.c	1674	SORT2.C	522
plot.c	2536	TWOFFT.C	684
plotTwo.c	2318	Boxcar.c	3088
PrintFunctions.c	902	DataAcq.Lib	1776
ReadSaveFile.c	842	LeCroy Transient D.c	4384
ReconstructCAMAC.c	2010	LI.c	4516
scale.c	1044	OpenBoard.Lib	116
Utilities.c	768	Serial Comm Initialize.c	420
Write.c	1112	Serial Comm Utilities.c	926
zoom.Windows.c	506	Serial Dlog.c	5820
ChangeValues.c	1586	SpexCommands.c	2108
CONVLY.C	908	StartStopScan.c	1666
Convolutionfit.c	1828	Unidex Commands.c	590
covsrt.c	708	initialize.c	36
DataManipulateDlog.c	2592	Math881	1042
DoConvolution.c	1716	stdio881	19902
Fit.NLS.c	6548	storage	394
FOUR1.C	930	strings	582
Fourier.c	4486	unix881	5204
funcs.c	2786	MacTraps	9792
gaussj.c	1690	AboutProgram.c	546
mrqcof.c	680		

Figure 3

Data Analysis-047A		Data Analysis-047A	
Name	obj size	Name	obj size
Data Analysis.c	4198	funcs.c	2788
Decode.c	426	gaussj.c	1690
dialogRoutines.c	1036	Generate.c	1434
file.mini.c	2316	mrqcof.c	680
FitConvolveDlog.c	3594	mrqmin.c	1306
Help.windows.c	1608	REALFT.C	1042
MenusAndArrays.c	2386	SMOOF.T.C	856
mini.windows.c	1606	Smoothfit.c	784
MousePaint.c	242	TWOFFT.C	684
nrutil_fixed.c	1674	initialize.c	36
Plot.windows.c	452	Math881	1042
PrintFunctions.c	896	stdio881	19902
scale.c	1044	storage	394
SelectEdit.c	1184	strings	582
SORT2.C	522	unix881	5204
Utilities.c	746	MacTraps	9792
WindowsMenu.c	1684	ReadSaveFile.c	842
Write.c	1112	ReconstructCAMAC.c	2690
zoom.windows.c	506	AboutProgram.c	546
CONVLV.C	908	ChangeValuesConst.c	1546
Convolutionfit.c	1842	ChangeValuesFunc.c	2396
covsrt.c	708	plot.c	2520
DoConvolution.c	1720	plotTwo.c	2520
Fit.NLS.c	6558	AutoConvolve.c	3378
FOUR1.C	930	funcsNLSConvolve.c	2834
Fourier.c	5284	mrqcofConvolve.c	1052
funcs.c	2788	mrqminConvolve.c	1306
gaussj.c	1690	QSIMP.C	298
Generate.c	1434	TRAPZD.C	360
mrqcof.c	680		

Figure 4

CHAPTER 5

SOURCE FILES AND LIBRARIES DESCRIPTION

5.1 INTRODUCTION

In this chapter, a more specific description of the source files and libraries used in **Data Acquire** and **Data Analysis** is given. The main purpose is to outline the function of each module, its relationship to other functions, plus any other special notes that may be useful to know. The program source files contain comments to explain what is happening with the program code, and to facilitate improvements in program code efficiency. Some comments are useful for understanding how a routine works, described from a programmer's viewpoint, given a user-initiated event. Several data manipulation files have been adapted from Reference 1, and the reader is advised to go to that reference for a detailed discussion of the numerical methodology employed.

It is impossible to detail all the nuances of IEEE-488 and RS-232 serial communications interfacing. References important to this program are given in References 2-7. The program code listing also includes comments concerning any small details, often discovered by accident, which are particular to a given piece of equipment.

Because of the number of source files and header files, the chapter is organized into sections that focus on small groups of routines. These groups are outlined in subsequent paragraphs. Each section covers a specific aspect of the program operation. Each section begins with an explanation of the section's purpose. This is followed by a listing of the relevant source files. The function of the major routines in the source file are then discussed. Occasional reference are made to certain Macintosh Toolbox calls and their associated records in memory. Attempts have been made to keep the use of such terminology to a minimum. References 7-10 should be consulted for a full explanation of the Macintosh Toolbox.

All files used in the programs are listed below. Some files were provided by external sources, and the sources are indicated at the end of the list of filenames. The files are categorized according to their principal function. Source code files are designated by

XXX.c, while header files are designated as XXX.h. Many source files are used in both programs. There are a few cases where files with the same name are slightly different in the two programs, and these files are indicated by an asterisk. For features common to both programs, the header files are identical. Additional declarations and constants are for features unique to one program. If a source file name is followed by an asterisk, then there are two different versions, one for **Data Analysis** and one for **Data Acquire**. If a file has two versions, then both versions are printed in the supplemental source code listing. This is done for completeness and for minimizing confusion.

Macintosh Interface

AboutProgram.c
 Data Acquisition.c
 Data Analysis.c
 dialogRoutines.c
 FitConvolveDlog.c
 Help.windows.c
 initialize.c
 MenusAndArrays.c*
 mini.windows.c
 MousePaint.c
 Plot.windows.c
 Utilities.c*
 WindowsMenu.c
 zoom.windows.c
 Data Acquisition.h ²
 Data Analysis.h ³

Plotting

plot.c*
 plotTwo.c*
 scale.c

Memory Allocation ¹

nrutil_fixed.c
 nrutil.h

File Management

Decode.c
 file.mini.c
 PrintFunctions.c
 ReadSaveFile.c
 Write.c

Data Analysis

AutoConvolve.c
 ChangeValuesConst.c
 ChangeValuesFunc.c
 convlv.c ¹
 Convolutionfit.c
 covsrt.c ¹
 DoConvolution.c
 FitNLS.c
 four1.c ¹
 Fourier.c
 funcs.c
 gaussj.c ¹
 Generate.c ³
 mrqcof.c ¹
 mrqcofConvolve.c
 mrqmin.c ¹
 mrqminConvolve.c
 qsimp.c ¹
 realft.c ¹
 smooft.c ¹
 Smoothfit.c
 sort.c ¹

trapzd.c ¹

twofft.c ¹

complex.h ¹

nr.h ¹

Data Acquisition

Boxcar.c ²

DataAcq.Lib ⁴

LeCroy Transient D.c ²

LI.c ⁴

OpenBoard.Lib ⁴

ReconstructCAMAC.c

Serial Comm Initialize.c ²

Serial Comm Utilities.c ²

Serial Dlog.c ²

Spex Commands.c ²

StartStopScan.c ²

Unidex Commands.c ²

DrInterface.h ⁴

GPIBres.h ⁴

IEEE.h ⁴

sys.h ⁴

Project Name and Resources	Think C Libraries ⁵
Data Analysis-047A ³	Math881
Data Analysis-047A.R ³	stdio881
Data Analysis-047A.Rsrc ³	storage
Data Acquire-047A ²	strings
Data Acquire-047A.R ²	unix881
Data Acquire-047A.Rsrc ²	MacTraps

- 1 Adapted from the book **Numerical Recipes in C**
- 2 Relevant to **Data Acquire** program only
- 3 Relevant to **Data Analysis** program only
- 4 Provided by National Instruments
- 5 Provided by Think C, version 3

5.2 MACINTOSH INTERFACE

This section is concerned primarily with the files needed to implement the visual aspects of the Macintosh interface. Nonvisual aspects, such as file management and printing, are left for later sections.

5.2.1 AboutProgram.c

This file is used to create the entertaining credits display when the user chooses **About Data Acquire** or **About Data Analysis** from the **Apple** menu. The displayed text can be altered using the routine titled Credits().

5.2.2 Data Analysis.c and Data Acquisition.c

These files contain the global variable declarations, the main program, the routine MainEvent() (the main event loop), and some of the major routines called by MainEvent(). These are some of the most important files to understand, thus they are discussed in some detail. The routines, in order of their appearance in the code listing of Appendix II, are briefly discussed in the following paragraphs.

The routine main() is the main program. First, the Macintosh Toolbox is initialized for the new application using the routine named initialize(). Then the application's cursors, menus, windows, and filename strings are set up. Next, main() allocates a few extra master pointer blocks to minimize memory fragmentation [7-10]. The initialize() segment is then unloaded since it is no longer needed. Finally, main() checks whether the Macintosh is being run under MultiFinder. Program control is then transferred to MainEvent().

MainEvent() appears complicated, but is easily understood. It first updates the menus and cursors. Next it gets an event from the event queue, using WaitNextEvent() or GetNextEvent(). Then it enters the switch loop to evaluate the event and process it. The

switch loop first checks to see if it was a mouse event. If so, it then determines where the mouse event occurred in the following order: the Finder desktop, the close box of a window, the menu bar, a system window (*e.g.*, desk accessory), the title bar of a window, a window's size box, a window's content region, or a window's zoom box. Keyboard events are evaluated next, and the case of a key being depressed continuously is taken into account. Next come events that indirectly result from a user action: activation and updating. An example is when an obscured window is selected: The obscured window must first be activated, and then its hidden contents updated to be made visible. After the event has been processed, the status of data acquisition is checked. Lastly, all nonessential code segments are made purgeable to minimize memory fragmentation.

SetUpMenus() constructs menus either from code or by loading the available menu resources from the resource file. Once the menus are constructed, certain menu items are checked off or turned off as required by the state of the program. Once all the menus are constructed and initialized properly, the menu bar is drawn.

DoCommand() is used to evaluate the menu chosen and the menu item chosen, and directs the program to the specific task requested. When a menu is chosen, its title is highlighted so the last thing DoCommand() does is to dehighlight the menu title.

The next three routines are MaintainCursors(), MaintainMenus(), and SetUpCursors(). All cursors in this program (arrow, text, wristwatch) are predefined in the Macintosh Toolbox; therefore, it was not necessary to create any custom cursor resources. SetUpCursors() simply gets the predefined cursor resources and assigns them to handles to be used throughout the program. MaintainCursors() is used to adjust the cursor appearance to the text cursor if in the **Data Window** and the arrow otherwise. MaintainMenus() turns on and off some menu items, depending on whether the **Plot Window** or **Data Window** is active. Note that MaintainMenus() operates only on individual menu items, not on the whole menu.

The next five routines are diagnostic routines, which are used as safeties. The four routines called `oursXXX()` return true if the window exists and is being properly pointed to. `CantOpen()` is called by `main()`, and makes sure that the resource file is in good shape when the program is launched from the Finder desktop.

`DealWithUpdates()` handles window updating events. The structure of the update procedure is standard, but it employs the brute force method of essentially updating every window. Typically, updating requires redrawing the size box for the plotting windows, and the size box and text for the text windows.

The last four routines all deal with updating the interface in some regard. `PleaseWait()` sets the cursor to the wristwatch, indicating that an extended operation is in progress. `RedrawPlotWind()` is called whenever the plotting window size changes. First the routine checks to see whether anything is drawn on the window, gets the new dimensions, and then scales the plot accordingly. `UpdateMenuBar()` turns on and off menus, depending on whether the menus are relevant to the current state of the program. `UpdateHelpMenuBar()` functions similarly to `UpdateMenuBar()` but is very specific to the presence of the **Help Window**.

5.2.3 **dialogRoutines.c**

This file contains all the dialog routines to set up and perform text editing on dialog items. Routines are provided for variables of type integer, long integer, and double. In addition, the file contains the routines from checking off a dialog item, and for framing a button if it is the first item in the dialog list.

5.2.4 **FitConvolveDlog.c***

This file contains the routines which display and monitor the user's actions on the dialog boxes used for NLS Fitting (`DoFitDlog()`), NLS Convolution

(DoAutoConvolveDlog()), and ordinary convolution (DoConvolveDlog()). The **Data Acquire** version does not have a routine for NLSConvolution.

5.2.5 **Help.windows.c, mini.windows.c, and Plot.Windows.c**

These files contain the routines necessary for creating and maintaining the various windows. **Help.windows.c** regulates the **Help Window**, **mini.windows.c** governs the **Data Window**, and **Plot.windows.c** regulates the **Plot Window** and **Plot Window Two**. The main difference between the windows is the lack of text associated with the plotting windows. There are a number of window routines, but the ones that are encountered most often are those called by **MainEvent()**. Other miscellaneous routines are used to update other window parameters, but are implemented only by the window routines called by **MainEvent()**. Currently, the window routines for each window are largely the same. If a window parameter is irrelevant to the active window (*e.g.*, text editing and controls on the plotting windows), then it remains at the given default value when the window was first created. These default values are part of the window record created in memory by the Toolbox. In the future, the window routines should be rewritten as utilities analogous to **dialogRoutines.c**. In the following discussion, the **Help Window** is neglected since it is virtually identical to the **Data Window**.

SetUpWindows(), called during program startup, gets the window resource template and constructs the window plus its associated controls. The routine also establishes the associated font and text handles. **DoContent()** is concerned with the place in the window where the mouse button was pressed. **MyGrowWindow()** updates the window when the size box is moved. **UpdateWindow()** is used after any change in a window to recalculate controls, lines of text, and to redraws the window's controls and Grow icons (in the window's size box).

The equivalent routines for the plotting windows are much the same, except that all references to controls and text handles have been eliminated since they are irrelevant. The only additional routine added for the plotting windows is the routine `RedrawPlotWind()` to replot the graph as discussed in Section 5.2.2. In the case of the **Help Window**, the routines are completely analogous to the **Data Window** except that the variables for the controls, text handle, lines in folder, etc. are different (*e.g.*, `HelpTEH` vs `TEH`).

5.2.6 `initialize.c`

This file contains the routine required to initialize the Macintosh Toolbox for a given application. It is program independent and may be used for any user project. The ordering of the calls should not be changed since the Macintosh Toolbox has a very strict order of initialization [1-4].

5.2.7 `MenusAndArrays.c*`

This file serves two purposes. The file contains the routines necessary to allocate global data arrays. In addition, the file contains the routines used to evaluate what menu item was selected as well as to direct the program to the appropriate action based on the menu item selected.

5.2.8 `MousePaint.c`

This file contains the routine (`MousePaint()`), which enables the user to select and shade a portion of a window. The routine, which operates on the **Plot Window** and **Plot Window Two**, is used when the user wants to fit or expand a data file selectively. `MousePaint()` returns the local window coordinates that correspond to where the mouse button was depressed and released.

5.2.9 Utilities.c*

This file contains various debugging statements that can be used as diagnostics in the program. The MacsBug debugger (or equivalent) must be in the Macintosh System Folder. When the debugging statements are called, MacsBug is automatically implemented. In addition, the file contains the routine DoCaution() and DoCautionDlog(). DoCaution(), called by nerror() in the file nrutil_fixed.c (section 5.3.1), calls DoCautionDlog(). The dialog box associated with DoCautionDlog() allows the user to pause the current procedure, or to abort the program. The Data Analysis version also contains a utility routine called ScanMessage(), which can be used to display alert messages.

5.2.10 WindowsMenu.c

This file contains the routines necessary to maintain the **Windows** menu, which keeps track of which windows are open, and which window is the active window. Several routines are involved. SetUpWindowsMenu() is called when the program is launched from the Finder desktop. AddToWindowsMenu() is called when a window is opened. MaintainWindowsMenu() keeps track of which visible window is active. DeleteFromWindowsMenu() is called when a window is closed.

5.2.11 zoom.windows.c

This file contains the routine (MyZoomWindow()), which recalculates a window's parameters after a window is zoomed. These parameters include the number of lines of text that can be visible, the position of controls within the scroll bar, etc. The effects of the new parameter values are seen when the window is updated by UpdateWindow() (Section 5.2.5). If the **Plot Window** or **Plot Window Two** is zoomed, then MyZoomWindow() also calls the function RedrawPlotWind() (Section 5.2.2), so that graphs on the plotting windows are rescaled and redrawn to fit the new window

dimensions. The window updated depends on what window pointer is passed to the routine.

5.2.12 Data Acquisition.h and Data Analysis.h

These files are the main header files for **Data Acquire** and **Data Analysis**. They contain all header definitions for the various resources as well as for the miscellaneous constants and MultiFinder checks and data acquisition flags.

5.3 MEMORY ALLOCATION

This section is pertinent to the source files that contain the routines for dynamic memory allocation. Dynamic memory allocation is used extensively in the program in order to try to maximize the amount of memory available at any particular time.

5.3.1 nrutil_fixed.c

This file contains the dynamic memory allocation routines. Arrays and matrices of type integer, long int, float, and double may be allocated and freed. There is also a utility routine (nrerror()) which is needed by some of the data manipulation routines [8]. If an error is encountered by these routines, nrerror() pauses the program and displays a dialog box. The dialog box allows the user to continue, to stop the current fitting procedure (NLS Fitting and NLS Convolution), or to immediately quit the program. Unless the error is in memory allocation, it is not necessary to quit the program. The routines for the dialog box called by nrerror() are in the file Utilities.c (section 5.2.9).

5.3.2 nrutil.h

This header file contains the declarations for the various memory allocation routines.

5.4 PLOTTING

These files serve three main purposes. First, they contain the routines needed to plot the data in the XData and YData arrays on the plotting windows. Second, they allow one to draw single data points on the plotting windows. Finally, they contain a routine that calculates the plot axes dimensions for the current geometry of the plotting window.

5.4.1 plot.c* and plotTwo.c*

These files contain the routines needed for plot data on the **Plot Window** and **Plot Window Two**. Only plot.c is discussed here. This is because plotTwo.c is identical to plot.c except that the routines operate on **Plot Window Two**. The names of routines in plotTwo.c are of the form (plot.c name)Two().

DrawPlotWind() is the master plotting routine. The values of the axes are set by SetPlotAxesMinMax(). The axes and axes labels are produced by DrawAxes() and DrawLabels(). The data points are drawn if the flag called DataTakenFlag is true. DataTakenFlag is normally true except at the start of data acquisition. If the pointer variable TheFunc is not set to NIL, then the current function (in funcs.c) being pointed to by TheFunc is drawn. These are the same functions used in NLS fitting, convolution (not NLS convolution), and function generation through the **Functions** menu.

Two other very important routines are DrawADataPoint() and GetPlotAxesRect(). DrawADataPoint() allows one to draw a single data point on the **Plot Window**, and is used for both data acquisition and NLS convolution. GetPlotAxesRect() calculates the dimensions of the plotting axes based on the current size of the **Plot Window**, and is called whenever the size of the **Plot Window** changes.

An important point to remember is that the **Plot Window** displays the plot as a picture. Displaying plots as pictures greatly simplifies the window updating process. Only one picture can be open at a time. Pictures are opened by calling the Toolbox routine

OpenPicture(). OpenPicture() returns a PicHandle [1-3], called PlotWindPic, to the new picture. After the plot is created internally by calling the necessary QuickDraw routines, the picture is closed by calling the Toolbox routine ClosePicture(). The picture is then drawn on the **Plot Window**, and this is immediately followed by a call to the Toolbox routine SetWindowPic(). SetWindowPic() is important since it makes the picture part of the window record. Once the picture is part of the window record, selecting the window causes the picture to be drawn rather than generating an update event.

5.4.2 scale.c

This file contains the routine (scale()) used to determine the scaling of the X and Y axes when plotting a data file. When a plot is made, scale() is called by the routine called SetPlotAxesMinMax (Section 5.4.1).

5.5 FILE MANAGEMENT

The files in this section perform various tasks related to creating and saving files, printing files displayed in the various windows, and loading data from saved files into the global data analysis arrays (XData, YData) of the program.

5.5.1 Decode.c

This file contains the routines needed to load the X and Y data of a saved data file into the XData and YData arrays of the program.

5.5.2 file.mini.c

This file contains the routines needed to open and save files through the **File** menu. It is designed to operate on data shown in the **Data Window** and the **Help Window**. However, saving data shown on the **Help Window** is not supported.

5.5.3 **PrintFunctions.c**

This file contains the routines needed to print out data that are in the **Data Window**, **Plot Window**, or **Plot Window Two**. The **Data Window** is printed as ordinary text, while the plotting windows are printed out as pictures. Currently, printing a file from the **Help Window** is not supported.

5.5.4 **ReadSaveFile.c**

This file contains the routines needed to create unlinked text data files using Think C. These routines are crucial for creating the temporary files (*e.g.*, **Most Current Scan**) and for creating data files when saving mass spectra files automatically. Also they are important for reading these saved mass spectra files into the global arrays, CAMACXData and CAMACYData, which are used when reconstructing data transients. CreateNewFile() returns a pointer to a new file with a user specified filename. ReadOldFile() reads and loads the data from a saved file into the CAMACXData and CAMACYData arrays for use in reconstruction. SaveNewFile() saves data in the XData and YData arrays to a file. SaveMassSpectrum() gets the default filename when autosaving mass spectra. FindFilesToCreateDecay() gets the global filename to be used for reading files for the reconstruction process.

5.5.5 **Write.c**

This file contains the routines needed to write the data in the XData and YData arrays to a data file using the **Collection** menu. There are three routines available. The default filename is created by MakeDefaultFilename(). If files are to be saved as unlinked text, then the file is saved by WriteTextFile(). If the file is to be saved as a file linked to CricketGraph or to Excel, then the file is saved using WriteData().

5.6 DATA ANALYSIS

This section contains the files used to perform the data analysis. Some of the files are purely data manipulative in design [8], while others are master routines that use the routines in the data manipulation files.

5.6.1 AutoConvolve.c

This file contains the main driver routines needed to implement a Marquardt NLS fit of a convolved data file to the given functions listed in the **NLS Convolve** menu.

5.6.2 ChangeValuesConst.c

This file contains the driver and dialog routines needed to alter the X and Y data from a data file by a constant.

5.6.3 ChangeValuesFunc.c

This file contains the driver and dialog routines needed to alter the X and Y data from a data file by a function.

5.6.4 convlv.c

This file [1] contains the routine to convolve or deconvolve a real data set (including user-supplied zero padding) with a response function.

5.6.5 Convolutionfit.c

This file contains the main driver routine needed to perform convolution of a data file with a response function through the **Convolve** menu..

5.6.6 covsrt.c

This file [1] contains the routine to repack the covariance matrix to the true order of the parameters, given the covariance matrix of a fit for some number of the total parameters and their ordering.

5.6.7 DoConvolution.c

This file contains the routine (DoConvolution()), which prepares the data and chosen response function for convolution. The actual convolution is done utilizing the routines in **convlv.c**.

5.6.8 FitNLS.c

This file contains the main driver routines needed to implement a Marquardt NLS fit of a data file to the given functions listed in the fitting menu.

5.6.9 four1.c

This file [1] contains the routine that calculates the discrete Fourier transform given a complex data array.

5.6.10 Fourier.c

This file contains the driver and dialog routines needed to perform a time-to-frequency Fourier transform. Real or complex Fourier transforms can be done.

5.6.11 funcs.c

This file contains the functions used to convolve or NLS fit data, using specific functional forms. The functional forms are the same as those given in the NLS Fit and Convolve menus.

5.6.12 funcsNLSConvolve.c

This file contains the functions used to NLS convolve data, using specific functional forms. The functional forms are the same as those given in the NLS Convolve menu.

5.6.13 gaussj.c

This file [1] contains the routine needed to implement the solution of a matrix of linear equations by the Gauss-Jordan elimination method. This routine is used in conjunction with NLS Fitting and NLS Convolution.

5.6.14 Generate.c

This file contains the routines needed to generate files of a given function, and stores the new data in the XData and YData arrays of the program.

5.6.15 mrqcof.c

This file [1] contains the routine needed to evaluate the linearized fitting matrix alpha and vector beta that are used in mrqmin.c.

5.6.16 mrqcofConvolve.c

This file is based on **mrqcof.c**. It is used for NLS convolution, and has been adjusted to account for the use of numerical integration in the NLS convolution process. In all other respects, it is identical to **mrqcof.c**.

5.6.17 mrqmin.c

This file [1] contains the routine needed to perform one iteration of the Levenberg-Marquardt method to minimize the value of the chi-square of a fit between a set

of points with individual standard deviations and a nonlinear function dependent on coefficients.

5.6.18 mrqminConvolve.c

This file is based on **mrqmin.c**. It is used for NLS convolution, and has been adjusted to account for the use of numerical integration in the NLS convolution process. In all other respects, it is identical to **mrqmin.c**.

5.6.19 qsimp.c

This file [1] performs Simpson integration and returns the integral of a function from boundary points a to b.

5.6.20 realft.c

This file [1] contains the routine to calculate the Fourier transform of a set of 2n real-valued data points. It replaces these data by the positive frequency half of its complex Fourier transform. The routine is also capable of calculating the inverse transform of a complex data array if it is the transform of real data.

5.6.21 smooft.c

This file [1] contains the routine needed to smooth the Y data, while the X and Y data remain associated.

5.6.22 Smoothfit.c

This file contains the driver and dialog routines needed to smooth a data file.

5.6.23 sort2.c

This file [1] contains the routine needed to sort an array into ascending numerical order, using the Heapsort algorithm, while making the corresponding rearrangements of the partner array.

5.6.24 trapzd.c

This file [1] contains the routine needed to compute the nth stage of refinement of an extended trapezoidal rule. It is used in conjunction with qSimp.c.

5.6.25 twofft.c

This file [1] contains the routine, which takes two real arrays as input, that calls fourl() and returns two complex output arrays. Each of the complex arrays is of length n, and contain the Fourier transforms of the respective input data.

5.6.26 complex.h

This header file contains the definitions needed to perform complex function operations using functions provided by Reference 1.

5.7 DATA ACQUISITION

This section contains the source files needed to perform data acquisition. Data are taken using a boxcar integrator or a CAMAC crate based LeCroy Waveform Analyzer.

5.7.1 Boxcar.c

This file contains the routines needed to take a data point using the boxcar.

5.7.2 DataAcq.Lib and OpenBoard.Lib

These libraries are required for the operation of the NB-M10-16H-9 board used by the boxcar.

5.7.3 LeCroy Transient D.c

This file contains the routines needed to take a single data scan using the CAMAC crate-based LeCroy Waveform Analyzer.

5.7.4 LI.c

This file contains the routines needed for the laboratory interface via GPIB.

5.7.5 ReconstructCAMAC.c

This file contains the driver and dialog routines needed to reconstruct transients from previously saved mass spectra.

5.7.6 Serial Comm Initialize.c

This file contains the routines needed to initialize the serial drivers for setting the proper communication parameters for the Unidex controller [5] and the Spex CD2A CompuDrive [6].

5.7.7 Serial Comm Utilities.c

This file contains various utility routines needed for serial communications.

5.7.8 Serial Dlog.c

This file contains the various routines for the dialog boxes pertinent to communication with external equipment. These are the delay line, boxcar, CAMAC crate, and CD2A Compudrive.

5.7.9 Spex Commands.c

This file contains the routines needed to communicate with the Spex CD2A Compudrive. The CD2A Compudrive regulates the position of the monochromator.

5.7.10 StartStopScan.c

This file contains the routines needed to initialize, start, and stop the data acquisition process.

5.7.11 Unidex Commands.c

This file contains the routines needed to communicate with the Aerotech Unidex 1 motion controller. This controller then regulates the motion of the optical delay line.

5.7.12 DrInterface.h

This header file is the include file for the interface between LI.c and the Driver. It **MUST** be included in both ends of the interface.

5.7.13 GPIBres.h

This header file defines the GPIB resources. The resources should be opened with `GetNamedResource` since the resources may be moved into the system file, in which case the ID's may be changed by the installer.

5.7.14 IEEE.h

This header file contains the definitions for the status codes for GPIB.

5.7.15 sys.h

This header file contains the various system definitions for GPIB communication.

5.8 PROJECT NAME AND RESOURCES

These files are required to construct the Think C project.

5.8.1 Data Analysis-047A and Data Acquire-047A

These are the Think C project files for Data Analysis and Data Acquire.

5.8.2 Data Analysis-047A.R and Data Acquire-047A.R

These are the RMaker source files used to create the Version resources for Data Analysis and Data Acquire.

5.8.3 Data Analysis-047A.Rsrc and Data Acquire-047A.Rsrc

These are the resource files associated with Data Analysis and Data Acquire. They are editable using ResEdit.

5.9 C PROGRAMMING ENVIRONMENT LIBRARIES

These are the standard libraries that are part of the C programming language and the Think C development environment. If the library name is followed by 881, this is the version of the library required if the project is to utilize the 68881 math coprocessor properly.

5.9.1 Math881, stdio 881, storage, strings, and unix881

These libraries are part of the C language. The C standard input and output library is **stdio881**. Mathematics routines are given in **math881**. Dynamic memory allocation is possible by using the functions in the **storage** library. The **strings** library contains the C routines needed for putting together strings. Finally, **unix881** contains the C routines needed for converting strings to numbers, getting the time, and aborting the program in an emergency.

5.9.2 MacTraps

This library provides the interface between the Think C development environment and the Macintosh Toolbox. MacTraps will be required for any Think C project using that uses the Macintosh Toolbox .

5.10 REFERENCES

1. W. H. Press, B. P. Flannery, S. A. Teukolsky, and W. T. Vetterling, *Numerical Recipes in C* (Cambridge Univ. Press, Cambridge, 1988).
2. Aerotech, *Unidex 1 Owner's manual*, 1988.
3. Spex Industries, *CD2A Owner's manual*, 1985.
4. LeCroy, *Operator Manual for 6010/6010A Magic Controller*, May 1986.
5. National Instruments, *LabDriver Software Reference Manual*, January 1988.
National Instruments, *NB-M10-16 User Manual*, February 1988.
6. National Instruments, *NI-488 Software Manual for the Macintosh*, August 1988.
National Instruments, *NB-DMA-8-G User Manual*, 1988.
7. Apple Computer, Inc., *Inside Macintosh, volumes 1-5* (Addison-Wesley, Reading, 1988).
8. Stephen Chernicoff, *Macintosh Revealed, volumes 1-3* (Hayden, Indianapolis, 1987-89).
9. David Mark and Cartwright Reed, *Macintosh Programming Primer* (Addison-Wesley, Reading, 1989).
10. Scott Knaster, *How to Write Macintosh Software, 2nd Edition* (Hayden, Indianapolis, 1988).

CHAPTER 6

PROGRAM MODIFICATION: A TUTORIAL

6.1 INTRODUCTION

In this chapter, a tutorial is given for modifying **Data Acquire** and **Data Analysis**, using the Think C development environment. The abbreviated code listing used in this chapter will show the reader where the modifications have been installed in the actual source code. Here, a fully worked out example is given for a simple program modification. This example assumes that one wishes to add a new feature to do some type of calculation. Furthermore, the parameters for the calculation are to be adjusted through a dialog box, and the dialog box will be accessed through a menu. In this example, the additions are made to the **Data Analysis** program. For simplicity, the new menu item is added to the existing **Functions** menu. The new menu item is called **New Item**. The dialog box, entitled **New Dialog**, allows the user to enter a number and click an **OK** or **CANCEL** button. If **OK** is pressed, then the entered number is taken as the slope of a line. The line, with an intercept of zero, is then plotted on the **Plot Window**. If **CANCEL** is pressed, then nothing happens.

The modification procedure is as follows. The program resources (menus and dialog boxes) are modified as needed, and any new resources are created. Then the main body of the program code is modified to utilize the new resources. The actual C code for the calculation is then developed, and it is shown how to utilize the plotting routines. The order for the code modification used here is not rigid, and one could modify the code for the calculation first. Working with the interface is often assumed, perhaps inaccurately, to be the most obscure part of the program. Bugs encountered with code for the calculation are due to incorrect use of the C language, not to the Macintosh. To assist the reader in this tutorial, the relevant variables (local and external) are declared each time a part of the source code is shown. Obviously, the variables would be declared only once in the actual program code.

6.2 CREATING THE NEW RESOURCES

First we create the dialog box, using the **ResEdit** (provided by Think C) application. Open up the project resource file to list the resource types used in the program. Open the **DLOG** resource to list all the dialog box numbers (Figure 1). Choose **New** from the **File** menu to create a new dialog box. Note the number 21321. This number, assigned by **ResEdit**, is the dialog ID number (Figure 2). Use **Display As Text** in the **DLOG** menu to set the title and size of the dialog box on the screen (Figure 3). Double-clicking on the new dialog box brings up the **DITL** window. In this window are created and placed the needed dialog items (Figure 4). The **DITL** ID number is the same as the **itemsID** number in Figure 3. Choose **New** from the **File** menu to bring up a **ResEdit** dialog box, which allows the user to set the parameters for various kinds of dialog items. Use this box to create the **OK** button (Figure 5). Close the **ResEdit** dialog box to have the new button displayed on the **DITL** window. The new button can be placed anywhere in the **DITL** window. Repeat the process for the 3 remaining dialog items. The **CANCEL** button is item 2, the label **The number:** is item 3 and is **Static text**, and item 4 is **Editable text** for entering the new number (Figure 6). This is all that needs to be done using **ResEdit**. Save the new resource file and quit **ResEdit**.

Note that although the **Functions** menu was not altered with **ResEdit** in this example, it is because the **Functions** menu was built using code. However, it is trivial to modify a menu that has been built with **ResEdit**. Simply open the proper **MENU** resource, and click the menu item that will precede the new menu item. Choose **New** from the **File** menu adds a menu item titled **Blank** to the menu resource template. Type in the new menu item name, and click the **Do It** button. The new menu item should now be added to the menu. Save the new resource file to record the changes.

6.3 MODIFYING THE CODE TO USE THE NEW RESOURCES

The **Functions** menu was built with code. The routine `SetUpMenus()` in the source file `Data Analysis.c` handles the menu setup when the program is started up. The **Function** menu is built using the `AppendMenu()` Toolbox routine, and the various menu items are added in the order that they will appear. For simplicity, the new menu item is added to the end. The modified statements in `SetUpMenus()` for the **Functions** menu are given below. Note the `MenuHandle` declaration called `Generate`. Menus are accessed in memory through `MenuHandles`. This declaration is included here, but is normally in the global declaration list at the beginning of the `Data Analysis.c` source file. The menu associated with the `Generate` `MenuHandle` is the **Functions** menu seen on the screen.

```
MenuHandle  Generate;

Generate = NewMenu(GenerateID, "\pFunctions"); /*create Generate menu*/
AppendMenu(Generate, "\pGaussian");
AppendMenu(Generate, "\pLorentzian");
AppendMenu(Generate, "\pSech Squared");
AppendMenu(Generate, "\p(-----)");
AppendMenu(Generate, "\pExp Step");
AppendMenu(Generate, "\pSingle Exp");
AppendMenu(Generate, "\pDouble Exp");
AppendMenu(Generate, "\pLine");
AppendMenu(Generate, "\pNewItem");           <----- Add this line
InsertMenu(Generate, 0);
```

The **Functions** menu now contains the new menu item. If the program were tested now, one would see an updated menu. The Toolbox recognizes that the new menu item exists, but nothing will happen since the program itself does not yet know about the new item.

Now one needs to get the new menu item recognized when it is selected. First, the main header file (Data Analysis.h) is opened. The header contains the menu and dialog box declarations. In the declarations for the Generate menu, add a declaration for the new menu item. The relevant part of the header file after modification is

```
#define gfGaussian      1          /*Generate menu stuff-added LWP*/
#define gfLorentzian    2
#define gfHypSecant     3
#define gfExpStep       5
#define gfSingExp       6
#define gfDoubExp       7
#define gfLine          8
#define gfNewItem       9          <----- Add this line

#define SBarWidth      15

#define EXAMPLEDLOGID   21321 /*Example dialog*/ <-----Add this line
#define FITDLOGID       12322 /*NLS Fit -added LWP*/
#define CONVOLVEDLOGID  27492 /*Convolution-added LWP*/
#define ABOUTDLOGID     13946 /*Program help-added LWP*/
```

The arbitrary prefix **gf** indicates that these items are relevant to the **Functions** menu. The menu item number corresponds to its position in the menu: **New Item** is the ninth item in the **Functions** menu. The dashed lines count as menu items. If the new menu item was added in the middle of the **Functions** menu, then the numbers for all items after the new entry would need to be changed appropriately. Note that the dialog box ID number is also in the header file, and is called **EXAMPLEDLOGID**.

The program uses switch routines to associate an action with a particular menu item. Therefore, the switch routine for the **Functions** menu must have a case for the new menu item added to it. The switch routine is in the source file **MenusAndArrays.c** in the function called **DoGenerateMenu()**. In this example, we want the new dialog box to be displayed if the new menu item is chosen. The properly modified version of **DoGenerateMenu()** is given on the next page.

```

int    DoGenerateMenu(item)                                /*added LWP*/
register int    item;
{
    void    GaussianFunc();
    void    LorentzianFunc();
    void    HypSecantFunc();
    void    ExpStepFunc();
    void    SingExpFunc();    /*this plus other needed additions added LWP*/
    void    DoubExpFunc();    /*this plus other needed additions added LWP*/
    void    LineFunc();        /*this plus other needed additions added LWP*/

    imode = item;                                /* ***very important!*** */

    switch (item) {
        case gfGaussian:
            GenerateFunctions(GaussianFunc);
            break;
        case gfLorentzian:
            GenerateFunctions(LorentzianFunc);
            break;
        case gfHypSecant:
            GenerateFunctions(HypSecantFunc);
            break;
        case gfExpStep:
            GenerateFunctions(ExpStepFunc);
            break;
        case gfSingExp:
            GenerateFunctions(SingExpFunc);
            break;
        case gfDoubExp:
            GenerateFunctions(DoubExpFunc);
            break;
        case gfLine:
            GenerateFunctions(LineFunc);
            break;
        case gfNewItem:                                <-----Add this case
            CreateLine();
            break;
        default:
            break;
    }
}

```

The new function, here called `CreateLine()`, will be the main routine for generating and plotting the line. `CreateLine()` will call the function `DoExampleDlog()`. `DoExampleDlog()` will be used to handle the new dialog box. The code for `CreateLine()` is given in Section 6.4. The code for `DoExampleDlog()` is listed on the next page.

```

double Number = 0;                                /*declaration of variable*/

int DoExampleDlog()                                /*EXAMPLE DIALOG*/
{
    DialogPtr theDialog;
    int itemHit;
    WindowPtr tmpWindPtr;
    double tempNumber;                            /*Number to be entered*/

    tempNumber = Number;                          /*create local variable for number to be entered*/

    GetPort(&tmpWindPtr);                          /* Point at current window*/

    theDialog = GetNewDialog(EXAMPLEDLOGID, &DlogRec, (WindowPtr)(-1) );
    /*Get the dialog box, and bring it to the front*/
    SetPort(theDialog);
    /*Make the dialog the active graphics port*/

    /*Setting up the initial conditions*/

    SetUpTEDlogDouble(theDialog,4,tempNumber);      /*set up dialog item*/

    ShowWindow(theDialog);                          /*make dialog visible */
    frameOkbox(theDialog);                          /*make OK button the default */

    /*Start Dialog loop*/
    do{
        ModalDialog(NIL, &itemHit);                /*calls filter before handling*/
        switch (itemHit){
            case 1 :                                /* OK button */
            case 2 :                                /* CANCEL button*/
                break;
            case 4:                                /* value of the number*/
                DoTEDlogDouble(theDialog,itemHit,&tempNumber);
                break;
            default:
                break;
        }
        /*the case of what item was hit*/
    } while (itemHit != 1 && itemHit != 2);

    CloseDialog(theDialog);
    SetPort(tmpWindPtr);

    if (itemHit != 2) {                             /* Unless it was cancel... */
        Number = tempNumber;                        /*assign new value for the number*/
        return(1);
    } else{
        return(0);
    }
}

```

Every dialog box in this program is structured in the same way. The dialog routines are in either the source file `FitConvolveDlog()`, or a source file particular to a given task (*e.g.*, the Fourier dialog in the `Fourier.c` source file). Note that the case number in the dialog loop corresponds to the order in which the dialog items were added when the dialog box was built in **ResEdit**. Routines that handle the various dialog items in the dialog boxes (*e.g.*, `DoTEDlogDouble()`) are in the source file `dialogRoutines.c`. The routines in `dialogRoutines.c` are utilities in which the necessary Toolbox calls have been collected for convenience. Note that the ampersand is required for `DoTEDlogDouble()` to function properly (*e.g.*, case 4 in `DoExampleDlog()`). The ampersand is not used in the function `SetUpTEDlogDouble()`.

6.4 CODE FOR CALCULATION AND PLOTTING

Next we need to construct the arrays and the data for the sine wave. As mentioned previously in Chapter 3, the `XData` and `YData` arrays are global ones used for plotting, creating and writing files. Other arrays, both local and global, are designated for special tasks by the programmer. For simplicity, these arrays are used directly. An example function, called `CreateLine()`, for generating and plotting a line, is given below. `StartPos`, `EndPos`, and `CurrYRow` may change in different parts of the program, so their values need to be set properly.

```
extern int NumOfDataPts = 100;          /*set to 100 for this example only*/
extern float *XData;                   /*X data array*/
extern float **YData;                  /*Y data matrix*/
extern int CurrYRow = 0;                /*which Y row the data is in*/
extern int NumYRows = 4;               /*maximum of 4 rows available for now*/
extern int StartPos = 0;               /*first data point*/
extern int EndPos = NumOfDataPts;      /*last data point*/

double Number = 0;                    /*declaration of variable*/
```

```

void CreateLine();
{
    int i;                /*looping variable*/
    int ExampleDlogStatus; /*was the OK or CANCEL button pressed?*/

    ExampleDlogStatus = DoExampleDlog();
        /*evaluate the user response to the dialog box*/

    if(ExampleDlogStatus==1) { /*was OK button pressed?*/
        MakeDataArrays(NumOfDataPts); /*allocate memory for arrays*/

        for(i=0;i<NumOfDataPts;i++) { /*load the data*/
            XData[i] = i;
            YData[CurrYRow][i] = Number*i;
        }

        DrawPlotWind(TRUE,XData,YData,StartPos,EndPos,NumYRows,CurrYRow,NIL);
            /*plot the data on the Plot Window*/
    }
}

```

Note that if the data were to be drawn on **Plot Window Two**, the calling routine is: `DrawPlotWindTwo(TRUE,XData,YData,StartPos,EndPos,NumYRows,CurrYRow,NIL);` with `CurrYRow` now being equal to one. Although there are three additional variables for plotting, they are assigned as `NIL` because they are irrelevant to this procedure.

6.5 TESTING AND FINAL COMMENTS

The new program can now be tested. Running the project under Think C, the program starts up as usual. Since the main header file (`Data Analysis.h`) was modified, there may be a short delay in running the project as the compiler will recompile every source file that accessed that header. Selecting the new menu item gives the screen shown in Figure 7. Test to see whether the number value is retained and the line plotted (Figure 8) when pressing the **OK** button, and unchanged (and nothing happens) when pressing the **CANCEL** button. If things work properly, we are nearly finished.

A final important point. The user should note that once the data are properly loaded into the XData and YData arrays, the data are available to be used with all other program features. No other files need to be changed. This provides a means for another check to make sure that the data are loaded properly in the XData and YData arrays. One should be able to plot the data (default or selective plot), save the data, and perform a simple analysis in any random order. If this is successful, then it can be said that things are working properly.

FIGURE CAPTIONS

- Figure 1:** The ResEdit listing of all the dialog resources (DLOG) used in the Data Analysis program.
- Figure 2:** The newly created dialog box displayed graphically using ResEdit. The location of the dialog box on the screen can be adjusted by dragging the dialog box with the mouse.
- Figure 3:** The newly created dialog box displayed as text using ResEdit. In text mode one can adjust the size, location, and appearance of the dialog box.
- Figure 4:** The newly created dialog box template (DITL) displayed using ResEdit.
- Figure 5:** The ResEdit dialog box for creating new dialog items such as buttons, checkboxes, and text items.
- Figure 6:** The completed dialog box template (DITL) for the new dialog box displayed using ResEdit.
- Figure 7:** The new dialog box as it appears in the modified Data Analysis program.
- Figure 8:** The line plotted on the Plot Window if the entered number is equal to 5.

Data Analysis-047A.Rsrc	
ALRT	
BNDL	
DITL	
DLOG	
FREF	
ICN#	
MENU	
PENH	
WIND	

DL0Gs from Data Analysis	
DL0G ID = 21570	↑
DL0G ID = 21038	
DL0G ID = 16861	
DL0G ID = 18045	
DL0G ID = 12322	
DL0G ID = 2141	
DL0G ID = 10809	
DL0G ID = 3325	
DL0G ID = 4844	
DL0G ID = 14907	↓

Figure 1

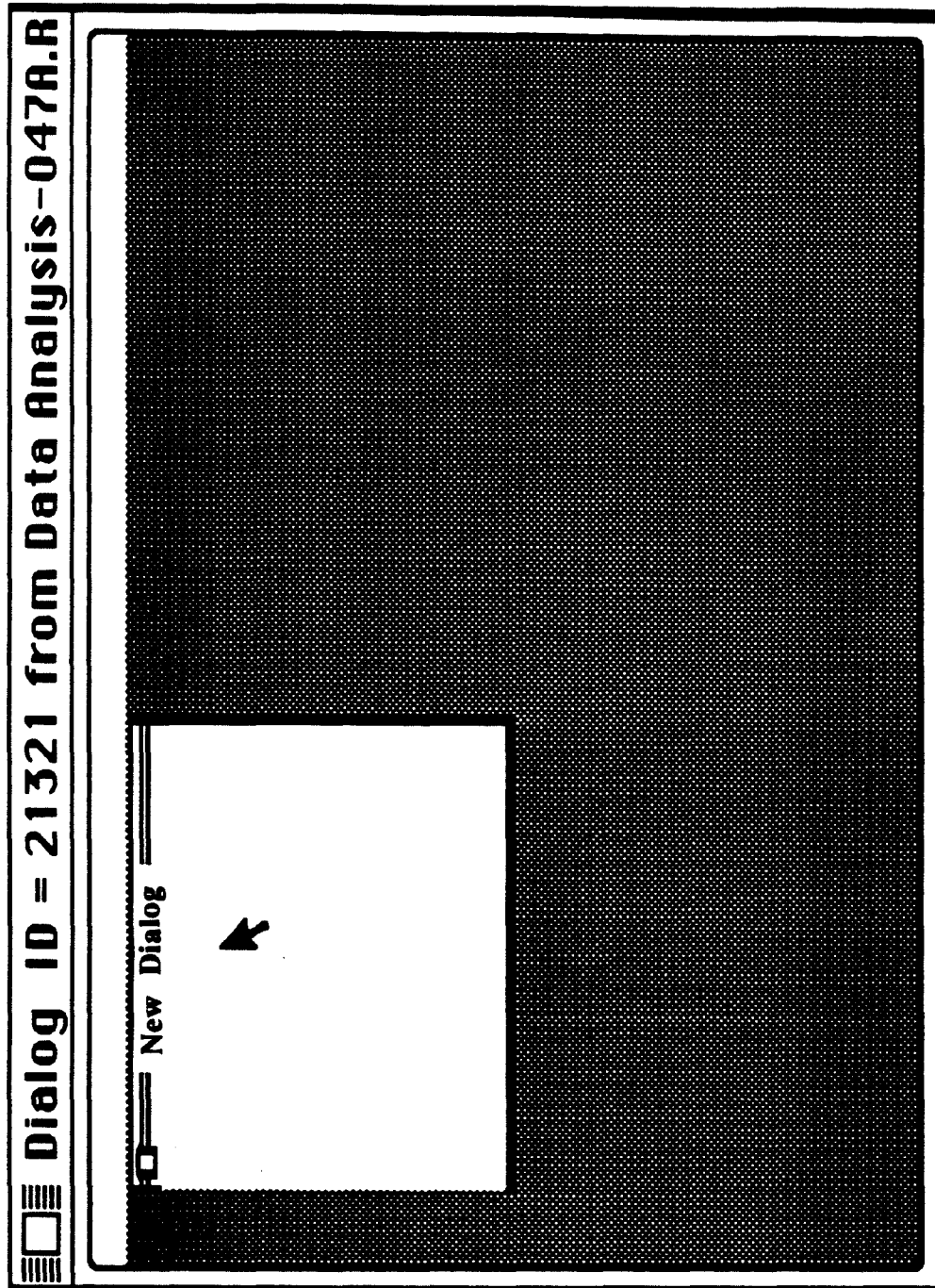


Figure 2

Dialog ID = 21321 from Data Analysis-047A.R

Window title:

New Dialog

top	40	bottom	240
left	40	right	480
procID	0	refCon	0
itemsID	0		

☒ Visible

☒ goAwayFlag

Figure 3

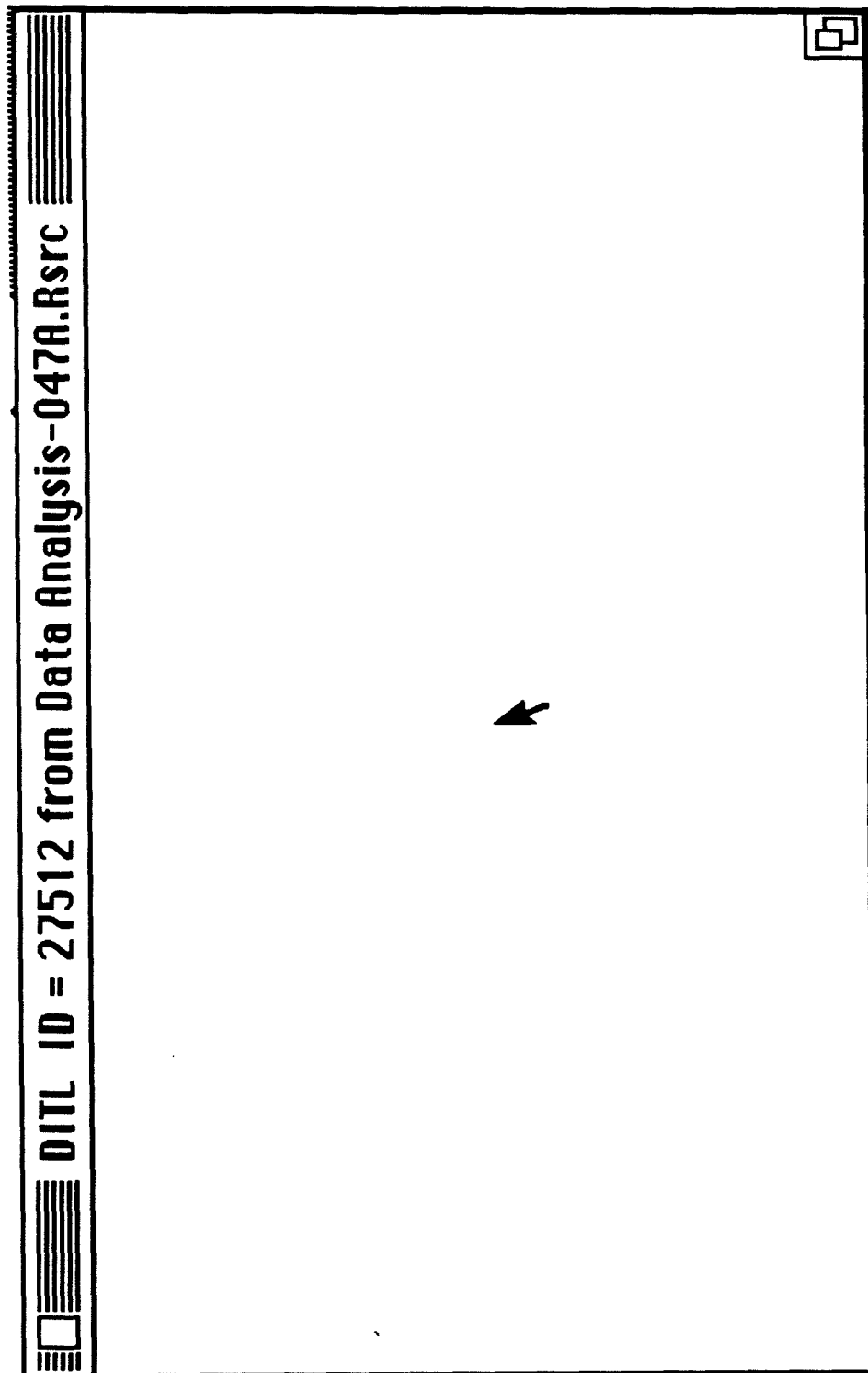


Figure 4

Edit DITL Item #1	
<input checked="" type="radio"/> Button	<input checked="" type="radio"/> Enabled
<input type="radio"/> Check box	<input type="radio"/> Disabled
<input type="radio"/> Radio control	
<input type="radio"/> Static text	top 90
<input type="radio"/> Editable text	left 190
<input type="radio"/> CNTL resource	bottom 110
<input type="radio"/> ICON resource	right 250
<input type="radio"/> PICT resource	
<input type="radio"/> User item	
<hr/>	
Text	OK

Figure 5

The image shows a graphical user interface window. The title bar at the top contains a small square icon on the left and the text "Dialog item list ID = 27512 from" in the center. The main area of the window is white. In the center, there is a label "The Number:" followed by a rectangular text input field. Below the input field, there are two buttons: "NEW" on the left and "CANCEL" on the right. In the bottom right corner of the window, there is a small square icon with a plus sign inside.

Figure 6

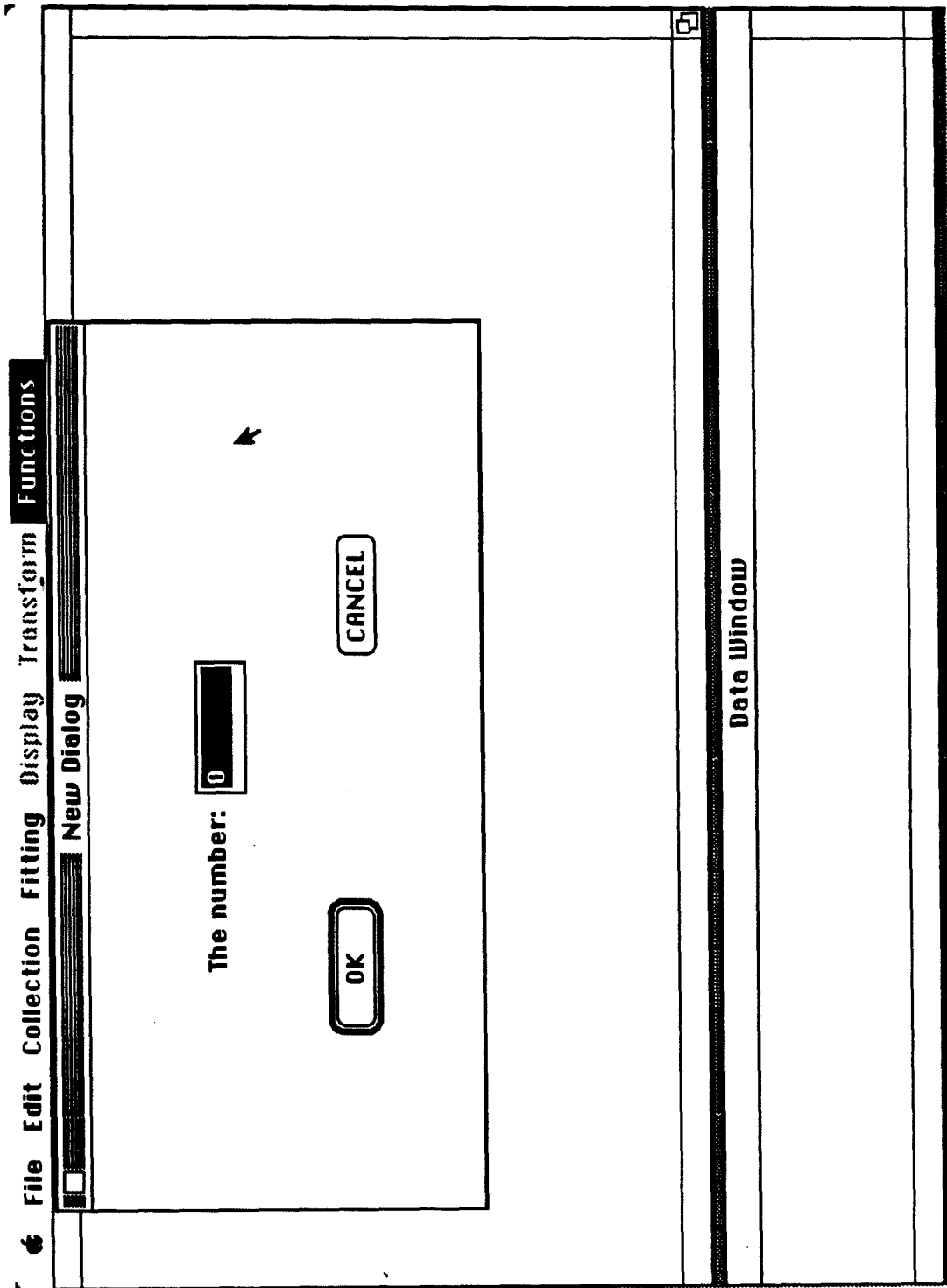


Figure 7

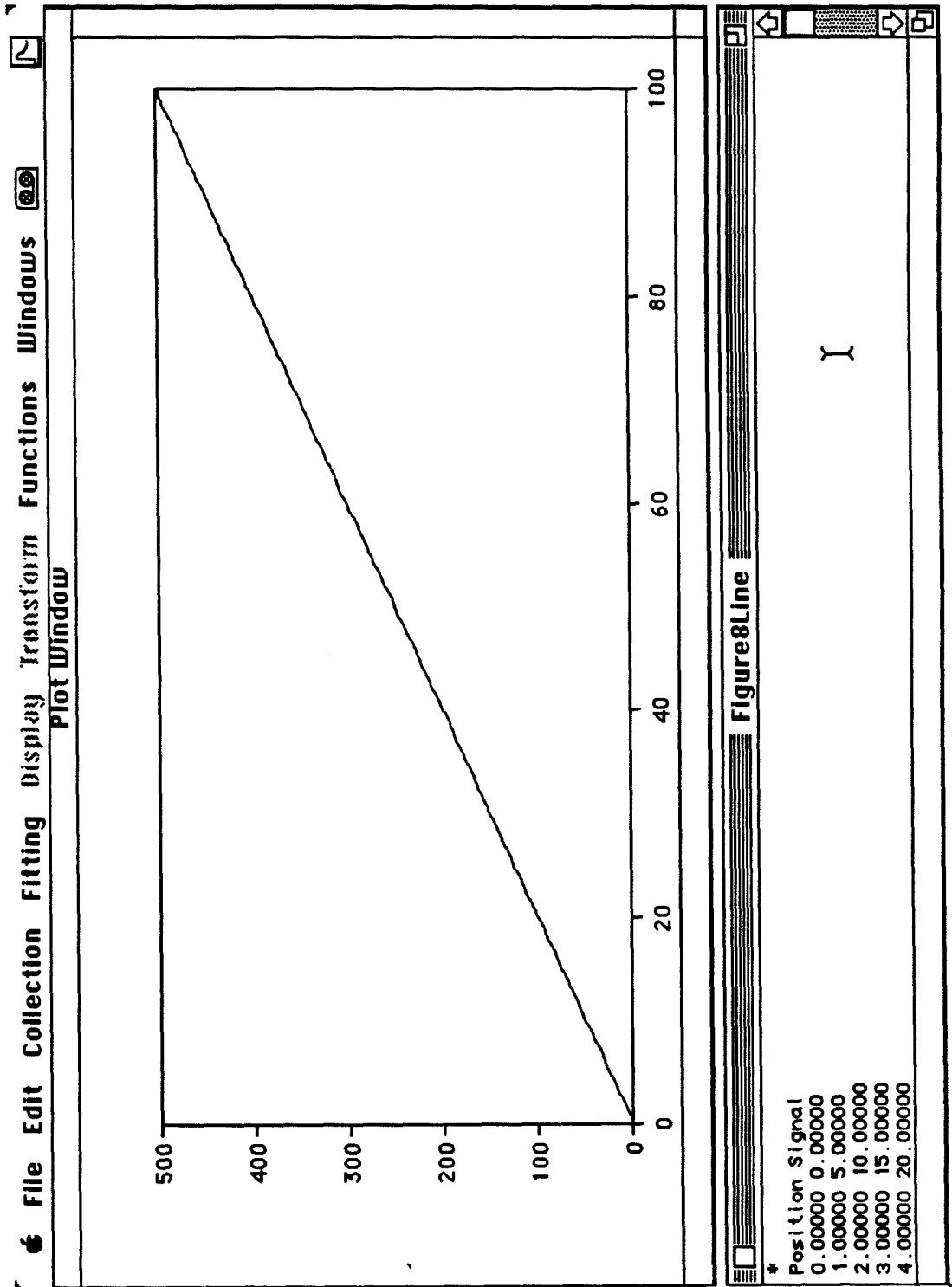


Figure 8

CHAPTER 7

TROUBLE-SHOOTING

7.1 INTRODUCTION

This is the known list of problems and their current fixes. Sections 7.2-7.5 relate to communication with laboratory equipment during data acquisition. Section 7.6 deals with crashes that are due to improper data file formats. Finally, Section 7.7 is concerned with a rare problem regarding the program development environment.

7.2 LOSS OF COMMUNICATION BETWEEN THE COMPUTER AND DATA ACQUISITION BOARDS

After a crash, the Macintosh may lose track of the NB-DMA-8-G board, which is used for GPIB-488 communication with the CAMAC crate. Verify the problem using the Control Panel through the Apple menu. The control panel will indicate that no NB-DMA-8-G board is in a slot, or that the NB-DMA-8-G board is there but not active. To recover from this problem, first try rebooting the Macintosh. If this does not help, try turning off the Macintosh with the power switch in the back, wait a few seconds, and turn it back on. So far, assuming no hardware damage, this always solves the problem. If things still do not work, try reinstalling the NI-488 software (Section 6.3). Turning off the Macintosh via the power switch in the back is an abnormal procedure, so the reboot switch should always be tried first.

The NuBus board associated with the boxcar is the NB-M10-16H-9. The NB-M10-16H-9 must be connected to the NB-DMA-8-G to work properly. So far the problem seen with the NB-DMA-8-G board has not been observed with the NB-M10-16H-9 board.

7.3 CRASHES DUE TO A BAD TRIGGER

When using the boxcar, error number -76 (overflow error) has been seen. This error has three possible causes. First, the NB-M10-16H-9 is connected to a trigger after data acquisition begins. Second, the trigger load setting on the Stanford Pulse Generator (use the output button on the pulse generator to set the load) is wrong. For the NB-M10-16H-9 the load setting is High Z, versus 50 Ohms for the CAMAC crate. Only the NB-M10-16H-9 board has exhibited sensitivity to the load setting. Third, a spurious trigger occurred. The rate of spurious triggers may be related to the load setting. A checkloop has been installed to prevent an occasional bad trigger from giving the -76 error. No data point is taken until all initial error checks are completed. If a bad trigger occurs, the data point is thrown away and the program tries to take the data point again from scratch. The program stops if 20 consecutive bad triggers occur, since presumably something is seriously wrong with the trigger source.

7.4 CRASHES THAT ARE DUE TO THE DELAY LINE UNIDEX CONTROLLER

At random times the Unidex delay line controller crashes. During a crash, the controller stalls and sends no string back to the Macintosh. Another problem, not directly resulting in a crash, is that the serial request returned string is not always the required % sign. This % sign problem is not fatal since the returned string is not used. The crash has been traced to a loss of synchronization between the Macintosh and the controller. After a crash, the controller still communicates with the Macintosh when using Red Ryder (a RS-232 communication utility program). Delay line motion is resumed if the controller is cleared to power up conditions or is sent a number of serial polls. Currently the program waits 20 seconds for a returned string from the controller. 20 seconds should be more than enough time for the delay line to complete its motion. If no string is received, then the

program will send 25 serial polls every 20 seconds to the controller until the delay line moves. The computer will emit a beep for each serial poll sent. So far, sending serial polls solves the problem. If all else fails, reboot the computer and controller. The synchronization loss may be due to the controller or to the RS-232 cable being flooded by excess RF noise, large amounts of RS-232 traffic in the cable from strings being sent and echoed, or to something else.

7.5 CRASHES THAT ARE DUE TO THE DATA ACQUISITION BOARDS OR BAD DATA ACQUISITION SYSTEM FILES

This crash is manifested by either a system error, or by a complete failure of one of the NuBus boards to respond. There are two possible reasons for this problem. First, the the NB-M10-16H-9 and NB-DMA-8-G boards are not connected to each other (via 50 pin connectors on each board). Second, the **NI-488 Init** file in the System Folder is erroneous. By default, the init file provides enough room in the system file for one of the data acquisition NuBus boards. When a second board is used, the init file needs to be expanded in order to accomodate the second board.

The solution to an erroneous **NI-488 Init** file is straightforward [1,2]. The **NI-488 Init** file is opened using **ResEdit**. Two items, called **INIT** and **sysz**, appear. **INIT** remains unchanged, but **sysz** needs to be ungraded. The first line of **sysz** should be changed from **00000000 0001 0000 0000** to read **00000000 0002 0000 0000**. Only the middle two sets of four numbers (*e.g.*, **0001 0000**) are adjustable. Save the changes to the **NI-488 Init** and reboot the computer. No changes were made to the **LabInit** file, but for reference the first line reads as **00000000 0000 C000 00?0** (the question mark is actually upside down).

7.6 CRASHES THAT ARE DUE TO A BAD DATA FILE

Crashes that are due to bad data files are indicated in several ways. First is that the **Data Window** shows nonsense, the **Plot Window** may or may not show a plot, and program operation freezes. Second is that the **Data Window** shows more than two columns of data, and the **Plot Window** shows nonsense. Third is that the **Data Window** shows two columns of data, but some data analysis routines (e.g., those in the **Display** menu) give incorrect plots. Fourth is that when a file is opened, the **Data Window** title is correct, but the **File** menu is highlighted and nothing is shown in the **Data** or **Plot Windows**. Most of the time, the problem can be traced to an erroneous text file structure (Chapter 4, Section 7).

There are four known ways in which these errors can happen. First, the file may not be saved as tab-delimited TEXT. Second, the file may be in TEXT format, but may possess more than two columns. Third, the file length is more than 32K lines. Fourth, the data file (especially if it is data taken with earlier program versions) may contain a duplicate of the first or last data point. The first problem is solved by going back to the application that created the file and saving the file again in TEXT format. To solve the second problem, go back to the data file and eliminate the excess columns. The routine that reads a data file (in the source file **Decode.c**) is set up for only two columns. The third problem is solved by going back to the data file and eliminating excess lines. The 32K restriction is the maximum number of lines allowed in a standard Toolbox text file record. The fourth problem is solved by eliminating the duplicate data point. Some **Display** menu options use the first or last data point in the file as a reference. For example, the **Selective Plot** option uses the first point to establish the location of the selected data range with respect to the location of plotting axes on the screen. If a duplicate first point is present, the routine gets confused.

7.7 CRASH DUE TO THE DEVELOPMENT ENVIRONMENT

This crash is rare, and is manifested by a previously working Think C project malfunctioning for no apparent reason. The project works satisfactorily in some respects, but consistently fails in others. The crash has only been observed while the program code was being extensively modified. Presumably, this means that the project file has lost track of the location of a source file in memory.

Assuming that the crash cannot be traced to some error in the program code, then there are three possible solutions. First, the project can be unloaded and then reloaded. Second, if the crash can be localized to a particular source file(s), those file(s) can be deleted from the project and then re-added. In the worst case, the third possibility is to recreate the project and reload the entire source code from scratch. The procedures for implementing the three solutions are given in Reference 3.

7.8 REFERENCES

1. (a) National Instruments, NB-M10-16 User Manual, February 1988.
(b) National Instruments, NB-DMA-8-G User Manual, 1988.
2. (a) National Instruments, LabDriver Software Reference Manual, January 1988.
(b) National Instruments, NI-488 Software Manual for the Macintosh, August 1988.
3. Symantec, *Think C User's Manual, version 3* (1988).

CHAPTER 8

DEVELOPMENT ENVIRONMENT PARAMETERS

This chapter documents the Think C options under which the programs were developed [1]. If an option is not listed, it was not used. The Think C Source debugger and MacsBug were used to debug the program. MacsBug, which works in assembly language, was used with various Debug statements. Debug statements are listed in the file `Utilities.c`. The options used are listed below.

Search Option:	Ignore case box checked
Code Generation:	All boxes checked except Profile box.
Source Debugger:	Use 2 nd screen box checked.

Precompilation was done with the Think C **MacHeaders** file. **MacHeaders** includes the most common declarations and low level memory globals for the Macintosh Toolbox, and is available to all project source files. To minimize compilation time, all superfluous Toolbox header files have been deleted from the project. For this program, **MacHeaders** was expanded to allow recognition of the code generated for the math coprocessor. The new version, with the changes indicated, is listed in Table I. If the original **MacHeaders** is used, preprocessor statements for the math coprocessor must be added where needed throughout the project.

To make the program function without the coprocessor, go back to the Think C project and remove all references to the coprocessor. This involves several steps. First, a new **MacHeaders** file must be created that does not contain any preprocessor statements for the 68881 coprocessor. This new **MacHeaders** replaces the one shown in the Table I. The previous **MacHeaders** does not have to be deleted, but it must be in a different folder from the Think C application. Second, one must replace all 68881 libraries with their non-68881 equivalents (*e.g.*, `stdio` instead of `stdio881`). Third, the code generation option for the 68881 should be unchecked. Finally, the entire project needs be recompiled.

As of this writing, version 4 is the most current Think C development environment. Think C version 4 will automatically convert projects created with version 3. However, several items must be noted. Now that C has an ANSI standard, Version 4 is now closely in line with the ANSI C standard. Normally this should not be a serious concern since the version 3 compiler was already close to the ANSI standard. However, it is possible that small adjustments in the code may have to be made in order to comply fully with the ANSI standard imposed by version 4. In addition, the names and organization of the version 4 libraries are different from version 3. Therefore, one will need to replace all version 3 libraries. This includes the MacTraps library. Finally, the MacHeaders file given in Table 1 will be unnecessary. It should be replaced by the MacHeaders file given by version 4. MacHeaders of version 4 does not need to be modified for the math coprocessor. For further information, consult the version 4 documentation.

REFERENCE

1. Symantec, *Think C User Manual, Version 1* (1986).

TABLE I**New MacHeaders for using the 68881 coprocessor**

These declarations are the original MacHeaders.

```
#include "ControlMgr.h"
#include "DeskMgr.h"
#include "DeviceMgr.h"
#include "DialogMgr.h"
#include "EventMgr.h"
#include "FileMgr.h"
#include "FontMgr.h"
#include "HFS.h"
#include "IntlPkg.h"
#include "ListMgr.h"
#include "MacTypes.h"
#include "MemoryMgr.h"
#include "MenuMgr.h"
#include "OSUtil.h"
#include "PackageMgr.h"
#include "Quickdraw.h"
#include "ResourceMgr.h"
#include "ScrapMgr.h"
#include "SegmentLdr.h"
#include "StdFilePkg.h"
#include "TextEdit.h"
#include "ToolboxUtil.h"
#include "WindowMgr.h"
#include "asm.h"
#include "pascal.h"
```

These preprocessor declarations were added for the math coprocessor and standard error checking.

```
#ifndef _MC68881_
#define _MC68881_
#include "Math.h"
#endif

#ifndef _ERRORCHECK_
#define _ERRORCHECK_
#endif
```

TABLE I (continued)

These declarations are not part of the new or original MacHeaders. They can be included when necessary.

```
#include "Appletalk.h"  
#include "nAppletalk.h"  
#include "Color.h"  
#include "ColorToolbox.h"  
#include "DeskBus.h"  
#include "DiskDvr.h"  
#include "PrintMgr.h"  
#include "ScriptMgr.h"  
#include "SCSIMgr.h"  
#include "SerialDvr.h"  
#include "SlotMgr.h"  
#include "SoundDvr.h"  
#include "SoundMgr.h"  
#include "StartMgr.h"  
#include "TimeMgr.h"  
#include "VRetraceMgr.h"
```

APPENDIX

UPDATE NOTES FOR NATIONAL INSTRUMENTS NI-488 AND LABDRIVER SOFTWARE

This appendix is taken from the NI-488 Distribution Disk provided by National Instruments, Inc. 1989

National Instruments Macintosh NI-488 Release 2.3

Copyright 1988, 1989 National Instruments Corporation.

All Rights Reserved.

This file contains up-to-date information not in the "NI-488 Software for the Macintosh User Manual" (part number 320102-01). This information includes release notes for all versions of this software. The information pertaining to the latest version is at the top of this file.

Important differences between NI-488 Release 2.3 and Driver Software Version 2.2:

Two handler functions, `ibdev` and `ibln`, were added to allow run-time configuration and device presence testing. The board index parameter of `ibdev` is a value in the range 0 through 5.

In addition to the remarks about the function `ibdev` in the August 1989 edition of the "NI-488 Software for the Macintosh User Manual," you should not call `ibfind` to open a device after using `ibdev` because `ibfind` can open on-line devices. Doing so changes `ibdev`'s dynamic configuration of the device to the default configuration as set by the configuration program. If the `ERR` bit of `ibsta` is set, the error code in `iberr` will indicate what the problem is so that your application can take appropriate action. The error code can be one of the following.

EDVR: No GPIB handler is loaded (no handler INIT in the System Folder or no GPIB board installed) or too many devices are open by previous calls to `ibdev` and `ibfind`. The Macintosh OS error code is returned in `ibcnt`.

EARG: If `ibdev` returns a negative number, the `bus_index` is out of range; otherwise, one of the other arguments is out of range.

ENEB: Nonexistent GPIB board in the slot associated with `bus_index`.

ECAP: The handler has no capability for this call. Ask the user to install the NI-488 Handler INIT Release 2.3 or higher.

The `ibfind` function returns status in `ibsta` and an error code in `iberr`. If the `ERR` bit of `ibsta` is set, the error code in `iberr` will indicate what the problem is so that your application can take appropriate action. The error code can be one of the following.

EDVR: No GPIB handler is loaded (no handler INIT in the System Folder or no GPIB board installed). The Macintosh OS error code is returned in `ibcnt`.

EARG: The board or device name is too long or no such name exists.

ENEB: Nonexistent GPIB board associated with board or device name.

The Microsoft BASIC interface was replaced with the Microsoft QuickBASIC interface.

In the utility application `ibic`, the `ibrdf` and `ibwrtf` file I/O functions accept file names, and the `ibfind` function accepts a device name enclosed in double quotation marks. This method allows names with white-space and special characters to be used.

Important differences between Driver Software Version 2.2 and Driver Software Version 2.1:

The ibconf configuration program version 1.3, in this release, runs correctly with Apple's System Software 6.0.1 and 6.0.2 on the Macintosh IIfx. The ibconf version 1.2, in the previous release, ran correctly with System Software 6.0, but does not with the later versions.

The NB Handler INIT in this release correctly handles driver ID assignments. The NB Handler INIT had a bug that caused an INIT driver whose ID was changed on a collision during a previous startup to be overwritten by a driver involved in a new ID collision.

The C language interface has been upgraded for Macintosh Programmer's Workshop 3.0.

Compile LI.c with the command:

```
c -d MPW LI.c
```

For MPW 2.0, compile LI.c with the command:

```
c -d MPW2 LI.c
```

Note: The November 1988 edition of the "NI-488 Software for the Macintosh User Manual," page 4B-1, has an error in the MPW command to compile LI.c; there should be a space between the flag -d and the name MPW.

Important differences between Driver Software Version 2.1 and NI-488 Version 1.0:

The C language interface, LI.c, can be compiled with either THINK C or Macintosh Programmer's Workshop C. Refer to Section 4B of "NI-488 Software for the Macintosh User Manual." A source code example is in the folder "Mac II Board Find" to demonstrate finding any type of National Instrument's boards.

The default for device to slot associations has changed from slot one to slot six for all devices. You can use the ibconf configuration program to change the associations.

The file spooling commands, ibwrtf and ibrdf, are now three times faster than the previous versions.

The NI-488Test program now puts the handler into a known state before starting the test. The test will abort if no GPIB boards are present. It will begin automatically if only one GPIB board is present and will display the boards and prompt for selection if more than one board is present.

The utility programs, NI-488Test and ibic, now quit in response to cmd-Q.

A HyperTalk language interface and examples have been included on a separate disk.

The handler has these corrections:

1. One byte reads no longer fail.
2. NB-GPIB handler now works in DMA mode.
3. Reads and writes are no longer limited to 64K bytes.
4. Wait for SRQI no longer returns immediately.
5. ibloc, ibclr, ibppc, ibtrg, and ibpct functions now report errors to iberr.
6. Mac SE handler now detects the presence of DMA controller.
7. The handler is loaded into memory at startup preventing the system from giving memory needed by the handler to other INIT's or cdev's.
8. Serial poll now sends the serial poll disable command if it timed out.
9. The device function ibwrtf no longer bombs if there are no devices at the configured address.
10. Reads and writes no longer fail if the data buffer address is odd.
11. Serial Poll of a device that set END with its response byte no longer puts the handler in data hold off state until the next ibonl.
12. The device name length has been increased to 31 bytes and will truncate longer names (ibconf will accept names up to 255 bytes in length). Previously, device names of 17 bytes or more would cause ibfind to bomb.

The example program pbcontrolcalls.c is no longer missing storage allocation for a structure that it uses.

The ibic utility no longer bombs if the function ibrd is given a count greater than 32,767. The new maximum count, 65,535, is a limitation of the utility, not the handler. The handler will accept counts to 2,147,483,647 or the limit of available memory.

How to Remove NI-488 v1.0 and LabDriver v1.0

This Driver Software Version replaces NI-488 v1.0 and LabDriver v1.0, which were installed with Apple's Installer program into the System File. Three methods are given by which you can remove NI-488 or LabDriver versions 1.0.

Removing NI-488 Version 1.0 and LabDriver Version 1.0 from the Macintosh II

If you have the NI-488Init and/or the LabInit file in your System Folder, then NI-488 v1.0 and/or LabDriver v1.0 need to be removed before installing the new driver software.

The "NB Handler INIT" replaces both NI-488 v1.0 and LabDriver v1.0. To remove NI-488 v1.0, follow these steps:

1. Drag the NI-488Init file from your System Folder.
2. Shutdown the Macintosh and insert the original NI-488 Version 1.0 diskette, "NI-488 for Macintosh," into a diskette drive.
3. Start up your Macintosh from the NI-488 Version 1.0 diskette. This procedure causes the Macintosh to use the system on the diskette.
4. Double-click on the Installer application contained on that diskette.
5. Click on the line "NI488 for the Mac II (v1.0)" in the window and click the Remove button. The installer will remove the handler resources from the System File.
6. Restart the Macintosh.

To remove LabDriver v1.0, follow these steps:

1. Drag the LabInit file from your System Folder.
2. Shutdown the Macintosh and insert the original LabDriver Version 1.0 diskette, "LabDriver Software Package Installation," into a diskette drive.
3. Start up your Macintosh from the LabDriver Version 1.0 diskette. This procedure causes the Macintosh to use the system on the original diskette.
4. Double-click on the Installer application contained on that diskette.
5. Click on the line "National Instruments LabDriver (v1.0)" in the window and click the Remove button. The installer will remove the handler resources from the System File.
6. Restart the Macintosh.

Removing NI-488 Version 1.0 from the Macintosh SE

If you have the NI-488Init file in your System Folder, then NI-488 1.0 needs to be removed before installing the new driver software. The "SE Handler INIT" replaces NI-488 v1.0. To remove NI-488 v1.0, follow these steps:

1. Drag the NI-488Init file from your System Folder.
2. Shutdown the Macintosh and insert the original NI-488 Version 1.0 diskette, "NI-488 for Macintosh," into a diskette drive.
3. Start up your Macintosh from the NI-488 Version 1.0 diskette. This procedure causes the Macintosh to use the system on the original diskette.
4. Double-click on the Installer application contained on that diskette.
5. Click on the line "NI488 for the Mac SE (v1.0)" in the window and click the Remove button. The installer will remove the handler resources from the System File.
6. Restart the Macintosh.

Alternate Methods of Removing NI-488 and LabDriver Versions 1.0.

In the discussion that follows, both NI-488 v1.0 and LabDriver v1.0 will be referred to as "handler v1.0" or "the handler."

Using the installer is the preferred method of removing handler v1.0 from your system. If you don't have the handler v1.0 distribution disk and you know how to replace your System File or use ResEdit, then you can use one of the alternate methods to remove the handler.

The handler can be removed by starting up from Apple's System Tools disk, removing the System File that has the handler v1.0, and running the installer; however, you will also remove any desk accessory or font that has been added to the system.

If you don't want to replace the System File, you can remove the handler with ResEdit. With ResEdit, open the DRVR resources of the System File and make a note of the driver ID's of all the National Instruments drivers. These are named drivers with the names listed below. In some cases, only a few of these drivers will be present. Then remove these DRVR resources and all DATA and STR# resources owned by any of these drivers. Below are the names and default ID's. The ID's may have been changed by the installer. Make sure that the DATA and STR# resources are owned by one of the drivers listed before removing it. Select the DATA or STR# resource and get info to identify the owner.

Driver Name	Default ID
".NB-MIO"	51
".NB-DIO"	52
".NB-DMA"	53
".NB-MIO2"	54
".LabDriver"	55
".NB-AO-"	56
".GPIB Driver"	57
".NB-GPI"	59

Refer to Section Two of the "NI-488 Software for the Macintosh User Manual" for the new handler's installation procedure.

If after you restart your computer you get the error messages

"The driver installation failed."

"Remove old or duplicate NI drivers."

then either NI-488 v1.0 or LabDriver 1.0 is installed or another copy of "NB Handler INIT" or "SE Handler INIT" is in the System Folder under a different name. Remove any older version of the driver software from the System Folder. If no other driver software file is in the System Folder, then version 1.0 of the handler needs to be removed.